CHALMERS
UNIVERSITY OF TECHNOLOGY

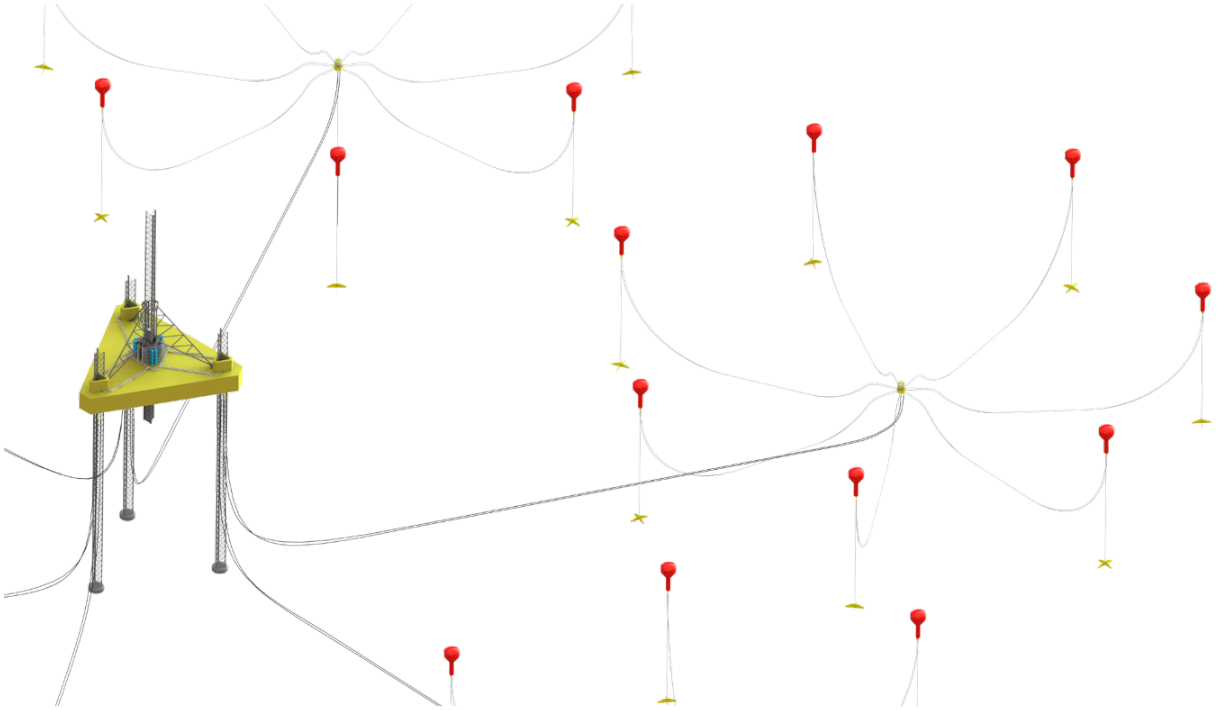

Optimal Control for Wave Energy Generation

Modelling, Simulation and Control of a Wave Energy Farm with Gravity-Based Energy Storage

Master's thesis in Systems, Control and Mechatronics

AHMED RASHID

Department of Electrical Engineering
CHALMERS UNIVERSITY OF TECHNOLOGY
Gothenburg, Sweden 2018

Master's thesis 2018:EX038

Optimal Control for Wave Energy Generation

Modelling, Simulation and Control of a Wave Energy Farm
with Gravity-Based Energy Storage

AHMED RASHID

CHALMERS
UNIVERSITY OF TECHNOLOGY

Department of Electrical Engineering
Automatic Control Group
Chalmers University of Technology
Gothenburg, Sweden 2018

Optimal Control for Wave Energy Generation
Modelling, Simulation and Control of a Wave Energy Farm
with Gravity-Based Energy Storage
AHMED RASHID

Supervisors: Assoc. Prof. Balazs Kulcsar, Chalmers University of Technology
Lecturer Anders Hultgren, Blekinge Institute of Technology
CEO Mikael Sidenmark, Ocean Harvesting Technologies AB
Examiner: Assoc. Prof. Balazs Kulcsar, Chalmers University of Technology

Master's Thesis 2018:NN
Department of Electrical Engineering
Automatic Control Group
Chalmers University of Technology
SE-412 96 Gothenburg
Telephone +46 31 772 1000

Cover: Visualization of the hydraulic collection system with central tower for electric power generation.

Typeset in LaTeX
Gothenburg, Sweden 2018

Optimal Control for Wave Energy Generation
Modelling, Simulation and Control of a Wave Energy Farm
with Gravity-Based Energy Storage
AHMED RASHID
Department of Signals and Systems
Chalmers University of Technology

Abstract

This thesis work is a part of a collaboration project between three Swedish WEC developers - Ocean Harvesting Technologies (OHT), CorPower Ocean (CPO) and Waves4Power (W4P) - with grant support from the Swedish Energy Agency. The collaboration project consists of the system design and development of wave energy systems that combine buoy technology from CorPower and Waves4Power and collection and power smoothing technology from OHT. In this thesis, an algorithm is developed to generate dynamic model for a hydraulic collection system with any topology. The generated hydraulic collection system model is integrated with OHT's gravity-based accumulator model and with hydrodynamic models of wave energy converters obtained from CPO and W4P in order to understand the potential benefits of replacing power smoothing and electricity generation in the buoys with a system where buoys instead transfer captured energy via a hydraulic connection to the hub system for centralized smoothing with the OHT's gravity storage and conversion to electricity. Moreover, a preview-based discrete-step damping force control strategy is implemented to improve the power capture performance of wave energy converters. The simulation results with the new control strategies and OHT's hydraulic collection system are compared against results obtained from standalone buoys with electrical power collection. Furthermore, a simple state machine and a controller is implemented to show the capability of the gravity storage to provide ancillary services like frequency control to the grid to increase the revenues from the plant. Finally, a test rig was built and a HIL simulation environment is set up to demonstrate the working principle of the OHT's collection system with gravity storage and central conversion to electricity in combination with simulated buoys from CorPower and Waves4Power and to validate the developed models.

Keywords: wave energy converter, model predictive control, hydraulic collection, power smoothing, energy storage, time shifting, constant damping, lump-parametric modelling, multi-pump control, corpower, waves4power, ocean harvesting, scaling rules, graph theory, ancillary services,

Acknowledgements

This report is the result of a Master's thesis project carried out in the Department of Signals and Systems at Chalmers University of Technology in collaboration with three Swedish WEC (wave energy converter) companies - Ocean Harvesting Technologies AB, CorPower Ocean AB and Waves4Power AB - with grant funding from the Swedish Energy Agency.

First of all, I would like to express my gratitude to the Swedish Energy Agency for supporting the initiative for creating the possibility for WEC companies to exchange ideas and knowledge that will foster the development of wave energy solutions. I am also greatly thankful to the WEC companies for providing their simulation models that enabled the conduction of this thesis work.

I would like to convey my sincere thanks to my supervisor Assoc. Prof. Balazs Kulcsar at Chalmers University for his support and encouragement from the very beginning of the project. Throughout the project he has been a really kind and a caring mentor to me. I will always remember the exciting discussion that we had on Skype during the project and the discussions that we had before the project in the tram on the way to university.

I don't know how many times I need to say "Thank You!" to my mentor Anders Hultgren at Blekinge Institute of Technology in order to express my endless gratitude for what he has done and given to me from the very beginning of my university education. Without his support and trust in me, I would have not been able to realize my dream to study systems and control at Chalmers University. I highly value his support and guidance and, most importantly, his accessibility at any time when you turn to him for help.

Furthermore, I would like to convey my special thanks to Mikael Sidenmark, CEO at Ocean Harvesting Technologies, for believing in me and giving me the chance to contribute in finding a solution for the world's energy problem. His continuous support throughout the whole project helped me to go beyond the proposed objectives of the thesis. I highly appreciate his commitment to what he believes in and that it is a great source of motivation to me.

All words are insufficient to express my gratitude to my beloved parents, Gullu and Metin Rashid, who has literally sacrificed their lives for me and for my brother so that one day we do not need to do the same sacrifice for our children.

I am extremely thankful to my brother Alkan Rashid and girlfriend Hulya Bayram who have always been beside me.

I also want to express the debt that I owe to Farhrettin and Maya Yilmaz, for the support and love that they have given to me during my stay in Sweden. They were like a second family to me.

Finally, I want to thank to all my friends and colleagues who have supported me with any means during the thesis and my studies.

Ahmed Rashid, Gothenburg, June 2018

Contents

List of Figures

List of Tables

1

Introduction

1.1 Introduction

Ocean waves provide enormous energy potential that outweighs the energy potential of any other renewable energy resource. It is expected that once wave energy establishes as a mature industry, it will provide the biggest contribution to the solution of the world's energy problem. Wave energy has been studied since 70's and a lot of wave energy converter concepts have been invented and developed. However, due to the multidisciplinary complex nature of developing an economically viable solution to harvest this resource, so far none of these concepts has proven to be a good enough solution. Therefore, the potential of wave energy remains still untapped. One of the main reasons for the lack of proliferation of wave energy is that harnessing the irregular reciprocating motion of the sea is not as straightforward as, for example, extracting energy from the wind. The captured power from the waves is greatly fluctuating with quite high peak to average ratio. Therefore, the machinery needs to be sized in order to cope with the peaks in the input power. However, increasing the size of components increases the capital expenditure and reduces the capacity factor of the system, thus, making it an unattractive solution. In order to decrease the cost of the system it is crucial that the power is smoothed efficiently at an earlier stage in the transmission before converted to an electrical power. The power smoothing technology needs to be implemented without compromising the power capture performance of the wave energy converter. Therefore, smoothing the mechanical power input to the generator at the same time as the damping force is adjusted for every wave to maximize power capture is one of the main issues that wave energy converter developers should face and provide good solutions to.

Moreover, increasing power quality and controllability to match power production to demand is increasingly important with the growing mix of renewables into the grid. Currently, the power production facilities get paid only for the quantity of energy sold to the grid. However, in future this pricing policy is likely to be changed to encourage also the quality and the controllability of the produced power. Power generators that can follow precisely the demand are likely to be compensated with a higher rate than the ones that cannot provide the same level of detail. Therefore, in order to be competitive in future market, wave energy converter developers must address the question of how to provide more control on the produced power.

It has been a well known fact that the wave energy converter must be in phase with incoming waves since the very beginning of wave energy research, or said in a different way, the natural frequency of the system must be close or equal to the

frequency of the waves in order to achieve optimal power absorption. However, due to the fact that the frequency of the wave changes, it is necessary either to be able to tune the natural frequency of the wave energy converter for each wave or to design a system with a wide baseband that covers all the frequency range of the waves. Once optimal phase condition is achieved, the problem reduces to finding the optimal damping/machinery force to extract maximum amount of energy from the waves. However, the limitations of components impose constraints on the system reducing the power capture performance of the buoy.

Most of the wave energy research has been focused on developing models and control techniques for a single buoy. Modelling and control of arrays of wave energy converters has gained attention only in the recent years due to the fact that several pre-commercial and commercial arrays are getting prepared to be installed. Studying the array behaviour is important because of many aspects. For instance, understanding the hydrodynamic wave interactions in an array will help to optimize the layout of the array in such a way to reduce the negative array effect on power absorption, to minimize power transmission costs etc. Moreover, studying the wave energy converters in an array is necessary in order to understand the smoothing effect on the power from all the buoys in the array. This in turn assists in sizing the machinery at the collection point.

1.2 Background

This section outlines the working principles and key technologies and features offered from the companies that participated in the project. Furthermore, it describes the adaptation of the WEC's from CorPower and Waves4Power for integration to OHT's collection system with the gravity storage. In addition, it gives an overview of the hydraulic collection system and tower, and outlines the main design changes during the project. In the end, the environmental condition that were used in the simulation study are discussed.

1.2.1 Ocean Harvesting Technology

1.2.1.1 Technology overview

Ocean Harvesting Technology (OHT) offers a high-pressure hydraulic collection system for wave energy arrays with gravity-based energy storage and conversion to electricity on a central platform. A weight is lifted with a rack and pinion drive on the platform to smooth captured power and output constant power from a set of generators. The storage provides time shifting of power production and can be charged with power from the grid in periods of low demand, to increase the plant utilization and revenues by supplying a variety of real time grid services such as frequency regulation. The weight also provides the hydraulic collection system with constant pressure, which can be combined with variable displacement pumps in the WEC´s to control the damping force. OHT offers generic PTO solutions to WEC developers with damping force and phase control features required for a high power capture

performance. Discrete damping force control is provided through an arrangement with multiple fixed displacement pumps connected to a common rack.

1.2.1.2 Working principle

Pressurized fluid is pumped from the wave energy converters through a hydraulic piping system to the hydraulic motors in a set of drive units positioned around a gear rack with an integrated counterweight in the collection tower. A concept design of the collection platform with the drive units and the counterweight is shown in figure 1.1.

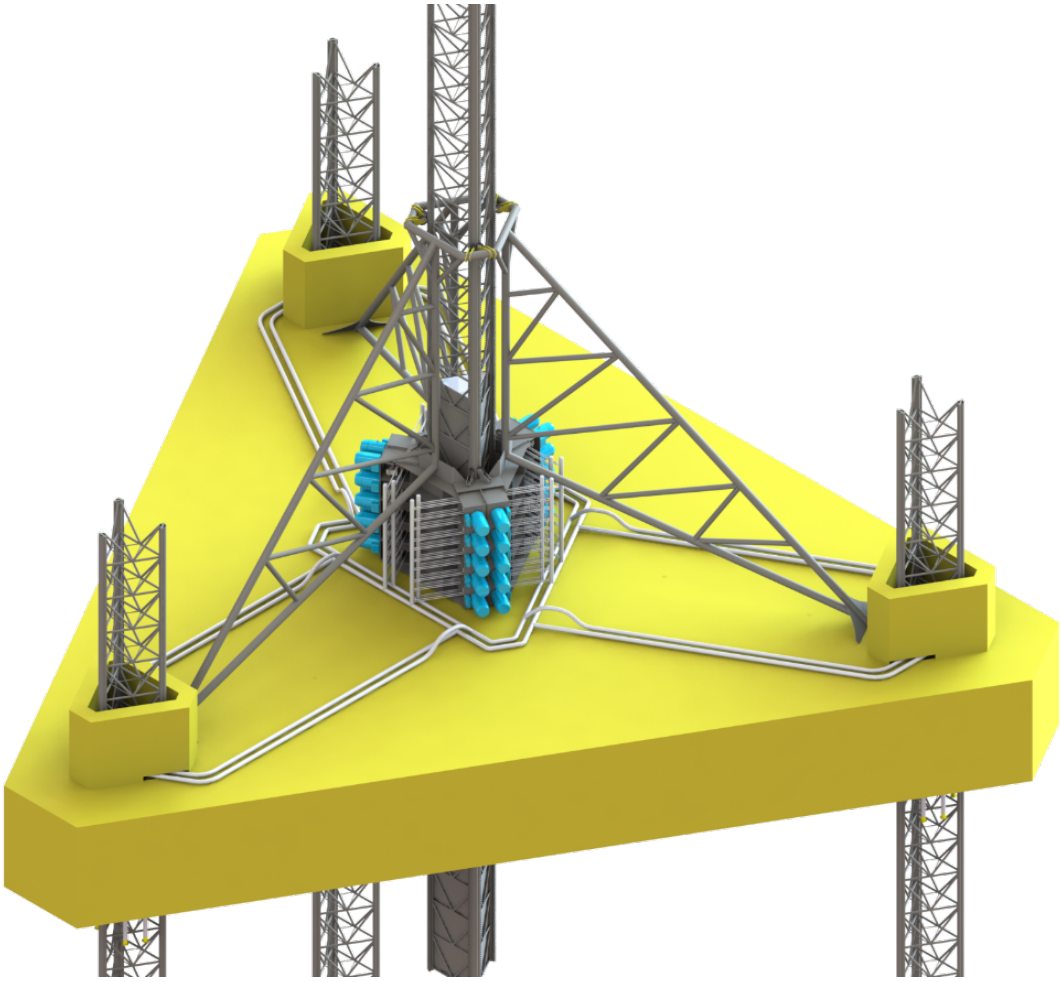

Figure 1.1: OHT´s collection platform with gravity storage.

Each drive unit comprises a hydraulic motor, a pinion, a generator and a 3-way planetary gearbox in the form of a wheel drive that connects these components. This way the accumulator can be charged by the hydraulic motors at the same time as it is discharged or charged by the generators. The concept design of a drive unit is shown in figure 1.2.

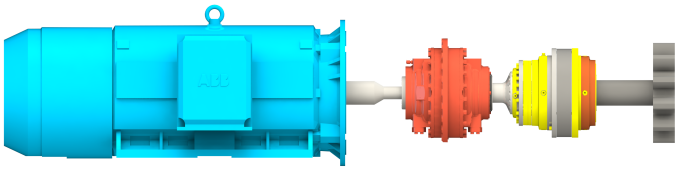

Figure 1.2: Concept design of OHT's tower drive unit.

Any difference between input and output power either lifts or lowers the weight to store or retrieve energy. The input flow to the motors varies with the wave motions and the speed of generator can be controlled to output power corresponding to the average captured power depending on the sea state. Output power can also be controlled to meet the demand changes on the grid, e.g. to time-shift power production depending on the grid frequency. In mild sea states with low power input from the WEC array, the accumulator can be charged by the generator with power from the grid during period of low demand, to be returned when the demand is high. This way the revenues from the power plant can be increased from time shifting of power production from the wave energy array as well as from grid storage services.

Favored by the constant pressure in the collection system, OHT is capable of providing PTO functionality to control the damping force of wave energy converters in a discrete manner by using multiple fixed displacement radial piston pumps that are connected through pinions to a common rack, as shown in figure 1.3.

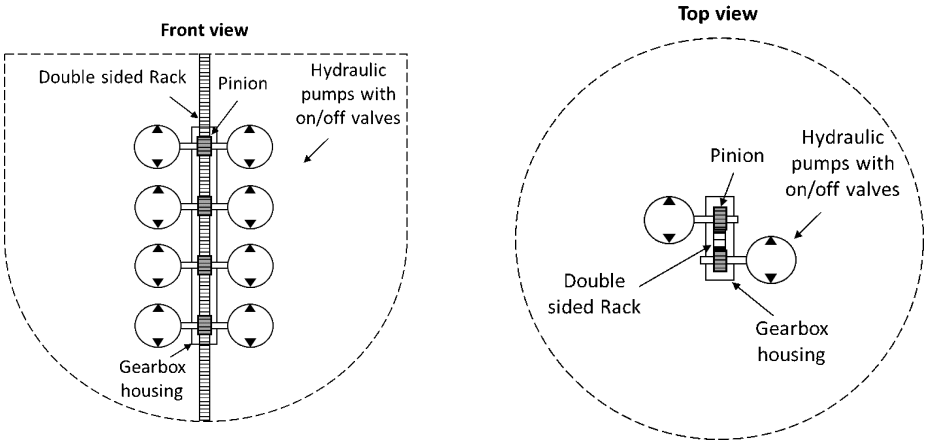

Figure 1.3: Front and top view of OHT's power take-off

Each pump unit can be engaged or disengaged from the hydraulic circuit which is common to all pumps and which has constant pressure, provided by the counterweight. This way the total displacement and, hence, the force applied to the rack can be changed in discrete steps. In order to prevent shock loads, the engagement and disengagement of pumps must occur at the turning points of the rack, i.e. when the velocity is equal to zero. The design of the selected radial piston pumps makes it

possible to disengaged pumps from the circuit without circulating any fluid. Therefore, there is almost no drag losses from disengaged units. Hence, the multi-pump force control arrangement is very efficient through the entire force range available.

1.2.2 CorPower

1.2.2.1 Technology overview

CorPower offers a lightweight resonant point-absorber device [1] that absorbs energy from the combined heave and surge motion. The buoy has 250kW rated output power. A single-point mooring connects the WEC to the seabed. A pneumatic pre-tension module enables the buoy to have light weight by providing the required force to hold the buoy in the equilibrium position. A lightweight double-sided rack and a novel lightweight gearbox, called Cascade gearbox, convert the linear motion of the rack into a rotation suitable to drive a conventional electrical generator. The Cascade gearbox distributes the damping force on eight pinions, allowing the rack to have small size and light weight. Equal number of pinions are placed on each side of the rack, i.e. four pinion on each side, that allows a balanced force on the rack. The Cascade gearbox is connected to two shafts with two sets of flywheels and generators. A freewheel mechanism enables driving one set of flywheel and generator in the up stoke and the other set in the down stroke. This arrangement allows the flywheels to be used both as a temporary energy storage for smoothing power and as a means to apply high damping force without increasing the size of the generators. A novel phase control technology called WaveSpring makes the system inherently resonant over a broad bandwidth strongly increasing the power capture performance of the wave energy converter without the need for a large machinery force and real-time wave information and prediction algorithm. Moreover, WaveSpring has the capability to detune the device in storm conditions. As a result, the WaveSpring enables reducing the size of the wave energy converter and increases the survivability of the system in storms. A cut view of CorPower's wave energy converter with a zoomed view of the power take-off and the Cascade gearbox is shown in figure 1.4.

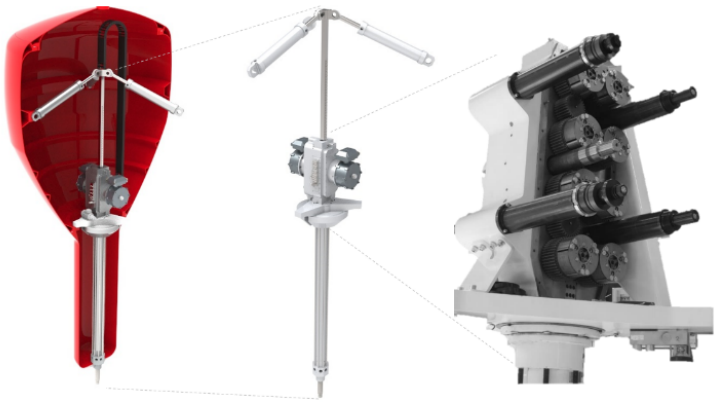

Figure 1.4: Cut view of CorPower's buoy with the power take-off inside it, [10].

[1] A point absorber is a type of oscillating wave energy converter, whose diameter is short compared to the incident wave length.

1.2.2.2 Working principle

CorPower develops a point absorber that comprises a pre-tension spring that provides a bidirectional power capture, a rack and cascade gearbox, that converts linear to rotary motion, a dual set of flywheels and generators that provides both damping and power smoothing and the so called WaveSpring technology, that acts as a negative spring to reduce the hydrostatic stiffness of the buoy and makes a light weight buoy to be resonant with the waves in a wide frequency range. A drawing of CorPower's PTO is shown in figure 1.5.

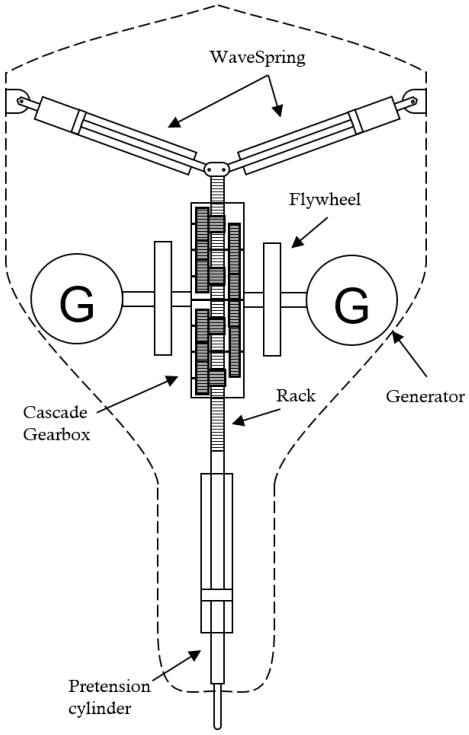

Figure 1.5: A drawing of CorPower's power take-off.

CorPower's point absorber captures energy from the combined surge and heave motion of the waves. The buoy is moored to the sea bed through a single point mooring rope connected with the pre-tension gas spring, that keeps the mooring rope tensed during both upwards and downwards motion of the buoy. The pre-tension gas spring is connected to the rack. A shaft with two sets of flywheels and generator passes through the Cascade gearbox. Each set connects to the shaft with a one-way bearing. One set locks to the shaft in the up-stroke, the other set in the down stroke and neither if the velocity of the rack is less than the velocity of both sets. For instance, when the rack starts accelerating up-wards and both sets are rotating with their own velocity, both sets will remain disengaged until the speed of the rack catches up with the speed of the set that is designed to be engaged during the up-stoke. The set will remain engaged until the rack starts decelerating. When this happens, the rack will decelerate more quickly than the disengaged set which will decelerate at a rate proportional to the damping torque from the generator, which now will be driven only by the stored energy in the flywheels. Similarly,

in the down-stoke the other set is either engaged or disengaged depending on the relative velocity of the rack and the set. In order to amplify the buoy motion and power capture, the so called WaveSpring technology is used that makes the system inherently resonant over a broad range of wave frequencies. It is basically another gas spring system, that is positioned perpendicular to the rack and that is initially compressed/pre-charged when the buoy is at zero sea level. For instance, when the buoy is moving upwards, the angle between the rack and the WaveSpring increases, and hence the spring extends and pushes the buoy up. Similarly, when the buoy is moving down, the WaveSpring pushes the buoy down.

1.2.3 Waves4Power

1.2.3.1 Technology overview

Waves4Power is developing a two-bodied point absorbing wave energy converter that consists of a buoy with a long vertical submerged tube below the buoy with open ends, a water piston inside the tube connected to a hydraulic power take-off system with on-board electricity generation and a mooring system that keeps the buoy on station without interfering with the buoy's vertical motion. Furthermore, W4P offers simple solution to prevent high forces at the end-stops that increases the survivability of the system. Currently, Waves4Power is doing full-scale trials of their 100kW-buoy at Runde site in Norway. An image of the WEC at Runde is shown in figure 1.6.

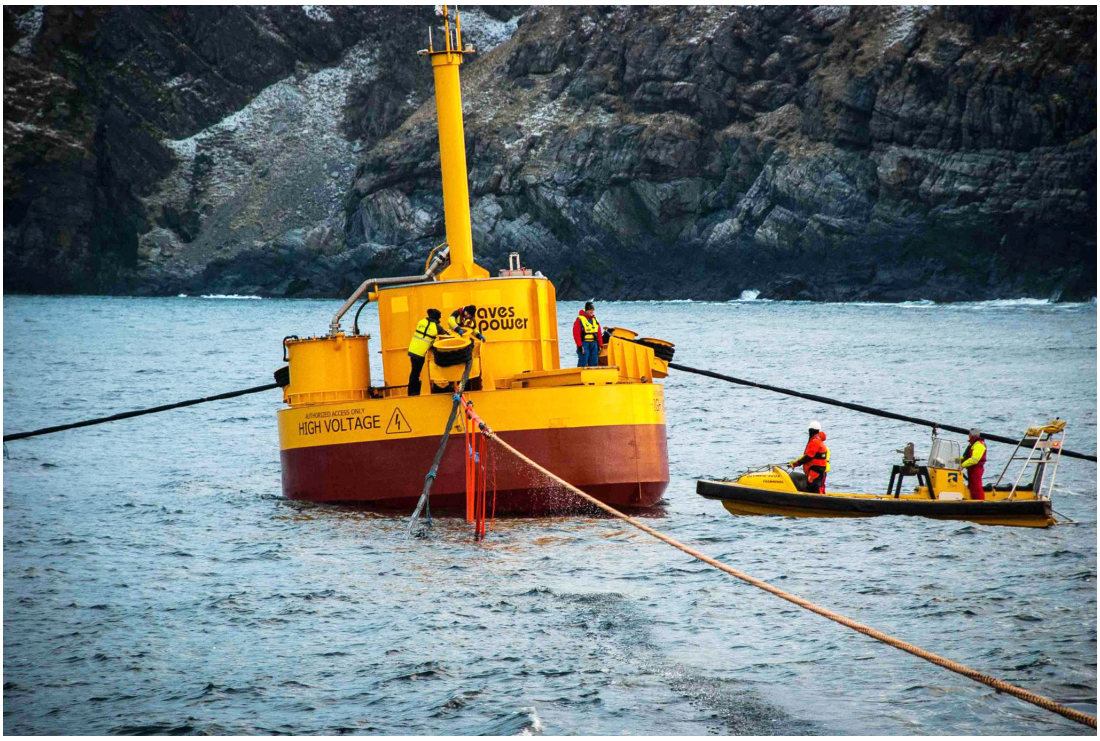

Figure 1.6: An image of the full-scale W4P buoy, installed at Runde, Norway, [11].

1.2.3.2 Working principle

The device represents a gigantic pump where two bodies act against each other. One body of the two-bodied point absorber is the buoy/tube unit and the other body is the inert water mass is the tube. The two bodies are designed to have different natural frequencies, making them oscillate out of phase when there is excitation from the waves and no damping from the power take-off. Damping the relative movement from the PTO forces them towards the same phase and allows energy to be captured by the conversion system. The power take-off system comprises of a hydraulic cylinder used as a pump, a rectifier bridge that the captured power, a hydraulic accumulator that smooths the captured power, a hydraulic motor, which converts hydraulic energy into mechanical energy, drives an on-board electric generator, that converts mechanical energy into electric energy. The piston rod of the hydraulic cylinder is connected to a large water piston situated inside the tube. The conceptual design of the buoy together with the PTO inside the buoy is shown in figure 1.7.

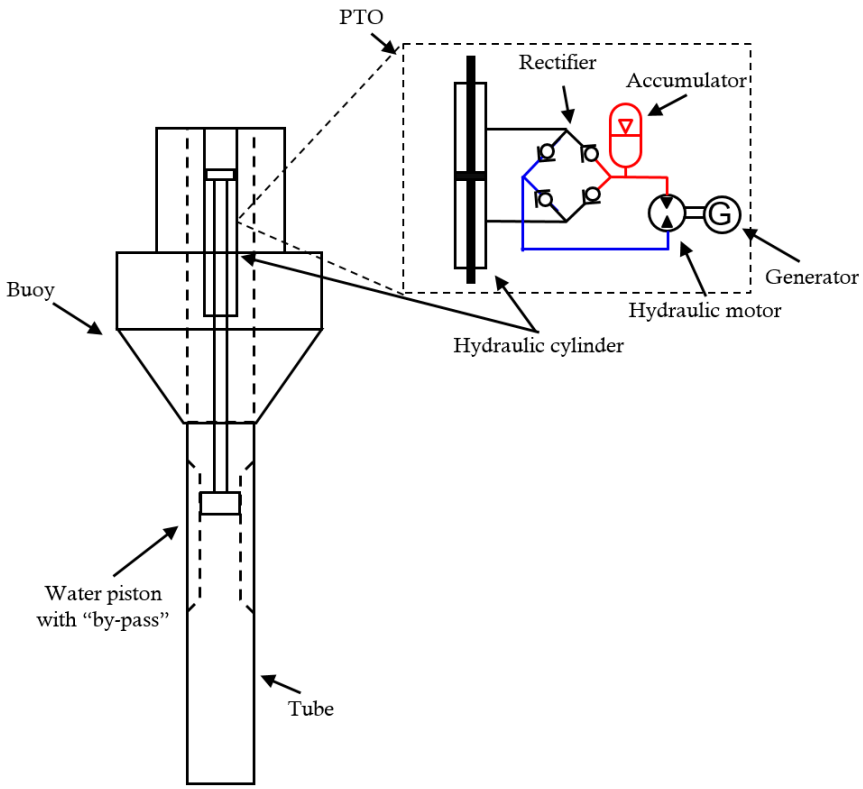

Figure 1.7: A drawing W4P's wave energy converter with its power take-off.

The water piston's motion relative to the buoy/tube is dampened by applying pressure in the hydraulic system, that makes the water piston pull the water column along, following the buoy motion with some phase difference. If there is no damping, the water piston and the water column will stand still. Therefore, the velocity difference between the water mass and the buoy/tube unit will be equal to the velocity of the buoy/tube unit. However, since there is no damping force, there will be no captured power. Increasing the amplitude of the damping force, decrease

the phase difference between the two bodies and eventually locks the two bodies together, making the velocity difference equal to zero, hence, no power is captured. Therefore, the amplitude of the damping force on the water piston must lie within two extremes in order to have power capture.

To solve the problem of the end-stops, the central part of the tube, along which the piston slides, bells out at both ends to limit the stroke of the piston. The water piston operates in the narrowing part of tube. Large waves causes the water piston to move outside the narrowing, which lets the water flow around the piston. This prevents high end stop loads which is a major difficulty for wave energy converters.

1.2.4 Adaptation of WEC's

The original power take-off units of CorPower and Waves4Power are modified in order to integrate them to OHT's collection system as shown in figure 1.8.

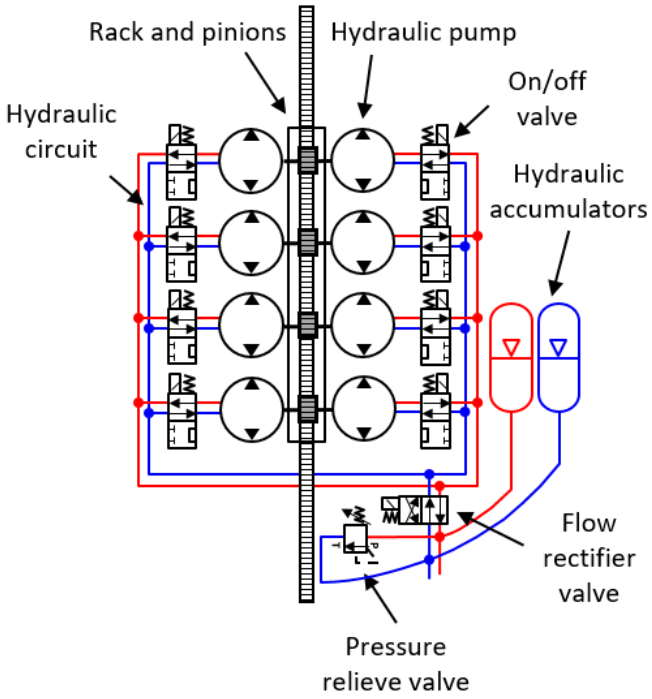

Figure 1.8: Adaptation of WECs for OHT's collection system.

The integration of CorPower's buoy with OHT's hydraulic collection system is done by replacing the Cascade gearbox, dual flywheels and generators with multiple fixed displacement pumps connected to the same rack with a pinion for each pump. Unlike CorPower's original PTO, in which only one set of flywheels and generator is engaged with the rack at a time, in the arrangement with multiple pumps, all pumps are always engaged with the rack, i.e. rotate with the same speed, but only selected number of pumps apply damping force to the rack at a time. This is done by engaged and disengaged pumps from the hydraulic circuit to control the applied damping on the rack based on a chosen control strategy. This pump arrangement is combined

with CorPowers WaveSpring module providing phase control and pre-tension gas spring module for bi-directional power capture.

Similarly, the integration of Waves4Power's buoy with OHT's collection system is done by replacing the hydraulic cylinder with a rack and multiple pinions with each pinion connected to a fixed displacement radial piston pump. Unlike the original PTO with a hydraulic piston that cannot provide damping force control, in the new arrangement, the rack is rigidly connected to the water piston and the damping force can be controlled by engaging and disengaging pump units. The original W4P buoy generates electricity on-board. On contrary, OHT uses hydraulic pipes to collect power in the form of pressurized fluid, which is converted into electricity in a central unit of the array. Therefore, the hydraulic motor and generator are removed from the original PTO. Moreover, a low-pressure accumulator is added to the Waves4Power power take-off, due to the fact that the radial piston pumps require certain charge pressure unlike hydraulic cylinders. Finally, in case of Waves4Power, the valves, that are used to engage and disengage each pump, are equipped with one more functionality. When the water piston goes out of the narrow part of the tube, the force on it must be reduced so that it can move back into narrowing, otherwise the piston will get stuck in the wider part of the tube. The force on the water piston with the new arrangement is reduced by disengaging all pump units. In the original PTO of Waves4Power, there was no need for extra functionality, since the pressure in the circuit is set by the input power from the cylinder and output power from the generator. Hence, when the water piston goes out of the narrowing, the input power decreases, while the generator continues to output power, making the pressure in the hydraulic system decrease gradually. In case of OHT's system, the pressure in the collection is set in the central collection tower and it is always more or less constant, even when the water piston goes out of the narrowing and there is no input power to the system.

A more detailed explanation of the hydraulic components, used in the new PTO, and their functionality is given in the next subsection.

1.2.5 Overview of the hydraulic collection system and tower

The hydraulic collection system with constant pressure from the gravity storage and control features for damping force and phase for the WEC units are designed to capture and transfer power from buoys to the central tower in the form of pressurized fluid without degrading the power capture performance or efficiency of the system. The collections system and tower are sized based on the following main specifications:

- 20 MW maximum hydraulic power input from the WEC array
- 10 MW maximum continuous electric power output to the grid
- 100 kWh storage capacity with 500-ton weight and 70-meter lift height, corresponding to approx. 35s discharge time

The third specification is based on an extensive simulation study, in which it is found that the 500-ton weight and 70-meter height is just sufficient to smooth the varying input power into a constant power output. In this project larger storage options are also evaluated in order to understand and quantify the benefits from increasing the storage capacity. The weights that were studied are 500, 1000, 2500, 5000 and

7500 tons with 122 meter height that approximately correspond to 1-, 2-, 5-, 10- and 15-minute discharge time, respectively.

A schematic is shown in figure 1.9 to give a general overview of the hydraulic collection system and tower in connection with a single WEC. Although, the figure is not representative for the latest design of the collection system, it is used to identify the main components and their functionality.

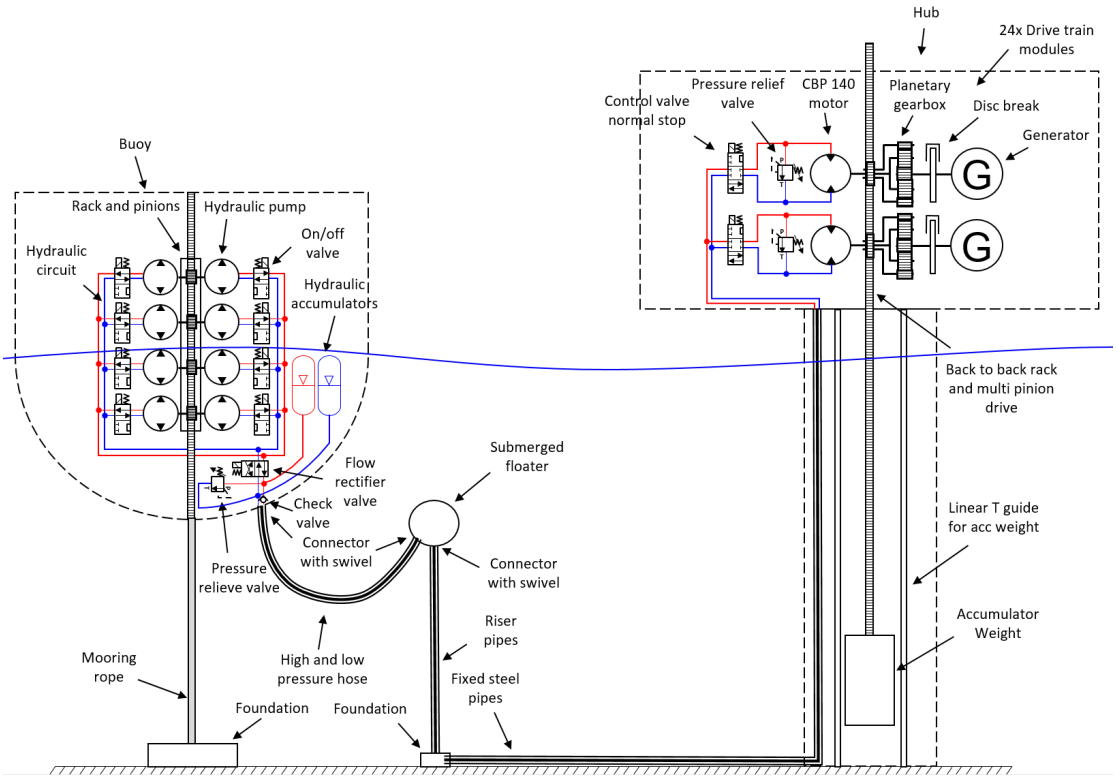

Figure 1.9: Schematics for the main components in the hydraulic system from a WEC to the collection tower.

First of all, a closed-loop hydraulic system is used for the collection, in which high-pressure fluid is pumped from buoys and low-pressure fluid is returned from the tower. Each buoy PTO comprises of eight pumps, a rectifier bridge, a pressure relief valve, a check valve, and a high-pressure and one low-pressure hydraulic accumulator. The 2-way on/off valves, shown in figure 1.9, are drawn for explanatory purpose only, i.e. in the actual system they do not exist as separate units, but instead the functionality to engage and disengage pumps is provided by the distributor valve of the pump. The rectifier bridge changes the direction of the flow to be always towards the tower in order to have active power transfer. The pressure relief valve limits the maximum pressure of the system to a specified value. The check valve is used to prevent back-flows in the system caused by the dynamic interaction of hydraulic accumulators, fluid compressibility and inertia. The high-pressure accumulator is utilized to reduce peak flows and therefore pressure drops and fluctuations and the low-pressure accumulator is used to keep sufficient charge pressure, necessary for the operation of the pumps and motors.

The tower side of the hydraulic collection comprises of multiple hydraulic motors, pressure relief and emergency stop valves. Both types of valves are drawn to convey the functionality to the reader. In reality, they come as an accessory when purchasing the motor. The pressure relief valve in the tower is utilized to limit the peak pressures, caused by the acceleration of the gravity storage, and in addition it is used to release the excessive amount o energy when the weight hits the top bumper.

Several designs have been considered throughout the project for the array topology, the collection tower structure and the drive train. The topology of the collection system that was proposed at the beginning of the project is shown in figure 1.10.

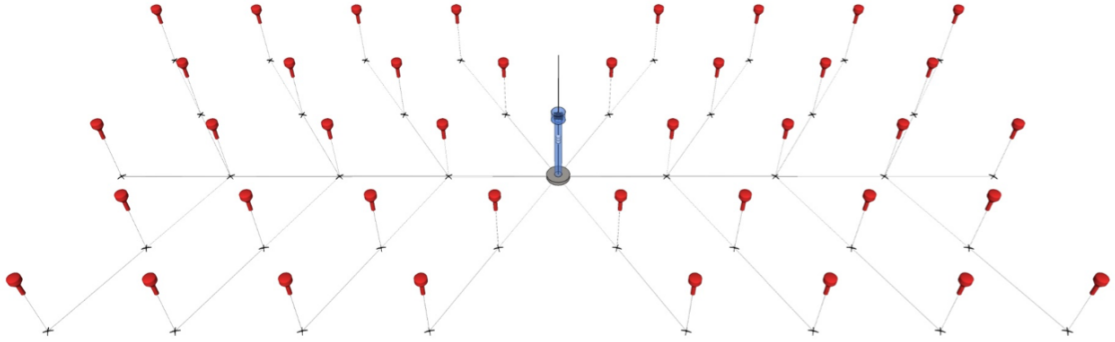

Figure 1.10: Topology of hydraulic collection with steel pipes.

The topology consists of 40 buoys, connected to a central tower with gravity storage. In this design steel pipes are utilized to collect the power from the WECs. Dynamic hoses from each buoy connect with riser pipes inside a submerged floater, placed close to the buoys, as shown in figure 1.9. The lengths of the steel pipes on the sea bed, the riser pipes and the dynamic hoses are respectively 80, 40 and 30 meters. The pipes are grouped based on the joint flow from the number of buoys located upstream to the pipe. The group that joins the flow from all pipes is given the lowest group number (group 0) and the group that contains the flow only from a single buoy is given the highest group number (group 5). Each group of pipes has the same diameter, which increases with decreasing the group number. The sizing of the pipes was an iterative process. The preliminary design is done in Excel based on static loss calculations with the objective to minimize the losses while keeping an eye on the estimated cost of the system. Further on simulations are run to validate the estimated losses with the dynamic losses obtained from the simulations. However, during the project it was found out that the installation costs for such piping system were too high due to the fact that the seabed is not flat, too many sub-sea expensive connectors are required and the steel pipes need flushing after installation since they will be contaminated with water during installation. Since this conclusion was drawn close to the end of the project, most of the simulation work was done using this topology.

The fixed piping system with junctions on the seabed is replaced with one that utilizes composite flexible pipes that are commonly used in offshore oil and gas industry. The selected topology comprises of 6 clusters with 7 WECs in each cluster that has a manifold, located in a submerged floater, to join the export and split the

return flow to the WEC´s. Each cluster manifold is then connected directly to the collection platform. The composite flexible pipes allow connection from the WECs to the manifold, and from the manifold to the collection tower without the need for any sub-sea connectors. Each buoy is placed with a minimum distance of 80 meter to the next buoy, and connects to a manifold in each cluster through 120 meter long flexible pipes for high and low pressure export and return flows. The manifolds are connected to the central platform through 300 meter long flexible pipes, resting on the seabed and then rising to the platform. A concept design of the hydraulic collection system is shown in figure 1.11.

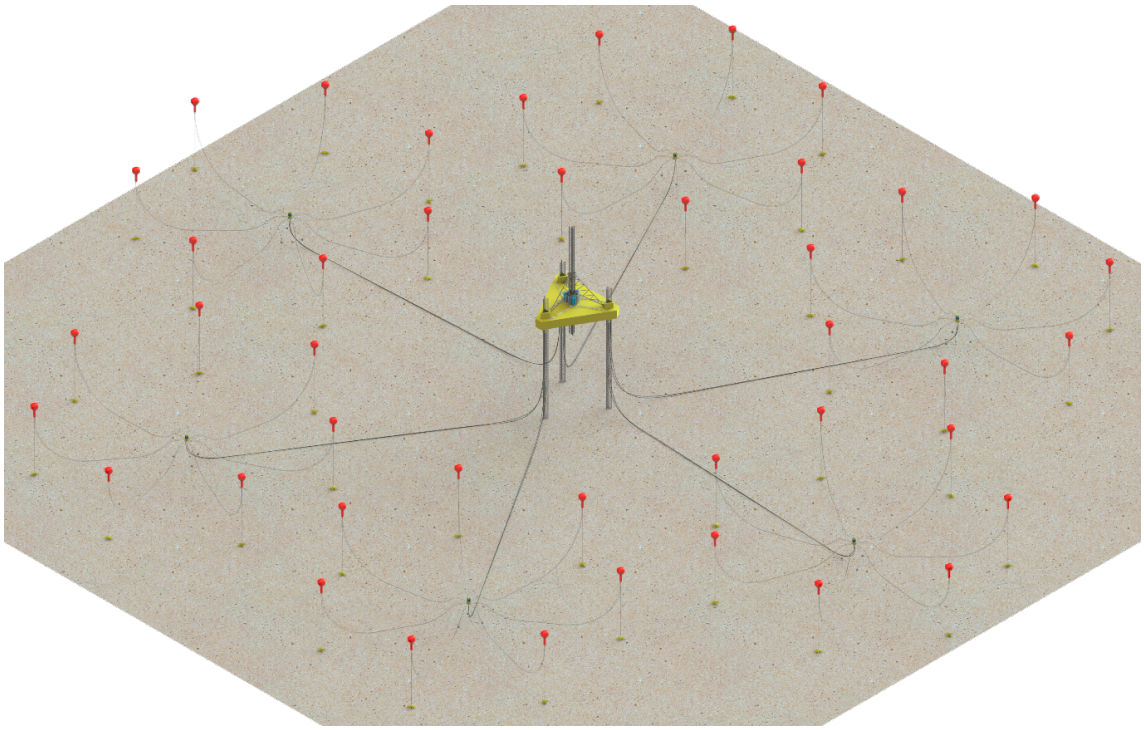

Figure 1.11: Topology of hydraulic collection with composite pipes.

Not only the design of the hydraulic collection system has changed during the project, but there was great development in the collection tower and the comprising drive train inside the tower. Initially, a concrete tower similar to the offshore wind towers was considered. However, it was found out that this solution is not scalable for larger weights and deeper sea. Therefore, during this project OHT has started to evaluate jack-up rigs[2], that is another proven technology in offshore oil and gas industry. The jack-up solution can be scaled to lift much larger weights and are available in designs with platform height 200 meters above the sea-bed. Unlike the previous design with the collection tower, in which the mass of the accumulator weight is located at the bottom of the rack and the weight is driven dry inside the tower, see figure 1.9, with the jack-up platform the weight integrated in a triangular framed structure with one double-sided gear rack in each corner and the weight is driven wet. Integrating the ballast with the rack structure makes it possible to use

[2]Jack-up rig is a self-elevating unit comprising of a platform and several movable legs, that can lift the platform above the sea surface.

the full platform height for lifting the weight to store energy. Moreover, the idea to integrate the weight with the rack is also motivated by the fact that the rack force will decrease with increasing volume of the weight inside the water and vice versa. If the mass is located at one point and the platform is above the water surface, there will be a step increase in rack force when the weight moves out of the water. However, if the mass is distributed evenly along the whole length, the change in force will be gradual and only a part of the rack will be submerged thus the change in rack force will be lower.

In the beginning of the project, OHT was considering a custom-made planetary gearbox in the drive train of the accumulator weight. In this assembly, the ring - to the counterweight, the sun gear - to the generator and the carrier was connected to the hydraulic motor, as shown in figure 1.9. During the project, the custom-made planetary gearbox was replaced with the off-the-shelf wheel drive. In the new assembly the ring gear is connected to the hydraulic motor, the carrier - to the counterweight and the sun gear - to the generator. The discovery of the wheel drive happened at an early phase of the project, therefore all the simulation study was conducted with the new assembly.

Initially, the generator and the hydraulic motor in a drive train unit were facing each other, i.e. they were connected to the planetary gearbox from opposing sides. Two such drive train units (one with flipped orientation) are shown in figure 1.12.

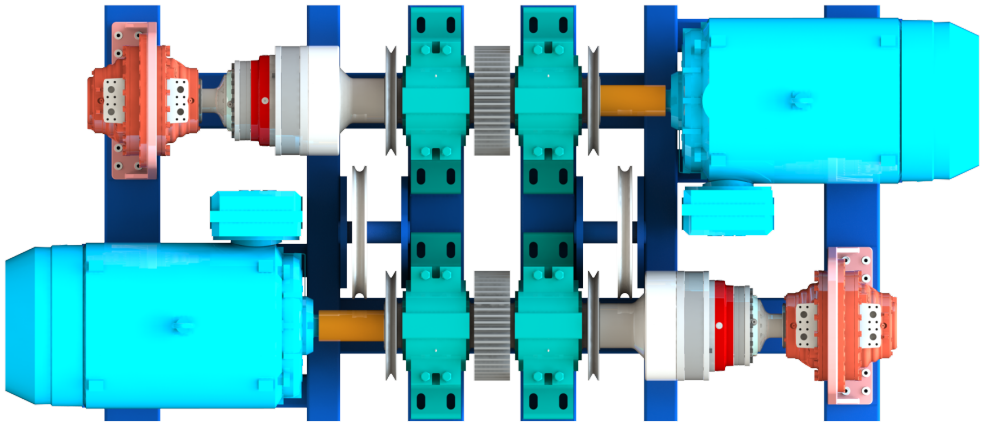

Figure 1.12: Two drive train units with generator and hydraulic motor, facing each other.

This arrangement of the drive train unit did not allow placing a gear stage between the carrier and the counterweight pinion that can be used to control the pressure in the hydraulic system in discrete manner and enable using larger accumulator weights with larger pinions and higher-speed hydraulic motors. Hence, a different arrangement was discovered during the project that outcome these limitation. In this assembly the generator and the hydraulic motor are placed on the same side

of the planetary gearbox. This is made possible by utilizing the hollow shaft of the radial piston motor. The new arrangement did not only allow placing a secondary gear stage between carrier and pinion, but it enabled the usage of triangular jack-up rack structure with one double-sided gear rack in each corner and a drive unit connected to each side of the rack. The top view of the rack and rive assembly is shown in figure 1.13.

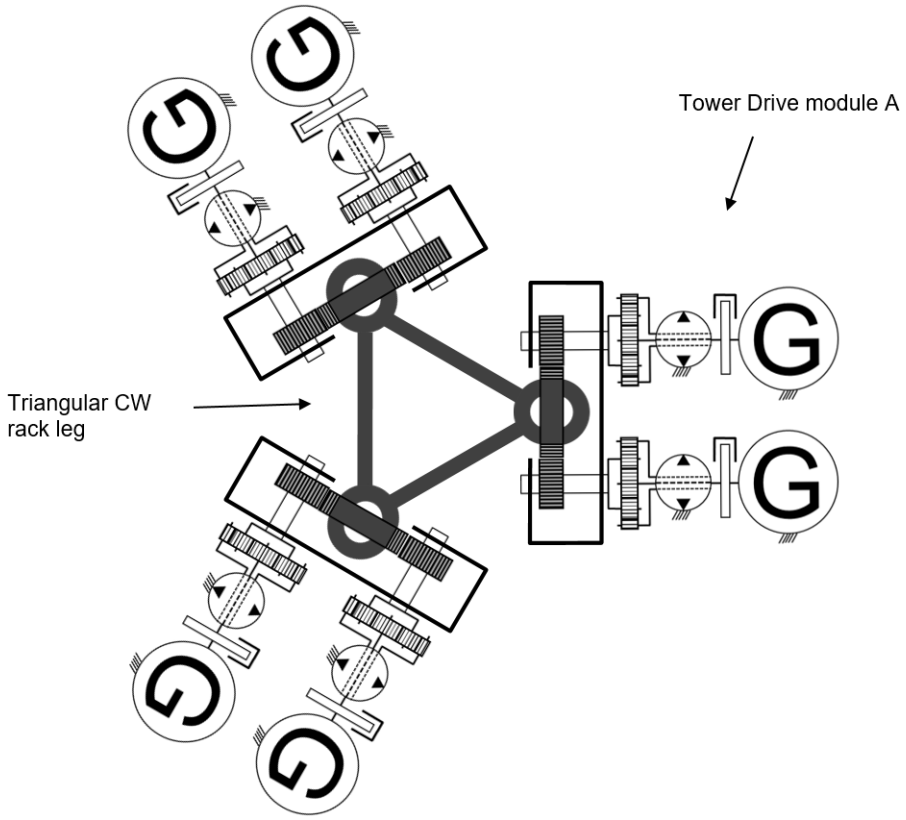

Figure 1.13: Top view of rack and drive assembly for tower.

There are several advantages with using a jacking system for the tower drive train. First of all, this is a conventional and proven technology where only the drive unit is modified to incorporate an hydraulic motor and a generator. The rack is furthermore a very strong and stiff structure that can be raised above the platform without folding. Moreover, the framed structure allows linear guiding that can take high loads in all directions. The height of the drive unit stack is significantly reduced with 6 drive units in each level, and the number of over-rollings from the pinions on each rack is reduced to 1/3. It is an open gear system that does not have to be encapsulated from seawater. And finally these gear systems are optimized for extremely high loads compared with the previous rack design considered in the project. A standard jacking unit carry up to 450 ton (one pinion), the previous design of the OHT tower shared 500 ton over 24 drive units (24 pinions). The main challenge with using this system for the wave power application is the much higher cycle number and the higher speed of the rack. The sizing of the jacking gear system must carefully consider the wear and tear to achieve the high number of cycles.

1.2.6 Environmental conditions

Two wave power test sites have been chosen as cases for this benchmarking study:

- EMEC site Billia Croo, Orkney, north Scotland
- Wave Hub, St. Ives Cornwall, south England

They have different wave conditions, which is desired for evaluating how the wave conditions impact the collection system.

The location of the sites is shown in figure 1.14.

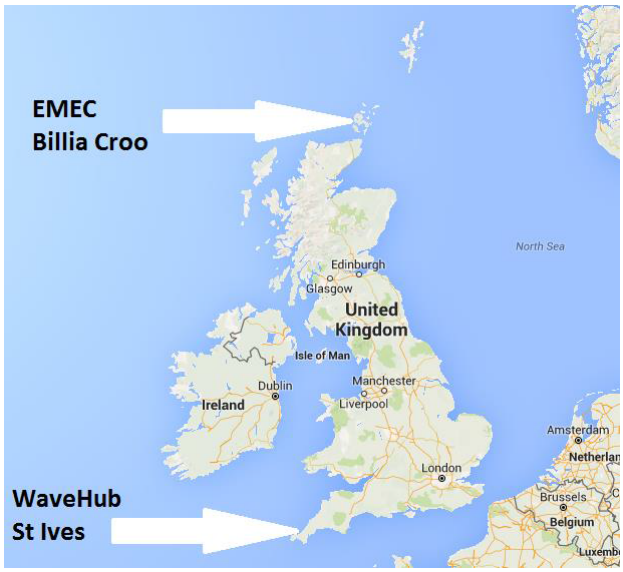

Figure 1.14: Locations of selected sites EMEC Billia Croo, Orkney, and Wave Hub St. Ives, Cornwall.

For simplicity in the study the wave spectrum is approximated with the commonly used JONSWAP spectrum with peak shape factor 3.3. The study will be restricted to mono-directional waves (long crested waves with a single wave direction). However, to assess the influence of wave direction simulations will be done with varied wave direction, see [20].

The wave resource at Billia Croo is 21.5 kW/m wave front annually. The predominant wind and wave direction is from west but waves from north-north-west are not uncommon. In the case study the annual wave climate is represented as a joint distribution of significant wave height[3], H_s, and peak wave period[4], T_p. The annual occurrence of each sea state in percentage is shown in figure 1.15. Sea states with an occurrence of less than 0.1% have been excluded from the figure.

[3]Significant wave height is defined as the mean wave height (trough to crest) of the highest third of the waves.

[4]The peak wave period is the wave period with the highest energy content.

Hs\Tp	0.0 -1.0	1.0- 2.0	2.0 - 3.0	3.0 - 4.0	4.0 - 5.0	5.0 - 6.0	6.0 - 7.0	7.0 - 8.0	8.0-9.0	9.0 - 10.0	10.0 - 11.0	11.0-12.0	12.0-13.0	13.0 - 14.0	14.0 -15.0
0.0 - 0.5							0,187		0,507	0,171					
0.5 - 1.0				0,139	0,152	0,565	1,246	1,297	4,901	1,769	1,913	0,695	0,78	0,339	0,252
1.0 - 1.5					0,318	0,719	1,697	1,947	4,914	2,695	3,802	1,121	1,461	0,914	0,642
1.5 - 2.0						0,556	1,09	1,788	2,87	1,567	3,789	1,531	1,35	1,239	0,862
2.0 - 2.5							0,777	1,189	1,964	1,366	2,977	1,638	1,323	1,297	1,044
2.5 - 3.0							0,37	0,544	1,259	1,035	1,918	1,189	1,001	1,213	1,223
3.5 - 4.0								0,305	0,587	0,808	1,229	1,068	0,597	0,991	1,35
4.5 - 5.0								0,127	0,234	0,56	0,862	0,847	0,493	0,678	1,141
5.5 -6.0									0,128	0,322	0,554	0,575	0,419	0,537	1,034
6.5 - 7.0										0,127	0,383	0,394	0,264	0,388	0,886
7.0 - 7.5											0,234	0,313	0,193	0,274	0,756
7.5 - 8.0												0,205	0,13	0,228	0,515
8.0 - 8.5												0,137		0,127	0,332
8.5 - 9.0														0,108	0,233
9.5 - 10.0															0,161
10.0 - 10.5															0,133

Figure 1.15: Annual wave scatter at EMEC site, Billia Croo.

The annual occurrence of each sea state in percentage for the WaveHub site is shown in figure 1.16. Again sea states with an occurrence of less than 0.1% have been excluded from the figure.

Hs\Tp	0 - 1.3	1.3-2.6	2.6-3.9	3.9-4.5	4.5-5.8	5.8 - 7.1	7.1 - 8.4	8.4-9.6	9.6-10.9	10.9-12.2	12.2-13.5
0.0 - 0.5			0,1	0,5	0,1	0,1					
0.5 - 1.0				4,6	6,9	2,6	1,5	0,1			
1.0 - 1.5				1,5	12,6	7,5	3,6	1,5	0,5		
1.5 - 2.0					4,1	9,9	4,5	2,2	0,7	0,1	
2.0 - 2.5					0,4	5,2	4	2,4	0,7	0,1	
2.5 - 3.0						1,3	3,2	1,6	0,8		
3.5 - 4.0						0,1	2,2	1,5	1,2	0,2	
4.5 - 5.0							1,2	1,6	0,9	0,3	0,1
5.5 -6.0							0,5	1,3	0,5	0,4	
6.5 - 7.0								1	0,5		0,1
7.0 - 7.5								0,2	0,3		
7.5 - 8.0								0,1	0,3		

Figure 1.16: Annual wave scatter at WaveHub site, St Ives.

In this study the sea bottom is simplified to be flat, i.e. the influence of bathymetric variations on the collection system are not considered. Constant water depth of 50 meters is chosen for both sites.

1.3 Project goals and methodology

The objectives of the thesis are summarized as follows:

- Modelling and implementation of a new CorPower buoy that does not contain algebraic equations. The previous CorPower model contained algebraic loops that did not allow efficient simulation of the wave energy farm and in some scenarios it generated errors that prevented simulations from completing. Euler-Lagrange method is proposed as a way to model the wave energy converter.
- Modelling of the hydraulic collection system with a proposed topology considering all loss sources. This objective was extended during the project with

creating an algorithm that can generate dynamic equation for a collection system with any topology. A graph-theoretic approach was used to achieve the extended objective in an efficient way.

- Modelling of the drive train and the gravity storage in the collection tower. Initially, a model for the drive train with the storage technology was provided by OHT. However, during the project the configuration has changed a few times due to learning, therefore the tower model needed to be recreated. A major addition to it was the capability to provide power routing to increase the overall efficiency of the system by disengaging some generators in small and mild sea states.
- Implementation of an efficient Simulink model to simulate a 10MW wave energy farm with 40 buoys. Due to the large size of the wave array model and the large number of simulations (several thousand) each with 30-minute of duration, that needs to be run, the model needs to be implemented in a way that allows fast enough to complete the simulation study. A simulation framework that can run multiple simulations at the same time was implemented from OHT in a previous project. The framework needs to be updated so that the models can be run in Accelerator mode in Simulink. In addition, vectorization of the Simulink model is proposed to increase the simulation speed.
- Implementation of a wave-by-wave-tuned preview based constant damping force control strategy for optimizing power capture performance of wave energy converters from CorPower and Waves4Power in combination with OHT's hydraulic collection and energy storage technology. The required ranges for the damping force (pump displacements) need to be investigated. Firstly, the maximum damping force to get the maximum power capture in largest waves is going to be identified, and then it is going to be investigated how much the force range can be narrowed down or how much the maximum damping force be reduced without losing too much of the annual power capture. The wave-by-wave force control is required to limit power capture above the rated power for the array by a co-ordinated control of the damping force in the buoys, to take advantage of increased smoothing we can get from this when we do not need to capture maximum power from the waves. This is a further development of the so called spill function currently implemented on the motor in the hub, which will now use fixed displacement. In addition the designed controller must consider constraints of the system.
- Implementation of a grid frequency control of the generators. This objective is proposed during the project.
- Sizing of the hydraulic piping system and hydraulic accumulators. The piping system is sized first of all using static loss calculations and then verified using the simulation models. The low-pressure hydraulic accumulators need to be sized with enough fluid and gas volume to hold enough charge pressure required for chosen hydraulic pumps and motors. The high-pressure accumulator need to be designed to have high pre-charge in order to make the required damping force range available to the buoys at all time.
- Update of component properties and parameters in the simulation model.

Component properties and parameters will be updated according to the system specification for the 10 MW array to be studied in the project, based on data sheets and information from suppliers on components such as operating range, efficiency, size, weight and inertia where applicable.

- Over-pressure relieve valves need to be added to the system to spill the excessive amount of energy. They will be activated when the the gravity accumulator hits the top limit. That will cause an increase in torque in the drive train and therefore increase in pressure in the hydraulic collection system, that will be triggered by the pressure relief valve.
- Upgrade of OHT's test rig to represent the developed simulation models with a hydraulic collection system to attach multiple buoys for centralized smoothing and conversion to electricity. This includes sensor and component sizing and selection for the extended test rig, setting up the control and data acquisition environment in Labview and Veristand, etc.
- Experimental validation of the simulation models. Hardware-in-the-loop (HIL) simulations are going to be run by integrating the control system and the developed models with the test rig.
- Presentation and analysis of the obtained results both from measurement and simulation.

1.4 Literature review

Although wave power has not yet been established as a mature industry, it has been under study since 1970s. One of the main figures in wave energy research is Johannes Falnes. In his book *Ocean Waves and Oscillating Systems*, [3], which is considered to be the bible of wave power research, he discusses the fundamentals of linear wave theory, the interaction between waves and oscillating bodies and derives the condition for optimal power extraction, which has a great analogy to the well-known impedance matching in electrical systems to transfer maximum amount of power. In his book he also proposes the latching technique as a suboptimal discrete control strategy to extract wave energy. The book is used in the thesis mostly to increase the understanding of how system parameters like mass and hydrostatic stiffness affects the behaviour of an oscillating point absorber.

This project is a continuation of a concept evaluation study that was carried out between April 2014 and February 2015, analyzing the possible benefits of combining technologies from Ocean Harvesting, CorPower and Waves4Power. A reference model was developed consisting of a hydraulic collection system that connects five buoys to a hub system with centralized energy storage and conversion to electricity. The work conducted during that project is summarized in [1] and [2] and in the current project it is used as a basis to build the simulation model for an 10 MW array from of wave energy converters CorPower and Waves4Power with centralized storage technology and conversion to electricity from OHT. In [2] the authors presented a benchmarking study between different types of control techniques. The power capture performance of standalone buoys from CPO and W4P (without OHT) is compared with the power capture performance of both buoys in combination with

OHT's sea-state tuned and wave-by-wave tuned constant damping control strategy, where sea-state tuned constant damping force control strategy refers to assigning an optimal constant damping force level that gives maximum power output from a range of discrete force levels for each sea state and the wave-by-wave - assigning an optimal constant damping force for each stroke of the wave. The wave-by-wave control was implemented in a simple way by running sets of simulations with different constant damping forces in each set throughout the whole simulation and after completion of the simulation selecting the damping force that gave the maximum power. Therefore, this technique did not account for the change in dynamics of the system by changing the damping force and hardly can be called a control strategy. However, the improvement of power capture performance by using wave-by-wave maximum power selection was the main motivation in this study to implement a predictive control strategy for selecting an optimal damping force for each wave-stoke.

Maximizing power capture of a wave energy device has been an active field of study since the very beginning of wave energy research. An extensive selection of control techniques for power optimization has been gathered and presented in the review paper from J.V. Ringwood, G. Bacelli and F. Fusco, [4], that was used as a main guide in finding relative literature. The paper does not only present state of the art control techniques to optimize power capture performance of a single buoy, but it also gives considerable amount of references to research papers in control of wave energy farms and wave forecasting. Since an extensive review of control strategies is presented in [3], it is omitted and the reader is advised to read the review paper to get familiar with the development in control of wave energy converters.

1.5 Thesis outline

The following part of the thesis is organized as follows.

Chapter 2 (Theory) This chapter describes the theoretical concepts that assisted in achieving the proposed objectives. It is organised in four sections. In the first subsection the fundamentals of hydrodynamic modelling of a heaving buoy is laid down. In this section also the condition for optimal power absorption is derived. Moreover, the influence of each parameter on the system dynamics is discussed. The second section describes the lump-parametric modelling of hydraulic piping systems. The third section presents the fundamentals of linear graph theory for modelling complex dynamical systems. Lastly, the fourth section describes the basic principles of model predictive control and its application to wave energy.

Chapter 3 (Modelling of Wave Energy Converters) This chapter presents the modelling of the CorPower and Waves4Power buoy. The Lagrangian method is identified as a potential modelling technique for modelling the CorPower's buoy. The chapter also presents scaling rules when modelling dynamical systems and application of them on Waves4Power's buoy.

Chapter 4 (Modelling of the Hydraulic Collection) In this chapter the complete model of the hydraulic collection system is described including models of all hydraulic components with their respective losses, lump-parametric model of the pipeline with losses from all loss sources like bends, manifolds, etc. Moreover, this

chapter presents an algorithm to generate state space models for a hydraulic collection system with any topology.

Chapter 5 (Analysis of Wave Energy Converters) This chapter presents an analysis of the dynamic behaviour of the studied wave energy converters.

Chapter 6 (Integration of Wave Energy Converters) This chapter presents the model of integration of the wave energy converters to OHT's hydraulic system. With the help of an electrical analogy of the system, the chapter explains the conducting and nonconducting modes of operation that are caused by the rectifier bridge and the constant pressure of the hydraulic system.

Chapter 7 (Modelling of the Collection Tower) This chapter presents the modelling of the collection tower with the gravity storage and the so called "power routing" method to increase the efficiency of the generators.

Chapter 8 (Simulation Framework Update and Vectorized Simulink Modelling) The chapter describes the simulation framework that simplifies simulation of multiple configuration and annual simulations, and the vectorization technique to increase the efficiency of large Simulink models.

Chapter 9 (Constant Damping Force Control) This chapter describes the sea-state tuned and wave-by-wave tuned constant damping force control strategies.

Chapter 10 (Grid Frequency Control) The chapter discusses the value of providing ancillary services to the grid using the gravity storage. It also presents a simple-state machine and a generator speed control strategy to control the power of the generator according to the frequency of the grid.

Chapter 11 (Simulation Results and Discussion) This chapter summarizes the simulation results obtained from running simulation with the developed models. It includes a benchmarking study between standalone buoys with electric collection versus the combined system with hydraulic collection and the control strategy, developed in this thesis. Prior to presenting the benchmarking study, an explanation is given on the choice of all system parameter values. Moreover, the chapter presents results from simulations of the wave energy plant with centralized storage for grid frequency control with and without purchasing power from the grid. The final section of the chapter includes the production of load date to calculate the life time of hydraulic pumps and motors.

Chapter 12 (Development of a HIL Simulation Environment) This section presents the test rig that was built during this project together with developed HIL simualtion environment with Labview. A link to a demonstration video is given at the end of the chapter.

Chapter 13 (Conclusions) This chapter includes a summary of the project and discussion on the accomplished and unaccomplished objectives.

Chapter 13 (Future Work) This chapter outlines some ideas for further investigation and development.

Appendix A (CA50 and CBP140 Motor Loss Curves.) This appendix presents the pressure and flow loss curves, and efficiency mappings of CA50 and CBP140 motors used in the project.

Appendix B (Simulink Model.) This appendix presents a high-level overview

of the developed Simulink model.

2
Theory

This chapter describes the theoretical concepts that assisted the author to accomplish the proposed tasks.

2.1 Hydrodynamic modelling

This section lays down the basic concepts in linear wave-body interaction theory.

2.1.1 Coordinates

Similar to any rigid body, the dynamics of a buoy interacting with waves is characterized by six degrees of freedom: a translation in each direction of a 3-axis orthogonal system and a rotation around each axis. Translations in x, y and z direction are most often termed as motion in surge, sway and heave, respectively, and rotations around x, y and z axis are called roll, pitch and yaw.

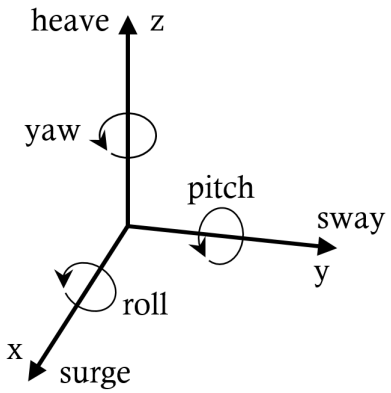

Figure 2.1: Coordinates and six degrees of freedom of a buoy.

A point-absorber type of wave energy converter captures power mostly from the oscillating motion in heave. Since both Waves4Power's and CorPower's WECs are of this type, the buoy dynamics in heave will be the main focus of analysis. Moreover, the simulation model, received from Waves4Power, considers only heave motion and the simulation model from CorPower considers heave, and also surge motion. However, for a site with large depth, like the 50-meter one, considered in this thesis, the surge motion does not influence the power capture much and therefore can also be ignored. The reason will be apparent in subsequent chapters.

2.1.2 Waves

Ocean waves are a result of the wind blowing over the water surface. Generally, they are determined as irregular. In linear wave theory an irregular wave can be modelled as a linear superposition of a set of regular waves

$$\eta(x,t) = \sum_{i=1}^{N} a_i cos(\omega_i t - k_i \xi(x,y) + \phi_i) \tag{2.1}$$

where t is time, $\xi(x,y)$ position along the wave's direction of travel, ϕ_i are random phases uniformly distributed between 0 and 2π, ω_i are angular frequencies, k_i are wavenumbers[1] and a_i are random amplitudes which are taken to be Rayleigh distributed with mean square value

$$E[a_i^2] = 2S(\omega)\Delta\omega_i \tag{2.2}$$

where $S(\omega)$ is the wave spectrum and $\Delta\omega_i$ is the frequency step between two frequency components. The amplitudes can be approximately computed as

$$a_i \approx \sqrt{2S(\omega)\Delta\omega_i} \tag{2.3}$$

Ocean waves are generally dispersive, meaning that waves with different wave lengths travel with different phase velocity. The phase velocity is the velocity, at which the phase of each frequency component of the wave travels. It is defined as

$$v_p = \frac{s}{t} \tag{2.4}$$

where s is the distance travelled by the wave within time t. It can intuitively found that the phase velocity is proportional to the angular frequency and inversely proportional to the wavelength,

$$v_p = \frac{\omega}{k} \tag{2.5}$$

The angular frequency and wavenumber are related through the dispersion equation (see [3])

$$\omega^2 = gk\tanh(kh) \tag{2.6}$$

where g is the gravity constant and h is the water depth. For sufficiently deep water ($kh \gg 1$) the dispersion equation reduces to

$$\omega^2 = gk \tag{2.7}$$

Using the dispersion relation for deep water, it follow that the phase velocity is

$$v_p = \frac{g}{\omega} = \sqrt{\frac{g}{k}} \tag{2.8}$$

Due to dispersion phenomenon interference of two or more sinusoidal waves with slightly different wavelengths results in a beat pattern, called a wave group, which moves with a group velocity v_g. The group velocity is formally defined as

$$v_g = \frac{\partial\omega}{\partial k} \tag{2.9}$$

[1] Wavenumber is the spatial frequency of a wave.

Using the dispersion relation for deep water, it yields

$$v_g = \frac{g}{2\omega} = \frac{v_p}{2} \tag{2.10}$$

The group velocity is important since it is the velocity with which the energy is transported by the wave (see [3]).

In this thesis, the waves are considered to be uni-directional. This implies that in an array of wave energy converters the same wave will hit each buoy after certain delay based on the position of the buoys in the array with respect to a reference and the wave direction. The distance of the buoy to the wave can be calculated by

$$\xi(x, y) = x\cos(\beta) + y\sin(\beta) \tag{2.11}$$

where β is the angle of the wave with respect to a chosen reference direction.

The wave spectrum can be characterized by the environmental parameters significant wave height H_s and peak wave period T_p, which were defined in section 1.2.6. The most common types of spectra that are used by the offshore industry are Pierson-Moskovitz, Bretschneider and JONSWAP spectrum. In this thesis the JONSWAP spectrum is used to generate irregular waves. The spectrum is proposed in [14], and it is originally formulated as

$$S(\omega) = \frac{\alpha_j g^2}{\omega^5} \exp\left[-\frac{5}{4}\left(\frac{\omega_p}{\omega}\right)^4\right] \gamma^{\Gamma} \tag{2.12}$$

where α_j is a non-dimensional variable that is a function of the wind speed and fetch length[2], ω is wave angular frequency, ω_p is peak wave angular frequency, γ is the wave peak enhancement factor that is typically set to 3.3 and Γ is the gamma-function given by

$$\Gamma = \exp\left[-\left(\frac{\frac{\omega}{\omega_p} - 1}{\sqrt{2}\sigma}\right)^2\right], \quad \sigma = \begin{cases} 0.07, & \omega \leq \omega_p \\ 0.09, & \omega > \omega_p \end{cases} \tag{2.13}$$

where σ is called the peak enhancement factor. However, as it can be seen from (2.12) this spectrum representation does not incorporate the significant wave height. Another form of the JONSWAP spectrum as a function of the significant wave height H_s and wave angular frequency ω_p is (see [22])

$$S(\omega) = A_\gamma \frac{5}{16} H_s^2 \frac{\omega_p^4}{\omega^5} \exp\left[-\frac{5}{4}\left(\frac{\omega_p}{\omega}\right)^4\right] \gamma^{\Gamma} \tag{2.14}$$

where A_γ is a normalizing factor that is equal to

$$A_\gamma = 1 - 0.287\ln(\gamma) \tag{2.15}$$

According to [22], the JONSWAP spectrum with $\gamma = 3.3$ is a reasonable model for

$$3.6 < \frac{T_p}{\sqrt{H_s}} < 5 \tag{2.16}$$

[2]Fetch length, or only fetch, is the distance to the shore in the direction of the wind.

and should be used with caution outside the interval. [22] also suggests using the following value for the peak shape parameter when no particular value is given.

$$\gamma = \begin{cases} 5, & \text{if } \frac{T_p}{\sqrt{H_s}} \leq 3.6 \\ \exp\left(5.75 - 1.15\frac{T_p}{H_s}\right), & \text{if } 3.6 < \frac{T_p}{\sqrt{H_s}} < 5 \\ 1, & \text{if } \frac{T_p}{\sqrt{H_s}} \geq 5 \end{cases} \tag{2.17}$$

The effect of γ on the wave spectrum is shown in figure 2.2

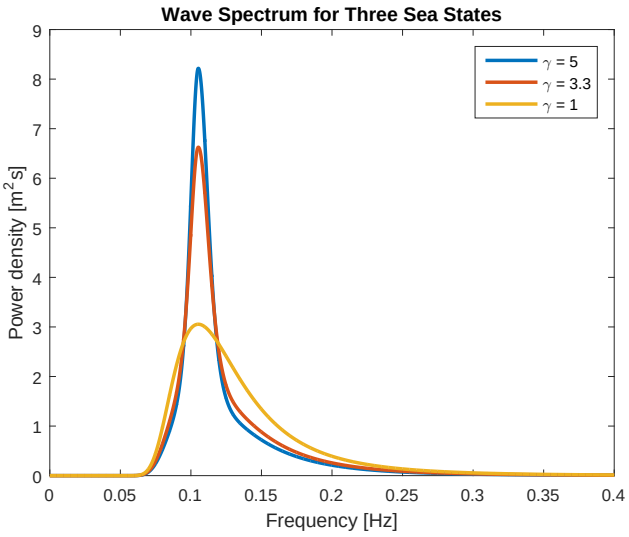

Figure 2.2: Wave spectrum with different peak shape factors.

It can be seen from the figure that the peak value of the spectrum increases and the bandwidth of the spectrum decreases with increasing shape enhancement factor.

In this project, CorPower suggested using a peak enhancement factor of $\gamma = 3.3$ for all sea states. Waves4Power failed to provide an update on their simulation model. Therefore, a peak shape parameter of $\gamma = 1$, which was used in a previous study (see [1]), was also used in this project. It is obvious from figure 2.2 that the power capture of each buoy is affected by γ. However, the intention of the study is not to do a direct comparison between CorPower's and W4P's WEC performance. Therefore, it is acceptable to use a different peak enhancement factor for each buoy. [3] The maximum value of the power spectrum occurs at $\omega = \omega_p$ and it is equal to

$$S_{max} = A_\gamma \frac{5}{16}\frac{H_s^2}{\omega_p} e^{-\frac{5}{4}\gamma} \tag{2.18}$$

The effect of the significant wave height and peak wave period, that define a sea state, is shown in figure 2.3. By looking at it, it can be derived that the wave spectrum for all sea states is characterized with a narrow bandwidth around each

[3] The JONSWAP spectrum with $\gamma = 1$ is the Pierson-Moskovitz spectrum

peak wave frequency. This implies that, in order to capture more energy from the waves, either the natural frequency of the wave energy converter must be tuned to the frequency of each incoming wave, or the bandwidth of the WEC must be tunable to cover the frequency range of the wave spectrum in each sea state, or the bandwidth of the WEC must be wide enough to cover the frequency range of all sea states at a given sea site. The first case corresponds to wave-by-wave phase control, the second one - to sea-state-tuned phase control and the third one - to passive control, meaning that the wave energy converter is designed to show good power capture performance in all sea states at a given sea site. Each sea site has different

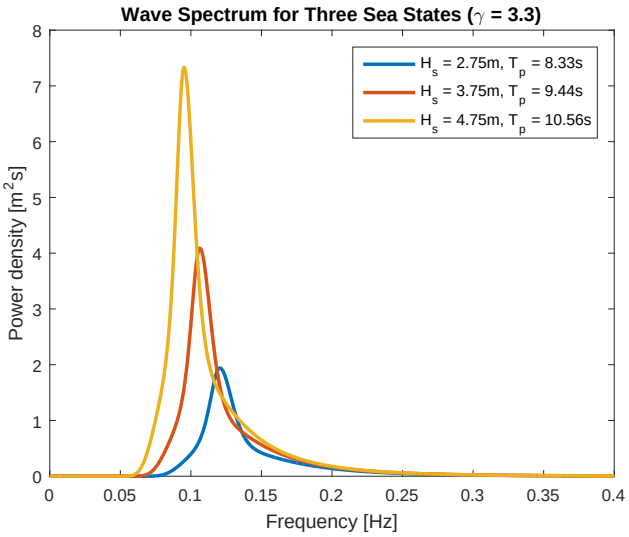

Figure 2.3: Wave spectrum of different sea states.

energy content and a different power distribution throughout the year. This can be seen by looking at figure 2.4 that shows the sum of power density spectra of all sea states at Billia Croo and Wave Hub sites weighted by the occurrence of each sea state in percentage. The curves in the figure imply that a given wave energy converter must be sized uniquely for each sea site.
The energy of a wave per unit horizontal area is (see [3])

$$E = \rho g \int_0^\infty S(\omega) d\omega \tag{2.19}$$

The significant wave height, beside being defined as the mean wave height of the highest third of the waves, is also defined as four times the square root of the integral of the power density function with respect to frequency,

$$H_s = 4\sqrt{\int_0^\infty S(\omega) d\omega} \tag{2.20}$$

Therefore, the energy per unit area as a function of the significant wave height is

$$E = \rho g \frac{H_s^2}{16} \tag{2.21}$$

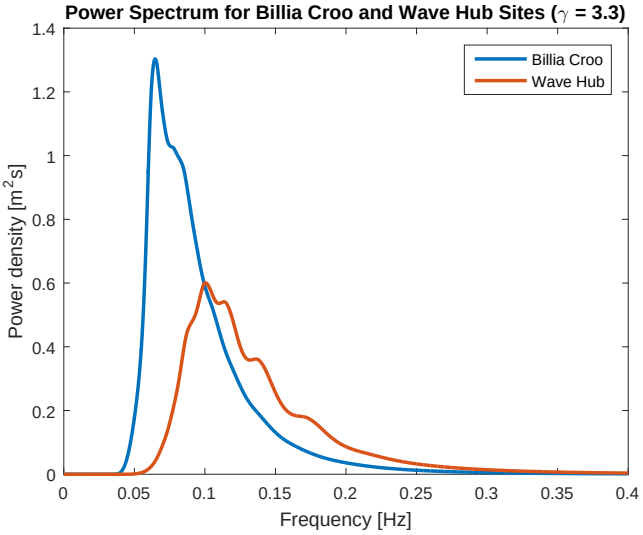

Figure 2.4: Cumulative wave spectra weighted by the occurrence of each sea state.

As waves propagate, they transport energy with velocity equal to the group velocity v_g. The energy transport is defined as power per unit width of wave front. It can be computed as the product of the group velocity and the energy of the wave.

$$J = v_g E = \frac{\rho g^2}{64\pi} H_s^2 T_e \tag{2.22}$$

where T_e is the called the wave energy period. The wave energy period can be interpreted as the period of a regular wave that has the same significant wave height and the same power density as the irregular sea condition under consideration. It is formally defined as

$$T_e = 2\pi \frac{\int_0^\infty \omega^{-1} S(\omega) d\omega}{\int_0^\infty S(\omega) d\omega} \tag{2.23}$$

The energy period and the peak period are related to each other with an approximate relation for Jonswap spectrum, (see [22])

$$\frac{T_e}{T_p} = \frac{4.2 + \gamma}{5 + \gamma} \tag{2.24}$$

Another often used wave period estimator in wave energy is the zero-crossing period, T_z, which is formally defined as

$$T_z = 2\pi \sqrt{\frac{\int_0^\infty S(\omega) d\omega}{\int_0^\infty \omega^2 S(\omega) d\omega}} \tag{2.25}$$

The zero-crossing period and the peak period are related to each other with an approximate relation for Jonswap spectrum, (see [22])

$$\frac{T_z}{T_p} = \sqrt{\frac{5 + \gamma}{11 + \gamma}} \tag{2.26}$$

2.1.3 Force balance

The elegance of the linear wave theory allows separation of the hydrodynamic forces acting on the floating body. It is well-known that a water wave gets reflected and diffracted upon encountering a fixed object. Moreover, the motion of a body inside calm water causes radiation of waves. Furthermore, a floating body, that is displaced vertically from its equilibrium position, tries to restore its equilibrium position. Thus the hydrodynamic force acting on the WEC consists of the the excitation force, caused by the incident and diffracted wave, the radiation force, caused by the radiated wave, and the hydro-static restoring force. In additions to these three forces, As all motions in a viscous environment, a buoy oscillating inside the water experiences a drag force acting against the motions the direction of its motion. The force balance on a floating wave energy converter can be formulated as

$$\mathbf{M}\ddot{\mathbf{x}}(t) = \mathbf{F_{exc}} + \mathbf{F_{rad}} + \mathbf{F_{hyd}} + \mathbf{F_{drag}} + \mathbf{F_{mooring}} + \mathbf{F_{PTO}} \tag{2.27}$$

where $\mathbf{M} \in \mathbb{R}^{6\times6}$ is the mass matrix, $\mathbf{F_{exc}} \in \mathbb{R}^{6\times1}$ is the wave excitation force, $\mathbf{F_{rad}} \in \mathbb{R}^{6\times1}$ is the radiation force, $\mathbf{F_{drag}} \in \mathbb{R}^{6\times1}$ is the drag force, $\mathbf{F_{hyd}} \in \mathbb{R}^{6\times1}$ is the hydro-static force, $\mathbf{F_{mooring}} \in \mathbb{R}^{6\times1}$ is the mooring force and $\mathbf{F_{PTO}} \in \mathbb{R}^{6\times1}$ is the machinery force from the power take-off. The irregular excitation force can be pre-calculated based on hydrodynamic parameters and wave elevation prior to a numerical simulation. The wave elevation of an irregular wave was defined in (2.1) as a linear superposition of N regular wave components with different amplitude, frequency and phase. Let us denote each wave component as η_i and say that each wave component is the real part of the complex-valued signal η_{ci}, i.e.

$$\eta_i(\xi(x,y),t) = \Re\left[\eta_{ci}\right] = \Re\left[a_i e^{\omega_i t - k_i\xi(x,y)+\phi_i}\right] = cos(\omega_i t - k_i\xi(x,y) + \phi_i) \tag{2.28}$$

The irregular wave excitation force is then defined as

$$\mathbf{F_{exc}}(t) = \Re\left[\sum_{i=1}^{N} \mathbf{H_x}(\omega_i)\eta_{ci}\right] \tag{2.29}$$

where $\mathbf{H_X} \in \mathbb{C}^{6\times N}$ is a complex-valued excitation force coefficient that is dependent on the buoy geometry.

The radiation force comprised of an inertia and a damping term and is given as

$$\mathbf{F_{rad}(t)} = -\mathbf{M_r}(\omega)\ddot{\mathbf{x}}(t) - \mathbf{R_r}(\omega)\dot{\mathbf{x}}(t) \tag{2.30}$$

where $\mathbf{M_r}(\omega) \in \mathbb{R}^{6\times6}$ and $\mathbf{R_r}(\omega) \in \mathbb{R}^{6\times6}$ are the added mass and radiation damping matrices, respectively, that are dependent on the wave frequency. Cummins [24] showed that the radiation force in (2.30) could be modelled in time domain as

$$\mathbf{F_{rad}}(t) = -\mathbf{M_r}(\infty)\ddot{\mathbf{x}}(t) - \int_0^t \mathbf{K_r}(t-\tau)\dot{\mathbf{x}}(\tau)d\tau, \tag{2.31}$$

where $\mathbf{M_r}(\infty) \in \mathbb{R}^{6\times6}$ is the added mass matrix at infinity frequency and $\mathbf{K_r} \in \mathbb{R}^{6\times6}$ is the radiation impulse response function. The convolution integral in (2.31) is

computationally expensive, therefore a state-space approximation with n number of states is used when dealing with numerical simulations. It can be written as

$$\begin{aligned} \dot{\mathbf{x}}_\mathbf{r}(t) &= \mathbf{A}_\mathbf{r}\mathbf{x}_\mathbf{r}(t) + \mathbf{B}_\mathbf{r}\dot{\mathbf{x}}(t), \qquad \mathbf{x}_\mathbf{r}(0) = \mathbf{0} \\ \int_{-\infty}^{t} \mathbf{K}_\mathbf{r}(t-\tau)\dot{\mathbf{x}}(t)d\tau &\approx \mathbf{C}_\mathbf{r}\mathbf{x}_\mathbf{r}(t) + \mathbf{D}_\mathbf{r}\dot{\mathbf{x}}(t), \end{aligned} \tag{2.32}$$

where $\mathbf{x_r} \in \mathbb{R}^{n\times 1}$ is the radiation state vector $\mathbf{A_r} \in \mathbb{R}^{n\times n}$, $\mathbf{B_r} \in \mathbb{R}^{n\times 6}$, $\mathbf{C_r} \in \mathbb{R}^{6\times n}$, $\mathbf{D_r} \in \mathbb{R}^{6\times 6}$ are the time-invariant state, input, output and feedthrough matrices. The system order and the state-space matrices can be found using realization theory, which was proposed by Kung [25].

The hydrostatic force is proportional to the submerged fluid V in reference to the equilibrium position and it can be calculated by

$$\mathbf{F_{hydr}}(t) = -\rho g V(z(t) - \eta(t))\mathbf{e_z}. \tag{2.33}$$

where $V(z-\eta)$ indicates that the submerged volume is a function of the difference between the heave displacement of the buoy z and the wave elevation η and $\mathbf{e_z} \in \mathbb{R}^{6\times 1}$ is a unit vector for heave direction.

The drag force is proportional to the square of the buoy velocity and it is given as

$$\mathbf{F_{drag}}(t) = -\frac{1}{2}\rho \mathbf{C_d}\mathbf{A_d}\dot{\mathbf{x}}(t)|\dot{\mathbf{x}}(t)| \tag{2.34}$$

where $\mathbf{C_d} \in \mathbb{R}^{6\times 6}$ is a diagonal matrix with discharge coefficients and $A_d \in \mathbb{R}^{6\times 6}$ is the characteristic area matrix.

The mooring line can simply be modelled as a lumped parameter model comprising a linear stiffness and a linear damping component,

$$\mathbf{F_{mooring}}(t) = -\mathbf{K_m}\mathbf{x}(t) - \mathbf{C_m}\dot{\mathbf{x}}(t). \tag{2.35}$$

In [26] a more sophisticated and accurate model of a mooring line dynamics is proposed that uses a lumped-mass formulation for modelling axial elasticity, hydrodynamics, and bottom contact.

The PTO force depends on the type of power take-off used in the system. It can be controlled to increase the power capture performance of the buoy.

2.1.4 Heave dynamics

As already mentioned that heave is the most important degree of freedom for a point absorber type of wave energy converter. Therefore, this section is devoted to do a system analysis of a heaving buoy. For that purpose, an ideal cylindrical buoy, which was studied in [19], is used. The parameters of the buoy are summarized in the Table 2.1.

Parameter	Notation	Value	Unit
Buoy mass	m_b	670140	kg
Added mass	m_∞	157840	kg
Surface area	S	78.54	m^2

Table 2.1: Cylindrical buoy parameters

The force balance of a cylindrical buoy without considering the drag force, the mooring force and the power take-off force is given by the system of equations

$$\begin{aligned}(m_b + m_\infty)\ddot{z}(t) &= F_{exc} - F_{rad,d} - \rho g S z(t) \\ \dot{x}_r(t) &= A_r x_r(t) + B_r \dot{z}(t) \\ F_{rad,d}(t) &= C_r x_r(t) + D_r \dot{z}(t)\end{aligned} \tag{2.36}$$

where $\mathbf{A_r} \in \mathbb{R}^{4\times4}$, $\mathbf{B_r} \in \mathbb{R}^{4\times1}$, $\mathbf{C_r} \in \mathbb{R}^{1\times4}$, $\mathbf{D_r} \in \mathbb{R}^{1\times1}$ are the radiation matrices, obtained using WAMIT[4]. Rewriting (2.36) in state-space form, yields

$$\begin{bmatrix}\ddot{z}\\ \dot{z}\\ \dot{x}_r\end{bmatrix} = \begin{bmatrix}-\frac{1}{(m_b+m_\infty)}D_r & -\frac{\rho g S}{(m_b+m_\infty)} & -\frac{1}{(m_b+m_\infty)}C_r\\ 1 & 0 & 0\\ B_r & 0 & A_r\end{bmatrix}\begin{bmatrix}\dot{z}\\ z\\ x_r\end{bmatrix} + \begin{bmatrix}\frac{1}{(m_b+m_\infty)}\\ 0\\ 0\end{bmatrix} F_{exc}. \tag{2.37}$$

It is easy to see that the total order of the system is 6. The Bode plot of the transmissibilty transfer function of the system in (2.37) is shown in figure 2.5. By looking

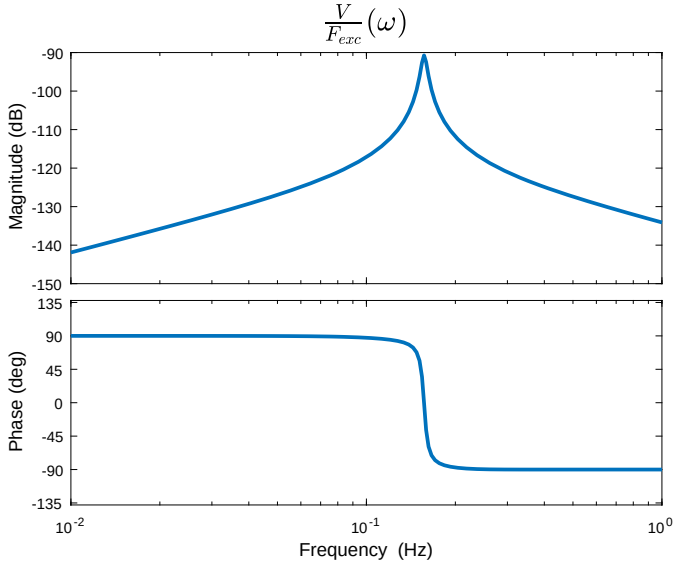

Figure 2.5: Bode plot of the buoy transmissibility transfer function.

at it, it can be seen that the bode plot is similar to the well-known transmissibility of an underdamped second-order system. This means that the sixth order system in (2.27) can be approximated with a second-order system. This can be done simply by disregarding the less significant modes of the system. By looking at the pole-zero map of the system in figure 2.6, it can be seen that two conjugate poles are close to two conjugate zeros. Since these poles and zeros are placed leftmost on the complex plane, they correspond to fast decaying response and therefore their contribution on the overall system dynamics is negligible. The reduction of the system order is done by removing these pole-zero pairs. This can easily be done using the $minreal(sys, tol)$ function in Matlab that cancels close pole-zero pairs in transfer

[4]WAMIT is a software calculates hydrodynamic parameters of a buoy such as excitation force coefficients, radiation matrices, added mass, etc using a boundary element method solver.

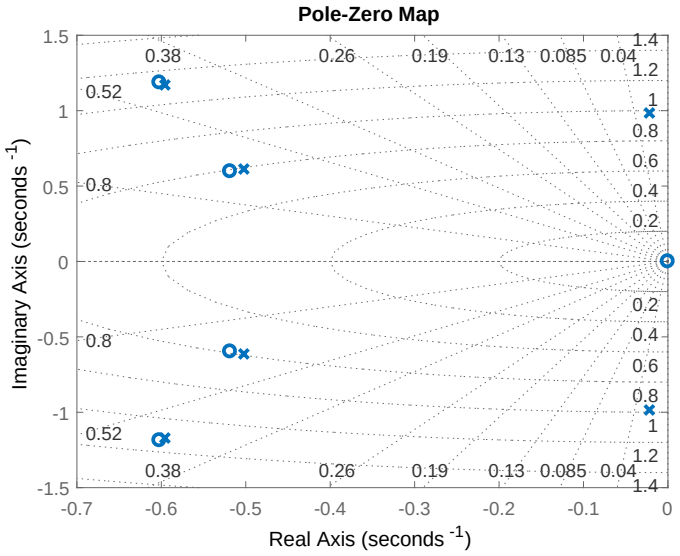

Figure 2.6: Pole-zero map of the buoy transmissibility transfer function.

functions. The tolerance is chosen using trial and error until only two poles remain in the reduced system transfer function. The transfer function of the original and reduced order transfer function are shown in figure 2.7 in order to verify that the reduced order system is a good approximation of the original one. Since the reduced

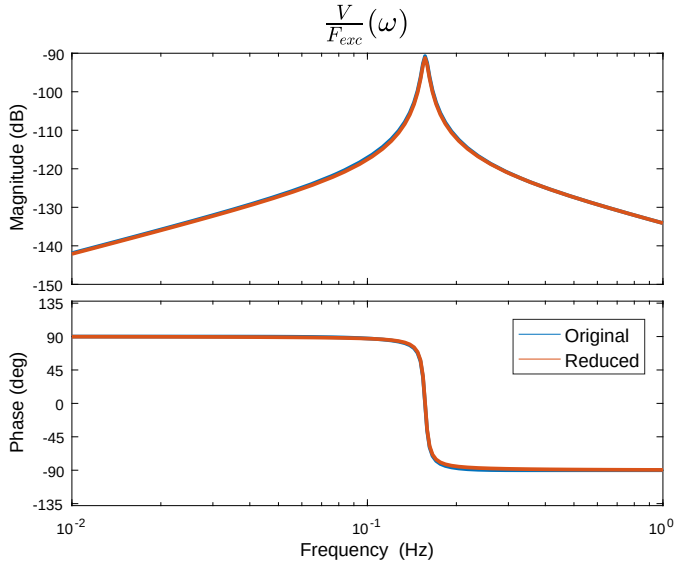

Figure 2.7: Bode plot of the original and reduced order system.

second-order model accurately describes the behaviour of the original sixth-order model, it can be used to do system analysis and controller design. The transfer function of the reduced-order system is

$$\frac{V}{F_{ext}}(s) = \frac{1.208 \times 10^{-6} s}{s^2 + 0.04386s + 0.9703}, \tag{2.38}$$

where $V = \mathcal{L}\{\dot{z}\}$. The denominator of a second-order transfer function with normalized parameters is written as

$$s^2 + 2\zeta\omega_n s + \omega_n^2, \tag{2.39}$$

where ω_n is the natural angular frequency and ζ is the damping factor of the system. By identification, we find the natural angular frequency and the damping factor of the system respectively to be

$$\omega_n = 0.985\frac{rad}{s}, \qquad \zeta = 0.0223 \tag{2.40}$$

Since the buoy dynamics can be described by a second-order system, we can also say that its dynamics are analogous to the dynamics of mass-spring-damper system, which is a well-known second-order system. The undamped natural frequency of a mass-spring-damper system can be calculates as

$$\omega_n = \sqrt{\frac{k}{m}}, \tag{2.41}$$

where k is the stiffness of the spring and m is the mass of the body. For a heaving buoy, the effective mass of the buoy is the sum of the body mass and the added mass, and the hydrostatic stiffness of the buoy corresponds to the mechanical stiffness of the spring in a mass-spring-damper system. Therefore, the undamped natural frequency of a buoy can be calculated as

$$\omega_n = \sqrt{\frac{G_h}{m_b + m_\infty}}, \tag{2.42}$$

where G_h is the hydrostatic stiffness, defined as

$$G_h = \rho g S. \tag{2.43}$$

It should be noted that the natural frequency calculated using (2.42) slightly differs from the natural frequency of the simplified system, shown in (2.40). However, in order to understand the influence of each physical parameter on the buoy dynamics, we rewrite the transfer function of the reduced order system in (2.38) in terms of the buoy parameters,

$$\frac{V}{F_{ext}}(s) = \frac{s}{(m_b + m_\infty)s^2 + R_r s + G_h}, \tag{2.44}$$

where R_r is the radiation resistance

$$R_r = 2\zeta\sqrt{G_h(m_b + m_\infty)}. \tag{2.45}$$

We rewrite (2.44) in terms of the angular frequency ω by using the substitution $s = j\omega$, where $j = \sqrt{-1}$ is the imaginary unit,

$$\frac{V}{F_{ext}}(\omega) = \frac{1}{R_r + j\left((m_b + m_\infty)\omega - G_h/\omega\right)}. \tag{2.46}$$

The magnitude function of (2.46) is

$$\left|\frac{V}{F_{ext}}(\omega)\right| = \frac{1}{\sqrt{R_r^2 + \left((m_b + m_\infty)\omega - G_h/\omega\right)^2}} \tag{2.47}$$

It is easy to see that the maximum of the magnitude function is

$$\left|\frac{V}{F_{ext}}(\omega)\right|_{max} = \frac{1}{R_r} \tag{2.48}$$

that occurs when the frequency is equal to the natural frequency of the system, namely

$$\omega = \omega_n = \sqrt{\frac{G_h}{m_b + m_\infty}} \tag{2.49}$$

It is clear that by changing either the hydrostatic stiffness or the equivalent mass of the buoy or both, we can tune the natural frequency of the system to the frequency of the incoming waves and make the buoy resonate. There are infinitely many combinations of the hydrostatic stiffness and equivalent mass of the buoy that will give a desired natural frequency[5]. Then, a natural question arises. What is the most optimal way to choose the mass and the hydrostatic constant of the buoy? In order to answer to this question, we will introduce the resonance bandwidth $\Delta\omega_{res}$. It is defined as the frequency interval, in which the kinetic energy exceeds half of the maximum value, or the frequency interval in which the transmissibility response is higher than the 70.71% $(1/\sqrt{2})$ of the maximum value at the resonance frequency.

$$\left|\frac{V}{F_{ext}}(\omega)\right| > \frac{1}{\sqrt{2}}\left|\frac{V}{F_{ext}}\right|_{max} = \frac{1}{\sqrt{2}R_r} \tag{2.50}$$

In order to find the resonance bandwidth we need to find the frequencies at which the magnitude response is equal to 70.71% of the its maximum value. Using (2.47) and (2.50), we obtain the equation

$$\left((m_b + m_\infty)\omega - \frac{G_h}{\omega}\right)^2 = 2R_r^2. \tag{2.51}$$

Equation (2.51) has two solutions that are the lower and upper edges of the resonance interval, ω_l and ω_u, respectively.

$$\omega_u(m_b + m_\infty) - \frac{G_h}{\omega_u} = \frac{G_h}{\omega_l} - \omega_l(m_b + m_\infty) = R_r. \tag{2.52}$$

The upper edge is derived as follows

$$\begin{aligned} \omega_u(m_b + m_\infty) - \frac{G_h}{\omega_u} &= R_r \\ (m_b + m_\infty)\omega_u - R_r\omega_u - G_h &= 0 \\ \omega_u = \frac{R_r + \sqrt{R_r^2 + 4(m_b + m_\infty)G_h}}{2(m_b + m_\infty)} & \end{aligned} \tag{2.53}$$

[5]It is assumed that the hydrostatic stiffness and the mass of the buoy are independent. In reality, there will be limitation in the minimum mass that a buoy can have for a given shape of the buoy, that will also determine the hydrostatic stiffness

The lower edge is derived as follows

$$\begin{aligned} \frac{G_h}{\omega_l} - \omega_l(m_b + m_\infty) &= R_r \\ (m_b + m_\infty)\omega_u + R_r\omega_u - G_h &= 0 \\ \omega_l = \frac{-R_r + \sqrt{R_r^2 + 4(m_b + m_\infty)G_h}}{2(m_b + m_\infty)} & \end{aligned} \tag{2.54}$$

Therefore, the resonance bandwidth is

$$\Delta\omega_{res} = \omega_u - \omega_l = \frac{R_r}{(m_b + m_\infty)} \tag{2.55}$$

The relative bandwidth is

$$\frac{\Delta\omega_{res}}{\omega_n} = \frac{R_r}{\sqrt{G_h(m_b + m_\infty)}} \tag{2.56}$$

Equation (2.56) tells us that increasing the effective mass of the buoy, decreases the

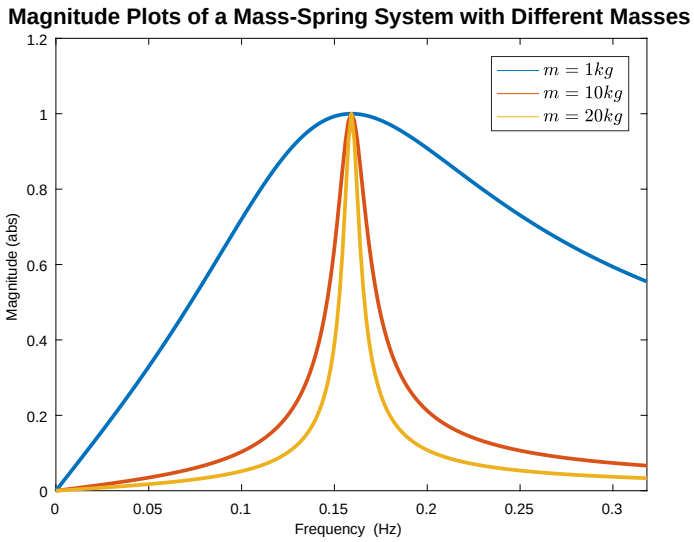

Figure 2.8: Magnitude plot for three mass-spring-damper systems with different masses.

relative bandwidth, and decreasing the hydrostatic stiffness of the buoy, increases the bandwidth of the system. This fact is important when designing a wave energy converter. If one wants to design a buoy that has wide enough bandwidth to capture all the wave frequencies without the need for active control, then the buoy must have light weight and low effective stiffness. The magnitude plots of three mass-spring-damper systems, all with the same damping resistance and natural frequency, but different mass and stiffness, are shown in figure 2.8. It can be clearly seen that the bandwidth widens with decreasing the mass and/or decreasing the hydrostatic stiffness.

The consequence on the choice of mass and hydrostatic stiffness can also be tracked in the time domain by looking at the general solution of the system. The time domain response of an initially charged mass-spring system without excitation is

$$x(t) = (C_1 cos(\omega_d t) + C_2 sin(\omega_d t))\, e^{-\delta t} \tag{2.57}$$

where C_1 and C_2 are determined based on initial conditions, and

$$\delta = \frac{R}{2m} \qquad \omega_d = \sqrt{\omega_n^2 - \delta^2} \tag{2.58}$$

are respectively the damping coefficient and damped natural frequency of the system. By comparing (2.55) and (2.58), it can be seen that the resonance bandwidth is proportional to the damping coefficient

$$\Delta\omega_{res} = 2\delta. \tag{2.59}$$

One way interpretation of the damping coefficient is to see as the speed to reach steady state. i.e. it is inversely proportional to the time constant of the system. The time to reach steady state is shorter for higher damping coefficient, which is desirable since this means reaching the peak amplification more quickly for sinusoidal excitation. From (2.58) it can be seen that the damping coefficient is proportional to the resistance and inversely proportional to the mass of the buoy. Since the former is related to the losses of the system, meaning that increasing the resistance, will decrease the gain of the system, the best way to increase the damping coefficient is to decrease the mass of the system. The response to a sinusoidal excitation of three mass-spring-damper systems with same natural frequency, equal to the frequency of the excitation, i.e. system at resonance, but with different damping coefficients is shown in figure 2.9. It can clearly be seen that the system with the lowest mass reaches steady state in shortest time.

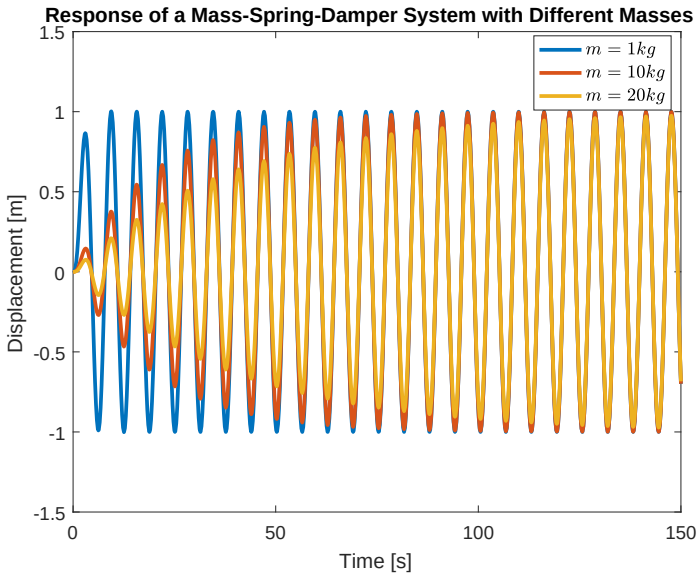

Figure 2.9: Response of three mass-spring-damper systems with different masses and same natural frequency to the same excitation.

When the system is not in resonance, i.e. the system is excited with a frequency different than the natural frequency of the buoy, the system with lowest mass will always have the highest amplification of the motion. In subsequent chapters, it will also be shown that a system with a lower mass, requires the least effort (force), to actively control the natural frequency of the system to match with the excitation frequency. Therefore, it can be concluded that the designer of a wave energy converter should strive for minimizing the mass of the buoy. The normalized magnitude plot for system (2.38) is shown in figure 2.10. It can be seen from the figure that the given buoy is quite narrow-banded with

$$f_n = 0.157Hz, \quad f_l = 0.153Hz, \quad f_u = 0.161Hz, \quad \Delta f_{res} = 0.008Hz \tag{2.60}$$

where $f = \omega/(2\pi)$. Therefore, the generic buoy, chosen to describe the dynamic behaviour of a wave energy converter, can only capture the energy of the waves in a narrow spectrum. Thus, making it a not so efficient example of a wave energy converter.

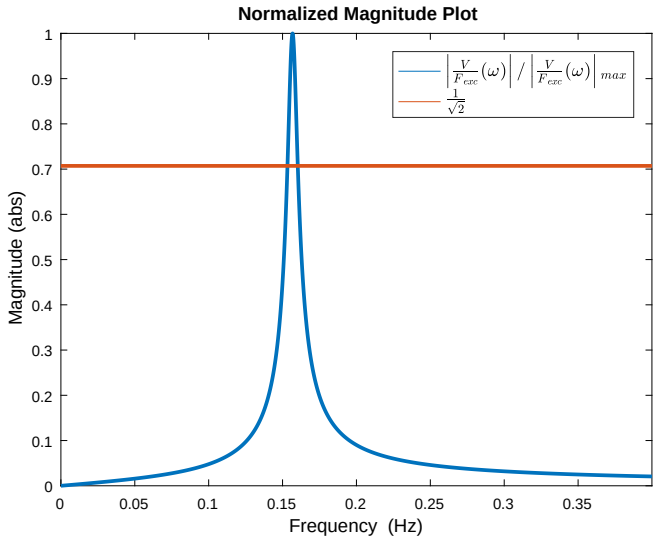

Figure 2.10: Normalized magnitude response and resonance bandwidth.

2.1.5 Optimality condition

In order to obtain the optimality condition for maximum power absorption, the machinery force is considered as just proportional to the velocity of the buoy, i.e.

$$F_{PTO}(t) = -R_{pto}\dot{z}(t) \tag{2.61}$$

where R_{pto} is damping coefficient of the power take-off. This type of force is equivalent to the force of a linear damper, therefore it can also be called the damping force. The choice of this force to be linear to the velocity of the buoy is justified by the fact that in a linear system only resistive type of forces contribute to the active

power transfer in the system. The transfer function of the buoy with linear damping from the power take-off is

$$\frac{V}{F_{ext}}(\omega) = \frac{1}{R_{pto} + R_r + j\left((m_b + m_\infty)\omega - G_h/\omega\right)} \tag{2.62}$$

The captured power from the power take off is (see [3])

$$P_{pto} = \frac{R_{pto}}{2}|V(\omega)|^2 = \frac{R_{pto}/2|F_{exc}|^2}{(R_{pto} + R_r)^2 + (\omega(m_b + m_\infty) - G_h/\omega)^2} \tag{2.63}$$

Noting that $P_{pto} = 0$ for $R_{pto} = 0$ and for $R_{pto} = \infty$, and that $P_a > 0$ for $R_{pto} > 0$, it can be concluded that there exist a maximum of captured power, which can be found by solving

$$\frac{\partial P_{pto}}{\partial R_{pto}} = 0 \tag{2.64}$$

Therefore, the maximum absorbed power occurs if

$$R_{pto,opt} = \sqrt{R_r^2 + (\omega(m_b + m_\infty) - G_h/\omega)^2} \tag{2.65}$$

and it is equal to

$$P_{pto,max} = \frac{|F_{exc}(\omega)|^2/4}{R_r + \sqrt{R_r^2 + (\omega(m_b + m_\infty) - G_h/\omega)^2}} \tag{2.66}$$

In resonance condition or also called optimal phase condition, i.e.

$$\omega(m_b + m_\infty) - G_h/\omega = 0 \tag{2.67}$$

the optimality condition is

$$R_{pto,opt} = R_r \tag{2.68}$$

and the maximum absorbed power is

$$P_{pto,max} = \frac{|F_{exc}|^2}{8R_r} \tag{2.69}$$

Furthermore, the optimal velocity, when both optimum amplitude and phase conditions are satisfied, is

$$V = \frac{F_{ext}}{2R_r} \tag{2.70}$$

It is interesting to observe that the optimum phase condition in (2.67) does not depend on the choice of the damping resistance of the power-take off R_{pto}. Once the optimum phase condition is satisfied, the problem reduces to just setting the damping resistance to the radiation resistance of the buoy. If the optimum phase condition is not satisfied, the optimum damping coefficient is calculated according to (2.65). Another interesting observation by looking at (2.65) is that the value of the damping coefficient is the lowest when the optimum phase condition is satisfied.

We will prove the same fact also for the damping force. The damping force is given by

$$F_{pto}(\omega) = -\frac{R_{pto}F_{exc}(\omega)}{R_{pto} + R_r + j\left((m_b + m_\infty)\omega - G_h/\omega\right)} \tag{2.71}$$

The magnitude of the damping force is equal to

$$|F_{pto}(\omega)| = \frac{R_{pto}|F_{exc}(\omega)|}{\sqrt{(R_{pto} + R_r)^2 + \left((m_b + m_\infty)\omega - G_h/\omega\right)^2}} \tag{2.72}$$

Substituting the optimal damping coefficient (2.65) in (2.72) and doing some algebraic manipulations, yields

$$|F_{pto,opt}(\omega)| = \frac{|F_{exc}(\omega)|}{\sqrt{2\left(1 + \frac{R_r}{\sqrt{R_r^2 + ((m_b + m_\infty)\omega - G_h/\omega)^2}}\right)}} \tag{2.73}$$

It is obvious from the equation above that the minimum is attained when the optimal phase condition is satisfied. Therefore,

$$|F_{pto,opt}(\omega)| \geq \frac{|F_{exc}(\omega)|}{2} \tag{2.74}$$

This implies that in order to capture more power when the optimal phase condition is not met, then the buoy must be dampened always with a higher force than the optimal damping force when the optimal phase condition is satisfied.

So far, we have considered that the machinery force from the power take-off to be pure damping-like, i.e. the damping force is in phase with the machinery force. In general this force can be controlled to have any phase with the buoy velocity. By tuning the phase of PTO force, one can aim at capturing more power by putting the buoy in resonance with the waves or detuning the system to limit power capture in large waves. In order to keep the physical intuition, let us introduce the virtual mass m_v, virtual stiffness G_v and virtual damping R_v, and consider the damping force to be a linear combination inertia, compression and damping force. Therefore,

$$F_{pto}(t) = -m_v\ddot{z}(t) - R_v\dot{z}(t) - G_v z(t) \tag{2.75}$$

We should say that, unlike real physical components, the virtual mass and the virtual stiffness can also have negative values. We assume that the virtual resistance is non-negative. The machinery force is not anymore in phase with the velocity of the buoy. This implies that it will not only dampen the buoy, but also the buoy at some instances. Hence, the power will flow in both directions - from buoy to power take-off and vice versa.

The transfer function of the buoy with the damping force in (2.75) is

$$\frac{V}{F_{ext}}(\omega) = \frac{1}{R_v + R_r + j\left((m_b + m_\infty + m_v)\omega - (G_h + G_v)/\omega\right)} \tag{2.76}$$

The net absorbed power comes only from the damping term of the machinery force, i.e. the mass and the stiffness term do not contribute to the active power transfer from buoy to power take-off. Therefore, the absorbed power is

$$P_{pto} = \frac{R_v}{2}|V(\omega)|^2 = \frac{R_v/2|F_{exc}|^2}{(R_v + R_r)^2 + (\omega(m_b + m_\infty + m_v) - (G_h + G_v)/\omega)^2} \tag{2.77}$$

The maximum absorbed power occurs if

$$R_{v,opt} = \sqrt{R_r^2 + (\omega(m_b + m_\infty + m_v) - (G_h + m_v)/\omega)^2} \tag{2.78}$$

and it is equal to

$$P_{pto,max} = \frac{|F_{exc}(\omega)|^2/4}{R_r + \sqrt{R_r^2 + (\omega(m_b + m_\infty + m_v) - (G_h + G_v)/\omega)^2}} \tag{2.79}$$

By knowing the physical parameters of the system and the frequency of the incoming wave, ans assuming there are no constraints in the system and damping force, the optimal phase condition can be guaranteed by tuning either the virtual mass or stiffness, or both according to

$$\omega(m_b + m_\infty + m_v) - (G_h + G_v)/\omega = 0 \tag{2.80}$$

Then, the optimal damping coefficient of the power take-off force is

$$R_{v,opt} = R_r \tag{2.81}$$

The derivations of the optimal conditions for power absorption are based on a linear system without constraints. In reality, the buoy dynamics are nonlinear and there are constraints in the system such as maximum displacement and velocity of the buoy, maximum allowed machinery force, etc, that needs to be considered when controlling the wave energy converter. We observed that by tuning the machinery force, we can always guarantee optimal phase condition in an unconstrained system. However, this feature comes with an expense. Additional force from the PTO is required to put the buoy in resonance. Writing the machinery force in frequency domain as a function of the velocity, yields

$$F_{pto}(\omega) = (R_v + i(\omega m_v - G_v/\omega))V(\omega) \tag{2.82}$$

Assuming that the optimal phase condition is satisfied, the amplitude of the damping force is

$$|F_{pto,opt}| = \frac{|F_{exc}|}{2R_r}\sqrt{R_r^2 + (\omega m_v - G_v/\omega)^2} \tag{2.83}$$

The minimum is attained when no reactive elements are included in the machinery force, i.e. when it is pure damping. Increasing the machinery force is associated with up-sizing components that increases the cost of the power take-off. For example, in a direct-drive system, providing reactive power through the generator to control the phase of the buoy requires increasing the size of the generator and the drive train. Moreover, there will be round trip losses due to the flow of power in both

directions, which will decrease the benefits obtained by controlling the phase of the buoy. Therefore, the designer of a wave energy converter must look for efficient ways to change the natural frequency of the buoy. This can be done either by changing the effective mass or the effective stiffness of the buoy. CorPower, for instance, has a light weight buoy, whose natural frequency is higher than the frequencies in the bandwidth of the wave spectrum. However, it uses the so called WaveSpring technology that can decrease the effective stiffness of the WEC, thus, reducing the natural frequency in a tunable fashion for each sea state in order to match the natural frequency to the most occurring frequency of excitation in this sea state. Due to the lower mass of the buoy, it is characterized as a wide-banded system that can effectively capture energy from the whole bandwidth of frequencies in a given sea-state without the need for active control.

2.2 Lump-parametric modelling

This section presents lump-parameteric modelling as a way to improve the accuracy of hydraulic pipe models.

A hydraulic pipe can be represented of successively connected basic building blocks, called lumps, that consist of compressibility, inductance and friction components. A model of a lump is shown in figure 2.11 using electrical analogy.

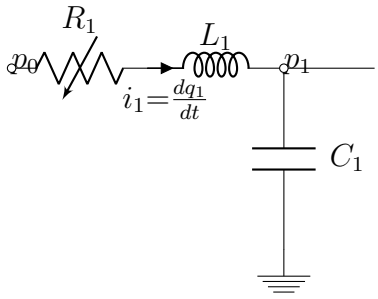

Figure 2.11: Model of a lump

The lump is modelled as follows:

$$\begin{aligned} \Delta p(t) &= p_0(t) - p_1(t) = R_1(q_1(t))q_1(t) + L_1\frac{dq_1}{dt}(t) \\ \frac{dp_1}{dt}(t) &= \frac{1}{C_1}q_1(t) \end{aligned} \tag{2.84}$$

where $R_1(q_1)$ is the fluid resistance that depends on pipe geometry, fluid properties and flow, L_1 is the fluid inertia and C_1 is the fluid capacitance. For laminar flow, the fluid resistance is constant and depends only on pipe geometry and fluid properties. For a circular pipe

$$R_f = \frac{128\rho\nu l}{\pi D^4} \tag{2.85}$$

where ρ is the density of fluid ν is the kinematic viscosity and l is the length of the pipe section. The fluid inertia L_f is proportional to the density of the fluid ρ and

to the pipe section length l, and inversely proportional to the cross section area A.

$$L_f = \rho \frac{l}{A} \tag{2.86}$$

There are two factors that contribute to the fluid capacitance. They are the pipe compliance and the fluid compressibility. We assume that the pipe is stiff and hence does not contribute to the fluid capacitance. The fluid compressibility is represented by a well-known parameter, called the *bulk modulus*. The bulk modulus is a constant/property of each fluid that expresses the stiffness of the fluid. Therefore, the fluid capacitance is inversely proportional to the bulk modulus and it is given by

$$C_f = \frac{V_f}{\beta} \tag{2.87}$$

where V_f is the volume of the pipe section.

Since there are two energy storage components, the lump is a second order system. The transfer function of a lump is

$$\frac{P_1}{P_0}(s) = \frac{1/(LC)}{s^2 + R/Ls + 1/(LC)} \tag{2.88}$$

where L, C and R are respectively the fluid inductance, capacitance and resistance. The transfer function of general second order system is

$$G(s) = \frac{K}{s^2 + 2\zeta\omega_n s + w_n^2} \tag{2.89}$$

By identification we wind

$$K = \frac{1}{LC} \qquad \omega_n = \frac{1}{\sqrt{LC}} \qquad \zeta = \frac{R}{2}\sqrt{\frac{C}{L}} \tag{2.90}$$

Substituting (2.85), (2.86) and (2.87) in (2.90) yields

$$K = \frac{\beta}{\rho l^2} \qquad \omega_n = \sqrt{\frac{\beta}{\rho l^2}} \qquad \zeta = \frac{16\nu l}{D^2}\sqrt{\frac{\rho}{\beta}} \tag{2.91}$$

It is interesting to note that the natural frequency of a pipe section does not depend on its diameter. A model of a pipe with three lumps is shown in figure 2.12.

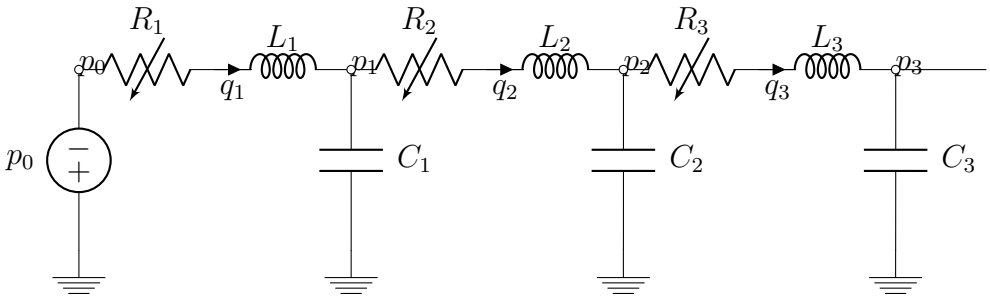

Figure 2.12: Lumped model of a hydraulic pipe

The mathematical model of the pipe is

$$\begin{aligned} L_i\dot{q}_i(t) &= p_{i-1}(t) - p_i(t) - R_i(q_i(t)) \\ C_i\dot{p}_i(t) &= q_i(t) - q_{i+1}(t) \qquad i = 1, \ldots, n. \end{aligned} \tag{2.92}$$

In a higher-order system like the lumped-parameter model of a pipe, there are more than one resonance frequency, called the modes of the system. The number of modes corresponds to the number of lumps of the pump. It can be proven that all the modes of the lumped-parameter model of a pipe are a function of LC only. Therefore, they depend on the pipe length and fluid properties, and not on the pipe width. The bode plot of fluid flow in a pipe with different number of lumps is shown in figure 2.13. The pipe geometry and fluid properties are summarized in Table 2.2.

Table 2.2: Cylindrical buoy parameters

Parameter	Notation	Value	Unit
Pipe diameter	D	76.2×10^{-3}	m
Pipe length	l	80	m
Fluid density	ρ	875	kg/m^3
Bulk modulus	β	1.6×10^9	Pa
Kinematic viscosity	ν	46×10^{-6}	m^2/s

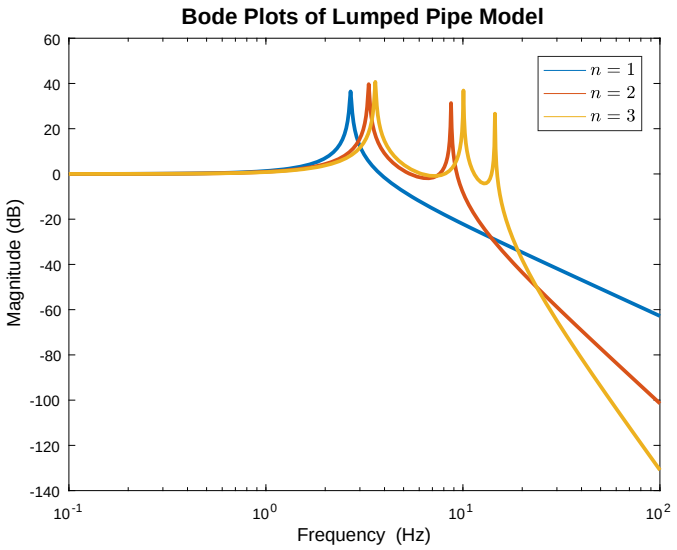

Figure 2.13: Bode plot of lumped parameter model of a pipe with different number of lumps.

By looking at the bode plots, a few observations can be made. Firstly, the low-frequency gain decreases with number of lumps. Secondly, the modes of the system with lower number of lumps occur at lower frequencies compared to the corresponding modes of the system with a higher number of lumps. Furthermore, the bandwidth between two modes decreases with increasing the frequency. Lastly, the high-frequency gain of the system decreases more rapidly with increasing the number of

the lumps. It is also important to say that a higher number of lumps increases model fidelity but decreases simulation speed when simulating the system. Then naturally this question arise: *How many lumps are needed to accurately model a pipe with certain length?* In this thesis, a practical approach is proposed to determine the number of lumps. The method assumes that the bandwidth of the excitation to the pipe is known. The highest frequency with a significant energy content is determined. Then the number of lumps is determined by finding the lowest order system whose last mode is at a frequency that is higher than the highest excitation frequency. This way, it is made sure that none of the significant modes of the system are missed. In our case, the bandwidth of the waves is well-known. Since a buoy exhibits more or less linear behaviour, the response has similar bandwidth to the excitation. However, the rectification of the input flow to the pipes introduces higher-order harmonics, therefore, it spreads the bandwidth to higher frequencies. By noting the most dominant harmonics, we can determine the highest input frequency to the piping system that can have noticeable effect on the response of the system.

Lump-parametric modelling and concepts from linear graph theory, which are explained in the next section, are used to model the hydraulic collection system.

2.3 Linear graph theory

This section informally provides some linear graph theory concepts. The information is mostly excerpted from [17], where the concepts are applied to model an electrical system. General physical systems can be modelled with the help of *graphs* [18]. A graph comprises of *nodes* and directed *branches* connecting the nodes. A graphical node represents a point on the physical systems that separates the physical components. A graphical branch represents a physical component. A *cycle* is a graph whose nodes and branches can be placed around a circle. A connected acyclic sub-graph of a graph is called a *tree*. A *spanning tree* is a tree connecting all the nodes of the graph. The branches in a tree are called *tree branches*. The remaining are called *links*. An example of a directed graph is shown in figure 2.14. The dots represent the nodes and the lines represent the branches. The direction is indicated by an adjacent arrow, defining a tail node and a head node of a branch. The solid lines indicate the tree branches, and the dotted lines are the lines. The branches are enumerated so the first ones are the tree branches and the last ones are the links.

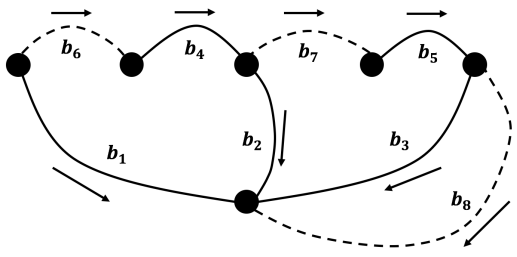

Figure 2.14: An example of a directed graph.

The fundamental cutset matrix is defined as

$$Q_{cutset} = \begin{bmatrix} Q_1 \\ \vdots \\ Q_r \end{bmatrix} \tag{2.93}$$

where Q_i, $1 \leq i \leq r$, is the fundamental cutset vector, defined in [ref] as

Definition: *Let t be a spanning tree for a directed graph. Remove the tree branch b_i , $1 \leq i \leq r$, then the tree is divided into two separate trees, the tree t_1 containing the tail node of b_i and the tree t_2 containing the head node of b_i. Define the fundamental cutset vector:*

$$Q_i = (Q_{i1}, ..., Q_{in}), \qquad 1 \leq i \leq r \tag{2.94}$$

where

$$Q_{ij} = \begin{cases} 1, & \text{if the head node of } b_j \text{ belongs to } t_2 \text{ and the tail node of } b_j \text{ belongs to } t_1 \\ 0, & f \text{ the end nodes of bj belong only to } t_1 \text{or only to } t_2 \\ -1, & \text{if the head node of } b_j \text{ belongs to } t_1 \text{ and the tail node of } b_j \text{ belongs to } t_2 \end{cases}$$

The fundamental cutset matrix always has the structure

$$Q_{cutset} = \begin{bmatrix} I_r & Q_{link} \end{bmatrix} \tag{2.95}$$

where I_r is the identity matrix. The fundamental cycle matrix is defined as

$$P_{cycle} = \begin{bmatrix} P_1 \\ \vdots \\ P_{n-r} \end{bmatrix} \tag{2.96}$$

where P_i, $1 \leq i \leq n - r$, is the fundamental cycle vector, defined in [17] as

Definition: *Let t be a spanning tree for a directed graph. t together with the link b_i , $r < i \leq n$, forms a graph which has one and only one cycle. The cycle consists of b_i and a set of tree branches. Define the fundamental cycle vector:*

$$P_i = (P_{i1}, ..., P_{in}), \qquad 1 \leq i \leq n - r \tag{2.97}$$

where

$$P_{ij} = \begin{cases} 1, & \text{if } b_j \text{ belongs to the cycle and its direction is the same as of } b_i, \\ 0, & \text{if } b_j \text{ does not belong to the cycle,} \\ -1, & \text{if } b_j \text{ belongs to the cycle and its direction is opposite as the end of } b_i. \end{cases}$$

The fundamental cycle matrix always has the structure

$$P_{cycle} = \begin{bmatrix} P_{tree} & I_{n-r} \end{bmatrix} \tag{2.98}$$

A physical system can be composed of flow and effort sources, capacitive, inductive and resistive components. Effort sources are always represented by a tree branch,

and flow sources are represented by a link. Capacitive, inductive and resistive components can be represented either by a tree branch or a link. Let us define the flow variables as

$$f^T = (f_{tree} \;\; f_{link}) \tag{2.99}$$

where

$$f_{tree}^T = (f_E^T \;\; f_C^T \;\; f_l^T \;\; f_X^T) \tag{2.100}$$
$$f_{link}^T = (f_Y^T \;\; f_c^T \;\; f_L^T \;\; f_F^T) \tag{2.101}$$

and the effort variables as

$$e^T = (e_{tree}^T \;\; e_{link}^T), \tag{2.102}$$

where

$$e_{tree}^T = (e_E^T \;\; e_C^T \;\; e_l^T \;\; e_X^T) \tag{2.103}$$
$$e_{link}^T = (e_Y^T \;\; e_c^T \;\; e_L^T \;\; e_F^T) \tag{2.104}$$

The variables with subscript E represent the flow and effort of an effort source, with subscript C - of a tree branch capacitive component, with subscript l - of a tree branch inductive component, with subscript X - of a tree branch resistive component, with subscript Y - of a link resistive component, with subscript c - of a link capacitive component, with subscript L - of a link inductive component, and with subscript F - of a flow source. The ordering of the variables is important in order to obtain the system matrices in a special form that will be apparent later. A general linear physical system can be described by the system of equations

$$\begin{bmatrix} f_{tree} \\ e_{link} \end{bmatrix} = \begin{bmatrix} 0 & -Q_{link} \\ -P_{tree} & 0 \end{bmatrix} \begin{bmatrix} e_{tree} \\ f_{link} \end{bmatrix} \tag{2.105}$$

that is derived based on the fundamental laws of physics, such as the conservation of flow at a node and conservation of effort in a closed cycle.
In [17] it is shown that

$$Q_{link} = -P_{tree}^T, \tag{2.106}$$

if the ordering of the variables is chosen according to equations (2.99) to (2.104). Hence, by knowing either Q_{link} or P_{tree}, one can obtain the whole system of equations.

2.4 Model predictive control

This section derives an MPC controller of a linear hydrodynamic wave-body interaction model in heave using maximization of the captured power as objective.

The simplified buoy model in heave was derived in previous sections and is rewritten here in state-space form

$$\begin{bmatrix} \dot{x}_1(t) \\ \dot{x}_2(t) \end{bmatrix} = \begin{bmatrix} 0 & 1 \\ -\frac{k}{m} & -\frac{b}{m} \end{bmatrix} \begin{bmatrix} x_1(t) \\ x_2(t) \end{bmatrix} + \begin{bmatrix} 0 \\ \frac{1}{m} \end{bmatrix} u(t) + \begin{bmatrix} 0 \\ \frac{1}{m} \end{bmatrix} w(t) \tag{2.107}$$

where $x_1(t)$ is the position of the buoy in meters, m, $x_2(t)$ is the velocity of the buoy in meters per second, m/s, $u(t)$ is the load force in mega-newtons, MN, $w(t)$ is the wave excitation force in MN, and m, b and k are the equivalent mass, viscous friction and buoyancy of the buoy that are equal to

$$m = 0.828 \ \frac{MNs^2}{m}, \qquad b = 0.0363 \ \frac{MNs}{m}, \qquad k = 0.8034 \ \frac{MN}{m} \tag{2.108}$$

Note the choice of the the units in (2.108). They are not chosen as SI units in order to keep the numerical values of the variables and inputs close. The extracted power from the buoy at time t is expressed as

$$P(t) = x_2(t)u(t) \tag{2.109}$$

and it has the units mega-wats, MW. The average power over a period T after initial time t_0 is

$$\bar{P} = \int_{t_0}^{t_0+T} x_2(t)u(t)dt \tag{2.110}$$

We aim at maximizing the average extracted power over a period of T, hence (2.110) is a good candidate as an objective function of the proposed MPC controller.

Since MPC is a discrete type of controller, we need to discretize the continuous model and use an objective function in discrete form. We discretize the model using zero-order hold and sampling period of $T_s = 0.1$

$$\mathbf{x}(k+1) = \mathbf{A}\mathbf{x}(k) + \mathbf{B}u(k) + \mathbf{B_w}w(k) \tag{2.111}$$

where

$$\mathbf{A} = \begin{bmatrix} 0.9952 & 0.09962 \\ -0.09666 & 0.9908 \end{bmatrix}, \qquad \mathbf{B} = \mathbf{B_w} = \begin{bmatrix} 0.006025 \\ 0.1203 \end{bmatrix}. \tag{2.112}$$

The objective function is formulated as the discrete version of (2.110)

$$\bar{P} = \frac{T_s}{T} \sum_{i=0}^{N} x_2(k+i|k)u(k+i|k), \tag{2.113}$$

where $var(.|k)$ notation is used to indicate that the variable is the predicted, and not the measured one. At the current time instant $t_0 = kT_s$ the states of the system are measured, hence $\mathbf{x}(k|k) = \mathbf{x}(k)$. In order to have only variables that can be optimized in the objective function, i.e. not measured, and to have a convex objective function, we augment it as

$$\bar{P} = \frac{T_s}{T} \sum_{i=0}^{N} x_2(k+1+i|k)u(k+i|k), \tag{2.114}$$

In order to have more design freedom, we are going to define a more general objective function, that will be used to derive the MPC controller. The system equations will

be the equality constraints, and, we will introduce inequality constraints on the states and inputs of the system. Hence, the problem is formulated as

$$\begin{aligned}\min_{\mathbf{x}(k+1:k+N|k),u(k:M-1|k)} \quad & \sum_{i=1}^{N}\frac{1}{2}\mathbf{x}^T(k+i|k)\mathbf{Q}\mathbf{x}(k+i|k) \\ & +\sum_{i=0}^{M-1}\left(\frac{1}{2}u^T(k+i|k)^T\mathbf{R}u(k+i|k)+\mathbf{x}^T(k+1+i|k)\mathbf{S}u(k+i|k)\right) \\ & +\sum_{i=M}^{N}\mathbf{x}^T(k+i|k)\mathbf{S}u(k+M-1|k) \\ \text{subj to } \mathbf{x}(k+1+i|k)=&\mathbf{A}\mathbf{x}(k+i|k)+\mathbf{B}u(k+i|k)+\mathbf{B}_{\mathbf{w}}w(k+i|k), \quad i=0,\ldots,N-1 \\ & x_{min}\le\mathbf{x}(k+i|k)\le x_{max}, \quad i=1,\ldots,N \\ & u_{min}\le u(k+i|k)\le u_{max}, \quad i=0,\ldots,M-1\end{aligned} \tag{2.115}$$

where N and M are respectively the state and input horizon, $\mathbf{Q}=diag(q_1,q_2)$, $\mathbf{R}$ and $\mathbf{S}=[0\ 1]^T$ are respectively the state, input and state-input weighting matrices. Let us define

$$\mathbf{z}(k)=\begin{bmatrix}\mathbf{x}^T(k+1|k) & \cdots & \mathbf{x}^T(N|k) & u(k|k) & \cdots & u(M-1|k)\end{bmatrix}^T \tag{2.116}$$

We can write the objective function in terms of the new variable

$$\begin{aligned}\min_{\mathbf{z}(k)} \quad & \frac{1}{2}\mathbf{z}^T(k)\mathbf{H}\mathbf{z}(k) \\ \text{subject to} \quad & \mathbf{G}\mathbf{z}(k)\le\mathbf{h}\end{aligned} \tag{2.117}$$

where

$$\mathbf{H}=\begin{bmatrix}\bar{\mathbf{Q}} & \bar{\mathbf{S}}\\ \bar{\mathbf{S}}^T & \bar{\mathbf{R}}\end{bmatrix} \qquad \in\mathbb{R}^{2N+M}$$

$$\bar{\mathbf{Q}}=\begin{bmatrix}\mathbf{Q} & \cdots & \mathbf{0}\\ \vdots & \ddots & \vdots\\ \mathbf{0} & \cdots & \mathbf{Q}\end{bmatrix} \qquad \in\mathbb{R}^{2N\times 2N}$$

$$\bar{\mathbf{S}}=\begin{cases}\begin{bmatrix}\mathbf{S} & \cdots & \mathbf{0}\\ \vdots & \ddots & \vdots\\ \mathbf{0} & \cdots & \mathbf{S}\end{bmatrix}, \text{if } M=N \\ \begin{bmatrix}\mathbf{S} & \cdots & \mathbf{0}\\ \vdots & \ddots & \vdots\\ \mathbf{0} & \cdots & \mathbf{S}\\ \vdots & \vdots & \vdots\\ \mathbf{0} & \cdots & \mathbf{S}\end{bmatrix}, \text{if } M<N\end{cases} \qquad \in\mathbb{R}^{2N\times M}$$

$$\bar{\mathbf{R}}=\begin{bmatrix}\mathbf{R} & \cdots & \mathbf{0}\\ \vdots & \ddots & \vdots\\ \mathbf{0} & \cdots & \mathbf{R}\end{bmatrix} \qquad \in\mathbb{R}^{M\times M}$$

$$\mathbf{G} = \begin{bmatrix} \mathbf{G_x} & \mathbf{0}^{4N\times M} \\ \mathbf{0}^{2N\times 2M} & \mathbf{G_u} \end{bmatrix} \qquad \in \mathbb{R}^{2(2N+M)\times 2N+M}$$

$$\mathbf{G_x} = \begin{bmatrix} \mathbf{I_2} & \mathbf{0} & \cdots & \mathbf{0} \\ \mathbf{0} & \mathbf{I_2} & \cdots & \mathbf{0} \\ \vdots & \vdots & \ddots & \vdots \\ \mathbf{0} & \mathbf{0} & \cdots & \mathbf{I_2} \\ -\mathbf{I_2} & \mathbf{0} & \cdots & \mathbf{0} \\ \mathbf{0} & -\mathbf{I_2} & \cdots & \mathbf{0} \\ \vdots & \vdots & \ddots & \vdots \\ \mathbf{0} & \mathbf{0} & \cdots & -\mathbf{I_2} \end{bmatrix} \qquad \in \mathbb{R}^{4N\times 2N}$$

$$\mathbf{G_u} = \begin{bmatrix} 1 & 0 & \cdots & 0 \\ 0 & 1 & \cdots & 0 \\ \vdots & \vdots & \ddots & \vdots \\ 0 & 0 & \cdots & 1 \\ -1 & 0 & \cdots & 0 \\ 0 & -1 & \cdots & 0 \\ \vdots & \vdots & \ddots & \vdots \\ 0 & 0 & \cdots & -1 \end{bmatrix} \qquad \in \mathbb{R}^{2M\times M}$$

$$\mathbf{h} = \begin{bmatrix} \mathbf{h_x} \\ \mathbf{h_u} \end{bmatrix} \qquad \in \mathbb{R}^{2(2N+M)\times 1}$$

$$\mathbf{h_x} = \begin{bmatrix} \mathbf{x_{max}} \\ -\mathbf{x_{min}} \end{bmatrix} \qquad \in \mathbb{R}^{4N\times 1}$$

$$\mathbf{h_u} = \begin{bmatrix} \mathbf{u_{max}} \\ -\mathbf{u_{min}} \end{bmatrix} \qquad \in \mathbb{R}^{2M\times 1}$$

$$\mathbf{x_{max}} = \begin{bmatrix} x_{max} \\ \vdots \\ x_{max} \end{bmatrix} \qquad \in \mathbb{R}^{2N\times 1}$$

$$\mathbf{x_{min}} = \begin{bmatrix} x_{min} \\ \vdots \\ x_{min} \end{bmatrix} \qquad \in \mathbb{R}^{2N\times 1}$$

$$\mathbf{u_{max}} = \begin{bmatrix} u_{max} \\ \vdots \\ u_{max} \end{bmatrix} \qquad \in \mathbb{R}^{M\times 1}$$

$$\mathbf{u_{min}} = \begin{bmatrix} u_{min} \\ \vdots \\ u_{min} \end{bmatrix} \qquad \in \mathbb{R}^{M\times 1}$$

Repeated use of the system equations gives the batch solution

$$\mathbf{x}(k+1|k) = \mathbf{A}\mathbf{x}(k) + \mathbf{B}u(k|k) + \mathbf{B_w}w(k|k)$$
$$\mathbf{x}(k+2|k) = \mathbf{A}^2\mathbf{x}(k) + \mathbf{A}\mathbf{B}u(k|k) + \mathbf{B}u(k+1|k) + \mathbf{A}\mathbf{B_w}w(k|k) + \mathbf{B_w}w(k+1|k)$$
$$\vdots$$

$$
\begin{aligned}
\mathbf{x}(k+M|k) &= \mathbf{A}^M\mathbf{x}(k) + \mathbf{A}^{M-1}\mathbf{B}u(k|k) + \cdots + \mathbf{B}u(k+M-1|k) \\
&\quad + \mathbf{A}^{M-1}\mathbf{B}_\mathbf{w}w(k|k) + \cdots + \mathbf{B}_\mathbf{w}w(k+M-1|k) \\
\mathbf{x}(k+M+1|k) &= \mathbf{A}^{M+1}\mathbf{x}(k) + \mathbf{A}^M\mathbf{B}u(k|k) + \cdots + (\mathbf{A}+\mathbf{I_2})\mathbf{B}u(k+M-1|k) \\
&\quad + \mathbf{A}^M\mathbf{B}_\mathbf{w}w(k|k) + \cdots + \mathbf{B}_\mathbf{w}w(k+M|k) \\
&\quad \vdots \\
\mathbf{x}(k+N|k) &= \mathbf{A}^N\mathbf{x}(k) + \mathbf{A}^{N-1}\mathbf{B}u(k|k) + \cdots + \sum_{i=0}^{N-M}\mathbf{A}^i\mathbf{B}u(k+M-1|k) \\
&\quad + \mathbf{A}^{N-1}\mathbf{B}_\mathbf{w}w(k|k) + \cdots + \mathbf{B}_\mathbf{w}w(k+N-1|k)
\end{aligned}
\tag{2.118}
$$

Rewriting in matrix form, yields

$$
\mathbf{X}(k) = \bar{\mathbf{A}}\mathbf{x}(k) + \bar{\mathbf{T}}\mathbf{U}(k) + \bar{\mathbf{W}}\mathbf{w}(k) \tag{2.119}
$$

where

$$
\begin{aligned}
\mathbf{X}(k) &= \begin{bmatrix}\mathbf{x}^T(k+1) & \cdots & \mathbf{x}^T(k+N)\end{bmatrix}^T \quad \in \mathbb{R}^{2N\times 1} \\
\mathbf{U}(k) &= \begin{bmatrix}u(k) & \cdots & u(k+M-1)\end{bmatrix}^T \quad \in \mathbb{R}^{M\times 1} \\
\mathbf{w}(k) &= \begin{bmatrix}w(k) & \cdots & w(k+N-1)\end{bmatrix}^T \quad \in \mathbb{R}^{N\times 1}
\end{aligned}
$$

$$
\bar{\mathbf{A}} = \begin{bmatrix}\mathbf{A} \\ \mathbf{A}^2 \\ \vdots \\ \mathbf{A}^N\end{bmatrix} \quad \in \mathbb{R}^{2N\times 2}
$$

$$
\bar{\mathbf{T}} = \begin{bmatrix}
\mathbf{B} & \mathbf{0} & \dots & \mathbf{0} & \mathbf{0} \\
\mathbf{AB} & \mathbf{B} & \dots & \mathbf{0} & \mathbf{0} \\
\vdots & \vdots & \ddots & \vdots & \vdots \\
\mathbf{A}^{M-2}\mathbf{B} & \mathbf{A}^{M-1}\mathbf{B} & \dots & \mathbf{B} & \mathbf{0} \\
\mathbf{A}^{M-1}\mathbf{B} & \mathbf{A}^{M-2}\mathbf{B} & \dots & \mathbf{AB} & \mathbf{B} \\
\mathbf{A}^M\mathbf{B} & \mathbf{A}^{M-1}\mathbf{B} & \dots & \mathbf{A}^2\mathbf{B} & (\mathbf{A}+\mathbf{I_2})\mathbf{B} \\
\vdots & \vdots & \ddots & \vdots & \\
\mathbf{A}^{N-1}\mathbf{B} & \mathbf{A}^{N-2}\mathbf{B} & \dots & \mathbf{A}^{N-M+1}\mathbf{B} & \sum_{i=0}^{N-M}\mathbf{A}^i\mathbf{B}
\end{bmatrix} \quad \in \mathbb{R}^{2N\times M}
$$

$$
\bar{\mathbf{W}} = \begin{bmatrix}
\mathbf{B}_\mathbf{w} & \mathbf{0} & \dots & \mathbf{0} \\
\mathbf{AB}_\mathbf{w} & \mathbf{B}_\mathbf{w} & \dots & \mathbf{0} \\
\vdots & \vdots & \ddots & \vdots \\
\mathbf{A}^{N-1}\mathbf{B}_\mathbf{w} & \mathbf{A}^{N-2}\mathbf{B}_\mathbf{w} & \dots & \mathbf{B}_\mathbf{w}
\end{bmatrix} \quad \in \mathbb{R}^{2N\times N} \tag{2.120}
$$

Noting that $\mathbf{z}(k) = [\mathbf{X}^T(k)\ \mathbf{U}^T(k)]^T$, we can write the objective function in (2.117) in terms of $\mathbf{X}(k)$ and $\mathbf{U}(k)$. It yields

$$
\begin{aligned}
\min_{\mathbf{X}(k),\mathbf{U}(k)} \quad & \frac{1}{2}\mathbf{X}^T(k)\bar{\mathbf{Q}}\mathbf{X}(k) + \mathbf{X}^T(k)\bar{\mathbf{S}}\mathbf{U}(k) + \frac{1}{2}\mathbf{U}^T(k)\bar{\mathbf{R}}\mathbf{U}(k) \\
\text{subject to} \quad & \mathbf{G_x}\mathbf{X}(k) \le \mathbf{h_x} \\
& \mathbf{G_u}\mathbf{U}(k) \le \mathbf{h_u}
\end{aligned}
\tag{2.121}
$$

Substituting (2.119) in (2.121), yields

$$\begin{aligned} \min_{\mathbf{U}(k)} \quad & \frac{1}{2}\left(\bar{\mathbf{A}}\mathbf{x}(k)+\bar{\mathbf{T}}\mathbf{U}(k)+\bar{\mathbf{W}}\mathbf{w}(k)\right)^T \bar{\mathbf{Q}}\left(\bar{\mathbf{A}}\mathbf{x}(k)+\bar{\mathbf{T}}\mathbf{U}(k)+\bar{\mathbf{W}}\mathbf{w}(k)\right) \\ & +\left(\bar{\mathbf{A}}\mathbf{x}(k)+\bar{\mathbf{T}}\mathbf{U}(k)+\bar{\mathbf{W}}\mathbf{w}(k)\right)^T \bar{\mathbf{S}}\mathbf{U}(k)+\frac{1}{2}\mathbf{U}^T(k)\bar{\mathbf{R}}\mathbf{U}(k) \\ \text{subject to} \quad & \mathbf{G_x}\left(\bar{\mathbf{A}}\mathbf{x}(k)+\bar{\mathbf{T}}\mathbf{U}(k)+\bar{\mathbf{W}}\mathbf{w}(k)\right) \leq \mathbf{h_x} \\ & \mathbf{G_u}\mathbf{U}(k) \leq \mathbf{h_u}. \end{aligned} \tag{2.122}$$

Performing a few algebraic manipulations on (2.122) and removing all the terms that do not depend on the optimization variable $\mathbf{U}(k)$, we obtain

$$\begin{aligned} \min_{\mathbf{U}} \quad & \frac{1}{2}\mathbf{U}^T(k)\mathbf{H_u}\mathbf{U}(k)+\mathbf{f_u}(k)\mathbf{U}(k) \\ \text{subject to} \quad & \mathbf{G}\mathbf{U}(k) \leq \mathbf{h}(k) \end{aligned} \tag{2.123}$$

where

$$\mathbf{H_u}=\bar{\mathbf{T}}^T\left(\bar{\mathbf{Q}}\bar{\mathbf{T}}+\bar{\mathbf{S}}\right)+\bar{\mathbf{R}} \qquad \mathbf{f_u}(k)=\left(\bar{\mathbf{A}}\mathbf{x}(k)+\bar{\mathbf{W}}\mathbf{w}(k)\right)^T\left(\bar{\mathbf{Q}}\bar{\mathbf{T}}+\bar{\mathbf{S}}\right)$$

$$\mathbf{G}=\begin{bmatrix}\mathbf{G_x}\bar{\mathbf{T}} \\ \mathbf{G_u}\end{bmatrix} \qquad \mathbf{h}=\begin{bmatrix}\mathbf{h_x}-\mathbf{G_x}\bar{\mathbf{A}}\mathbf{x}(k)-\mathbf{G_x}\bar{\mathbf{W}}\mathbf{w}(k) \\ \mathbf{h_u}\end{bmatrix}$$

Infeasibility handling

If the constraints that are enforced on the system are too strict, the optimization algorithm might fail to find an optimal solution in the feasible set. In this scenario the optimization will not give any control input, i.e. the system will run in open loop. Therefore, we need to find a way to handle these situations. One of the most common ways is softening the constraints by introducing slack variables in the optimization problem. We define the new control problem as

$$\begin{aligned} \min_{\mathbf{X}(k),\mathbf{U}(k),\epsilon} \quad & \frac{1}{2}\mathbf{X}^T(k)\bar{\mathbf{Q}}\mathbf{X}(k)+\mathbf{X}^T(k)\bar{\mathbf{S}}\mathbf{U}(k)+\frac{1}{2}\mathbf{U}^T(k)\bar{\mathbf{R}}\mathbf{U}(k)+\frac{1}{2}\epsilon^T(k)\bar{\mathbf{P}}\epsilon(k) \\ \text{subject to} \quad & \mathbf{x_{min}}-\mathbf{V}_{\mathbf{x_{min}}}\epsilon_{\mathbf{x}}(k) \leq \mathbf{X}(k) \leq \mathbf{x_{max}}+\mathbf{V}_{\mathbf{x_{max}}}\epsilon_{\mathbf{x}}(k) \\ & \mathbf{u_{min}}-\mathbf{V}_{\mathbf{u_{min}}}\epsilon_u(k) \leq \mathbf{U}(k) \leq \mathbf{u_{max}}+\mathbf{V}_{\mathbf{u_{max}}}\epsilon_u(k) \\ & \epsilon(k) \geq \mathbf{0} \end{aligned} \tag{2.124}$$

where $\epsilon(k)=[\epsilon_{\mathbf{x}}(k),\ \epsilon_u(k)]^T$ are the slack variables, $\bar{\mathbf{P}}=diag(\rho_{\mathbf{x}},\ \rho_u)$ is the weights for each slack variable, and $\mathbf{V}_{\mathbf{x_{min}}}$, $\mathbf{V}_{\mathbf{x_{max}}} \in \mathbb{R}^{2N\times 2}$, $\mathbf{V}_{\mathbf{u_{min}}}$ and $\mathbf{V}_{\mathbf{u_{max}}} \in \mathbb{R}^{M\times 1}$ are matrices with non-negative entries, where the larger the i-th entry, the relatively softer the corresponding i-th constraint is. We plug in the batch solution (2.119) into (2.124) to obtain the optimization problem in terms of the control inputs $\mathbf{U}(k)$ and slack variables $\epsilon(k)$,

$$\begin{aligned} \min_{\mathbf{U}(k),\epsilon(k)} \quad & \frac{1}{2}\mathbf{U}^T(k)\mathbf{H_u}\mathbf{U}(k)+\mathbf{f_u}(k)\mathbf{U}(k)+\frac{1}{2}\epsilon^T(k)\bar{\mathbf{P}}\epsilon(k) \\ \text{subject to} \quad & \mathbf{G_x}\bar{\mathbf{T}}\mathbf{U}(k)-\mathbf{V_x}\epsilon_{\mathbf{x}}(k) \leq \mathbf{h_x}-\mathbf{G_x}\bar{\mathbf{A}}\mathbf{x}(k)-\mathbf{G_x}\bar{\mathbf{W}}\mathbf{w}(k) \\ & \mathbf{G_u}\mathbf{U}(k)-\mathbf{V_u}\epsilon_u(k) \leq \mathbf{h_u} \\ & -\mathbf{I_3}\epsilon(k) \leq \mathbf{0} \end{aligned} \tag{2.125}$$

where

$$\mathbf{V_x} = [\mathbf{V_{x_{max}}^T}\ \mathbf{V_{x_{min}}^T}]^T, \qquad \mathbf{V_u} = [\mathbf{V_{u_{max}}^T}\ \mathbf{V_{u_{min}}^T}]^T \tag{2.126}$$

Let us define the new optimization vector $\mathbf{Z}$,

$$\mathbf{Z}(k) = [\mathbf{U}^T(k)\,\epsilon^T(k)]^T \tag{2.127}$$

The optimization problem written in terms of $\mathbf{Z}$ is

$$\begin{aligned} \min_{\mathbf{Z}}(k) \quad & \frac{1}{2}\mathbf{Z}^T(k)\bar{\mathbf{H}}\mathbf{Z}(k) + \bar{\mathbf{f}}(k)\mathbf{Z}(k) \\ \text{subject to} \quad & \bar{\mathbf{G}}\mathbf{Z}(k) \leq \bar{\mathbf{h}}(k) \end{aligned} \tag{2.128}$$

where

$$\bar{\mathbf{H}} = \begin{bmatrix} \mathbf{H_u} & \mathbf{0}^{M\times 3} \\ \mathbf{0}^{3\times M} & \bar{\mathbf{P}} \end{bmatrix}, \qquad \bar{\mathbf{f}}(k) = \begin{bmatrix} \mathbf{f_u}(k) & \mathbf{0}^{1\times 3} \end{bmatrix}$$

$$\bar{\mathbf{G}} = \begin{bmatrix} \mathbf{G_x}\bar{\mathbf{T}} & -\mathbf{V_x} & \mathbf{0}^{2N\times 1} \\ \mathbf{G_u} & \mathbf{0}^{M\times 2} & -V_u \\ \mathbf{0}^{2\times M} & -\mathbf{I_2} & \mathbf{0}^{2\times 1} \\ \mathbf{0}^{1\times M} & \mathbf{0}^{1\times 2} & -1 \end{bmatrix} \qquad \bar{\mathbf{h}}(k) = \begin{bmatrix} \mathbf{h}(k) \\ \mathbf{0}^{3\times 1} \end{bmatrix}$$

A sample output from applying the designed MPC on the generic buoy in the sea state $H_s = 4.75m$ and $T_e = 9.5s$, is shown in figure 2.15.

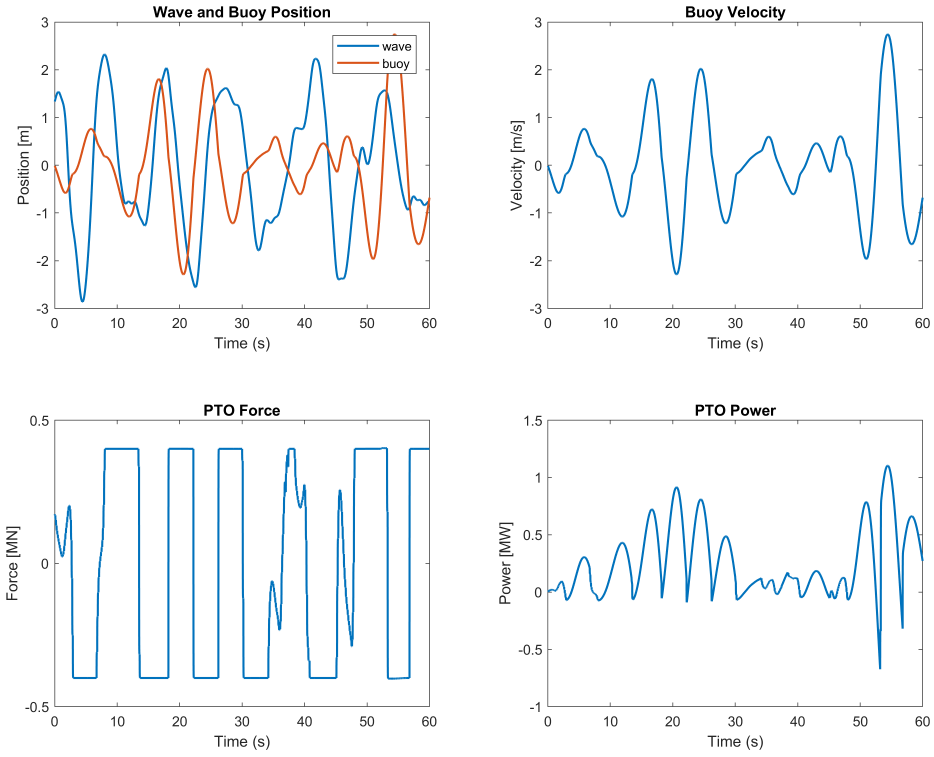

Figure 2.15: Timesieries with MPC and the generic buoy in sea state $H_s = 4.75m$, $T_e = 9.5s$.

The chosen constraints in the simulation are: 3.5m maximum displacement, 5m/s maximum velocity and 400kN maximum PTO force. The prediction and control horizon are both equal to 40s. It can be seen that the force constrain is not violated, and the displacement and velocity constraints are not reached during the shown time interval. It can also be observed that the PTO power is negative at some time instances. This implies that energy is returned to the buoy in order to amplify the motion.

3

Modelling of Wave Energy Converters

This chapter describes the modelling of CorPower and Waves4Power buoys.

3.1 Modelling of CorPower's buoy

CorPower's buoy will be modelled with energy approach using the Euler-Lagrange equations. In order to do that, firstly, the generalized coordinates will be selected and any constraints between them will be identified. Secondly, the total energy in the system will be written down. Finally, the Euler-Lagrange equation will be applied to obtain the dynamic equations of the system.

The drawing in 3.1 is used to assist the modelling of CPO's wave energy converter.

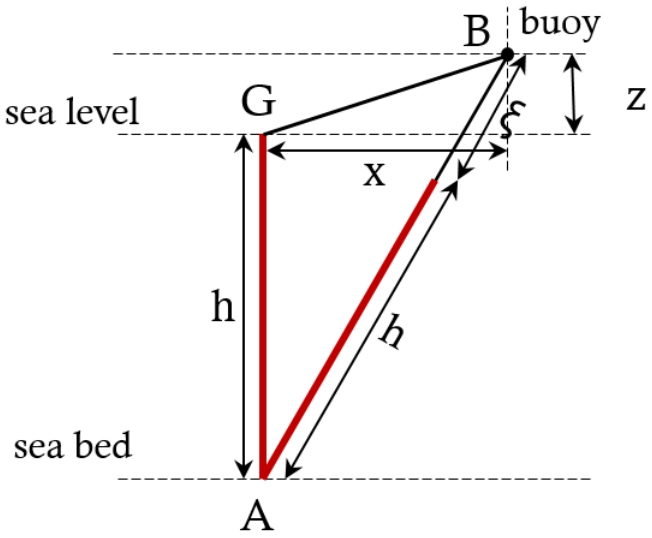

Figure 3.1: Geometric relation between buoy position and rack displacement.

The WEC captures power both from surge and heave motion, therefore two dimensions are considered when modelling the buoy. They are denoted as $x(t)$ and $z(t)$, respectively. The mooring wire is always tensed due to the pretension module and its length is always equal to the sea depth, denoted by h, i.e. the wire is assumed to be stiff. The displacement of the rack is denoted by $\xi(t)$ and it is constrained by

the surge and heave position of the buoy according to

$$h_1 : \sqrt{x^2(t) + (z(t) + h)^2} - h - \xi(t) = 0 \tag{3.1}$$

The angular displacement of the two shafts are denoted by $\theta_1(t)$ and $\theta_2(t)$ respectively. When either of the shafts are engaged their displacements are constrained to the displacement of the rack by

$$h_{2_i} : \xi(t) - n_c\theta_i(t) = 0 \tag{3.2}$$

where n_c is the total gear ratio of the cascade gearbox and $i = 1, 2$ denotes the shaft that is engaged to the rack. When the shafts are disengaged, they are not any more constrained by the rack, and rotate by the stored kinetic energy in the flywheels. The generalized coordinates are chosen to be $\mathbf{q}(t) = \begin{bmatrix} x(t) & z(t) & \xi(t) & \theta_1(t) & \theta_2(t) \end{bmatrix}^T$. From now on, we will omit the time argument from the generalized coordinates in all expressions to keep them more readable. The number of the generalized coordinates determines the number of degrees of freedom, which in this case is five. The two constraints will reduce the system to a three-degree-of-freedom one.
The kinetic energy of the of the system is

$$T = \frac{1}{2}m_{b_x}\dot{x}^2 + \frac{1}{2}m_{b_z}\dot{z}^2 + \frac{1}{2}m_r\dot{\xi}^2 + \frac{1}{2}J_1\dot{\theta}_1^2 + \frac{1}{2}J_2\dot{\theta}_2^2, \tag{3.3}$$

where m_{b_x}, m_{b_z}, m_r, J_1, J_2 are respectively the mass of the buoy in surge and heave direction, mass of the rack and inertia of the two shafts. The reason $m_{b_x} \neq m_{b_z}$ is that the masses also account for the added masses, which are different for surge and heave. The potential energy of the system is given

$$U = \frac{1}{2}S_h z^2, \tag{3.4}$$

where S_h is the hydrostatic stiffness. The Lagrangian is defined as

$$L(\mathbf{q}, \dot{\mathbf{q}}) = T(\dot{\mathbf{q}}) - U(\mathbf{q}) \tag{3.5}$$

Hence,

$$L = \frac{1}{2}m_{b_x}\dot{x}^2 + \frac{1}{2}m_{b_z}\dot{z}^2 + \frac{1}{2}m_r\dot{\xi}_r^2 + \frac{1}{2}J_1\dot{\theta}_1^2 + \frac{1}{2}J_2\dot{\theta}_2^2 - \frac{1}{2}S_h z^2 \tag{3.6}$$

The Lagrange equation is defined as

$$\frac{d}{dt}\left(\frac{\partial L}{\partial \dot{\mathbf{q}}}\right) - \frac{\partial L}{\partial \mathbf{q}} = \mathbf{F_g} \tag{3.7}$$

where $\mathbf{F_g}$ is a vector containing the generalized forces, that include

- F_{diss} - dissipative forces
- F_{in} - input forces
- F_{cst} - constraint forces

In our system we can identify the following generalized forces

- F_{w_x} - surge excitation force
- F_{w_z} - heave excitation force

- F_{r_x} - radiation force in surge
- F_{r_z} - radiation force in heave
- F_{d_x} - drag force in surge
- F_{d_z} - drag force in heave
- F_{d_ξ} - friction force of the rack
- τ_{d_i} - friction torque of shaft $i = 1, 2$
- τ_{g_i} - induced torque of generator $i = 1, 2$

The WaveSpring force F_{WS} and the gas-spring force F_{GS} act on the rack in parallel with the other generalized forces of the rack. Therefore, we can consider them as generalized forces without digging into their derivation. Though, it is not correct to name them as generalized forces, since they arise as a result of the stored potential energy in the gas springs.

The constraints given by (3.1) and (3.2) depend only on displacements. Therefore, they are called holonomic. For holonomic constraints, the constraint forces are defined as

$$F_{cst_i} = -\sum_{j=1}^{k} \lambda_j(t) \frac{\partial h_j}{\partial q_i} \tag{3.8}$$

where λ is the Lagrange multiplier and k is the number of constraints.

Applying the Euler-Lagrange equation in (3.7), we obtain the equations of motion

$$m_{b_x}\ddot{x} + F_{r_x} + F_{d_x} + \lambda_1 \frac{x}{\sqrt{x^2 + (z+h)^2}} = F_{w_x} \tag{3.9a}$$

$$m_{b_z}\ddot{z} + F_{r_z} + F_{d_z} + S_h z + \lambda_1 \frac{z+h}{\sqrt{x^2 + (z+h)^2}} = F_{w_z} \tag{3.9b}$$

$$m_r\ddot{\xi} + F_{d_r} + F_{GS} + F_{WS} - \lambda_1 + \alpha\lambda_{2_i} = 0 \tag{3.9c}$$

$$J_i\ddot{\theta}_i + \tau_{d_i} - n_c\alpha\lambda_{2_i} = -\tau_{g_i}, \qquad i = 1, 2 \tag{3.9d}$$

In (3.9) $\alpha = \{0, 1\}$ denotes the condition whether the rack is engaged to any of the shafts or it is disengaged. When it is disengaged, $\alpha = 0$, and when engaged, $\alpha = 1$. We can solve (3.9) either reducing the order of system by eliminating λ_1 and λ_{2_i} or by finding the second time-derivative of the constraint equations and solving the equations of motion together with the constraint equations.

3.1.1 Reduced order model

The reduced order model is derived by eliminating the constraint dynamics of the system. In order to do that, we will eliminate the Lagrange multipliers λ_1 and λ_{2_i} in (3.9). We start with λ_{2_i}. Combining (3.9c) and (3.9d), we obtain

$$\left(m_r + \alpha\frac{J_i}{n_c^2}\right)\ddot{\xi} + \alpha\frac{\tau_{d_i}}{n_c} + F_{d_r} + F_{GS} + F_{WS} - \lambda_1 = -\alpha\frac{\tau_{g_i}}{n_c} \tag{3.10}$$

Now, we will get rid of λ_1. It is expressed using equation (3.10) and substituted in (3.9a) and (3.9a).

$$m_{b_x}\ddot{x} + F_{r_x} + F_{d_x} + \left(\left(m_r + \alpha\frac{J_i}{n_c^2}\right)\ddot{\xi} + \frac{\tau_{d_i}}{n_c} + F_{d_r} + F_{GS} + F_{WS} + \frac{\tau_{g_i}}{n_c}\right) \frac{x}{\sqrt{x^2 + (z+h)^2}} = F_{w_x} \tag{3.11a}$$

$$m_{b_z}\ddot{z} + F_{r_z} + F_{d_z} + \left(\left(m_r + \alpha\frac{J_i}{n_c^2}\right)\ddot{\xi} + \frac{\tau_{d_i}}{n_c} + F_{d_r} + F_{GS} + F_{WS} + \frac{\tau_{g_i}}{n_c}\right) \frac{z+h}{\sqrt{x^2 + (z+h)^2}} + S_h z = F_{w_z} \tag{3.11b}$$

We differentiate the constraint (3.1) two times with respect to time and express the rack acceleration $\ddot{d}_r$.

$$\ddot{\xi} = \frac{((h+z)\dot{x} - x\dot{z})^2 + x(x^2 + (h+z)^2)\ddot{x} + (h+z)(x^2 + (h+z)^2)\ddot{z})}{(x^2 + (h+z)^2)^{\frac{3}{2}}} \tag{3.12}$$

Substituting (3.12) in (3.11) yields the reduced order equations of motion of the buoy.

$$A(x,z)\begin{bmatrix}\ddot{x}\\ \ddot{z}\end{bmatrix} + b(x,z,\dot{x},\dot{z}) + C(x,z,\dot{x},\dot{z}) = \begin{bmatrix}F_{w_x}\\ F_{w_z}\end{bmatrix} \tag{3.13}$$

where

$$A(x,z) = \begin{bmatrix} m_{b_x} + \left(m_r + \alpha\frac{J_i}{n_c^2}\right)\frac{x^2}{x^2+(h+z)^2} & \left(m_r + \alpha\frac{J_i}{n_c^2}\right)\frac{x(h+z)}{x^2+(h+z)^2} \\ \left(m_r + \alpha\frac{J_i}{n_c^2}\right)\frac{x(h+z)}{x^2+(h+z)^2} & m_{b_z} + \left(m_r + \alpha\frac{J_i}{n_c^2}\right)\frac{(h+z)^2}{x^2+(h+z)^2} \end{bmatrix} \tag{3.14}$$

$$b(x,z,\dot{x},\dot{z}) = \begin{bmatrix} \left(m_r + \alpha\frac{J_i}{n_c^2}\right)\left(\frac{x\left((h+z)\dot{x} - x\dot{z}\right)^2}{(x^2+(h+z)^2)^2}\right) \\ \left(m_r + \alpha\frac{J_i}{n_c^2}\right)\left(\frac{(h+z)\left((h+z)\dot{x} - x\dot{z}\right)^2}{(x^2+(h+z)^2)^2}\right) \end{bmatrix} \tag{3.15}$$

$$C(x,z,\dot{x},\dot{z}) = \begin{bmatrix}F_{r_x} + F_{d_x}\\ F_{r_z} + F_{d_z}\end{bmatrix} + \frac{1}{\sqrt{x^2 + (z+h)^2}} \left(\alpha\frac{\tau_{d_i}}{n_c} + F_{d_r} + F_{GS} + F_{WS} + \alpha\frac{\tau_{g_i}}{n_c}\right)\begin{bmatrix}x\\ h+z\end{bmatrix} \tag{3.16}$$

And the equation of motion of the disengaged shaft is simply given by

$$J_j\ddot{\theta}_j + F_{d_j} = -\tau_{g_j}, \tag{3.17}$$

where j denotes the number of the disengaged shaft.

3.1.2 Extended order model

In order to derive the extended order model, we need to express the constraints in terms of the accelerations $\ddot{\mathbf{q}} = \begin{bmatrix}\ddot{q}_1 & \ddot{q}_2 & \ddot{q}_3 & \ddot{q}_4 & \ddot{q}_5\end{bmatrix}^T = \begin{bmatrix}\ddot{x} & \ddot{z} & \ddot{\xi} & \ddot{\theta}_1 & \ddot{\theta}_2\end{bmatrix}^T$.
By differentiating the constraint equations and applying the chain rule, we obtain

$$\begin{aligned}
\frac{d^2h_1(q)}{dt^2} &= \frac{d}{dt}\left(\frac{\partial h_1}{\partial q_1}\right)\dot{q}_1 + \frac{\partial h_1}{\partial q_1}\ddot{q}_1 + \frac{d}{dt}\left(\frac{\partial h_1}{\partial q_2}\right)\dot{q}_2 + \frac{\partial h_1}{\partial q_2}\ddot{q}_2 + \frac{d}{dt}\left(\frac{\partial h_1}{\partial q_3}\right)\dot{q}_3 \\
&\quad + \frac{\partial h_1}{\partial q_3}\ddot{q}_3 + \frac{d}{dt}\left(\frac{\partial h_1}{\partial q_4}\right)\dot{q}_4 + \frac{\partial h_1}{\partial q_5}\ddot{q}_5 + \frac{d}{dt}\left(\frac{\partial h_1}{\partial q_5}\right)\dot{q}_5 + \frac{\partial h_1}{\partial q_5}\ddot{q}_5 = 0 \\
\frac{d^2h_{2_i}(q)}{dt^2} &= \frac{d}{dt}\left(\frac{\partial h_{2_i}}{\partial q_1}\right)\dot{q}_1 + \frac{\partial h_{2_i}}{\partial q_1}\ddot{q}_1 + \frac{d}{dt}\left(\frac{\partial h_{2_i}}{\partial q_2}\right)\dot{q}_2 + \frac{\partial h_{2_i}}{\partial q_2}\ddot{q}_2 + \frac{d}{dt}\left(\frac{\partial h_{2_i}}{\partial q_3}\right)\dot{q}_3 \\
&\quad + \frac{\partial h_{2_i}}{\partial q_3}\ddot{q}_3 + \frac{d}{dt}\left(\frac{\partial h_{2_i}}{\partial q_4}\right)\dot{q}_4 + \frac{\partial h_{2_i}}{\partial q_4}\ddot{q}_4 + \frac{d}{dt}\left(\frac{\partial h_{2_i}}{\partial q_5}\right)\dot{q}_5 + \frac{\partial h_{2_i}}{\partial q_5}\ddot{q}_5 = 0
\end{aligned} \tag{3.18}$$

Expressed in matrix form, equation 3.18 looks like

$$\begin{bmatrix}
\frac{\partial h_1}{\partial q_1} & \frac{\partial h_1}{\partial q_2} & \frac{\partial h_1}{\partial q_3} & \frac{\partial h_1}{\partial q_4} & \frac{\partial h_1}{\partial q_5} \\
\frac{\partial h_{2_i}}{\partial q_1} & \frac{\partial h_{2_i}}{\partial q_2} & \frac{\partial h_{2_i}}{\partial q_3} & \frac{\partial h_{2_i}}{\partial q_4} & \frac{\partial h_{2_i}}{\partial q_5}
\end{bmatrix}
\begin{bmatrix}\ddot{q}_1 \\ \ddot{q}_2 \\ \ddot{q}_3 \\ \ddot{q}_4 \\ \ddot{q}_5\end{bmatrix}
= -
\begin{bmatrix}
\sum_{j=1}^{5}\frac{d}{dt}\left(\frac{\partial h_1}{\partial q_j}\right) \\
\sum_{j=1}^{5}\frac{d}{dt}\left(\frac{\partial h_{2_i}}{\partial q_j}\right)
\end{bmatrix} \tag{3.19}$$

Note that there is only one or two constraints active at a time, depending on whether the shaft is disengaged or engaged. When both shafts are disengaged, we do not have the second constraint anymore. Therefore, equation (3.19) reduces to

$$\begin{bmatrix}
\frac{\partial h_1}{\partial q_1} & \frac{\partial h_1}{\partial q_2} & \frac{\partial h_1}{\partial q_3} & \frac{\partial h_1}{\partial q_4} & \frac{\partial h_1}{\partial q_5}
\end{bmatrix}
\begin{bmatrix}\ddot{q}_1 \\ \ddot{q}_2 \\ \ddot{q}_3 \\ \ddot{q}_4 \\ \ddot{q}_5\end{bmatrix}
= -\sum_{j=1}^{5}\frac{d}{dt}\left(\frac{\partial h_1}{\partial q_j}\right) \tag{3.20}$$

We can write the derived system of equations in (3.9) in general form as

$$M\ddot{q} + F_{diss} + F_q + \left(\frac{\partial h}{\partial q}\right)^T \lambda = F_{in} \tag{3.21}$$

where

$$M = diag(m_{b_x},\, m_{b_z},\, m_r,\, J_1,\, J_2)$$

$$F_{diss} = \begin{bmatrix} F_{d_x} + F_{r_x} \\ F_{d_z} + F_{r_z} \\ F_{d_r} \\ \tau_{d_1} \\ \tau_{d_2} \end{bmatrix} \qquad F_q = \begin{bmatrix} 0 \\ S_h z \\ F_{WS} + F_{GS} \\ 0 \\ 0 \end{bmatrix} \qquad \lambda = \begin{bmatrix} \lambda_1 \\ \lambda_{2_i} \end{bmatrix} \qquad F_{in} = \begin{bmatrix} F_{w_x} \\ F_{w_z} \\ 0 \\ -\tau_{g_1} \\ -\tau_{g_2} \end{bmatrix}$$

Combining (3.19) and (3.21), we obtain the system of equations when one of the shafts are engaged,

$$\begin{bmatrix} m_{b_x} & 0 & 0 & 0 & 0 & \frac{\partial h_1}{\partial q_1} & \frac{\partial h_{2_i}}{\partial q_1} \\ 0 & m_{b_z} & 0 & 0 & 0 & \frac{\partial h_1}{\partial q_2} & \frac{\partial h_{2_i}}{\partial q_2} \\ 0 & 0 & m_r & 0 & 0 & \frac{\partial h_1}{\partial q_3} & \frac{\partial h_{2_i}}{\partial q_3} \\ 0 & 0 & 0 & J_1 & 0 & \frac{\partial h_1}{\partial q_4} & \frac{\partial h_{2_i}}{\partial q_4} \\ 0 & 0 & 0 & 0 & J_2 & \frac{\partial h_1}{\partial q_5} & \frac{\partial h_{2_i}}{\partial q_5} \\ \frac{\partial h_1}{\partial q_1} & \frac{\partial h_1}{\partial q_2} & \frac{\partial h_1}{\partial q_3} & \frac{\partial h_1}{\partial q_4} & \frac{\partial h_1}{\partial q_5} & 0 & 0 \\ \frac{\partial h_{2_i}}{\partial q_1} & \frac{\partial h_{2_i}}{\partial q_2} & \frac{\partial h_{2_i}}{\partial q_3} & \frac{\partial h_{2_i}}{\partial q_4} & \frac{\partial h_{2_i}}{\partial q_5} & 0 & 0 \end{bmatrix} \begin{bmatrix} \ddot{q}_1 \\ \ddot{q}_2 \\ \ddot{q}_3 \\ \ddot{q}_4 \\ \ddot{q}_5 \\ \lambda_1 \\ \lambda_{2_i} \end{bmatrix} = \begin{bmatrix} F_{w_x} - F_{d_x} - F_{r_x} \\ F_{w_z} - F_{d_z} - F_{r_z} - S_h z \\ -F_{d_r} - F_{WS} - F_{GS} \\ -\tau_{d_1} - \tau_{g_1} \\ -\tau_{d_2} - \tau_{g_2} \\ -\sum_{j=1}^{5} \frac{d}{dt} \left(\frac{\partial h_1}{\partial q_j} \right) \\ -\sum_{j=1}^{5} \frac{d}{dt} \left(\frac{\partial h_{2_i}}{\partial x} \right) \end{bmatrix} \tag{3.22}$$

And combining (3.20) and (3.21), we obtain the system of equations when none of the shafts are engaged,

$$\begin{bmatrix} m_{b_x} & 0 & 0 & 0 & 0 & \frac{\partial h_1}{\partial q_1} \\ 0 & m_{b_z} & 0 & 0 & 0 & \frac{\partial h_1}{\partial q_2} \\ 0 & 0 & m_r & 0 & 0 & \frac{\partial h_1}{\partial q_3} \\ 0 & 0 & 0 & J_1 & 0 & 0 \\ 0 & 0 & 0 & 0 & J_2 & 0 \\ \frac{\partial h_1}{\partial q_1} & \frac{\partial h_1}{\partial q_2} & \frac{\partial h_1}{\partial q_3} & \frac{\partial h_1}{\partial q_4} & \frac{\partial h_1}{\partial q_5} & 0 \end{bmatrix} \begin{bmatrix} \ddot{q}_1 \\ \ddot{q}_2 \\ \ddot{q}_3 \\ \ddot{q}_4 \\ \ddot{q}_5 \\ \lambda_1 \end{bmatrix} = \begin{bmatrix} F_{w,x} - F_{d_x} - F_{r,x} \\ F_{w,z} - F_{d_z} - F_{r,z} - S_h z \\ -F_{d_r} - F_{WS} - F_{GS} \\ -\tau_{d_1} - \tau_{g_1} \\ -\tau_{d_2} - \tau_{g_2} \\ -\sum_{j=1}^{5} \frac{d}{dt} \left(\frac{\partial h_1}{\partial q_j} \right) \end{bmatrix} \tag{3.23}$$

By looking at the fourth and fifth row of the system of equations in 3.23, it can be seen that the flywheels are rotating with damping from friction and the generator.

3.2 Implementation of the reduced order model

The original CorPower model implements the system of equations in (3.11). Looking at these equations we can see that, in order to calculate the buoy acceleration in surge and/or heave, we need to know the rack acceleration. However, there exists an algebraic constraint between the rack acceleration and the buoy acceleration in heave and surge, which was shown by (3.12). Therefore the surge and heave accelerations will appear in both sides of (3.11). Hence, implementing (3.11) directly in Simulink will create an algebraic loop. The algebraic loops in Simulink are well known cause for slow simulations and even for compilation errors in some scenarios (for instance, it might work for some initial conditions but not for others). The reason why simulation aborts in an ill-defined system is that the solver does not know how to initialize the system, i.e. it does not know where is the beginning and end of the equation. A quick way to prevent the simulation from halting is to add the "Initial condition" block in Simulink and initialize the acceleration of the rack with some value. This block will help the solver to solve the loop. However, there can be still

some scenarios where this fix will not be sufficient. Therefore, in order to guarantee that the simulation runs for all scenarios, the algebraic loop needs to be eliminated by changing the way in which the model was set up initially. The modification is quite straightforward. The constraint equation in (3.12) is substituted in (3.11), which leads to the system of differential equations in (3.13) that contains no feedback of acceleration variables and hence no algebraic loop. The Simulink implementation of the buoy dynamics is shown in figure 3.2. Looking at the model it is easy to identify each term of equation (3.11). The *"Inverse A"* block calculates the inverse of matrix $A(x, z)$, given by (3.14). The block names *"Coriolis Forces"* calculates the vector $b(x, z, \dot{x}, \dot{z})$, given by (3.15). *"Projection × F_PTO_heave + F_hydro"* represents the $\begin{bmatrix} F_{w_x} & F_{w_z} \end{bmatrix}^T - C(x, z, \dot{x}, \dot{z})$ term in equation (3.11). The *"Inertia"* block in the model calculates the additional effective mass on the buoy due to the coupling of the buoy to the rack and to the engaged shaft. Depending on wheter a shaft is engaged or disengaged, the effective mass changes.

Equation (3.13) calculates the states of the buoy in surge and heave and using the constraint equations (3.1) and (3.2) the states of the rack and the engaged shaft can be calculated respectively. In the original CorPower model the states of the rack (displacement and velocity) are also calculated by integration of the rack acceleration that is obtained using (3.12). And in order to make sure that the states of the rack calculated by integration of the rack acceleration and the ones calculated using the algebraic constraints are equal to each other, the rack acceleration is corrected with the weighted deviation between the rack states obtained from constraints and from integration of the acceleration. Moreover, in a similar way the acceleration of the engaged shaft is corrected by the weighted deviation between the engaged shaft angular velocity obtained from the constraint given by (3.2) and from integration of the shaft angular acceleration. The reason for the correction of the acceleration is not well-motivated by CorPower. As stated previously the states of the rack and the engaged shaft can be obtained just using constraints, i.e. there is no need to calculate them again by integration of the accelerations. In the new implementation of the Simulink model this corrections of the accelerations are removed and now the states of the rack and the engaged shaft are calculated using only the constraints as you can see also in figure 3.2 for the states of the rack.

When the shaft is engaged with the rack, its states are constrained by the states of the rack, and when the shaft is disengaged, its states are calculated based on its own dynamics given by (3.17). Therefore, we need to integrate the acceleration only of the disengaged shaft in order to obtain its angular velocity. In the original CorPower model the states of the engaged shaft are calculated as it is unconstrained by the states of the rack, i.e. an integration block integrates the rack acceleration in order to obtain the engaged shaft velocity. And as mentioned above, in order to ensure that the error between the engaged shaft velocity and the corresponding rack velocity is equal to zero, the shaft acceleration is compensated by a feedback of the difference in the angular velocity of the shaft and the corresponding rack velocity. In the new implementation of the CorPower model, it is made sure that the dynamics of the engaged shaft is coupled to the dynamics of the rack, i.e. the states of the shafts are obtained directly from the states of the rack by an algebraic relation, and only the disengaged shaft is simulated as a decoupled dynamical system. Here we

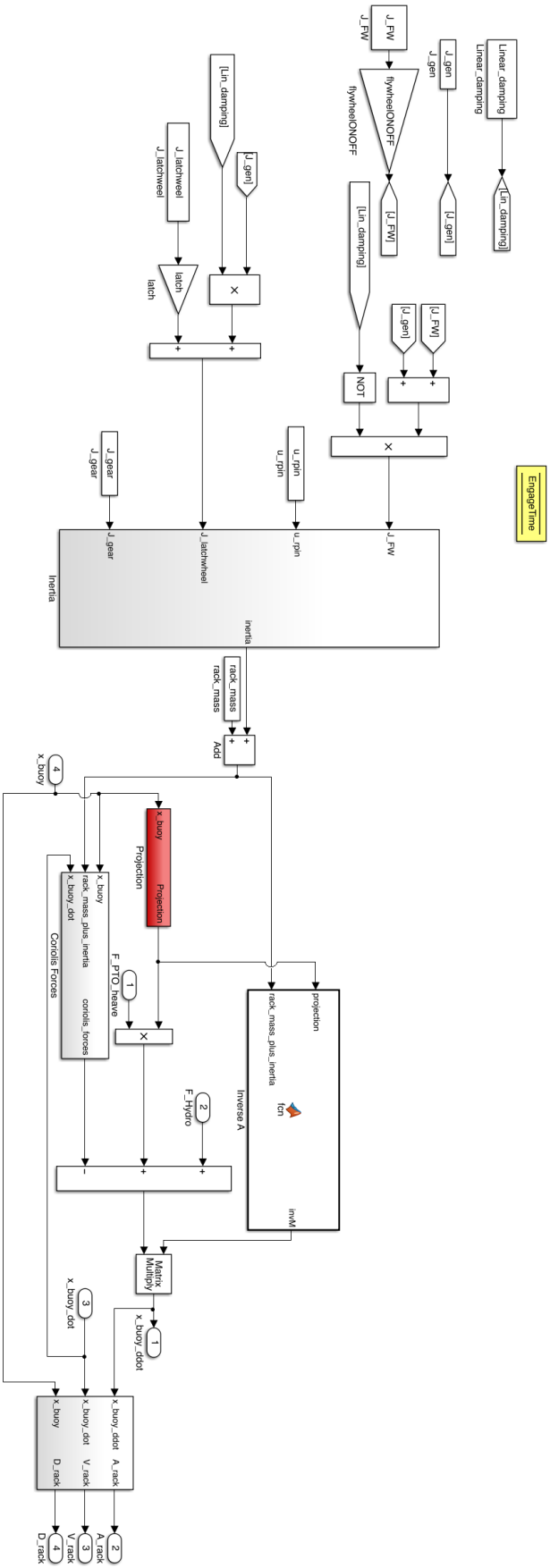

Figure 3.2: Simulink implementation of the buoy dynamics

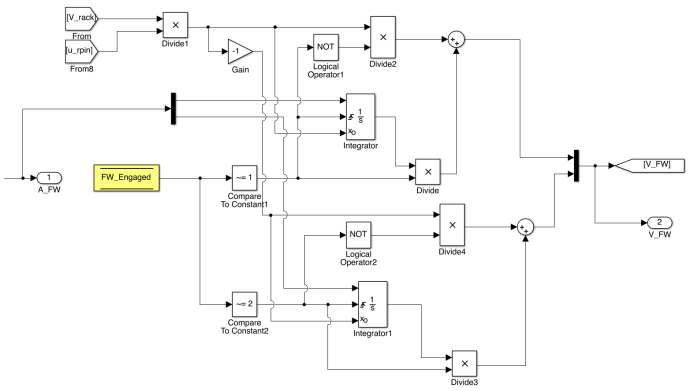

Figure 3.3: Implementation of the engaged and disengaged shaft dynamics

again have two separate integrators for both shafts, but they are only active if the shafts are disengaged. When any of the shafts is engaged, the angular velocity of the shaft is proportional to the velocity of the rack. The implementation of the engaged and disengaged shaft dynamics is shown in figure 3.3. When flywheel/shaft 1 gets disengaged, the upper integrator block is triggered and it is initialized by the velocity of shaft velocity. After this instant, its states are calculated by the integrator and they are no longer dependent on the rack states. Similarly, when flywheel/shaft 2 gets disengaged, the lower integrator is triggered and it is initialized by the velocity of the shaft. The integrator takes over again and calculates the states of shaft 2 that are no longer dependent on the states of the rack.
Figure 3.4 shows a comparison between the original CorPower model with algebraic loop and the implemented algebraic loop-free model. It can be seen that both models give identical results. Hence, the new CPO model can be used with confidence.

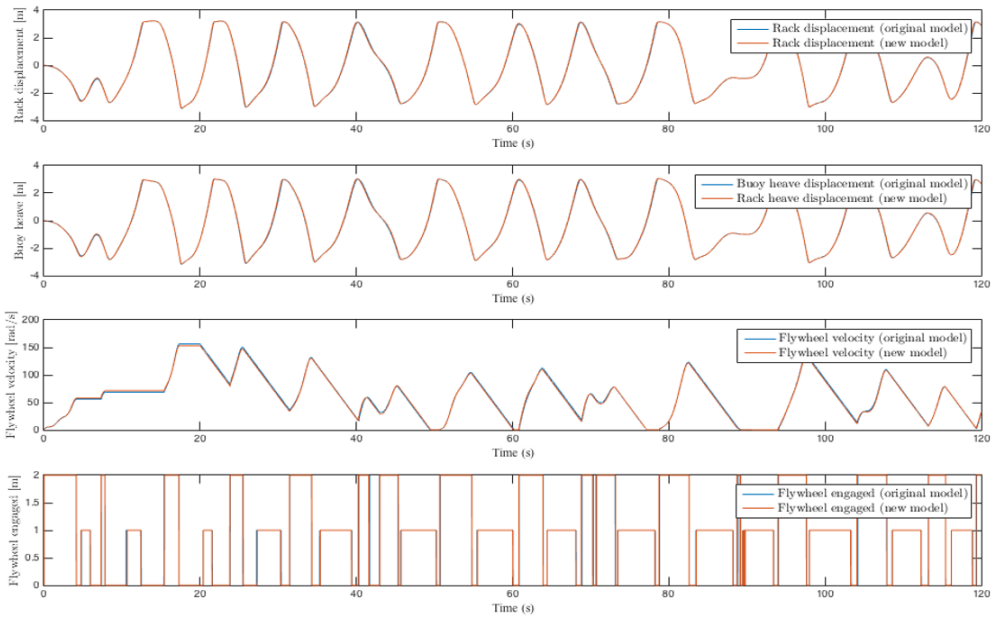

Figure 3.4: Comparison between original and algebraic loop-free CPO model.

3.3 Modelling of Waves4Power's buoy

In this section, the dynamic equations that model W4P's two-bodied heaving point absorber are presented. It should be mentioned that the equations are taken from the Simulink model that was provided by Waves4Power. Therefore, they are not derived during this project and they are assumed to correctly model W4P system. The simulation model provided by W4P is for the half scale buoy, tested at Vinga, a simulation model for the full scale WEC tested at Runde could not be provided for this study. The parameters of the half-scale buoy was scaled up to a full-scale ones using Freude scaling rules, shown in Table 3.1.

Parameters	Unit	Factor
Length	[m]	λ
Mass	[kg]	λ^3
Force	[N]	λ^3
Moment	[Nm]	λ^4
Acceleration	$[m/s^2]$	1
Time	[s]	$\sqrt{\lambda}$
Pressure	[Pa]	λ

Table 3.1: Froude scaling rules

Waves4Power is a type of heaving point absorber. Therefore, the same hydrodynamic principles, that govern a generic heaving device, governs also the behaviour of W4P's buoy-tube pair. However, in the received simulation model, Waves4Power uses a slightly different and simplified approach to represent the dynamics of their buoy. The wave excitation force is modelled as a linear combination of added mass, added damping, and added spring terms.

The hydrodynamic model of the floater-tube in heave is

$$m_b\ddot{z}_b + m_a(\ddot{z}_b - \ddot{z}_w) + b_a(\dot{z}_b - \dot{z}_w) + \rho g V + m_b g = F_{PTO} + F_{end-stop} + F_{lkb} \quad (3.24)$$

where m_b is the mass of the buoy, m_a and b_a are the added mass and damping, respectively, z_b and z_w are the buoy heave position and wave elevation, respectively, V is the instantaneous submerged volume, which is a nonlinear function of the relative difference between buoy position and wave elevation, F_{PTO} is the PTO force, $F_{end-stop}$ is the end-stop bumper force, F_{lkb} is the force acting on the buoy due to leakage pressure drop.

The added damping in (3.24), b_a, is modelled in W4P's simulation model as proportional to the submerged volume V_{subm} at mean water level and inversely proportional to the zero-crossing period T_z of the wave, i.e

$$b_a = \frac{\pi \rho V_{subm}}{2T_z}. \quad (3.25)$$

Waves4Power models their end-stop as a nonlinear spring, which acts when the

relative displacement between buoy and piston exceeds a certain threshold,

$$F_{end-stop} = \begin{cases} f(z_p - z_b), & \text{if } |z_p - z_b| > z_{thresh} \\ 0, & \text{otherwise} \end{cases} \tag{3.26}$$

The area between the water piston and the tube is called the leakage area, A_{leak}, which is a function of the relative displacement of the buoy-tube and can be derived from tube geometry. For a generic tube geometry the leakage area is given as

$$A_{leak} = A_t(z_p - z_b) - A_p \tag{3.27}$$

where A_t is the tube area at relative displacement $z_p - z_b$ and it is a value between the area of the narrow part, A_{narrow}, and the area of the wide part, A_{wide}, of the tube. It should be noted that the leakage area is always positive meaning that the tube area is always grater than the piston area. The leakage area and the relative motion of the piston and water inside the tube leads to a flow through the leakage area, and thus a pressure drop that is modelled by W4P as

$$\Delta p_{leak} = \frac{1}{2} K \rho \left(\frac{A_{wide}}{A_{narrow}} \dot{z}_{tw} - \left(\frac{A_{narrow}}{A_{leak}} - 1 \right) \dot{z}_p \right) \left| \frac{A_{wide}}{A_{narrow}} \dot{z}_{tw} - \left(\frac{A_{narrow}}{A_{leak}} - 1 \right) \dot{z}_p \right| \tag{3.28}$$

where K is a discharge coefficient, $\dot{z}_{tw}$ and $\dot{z}_p$ are the respectively the tube water and piston velocity. This pressure difference incurs a force on the buoy-tube though the horizontal projection of the area of tube transition region. Thus, this force is equal to

$$F_{lkb} = (A_{wide} - A_{narrow}) \Delta p_{leak} \tag{3.29}$$

When modelling the water piston dynamics, W4P assumes that volume of the piston head is negligible to volume of the piston rod. Hence, its dynamics are given by

$$m_p \ddot{z}_p + \rho g A_{rod}(z_p - z_{tw}) = F_{lkp} - F_{PTO} \tag{3.30}$$

where m_p is the water piston mass, A_{rod} is the piston rod area, z_p is the piston displacement, z_{tw} displacement of the water inside the tube, F_{lkp} is the force acting on the piston due to leakage pressure drop, i.e.

$$F_{lkp} = A_p \Delta p_{leak} \tag{3.31}$$

The dynamics of the water inside the tube is modelled as

$$-(A_{wide} - A_{narrow} + A_p)\Delta p_{leak} - \rho g A_{wide} z_{tw} = \rho A_{wide}(l_{tube} + z_{tw} - z_b)\ddot{z}_{tw} \tag{3.32}$$

where l_{tube} is the length of the tube.

4

Analysis of Wave Energy Converters

This chapter describes the system analysis of CorPower's and Waves4Power's buoys. Some parts of this section are omitted in the public report due to confidentiality.

4.1 Analysis of CorPower's buoy

Before we start our analysis, we need to note that heave is the most important degree of freedom. By looking at equations (3.13)-(3.16), it can be seen that the total PTO force projects in surge and heave direction respectively by

$$P_{surge} = \frac{x}{\sqrt{x^2 + (h+z)^2}} \qquad P_{heave} = \frac{h+z}{\sqrt{x^2 + (h+z)^2}} \tag{4.1}$$

This also means that the contribution of surge and heave forces or displacements in the direction of rack movement are scaled respectively by the same projections. Taking the limit case when the water depth h approaches infinity, yields

$$\lim_{h\to\infty} P_{surge} = 0 \qquad \lim_{h\to\infty} P_{heave} = 1 \tag{4.2}$$

For the sites, studied in this thesis, the water depth is $50m$, which is relatively deep for the surge to have significant contribution to power capture, e.g. $1m$ displacement in surge results in approximately $0.02m$ displacement of the rack. Therefore, the surge dynamics can safely be disregarded when doing an analysis of the system or designing a controller for simplification.

We will start our analysis by considering no PTO force and WaveSpring in order to understand the dynamics of the buoy itself. Firstly, the natural frequency of the buoy is determined according to (2.42). The total mass of the buoy in heave is the sum of the mass of the buoy and the added mass at infinity in heave direction and it is equal to

$$m_h = m_b + m_\infty^{heave} = 1.1014 \times 10^5\, kg \tag{4.3}$$

The hydrostatic stiffness for a circular cylinder is a function of the the horizontal or water plane area as shown in (2.43). The water plane area of CorPower's buoy is not uniform. It can be obtained by the geometry of the buoy for each water level or it can be calculated by taking the partial derivative of the submerged volume, obtained from geometry again, for each water level with respect to the displacement of the buoy in heave. The water plane area is shown in 4.1.

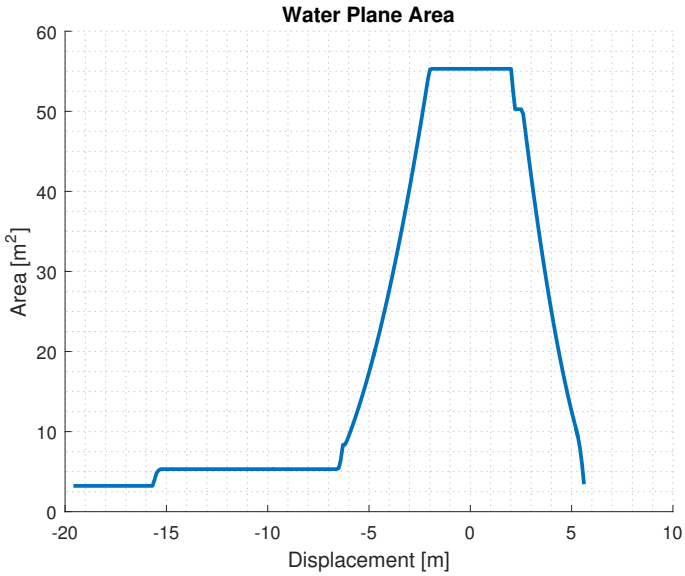

Figure 4.1: Water plane area for each displacement.

One thing that can be noted in the figure is that the area is constant around the equilibrium point and it is equal to

$$S = 55.31\,m^2, \qquad -2 < z_{wave} - z_{buoy} < 2 \tag{4.4}$$

Therefore, in low-amplitude motions, the natural period of the buoy is

$$T_n = 2\pi\sqrt{\frac{m_h}{\rho g S}} = 2.8s \tag{4.5}$$

In high-amplitude motions, it can be expected that the natural period will increase with increasing the amplitude of the excitation, since the area, and hence, the hydrostatic stiffness, decreases with higher buoy displacements. This behaviour is expected to be visible around or above $2m$ amplitude ($4m$ height), since the area of the buoy is constant for displacements up to $2m$. Therefore, the natural frequency will be constant for most of the sea states.

In low-amplitude waves the heave dynamics can be assumed to be linear and can be described by the state-space model

$$\begin{bmatrix} \ddot{z} \\ \dot{z} \\ \dot{x}_r \end{bmatrix} = \begin{bmatrix} 0 & -\frac{\rho g S}{m_h} & -\frac{1}{m_h}\mathbf{C_r} \\ 1 & 0 & \mathbf{0}^{1\times 6} \\ \mathbf{B_r} & \mathbf{0}^{6\times 1} & \mathbf{A_r} \end{bmatrix} \begin{bmatrix} \dot{z} \\ z \\ x_r \end{bmatrix} + \begin{bmatrix} \frac{1}{m_h} \\ 0 \\ \mathbf{0}^{6\times 1} \end{bmatrix} F_{exc} \tag{4.6}$$

where $\mathbf{A_r} \in \mathbb{R}^{6\times 6}$, $\mathbf{B_r} \in \mathbb{R}^{6\times 1}$, $\mathbf{C_r} \in \mathbb{R}^{1\times 6}$ are radiation state-space matrices. System's pole-zero map, shown in figure 4.2, displays near pole-zero cancellations, hence, it is a good candidate for model reduction, which simplifies analysis and controller design.

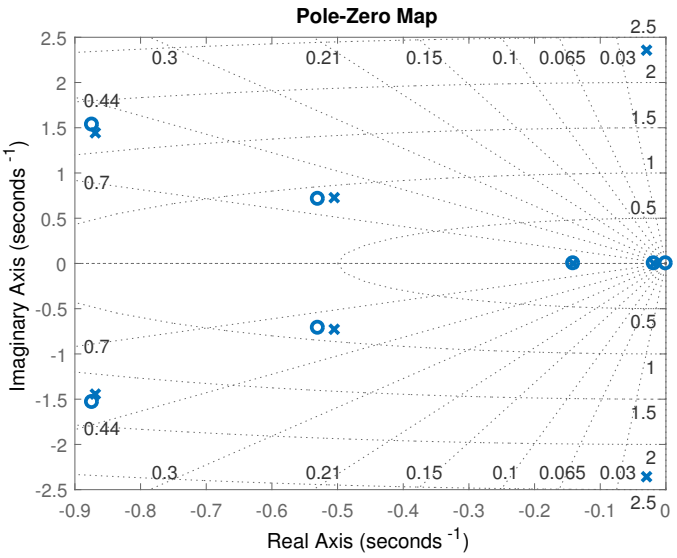

Figure 4.2: Pole-zero map of heave dynamics without WaveSpring

In order to find an appropriate low-order reduction, we examine the relative amount of energy per state using a Hankel singular value (HSV) plot, which is shown in figure 4.3.

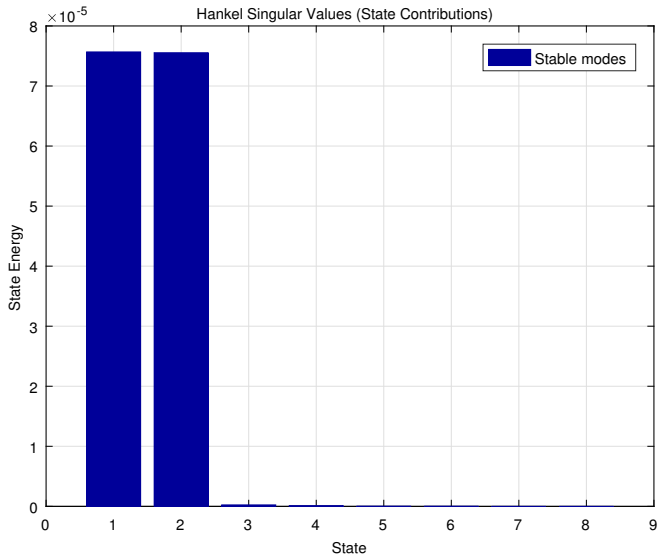

Figure 4.3: Hankel singular value plot for heave model of CorPower's buoy

From the HSV plot, it can be found out that the eight-order system can be reduced to a second-order system. This can be done with the command $ballred(sys, order)$ in Matlab. The $ballred()$ command produced a positive zero, which was not supposed to be there (it is known that the system is second-order and transmissibility transfer function, i.e. velocity-to-force transfer function, has a zero at the origin). By manually removing it, a better estimate is obtained. The transfer function of the full and reduced systems before and after the zero-removal is shown in figure 4.4.

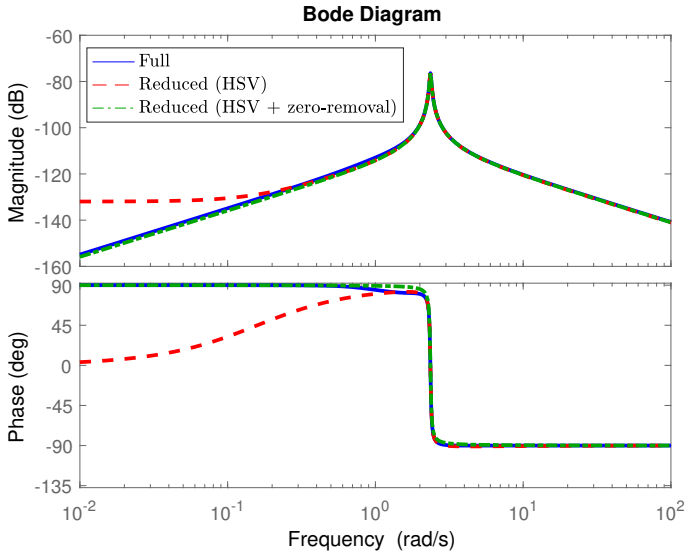

Figure 4.4: Bode plot with full and reduced system dynamics

It can be seen that with a second-order system, we can get a really good approximation of the higher-order system. The transfer function of the reduced order model is

$$\frac{V}{F_{exc}}(s) = \frac{8.932 \times 10^{-6} s}{s^2 + 0.05916s + 5.556} \tag{4.7}$$

The natural frequency, natural period and damping factor of the reduced system can be easily identified,

$$\omega_n = 2.35 \, \frac{rad}{s} \qquad T_n = 2.67 \, s \qquad \zeta = 0.0125 \tag{4.8}$$

Since the transfer function in (4.7) is a second order, it can be represent as the transfer function of a mass-spring-damper system,

$$\frac{V}{F_{exc}}(s) = \frac{s}{m_e s^2 + b_e s + k_e} \tag{4.9}$$

where m_e, b_e and k_e are respectively the effective mass, damping coefficient and stiffness equal to

$$m_e = 1.1195 \times 10^5 \, kg \qquad b_e = 0.0662 \times 10^5 \, \frac{Ns}{m} \qquad k_e = 6.22 \times 10^5 \, \frac{N}{m} \tag{4.10}$$

The analysis about the effect of the pretension and WaveSpring springs is ommited due to confidentiality.

4.2 Analysis of Waves4Power's buoy

It was presented in section 3.3 that the dynamics of the W4P's system is governed by three second-order equations, which are rewritten below

$$m_b \ddot{z}_b + m_a(\ddot{z}_b - \ddot{z}_w) + b_a(\dot{z}_b - \dot{z}_w) + \rho g V + m_b g = F_{PTO} + F_{end-stop} + F_{lkb} \tag{4.11}$$

$$m_p\ddot{z}_p + \rho g A_{rod}(z_p - z_{tw}) = F_{lkp} - F_{PTO} \tag{4.12}$$

$$-(A_{wide} - A_{narrow} + A_p)\Delta p_{leak} - \rho g A_{wide} z_{tw} = \rho A_{wide}(l_{tube} + z_{tw} - z_b)\ddot{z}_{tw} \tag{4.13}$$

where

$$F_{lkb} = (A_{wide} - A_{narrow})\Delta p_{leak}$$

$$F_{lkp} = A_p \Delta p_{leak}$$

$$\Delta p_{leak} = \frac{1}{2}\rho K \left(\frac{A_{wide}}{A_{narrow}}\dot{z}_{tw} - \left(\frac{A_{narrow}}{A_{leak}} - 1\right)\dot{z}_p\right)\left|\frac{A_{wide}}{A_{narrow}}\dot{z}_{tw} - \left(\frac{A_{narrow}}{A_{leak}} - 1\right)\dot{z}_p\right|$$

By looking at equations (4.11) and (4.12), it can be seen that the only coupling between the buoy-tube and the piston is through the PTO force, F_{PTO}. This implies that when the PTO force is zero, the piston will stay still and only the buoy will move due to the wave excitation. This is due to the simplification that the water inside the tube is completely isolated from the outside of the tube, thus it does not experience the hydrodynamic forces from the waves. The model also neglects the radiation waves inside the tube due to the motion of the buoy and more importantly the drag forces caused by the friction between the inner walls of the tube and the water. Since the water piston will remain still when there is no PTO force, the tube water will also remain still relative to a fixed reference frame due to lack of leakage pressure.

Since the system consists of three second-order equations, there exists three modes of oscillation. In order to identify them, the nonlinear system of equations needs to be linearized around the mean water level, i.e. at $z_b = z_w = z_p = z_{tw} = 0$ and $\dot{z}_b = \dot{z}_w = \dot{z}_p = \dot{z}_{tw} = 0$.

Waves4Power's buoy generates power by the the relative motion between the buoy-tube and the water piston. Therefore, the PTO force will be a function of the relative position, velocity and acceleration of the buoy-tube and piston. Let us assume a generic linear PTO force, comprising of a mass, damping and spring terms,

$$F_{PTO} = m_{PTO}(\ddot{z}_p - \ddot{z}_b) + b_{PTO}(\dot{z}_p - \dot{z}_b) + k_{PTO}(z_p - z_b) \tag{4.14}$$

where m_{PTO}, b_{PTO} and k_{PTO} are respectively linear PTO mass, damping and spring coefficient. At the linearization point, the end-stop force, $F_{end-stop}$, is zero. The gravity force is balanced by the Archimedes force from to the displaced volume at mean water level. Any relative displacement between wave and buoy, generates a restoring hydrostatic force, proportional to that displacement, i.e.

$$F_{hs}^{lin} = \rho g A_b(z_w - z_b) \tag{4.15}$$

where A_b is the area of the buoy at mean water level. The leakage area, A_{leak}, is constant and equal to the minimum leakage area, $A_{leak}^{min} = A_{narrow} - A_p$, around the linearization point. Due to the fact that the expression for the leakage pressure is non-smooth at the linearization point, it is not possible to linearize it. However, a linear curve can be constructed that minimizes the error between the actual and the linear curve. Since the pressure drop expression is drag-like, i.e. one comprising of a signed square of the difference of two velocities, it can be linearized using Morison

Drag Linearization technique (see [28]), which converts the non-smooth drag force function,

$$f_{drag} = \frac{1}{2}\rho C_d(u_1 - u_2)|u_1 - u_2|, \tag{4.16}$$

into a linear one,

$$f_{drag}^{lin} = \frac{1}{2}\rho C_d \alpha u_{rms}(u_1 - u_2), \tag{4.17}$$

where C_d is a discharge coefficient, α is a factor that is derived to be $\sqrt{\frac{8}{\pi}}$ in [28], u_{rms} is the root-mean-square of the relative velocity. Therefore, the linearized leakage pressure drop is

$$\Delta p_{leak}^{lin} = \frac{1}{2}\rho K\sqrt{\frac{8}{\pi}}u_{rms}\left(\frac{A_{wide}}{A_{narrow}}\dot{z}_{tw} - \left(\frac{A_{narrow}}{A_{leak}} - 1\right)\dot{z}_p\right) \tag{4.18}$$

where u_{rms} is the root mean square of $\frac{A_{wide}}{A_{narrow}}\dot{z}_{tw} - \left(\frac{A_{narrow}}{A_{leak}} - 1\right)\dot{z}_p$ that can be found by performing simulations of the nonlinear system.
The linearized equations can now be written in matrix form as

$$\mathbf{M}\ddot{\mathbf{x}} + \mathbf{B}\dot{\mathbf{x}} + \mathbf{K}\mathbf{x} = \mathbf{F} \tag{4.19}$$

where $\mathbf{M} \in \mathbb{R}^{3\times3}$, $\mathbf{B} \in \mathbb{R}^{3\times3}$ and $\mathbf{K} \in \mathbb{R}^{3\times3}$ are respectively the mass, damping and stiffness matrices, $\mathbf{x} \in \mathbb{R}^{3\times1}$ is the state vector and $\mathbf{F} \in \mathbb{R}^{3\times1}$ is the input force vector. They are given as follows

$$\mathbf{M} = \begin{bmatrix} m_b + m_a + m_{PTO} & -m_{PTO} & 0 \\ -m_{PTO} & m_p + m_{PTO} & 0 \\ 0 & 0 & \rho A_{wide} l_{tube} \end{bmatrix}$$

$$\mathbf{B} = \begin{bmatrix} b_a + b_{PTO} & -b_{PTO} & 0 \\ -b_{PTO} & b_{PTO} + \sqrt{\frac{2}{\pi}}\frac{A_p^2}{A_{leak}^{min}}\rho K u_{rms} & -\sqrt{\frac{2}{\pi}}\frac{A_{wide}}{A_{narrow}}A_p\rho K u_{rms} \\ 0 & -\sqrt{\frac{2}{\pi}}\left(A_{wide} - A_{leak}^{min}\right)\frac{A_p}{A_{leak}^{min}}\rho K u_{rms} & \sqrt{\frac{2}{\pi}}\left(A_{wide} - A_{leak}^{min}\right)\frac{A_{wide}}{A_{narrow}}\rho K u_{rms} \end{bmatrix}$$

$$\mathbf{K} = \begin{bmatrix} \rho g A_b + k_{PTO} & -k_{PTO} & 0 \\ -k_{PTO} & \rho g A_{rod} + k_{PTO} & -\rho g A_{rod} \\ 0 & 0 & \rho g A_{wide} \end{bmatrix}$$

$$\mathbf{x} = \begin{bmatrix} x_b \\ x_p \\ x_{tw} \end{bmatrix} \qquad \mathbf{F} = \begin{bmatrix} m_a\ddot{z}_w + b_a\dot{z}_w + \rho g z_w \\ 0 \\ 0 \end{bmatrix}$$

In order for the system to be stable, the mass and spring matrices need to be positive definite, and the damping matrix needs to be positive semi-definite.
The undamped eigenmodes of (4.19) are equal to the square root of the eigenvalues, $\lambda \in \mathbb{R}^{3\times1}$, of the characteristic equation

$$det(\mathbf{K} - \lambda\mathbf{M}) = \mathbf{0} \tag{4.20}$$

The undamped eigenmodes of the uncontrolled system, i.e. when $m_{PTO} = b_{PTO} = k_{PTO} = 0$, are

$$\omega_{\mathbf{uc}} = \left[\sqrt{\frac{\rho g A_b}{m_b + m_a}} \quad \sqrt{\frac{\rho g A_{rod}}{m_p}} \quad \sqrt{\frac{g}{l_{tube}}}\right]^T \tag{4.21}$$

The first entry of the vector is the buoy-tube eigenfrequency, the second one - the piston eigenfrequency, and the third one - the eigenfrequency of the water inside the tube. By substituting the full-scale system parameters.

$$A_b = 50.3m^2, \quad A_{rod} = 0.5m^2, \quad l_{tube} = 38m,$$

$$m_b = 104ton, \quad m_a = 46ton, \quad m_p = 4ton,$$

the undamped eigenfrequencies and eigenperiods ($T = 2\pi/\omega$) of the uncontrolled system are calculated to be

$$\omega_{\mathbf{uc}} = \begin{bmatrix}1.84 & 1.12 & 0.51\end{bmatrix}^T rad/s$$
$$\mathbf{T_{uc}} = \begin{bmatrix}3.42 & 5.59 & 12.37\end{bmatrix}^T s$$

Since it is sufficient to control either the PTO mass or the PTO stiffness to tune the eigenfrequencies of the system, we have chosen to express the relationship of the closed-loop eigenmodes to the PTO stiffness by assigning the PTO mass to zero. By looking at the stiffness matrix, $\mathbf{K}$, it is clear that the PTO stiffness does not have any influence to the eigenmode of the water inside the tube. Therefore, it remains equal to the eigenmode of the uncontrolled system. On contrary, the PTO stiffness affects the buoy and piston eigenmodes. The relation of the eigenperiods of the buoy and piston to the PTO stiffness is shown in figure 4.5.

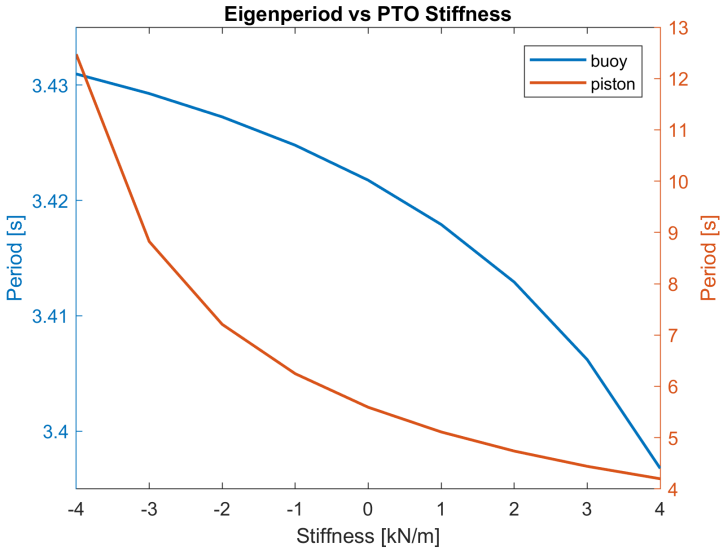

Figure 4.5: Relation of the closed-loop eigenperiods to the PTO stiffness

It is interesting to observe that the buoy eigenperiod is almost unaffected by the PTO stiffness. On the other hand, the piston eigenperiod increases exponentially

by decreasing the PTO stiffness and the system will eventually get unstable upon decreasing the PTO stiffness even further. It can be concluded that even if a reactive force term, such as the spring-like force, is applied through the PTO, the buoy-floater does not behave like a resonant buoy, bur rather like a wave-rider, i.e. one that follows the wave. However, the eigenfrequency, and hence the phase, of the piston can be controlled relative to the phase of the buoy to optimize the power capture.

Here we end our analysis about Waves4Power's wave energy converter. It should be highlighted that the performed analysis is done based on the model that was provided by Waves4Power without assessing whether the utilized modelling approach was correct.

5

Integration of Wave Energy Converters

It was presented in Chapter 1, that the power take-offs of the wave energy converters are modified to incorporate multiple fixed displacement pumps, connected to the same rack with a pinion for each pump. The pumps are engaged and disengaged to control the applied PTO force to optimize power capture. The combined flow from the pumps is rectified using a valve rectifier bridge. In this chapter we will present the modelling of the integration of the wave energy converters to the OHT's hydraulic system using the generic buoy model.

In Chapter 2 it was shown that a generic heaving buoy can be modelled as a second-order mass-spring-damper system,

$$m\ddot{x}(t) + b\dot{x}(t) + kx(t) = F_{exc} - F_{PTO} \tag{5.1}$$

where m is the total/effective mass of the buoy, b is the radiation resistance, k is the hydrostatic stiffness, F_{exc} is the wave excitation force and F_{PTO} is the PTO force. Since the motion is restricted to move only in heave, the displacement of the rack is equal to the displacement of the buoy. It is assumed that each drive module, comprising of a pinion pump and on/off valve, is identical, i.e. the physical parameters in each module are equal. This leads to have a a perfectly balanced system, i.e. the speed and toque of each shaft are equal. The model of a single drive module is

$$J_p\dot{\omega}_p(t) = \tau_{pin} - b_p\omega_p(t) - \tau_{pump} \tag{5.2}$$

where J_p and b_p are respectively the the total inertia and viscous friction of pinion, shaft and pump, ω_p is the angular velocity of the pump shaft velocity, τ_{pin} and τ_{pump} are respectively the pinion and pump torque. Due to a balanced system,

$$\begin{aligned} F_{PTO} &= n\frac{\tau_{pin}}{r_{pin}} \\ \dot{x} &= \omega_{pin} r_{pin} \end{aligned} \tag{5.3}$$

where $n \in \{1, ..., n_{max}\}$ is the number of engaged pumps and r_{pin} is the pinion radius. The pump can be modelled as

$$\tau_{pump} = D_p\Delta p_{pump} \qquad q_{pump} = D_p\omega_p \tag{5.4}$$

where D_p is the displacement/specific torque of the pump, Δp_{pump} is the pressure difference on the pump and q_{pump} is the flow through the pump. Combining (5.1-5.4),

yields

$$\left(m + n\frac{J_p}{r_{pin}^2}\right)\ddot{x}(t) + \left(b + n\frac{b_p}{r_{pin}^2}\right)\dot{x}(t) + kx(t) = F_{exc} - n\frac{D_p}{r_{pin}}\Delta p_{pump} \tag{5.5}$$

The rectifier bridge rectifies the flow of the pump and flips the sign of the pressure difference on the pump,

$$q_r = |q_{pump}| \qquad \Delta p_{pump} = sign(q_{pump})\Delta p_r \tag{5.6}$$

where q_r and p_r are respectively the flow and pressure difference after the rectifier. The rectifier bridge allows power to flow only from the buoy to the hydraulic system. The pressure difference after the rectifier bridge is assumed to be constant. Therefore, when the velocity of the buoy crosses zero, the buoy will remain still until the total hydrodynamic force exceeds the constant damping force, exerted on the buoy by the pumps. An analogy of the system can be made with an electrical full-bridge rectifier circuit with voltage source and voltage stiff load as shown in figure 5.1. For simplicity the pump shaft inertia and viscous friction are neglected.

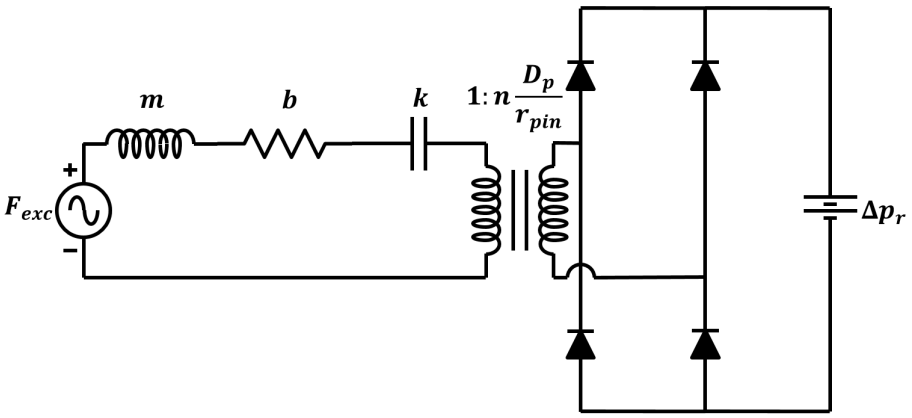

Figure 5.1: Electrical analogy of a generic buoy with a rectifier.

It is well-known fact that a full-bridge rectifier with voltage source and voltage stiff load has two modes of operation, namely conducting and non-conducting. The converter enters in non-conducting state when the current through the circuit is zero and the voltage on the source side of the rectifier is less than the voltage on the load side. The converter starts conducting again, when source side voltage exceeds the load side voltage. Therefore, when the the converter is conducting, the system dynamics are

$$\left(m + n\frac{J_p}{r_{pin}^2}\right)\ddot{x}(t) + \left(b + n\frac{b_p}{r_{pin}^2}\right)\dot{x}(t) + kx(t) = F_{exc} - n\frac{D_p}{r_{pin}}\Delta p_r sign(\dot{x}(t)) \tag{5.7}$$

and when the converter is in non-conducting state, the dynamics are described

$$\begin{aligned} \ddot{x}(t) &= 0 \\ \dot{x}(t) &= 0 \\ x(t) &= x_0 \end{aligned} \tag{5.8}$$

where x_0 is the buoy position right before the transition from the conducting to non-conducting state.

Figure 5.2 shows the conduction and conduction modes of the wave energy converter, excited with a sinusoidal force and damped with constant PTO force. It can be seen that the wave energy converter starts conducting when the sum of all hydrodynamic forces exceeds the damping force. Since the velocity and acceleration are zero at non-conduction mode, the inertia and friction forces are also 0. Therefore, the buoy starts conducting, when

$$|F_{exc} - kx(t)| \geq |F_{PTO}| \tag{5.9}$$

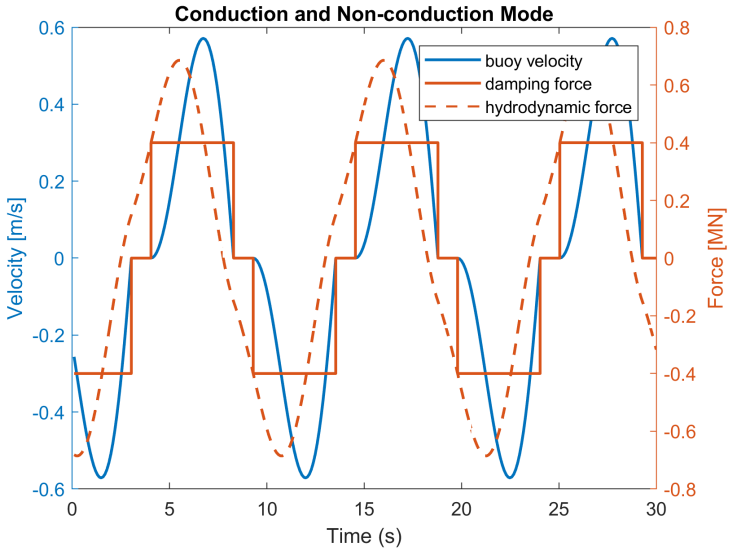

Figure 5.2: Conducting and non-conducting modes of wave energy converter with sinusoidal excitation and constant damping force.

Capturing the conducting and non-conducting modes of the wave energy converter with a passive rectifier in the PTO and constant load is vital for modelling correctly the behaviour of the buoy, which needs to be accounted for also inside the model predictive controller, that will be presented in subsequent chapters.

6

Modelling of the Hydraulic Collection

It is well known that there are similarities between the fundamental laws of different physical systems. The physical systems can be represented as a connection of storage and dissipative components, where the former can be further divided into two types: flow and effort storage components. Due to these analogies, there have been developed several systematic and application-independent modeling techniques such as Bond Graphs (BG) [14] , Power-Oriented Graphs (POG) [15] etc. In this paper, concepts from Linear Graph Theory [16] are used to systematically model and generate the governing equations of the OHT's hydraulic collection system. The reason that a graph-theoretical approach is chosen, is due to the fact that it is easy to see a pattern of entries in the system matrices. This allows one to model a very complex system by following a simple procedure. Moreover, when the states of system are ordered in a special way, the obtained system matrix obeys a skew-symmetric structure that makes it possible to obtain the flow equation given the effort equations or vice versa. The developed algorithm is capable to generate the system matrices for a general topology. Due to the existing analogies between hydraulics and electrical systems, it can be used to generate the equations for a general electrical collection system. Moreover, the algorithm divides the medium of propagation of the flow (pipe for hydraulic systems and cable for electrical systems) based on the length of the medium into simple lumps, comprising of basic dissipative and storage of flow and effort components.

The following two sections describe the graph-theoretic way of modelling of the two basic components of a piping system - hydraulic pipes and T-connections - in order to prepare the reader for the algorithm to generate the system of equations for a hydraulic collection system with generic topology. The fourth section presents modelling of hydraulic accumulators and the fifth and the last section describes the losses of all loss sources in the hydraulic collection system.

6.1 Modelling hydraulic pipes

A model of a pipe comprising of two lumps with a pressure source, for instance pump, and an outflow, modelled as a flow source, is shown in figure 6.1. Let us assume for simplicity that the friction terms are linear.

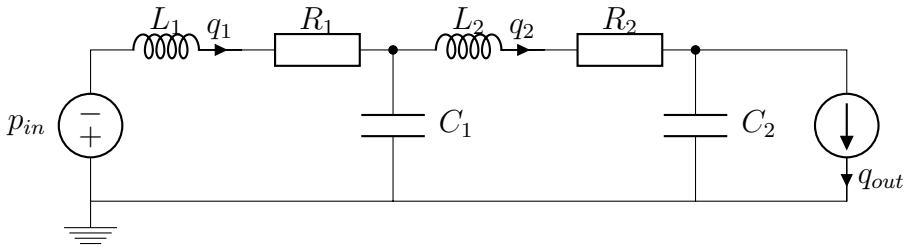

Figure 6.1: Lumped model of a hydraulic pipe

The pipe can be with the help of linear graph theory. The first step is to build the graph of the pipe, enumerate the branches and assign their directions. The graph of the pipe is shown in Figure 6.2.

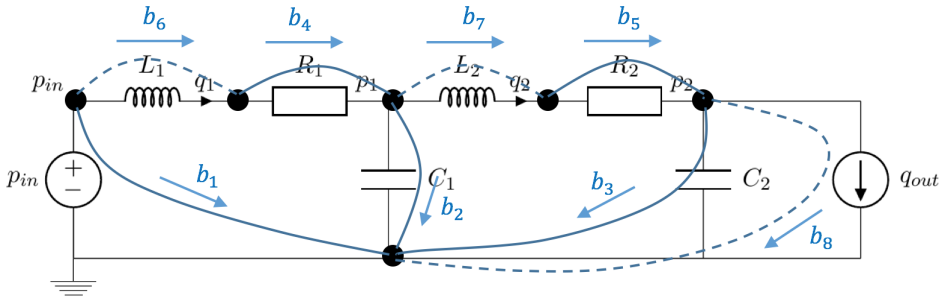

Figure 6.2: Directed graph of a pipe with pressure and flow source

It can be seen that there are five tree branches and three links. As we stated earlier, we need to find either Q_{link} or P_{tree} in order to obtain the system of equations. Let us choose the later due the lower number of links. Then, the system of equations becomes

$$\begin{bmatrix} q_{tree} \\ p_{link} \end{bmatrix} = \begin{bmatrix} 0 & P_{tree}^T \\ -P_{tree} & 0 \end{bmatrix} \begin{bmatrix} p_{tree} \\ q_{link} \end{bmatrix} \tag{6.1}$$

where

$$q_{tree} = \begin{bmatrix} q_{in} & q_{C_1} & q_{C_2} & q_{R_1} & q_{R_2} \end{bmatrix}^T, \tag{6.2}$$

$$p_{link} = \begin{bmatrix} p_{L_1} & p_{L_2} & p_{out} \end{bmatrix}^T, \tag{6.3}$$

$$p_{tree} = \begin{bmatrix} p_{in} & p_{C_1} & p_{C_2} & p_{R_1} & p_{R_2} \end{bmatrix}^T, \tag{6.4}$$

$$q_{link} = \begin{bmatrix} q_{L_1} & q_{L_2} & q_{out} \end{bmatrix}^T \tag{6.5}$$

Using the definition of the fundamental cycle vector, we obtain

$$P_{tree} = \begin{bmatrix} -1 & 1 & 0 & 1 & 0 \\ 0 & -1 & 1 & 0 & 1 \\ 0 & 0 & -1 & 0 & 0 \end{bmatrix}. \tag{6.6}$$

The system of equations is

$$\begin{bmatrix} q_{in} \\ q_{C_1} \\ q_{C_2} \\ q_{R_1} \\ q_{R_2} \\ p_{L_1} \\ p_{L_2} \\ p_{out} \end{bmatrix} = \begin{bmatrix} 0 & 0 & 0 & 0 & 0 & -1 & 0 & 0 \\ 0 & 0 & 0 & 0 & 0 & 1 & -1 & 0 \\ 0 & 0 & 0 & 0 & 0 & 0 & 1 & -1 \\ 0 & 0 & 0 & 0 & 0 & 1 & 0 & 0 \\ 0 & 0 & 0 & 0 & 0 & 0 & 1 & 0 \\ 1 & -1 & 0 & -1 & 0 & 0 & 0 & 0 \\ 0 & 1 & -1 & 0 & -1 & 0 & 0 & 0 \\ 0 & 0 & 1 & 0 & 0 & 0 & 0 & 0 \end{bmatrix} \begin{bmatrix} p_{in} \\ p_{C_1} \\ p_{C_2} \\ p_{R_1} \\ p_{R_2} \\ q_{L_1} \\ q_{L_2} \\ q_{out} \end{bmatrix} \tag{6.7}$$

Let us split the system of equations in (6.7) and the state vector into three systems of equations and three vectors, respectively - one for the source variables, one for the storage variables and one for the dissipative variables.

$$\begin{bmatrix} q_{in} \\ p_{out} \end{bmatrix} = \begin{bmatrix} 0 & 0 & -1 & 0 \\ 0 & 1 & 0 & 0 \end{bmatrix} \begin{bmatrix} p_{C_1} \\ p_{C_2} \\ q_{L_1} \\ q_{L_2} \end{bmatrix} + \begin{bmatrix} 0 & 0 \\ 0 & 0 \end{bmatrix} \begin{bmatrix} p_{R_1} \\ p_{R_2} \end{bmatrix} + \begin{bmatrix} 0 & 0 \\ 0 & 0 \end{bmatrix} \begin{bmatrix} p_{in} \\ q_{out} \end{bmatrix} \tag{6.8}$$

$$\begin{bmatrix} q_{C_1} \\ q_{C_2} \\ p_{L_1} \\ p_{L_2} \end{bmatrix} = \begin{bmatrix} 0 & 0 & 1 & -1 \\ 0 & 0 & 0 & 1 \\ -1 & 0 & 0 & 0 \\ 1 & -1 & 0 & 0 \end{bmatrix} \begin{bmatrix} p_{C_1} \\ p_{C_2} \\ q_{L_1} \\ q_{L_2} \end{bmatrix} + \begin{bmatrix} 0 & 0 \\ 0 & 0 \\ -1 & 0 \\ 0 & -1 \end{bmatrix} \begin{bmatrix} p_{R_1} \\ p_{R_2} \end{bmatrix} + \begin{bmatrix} 0 & 0 \\ 0 & -1 \\ 1 & 0 \\ 0 & 0 \end{bmatrix} \begin{bmatrix} p_{in} \\ q_{out} \end{bmatrix} \tag{6.9}$$

$$\begin{bmatrix} q_{R_1} \\ q_{R_2} \end{bmatrix} = \begin{bmatrix} 0 & 0 & 1 & 0 \\ 0 & 0 & 0 & 1 \end{bmatrix} \begin{bmatrix} p_{C_1} \\ p_{C_2} \\ q_{L_1} \\ q_{L_2} \end{bmatrix} + \begin{bmatrix} 0 & 0 \\ 0 & 0 \end{bmatrix} \begin{bmatrix} p_{R_1} \\ p_{R_2} \end{bmatrix} + \begin{bmatrix} 0 & 0 \\ 0 & 0 \end{bmatrix} \begin{bmatrix} p_{in} \\ q_{out} \end{bmatrix} \tag{6.10}$$

The consitutive equations of the system are

$$C_1 \frac{dp_{C_1}}{dt} = q_{C_1}, \qquad C_2 \frac{dp_{C_2}}{dt} = q_{C_2}, \tag{6.11}$$

$$L_1 \frac{dq_{L_1}}{dt} = p_{L_1}, \qquad L_2 \frac{dq_{L_2}}{dt} = p_{L_2}, \tag{6.12}$$

$$p_{R_1} = R_1 q_{R_1}, \qquad p_{R_2} = R_2 q_{R_2}. \tag{6.13}$$

Combining (6.10) and (6.13), yields

$$\begin{bmatrix} p_{R_1} \\ p_{R_2} \end{bmatrix} = \begin{bmatrix} R_1 & 0 \\ 0 & R_2 \end{bmatrix} \begin{bmatrix} 0 & 0 & 1 & 0 \\ 0 & 0 & 0 & 1 \end{bmatrix} \begin{bmatrix} p_{C_1} \\ p_{C_2} \\ q_{L_1} \\ q_{L_2} \end{bmatrix} = \begin{bmatrix} 0 & 0 & R_1 & 0 \\ 0 & 0 & 0 & R_2 \end{bmatrix} \begin{bmatrix} p_{C_1} \\ p_{C_2} \\ q_{L_1} \\ q_{L_2} \end{bmatrix} \tag{6.14}$$

Substituting (6.11), (6.12) and (6.14) in (6.9) and after performing some algebraic manipulations, we obtain the system of differential equations

$$\begin{bmatrix} C_1 \frac{dp_{C_1}}{dt} \\ C_2 \frac{dp_{C_2}}{dt} \\ L_1 \frac{dq_{L_1}}{dt} \\ L_2 \frac{dq_{L_2}}{dt} \end{bmatrix} = \begin{bmatrix} 0 & 0 & 1 & -1 \\ 0 & 0 & 0 & 1 \\ -1 & 0 & -R_1 & 0 \\ 1 & -1 & 0 & -R_2 \end{bmatrix} \begin{bmatrix} p_{C_1} \\ p_{C_2} \\ q_{L_1} \\ q_{L_2} \end{bmatrix} + \begin{bmatrix} 0 & 0 \\ 0 & -1 \\ 1 & 0 \\ 0 & 0 \end{bmatrix} \begin{bmatrix} p_{in} \\ q_{out} \end{bmatrix} \tag{6.15}$$

In this example the friction terms were assumed to be linear. Generally friction is a nonlinear phenomenon, i.e.

$$p_{R_1} = f(q_{R_1}, R_1) \qquad p_{R_2} = f(q_{R_2}, R_2). \tag{6.16}$$

If this is the case, we can regard the friction as a disturbance input to the system. The matrix multiplying the vector with the dissipative variables in equation (6.9) shows the way the friction terms enter the system. Hence the system of equations with nonlinear losses is

$$\begin{bmatrix} C_1\frac{dp_{C_1}}{dt} \\ C_2\frac{dp_{C_2}}{dt} \\ L_1\frac{dq_{L_1}}{dt} \\ L_2\frac{dq_{L_2}}{dt} \end{bmatrix} = \begin{bmatrix} 0 & 0 & 1 & -1 \\ 0 & 0 & 0 & 1 \\ -1 & 0 & 0 & 0 \\ 1 & -1 & 0 & 0 \end{bmatrix} \begin{bmatrix} p_{C_1} \\ p_{C_2} \\ q_{L_1} \\ q_{L_2} \end{bmatrix} + \begin{bmatrix} 0 & 0 \\ 0 & -1 \\ 1 & 0 \\ 0 & 0 \end{bmatrix} \begin{bmatrix} p_{in} \\ q_{out} \end{bmatrix} + \begin{bmatrix} 0 & 0 \\ 0 & 0 \\ -1 & 0 \\ 0 & -1 \end{bmatrix} \begin{bmatrix} f(q_{R_1}, R_1) \\ f(q_{R_2}, R_2) \end{bmatrix} \tag{6.17}$$

By looking at 6.17, it is not so difficult to identify the pattern of non-zero entries in the matrices. We can write the system equations for a hydraulic pipe comprising n lumps with inertia, compressibility and nonlinear friction components.

$$\begin{bmatrix} C_1\frac{dp_{C_1}}{dt} \\ C_2\frac{dp_{C_2}}{dt} \\ \vdots \\ C_{n-1}\frac{dp_{C_{n-1}}}{dt} \\ C_n\frac{dp_{C_n}}{dt} \\ L_1\frac{dq_{L_1}}{dt} \\ L_2\frac{dq_{L_2}}{dt} \\ \vdots \\ L_{n-1}\frac{dq_{n-1}}{dt} \\ L_n\frac{dq_n}{dt} \end{bmatrix} = \begin{bmatrix} 0 & 0 & \dots & 0 & 0 & 1 & -1 & \dots & 0 & 0 \\ 0 & 0 & \dots & 0 & 0 & 0 & 1 & \ddots & 0 & 0 \\ \vdots & \vdots & \ddots & \vdots & \vdots & \vdots & \vdots & \ddots & \ddots & \vdots \\ 0 & 0 & \vdots & 0 & 0 & 0 & 0 & \dots & 1 & -1 \\ -1 & 0 & \dots & 0 & 0 & 0 & 0 & \dots & 0 & 0 \\ 1 & -1 & \dots & 0 & 0 & 0 & 0 & \dots & 0 & 0 \\ \vdots & \ddots & \ddots & \vdots & \vdots & \vdots & \vdots & \ddots & \vdots & \vdots \\ 0 & 0 & \ddots & -1 & 0 & 0 & 0 & \vdots & 0 & 0 \\ 0 & 0 & \vdots & 1 & -1 & 0 & 0 & \vdots & 0 & 0 \end{bmatrix} \begin{bmatrix} p_{C_1} \\ p_{C_2} \\ \vdots \\ p_{C_{n-1}} \\ p_{C_n} \\ q_{L_1} \\ q_{L_2} \\ \vdots \\ q_{L_{n-1}} \\ q_{L_n} \end{bmatrix} \tag{6.18}$$

$$+ \begin{bmatrix} 0 & 0 \\ 0 & 0 \\ \vdots & \vdots \\ 0 & -1 \\ 1 & 0 \\ 0 & 0 \\ \vdots & \vdots \\ 0 & 0 \\ 0 & 0 \end{bmatrix} \begin{bmatrix} p_{in} \\ q_{out} \end{bmatrix} + \begin{bmatrix} 0 & 0 & \dots & 0 & 0 \\ 0 & 0 & \dots & 0 & 0 \\ \vdots & \vdots & \ddots & \vdots & \vdots \\ 0 & 0 & \dots & 0 & 0 \\ -1 & 0 & \dots & 0 & 0 \\ 0 & -1 & \dots & 0 & 0 \\ \vdots & \vdots & \ddots & \vdots & \vdots \\ 0 & 0 & \dots & -1 & 0 \\ 0 & 0 & \dots & 0 & -1 \end{bmatrix} \begin{bmatrix} f(q_{R_1}, R_1) \\ f(q_{R_2}, R_2) \\ \vdots \\ f(q_{R_{n-1}}, R_{n-1}) \\ f(q_{R_n}, R_n) \end{bmatrix}$$

The model of the hydraulic pipe will be the basic block in building the model of the hydraulic collection system for a general topology. Before starting to describe the algorithm to generate the system equations, we need to address the modelling of the situation when three or more pipes are connected.

6.1.1 Modelling of a T-connection

The topology of the hydraulic collection system is formed by the connections of multiple pipes in some manner. In this section, we will model one such connection, namely two pipes connected to a third one. The model of the connection is shown in Figure 6.3 with an electrical analogy. Superscripts of the parameters indicate the number of the pipes, and the subscripts indicate the number of the lumps in each pipe. Pipes 1 and 2 are connected to the pressure sources p_{in}^1 and p_{in}^2, respectively, and pipe 3 has an open end that is modelled as a flow source, shown as q_{out} in Figure 6.3. We assume that all pipes consists of two lumps. However, by looking at Figure 6.3, we can see that the second lumps of pipes 1 and 2 does not have a capacitance component and the third pipe has one in excess that is named as C_0^3. This capacitance can be seen as the common capacitance or sum of the capacitance of the last lump of pipe 1 and 2. If the individual capacitance of the first and second pipe were kept, then the causality of the model would be broken, because there would be two capacitance components in parallel that would form an algebraic constraint between their pressure states. The reason that it is denoted with a superscript 3 and with a subscript 0 is due to the convention used to order the state variables in the state vector.

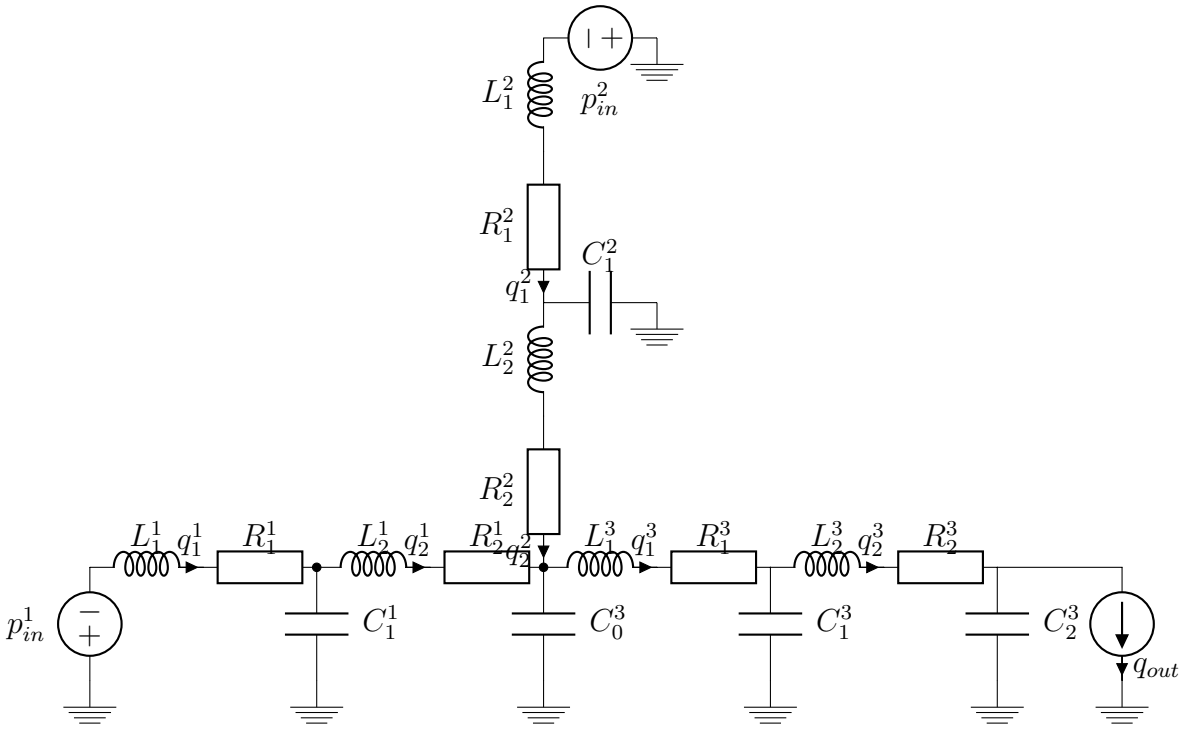

Figure 6.3: Lumped model of a T-connection

The T-connection will be modelled using the graph-theoretic approach. The graph of the system is shown in Figure 6.4. All nodes at the grounds represent a single node. The system of equations is

$$\begin{bmatrix} q_{tree} \\ p_{link} \end{bmatrix} = \begin{bmatrix} 0 & P_{tree}^T \\ -P_{tree} & 0 \end{bmatrix} \begin{bmatrix} p_{tree} \\ q_{link} \end{bmatrix} \tag{6.19}$$

where

$$q_{tree} = \begin{bmatrix} q^1_{in} & q^2_{in} & q^1_{C_1} & q^2_{C_1} & q^3_{C_0} & q^3_{C_1} & q^3_{C_2} & q^1_{R_1} & q^1_{R_2} & q^2_{R_1} & q^2_{R_2} & q^3_{R_1} & q^3_{R_2} \end{bmatrix}^T, \tag{6.20}$$

$$p_{link} = \begin{bmatrix} p^1_{L_1} & p^1_{L_2} & p^2_{L_1} & p^2_{L_2} & p^3_{L_1} & p^3_{L_2} & p_{out} \end{bmatrix}^T, \tag{6.21}$$

$$p_{tree} = \begin{bmatrix} p^1_{in} & p^2_{in} & p^1_{C_1} & p^2_{C_1} & p^3_{C_0} & p^3_{C_1} & p^3_{C_2} & p^1_{R_1} & p^1_{R_2} & p^2_{R_1} & p^2_{R_2} & p^3_{R_1} & p^3_{R_2} \end{bmatrix}^T, \tag{6.22}$$

$$q_{link} = \begin{bmatrix} q^1_{L_1} & q^1_{L_2} & q^2_{L_1} & q^2_{L_2} & q^3_{L_1} & q^3_{L_2} & q_{out} \end{bmatrix}^T \tag{6.23}$$

Using the definition of the fundamental cycle vector, we obtain

$$P_{tree} = \begin{bmatrix} -1 & 0 & 1 & 0 & 0 & 0 & 0 & 1 & 0 & 0 & 0 & 0 & 0 \\ 0 & 0 & -1 & 0 & 1 & 0 & 0 & 0 & 1 & 0 & 0 & 0 & 0 \\ 0 & -1 & 0 & 1 & 0 & 0 & 0 & 0 & 0 & 1 & 0 & 0 & 0 \\ 0 & 0 & 0 & -1 & 1 & 0 & 0 & 0 & 0 & 0 & 1 & 0 & 0 \\ 0 & 0 & 0 & 0 & -1 & 1 & 0 & 0 & 0 & 0 & 0 & 1 & 0 \\ 0 & 0 & 0 & 0 & 0 & -1 & 1 & 0 & 0 & 0 & 0 & 0 & 1 \\ 0 & 0 & 0 & 0 & 0 & 0 & -1 & 0 & 0 & 0 & 0 & 0 & 0 \end{bmatrix} \tag{6.24}$$

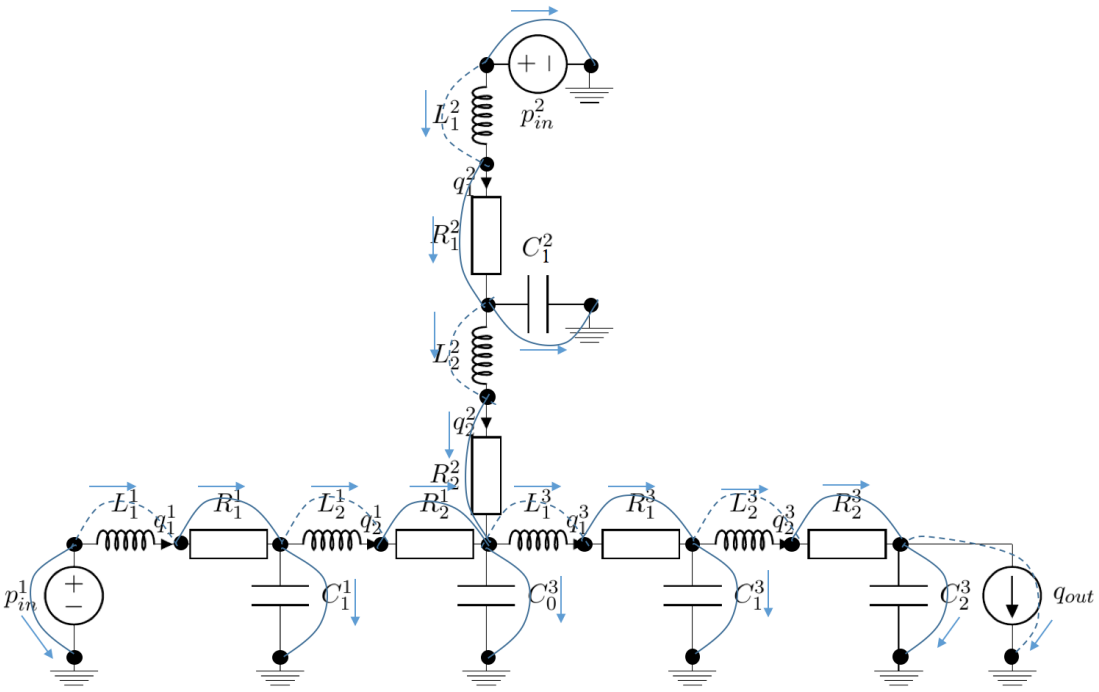

Figure 6.4: Directed graph of a connection of three pipes

Then, the system of equations is

$$\begin{bmatrix} q^1_{in} \\ q^2_{in} \\ q^1_{C_1} \\ q^2_{C_1} \\ q^3_{C_0} \\ q^3_{C_1} \\ q^3_{C_2} \\ q^1_{R_1} \\ q^1_{R_2} \\ q^2_{R_1} \\ q^2_{R_2} \\ q^3_{R_1} \\ q^3_{R_2} \\ p^1_{L_1} \\ p^1_{L_2} \\ p^2_{L_1} \\ p^2_{L_2} \\ p^3_{L_1} \\ p^3_{L_2} \\ p_{out} \end{bmatrix} = \begin{bmatrix} 0 & 0 & 0 & 0 & 0 & 0 & 0 & 0 & 0 & 0 & 0 & 0 & 0 & -1 & 0 & 0 & 0 & 0 & 0 & 0 \\ 0 & 0 & 0 & 0 & 0 & 0 & 0 & 0 & 0 & 0 & 0 & 0 & 0 & 0 & 0 & -1 & 0 & 0 & 0 & 0 \\ 0 & 0 & 0 & 0 & 0 & 0 & 0 & 0 & 0 & 0 & 0 & 0 & 0 & 1 & -1 & 0 & 0 & 0 & 0 & 0 \\ 0 & 0 & 0 & 0 & 0 & 0 & 0 & 0 & 0 & 0 & 0 & 0 & 0 & 0 & 0 & 1 & -1 & 0 & 0 & 0 \\ 0 & 0 & 0 & 0 & 0 & 0 & 0 & 0 & 0 & 0 & 0 & 0 & 0 & 0 & 1 & 0 & 1 & -1 & 0 & 0 \\ 0 & 0 & 0 & 0 & 0 & 0 & 0 & 0 & 0 & 0 & 0 & 0 & 0 & 0 & 0 & 0 & 0 & 1 & -1 & 0 \\ 0 & 0 & 0 & 0 & 0 & 0 & 0 & 0 & 0 & 0 & 0 & 0 & 0 & 0 & 0 & 0 & 0 & 0 & 1 & -1 \\ 0 & 0 & 0 & 0 & 0 & 0 & 0 & 0 & 0 & 0 & 0 & 0 & 0 & 0 & 1 & 0 & 0 & 0 & 0 & 0 \\ 0 & 0 & 0 & 0 & 0 & 0 & 0 & 0 & 0 & 0 & 0 & 0 & 0 & 0 & 0 & 1 & 0 & 0 & 0 & 0 \\ 0 & 0 & 0 & 0 & 0 & 0 & 0 & 0 & 0 & 0 & 0 & 0 & 0 & 0 & 0 & 0 & 1 & 0 & 0 & 0 \\ 0 & 0 & 0 & 0 & 0 & 0 & 0 & 0 & 0 & 0 & 0 & 0 & 0 & 0 & 0 & 0 & 0 & 1 & 0 & 0 \\ 0 & 0 & 0 & 0 & 0 & 0 & 0 & 0 & 0 & 0 & 0 & 0 & 0 & 0 & 0 & 0 & 0 & 0 & 1 & 0 \\ 0 & 0 & 0 & 0 & 0 & 0 & 0 & 0 & 0 & 0 & 0 & 0 & 0 & 0 & 0 & 0 & 0 & 0 & 1 & 0 \\ 1 & 0 & -1 & 0 & 0 & 0 & 0 & -1 & 0 & 0 & 0 & 0 & 0 & 0 & 0 & 0 & 0 & 0 & 0 & 0 \\ 0 & 0 & 1 & 0 & -1 & 0 & 0 & 0 & -1 & 0 & 0 & 0 & 0 & 0 & 0 & 0 & 0 & 0 & 0 & 0 \\ 0 & 1 & 0 & -1 & 0 & 0 & 0 & 0 & 0 & -1 & 0 & 0 & 0 & 0 & 0 & 0 & 0 & 0 & 0 & 0 \\ 0 & 0 & 0 & 1 & -1 & 0 & 0 & 0 & 0 & 0 & -1 & 0 & 0 & 0 & 0 & 0 & 0 & 0 & 0 & 0 \\ 0 & 0 & 0 & 0 & 1 & -1 & 0 & 0 & 0 & 0 & 0 & -1 & 0 & 0 & 0 & 0 & 0 & 0 & 0 & 0 \\ 0 & 0 & 0 & 0 & 0 & 1 & -1 & 0 & 0 & 0 & 0 & 0 & -1 & 0 & 0 & 0 & 0 & 0 & 0 & 0 \\ 0 & 0 & 0 & 0 & 0 & 0 & 1 & 0 & 0 & 0 & 0 & 0 & 0 & 0 & 0 & 0 & 0 & 0 & 0 & 0 \end{bmatrix} \begin{bmatrix} p^1_{in} \\ p^2_{in} \\ p^1_{C_1} \\ p^2_{C_1} \\ p^3_{C_0} \\ p^3_{C_1} \\ p^3_{C_2} \\ p^1_{R_1} \\ p^1_{R_2} \\ p^2_{R_1} \\ p^2_{R_2} \\ p^3_{R_1} \\ p^3_{R_2} \\ q^1_{L_1} \\ q^1_{L_2} \\ q^2_{L_1} \\ q^2_{L_2} \\ q^3_{L_1} \\ q^3_{L_2} \\ q_{out} \end{bmatrix} \tag{6.25}$$

We separate the equations of the enegy storage variables from all the equations of the dissipative variables.

$$\begin{bmatrix} q^1_{C_1} \\ q^2_{C_1} \\ q^3_{C_0} \\ q^3_{C_1} \\ q^3_{C_2} \\ p^1_{L_1} \\ p^1_{L_2} \\ p^2_{L_1} \\ p^2_{L_2} \\ p^3_{L_1} \\ p^3_{L_2} \end{bmatrix} = \begin{bmatrix} 0 & 0 & 0 & 0 & 0 & 1 & -1 & 0 & 0 & 0 & 0 \\ 0 & 0 & 0 & 0 & 0 & 0 & 0 & 1 & -1 & 0 & 0 \\ 0 & 0 & 0 & 0 & 0 & 0 & 1 & 0 & 1 & -1 & 0 \\ 0 & 0 & 0 & 0 & 0 & 0 & 0 & 0 & 0 & 1 & -1 \\ 0 & 0 & 0 & 0 & 0 & 0 & 0 & 0 & 0 & 0 & 1 \\ -1 & 0 & 0 & 0 & 0 & 0 & 0 & 0 & 0 & 0 & 0 \\ 1 & 0 & -1 & 0 & 0 & 0 & 0 & 0 & 0 & 0 & 0 \\ 0 & -1 & 0 & 0 & 0 & 0 & 0 & 0 & 0 & 0 & 0 \\ 0 & 1 & -1 & 0 & 0 & 0 & 0 & 0 & 0 & 0 & 0 \\ 0 & 0 & 1 & -1 & 0 & 0 & 0 & 0 & 0 & 0 & 0 \\ 0 & 0 & 0 & 1 & -1 & 0 & 0 & 0 & 0 & 0 & 0 \end{bmatrix} \begin{bmatrix} p^1_{C_1} \\ p^2_{C_1} \\ p^3_{C_0} \\ p^3_{C_1} \\ p^3_{C_2} \\ q^1_{L_1} \\ q^1_{L_2} \\ q^2_{L_1} \\ q^2_{L_2} \\ q^3_{L_1} \\ q^3_{L_2} \end{bmatrix}$$
$$+ \begin{bmatrix} 0 & 0 & 0 & 0 & 0 & 0 \\ 0 & 0 & 0 & 0 & 0 & 0 \\ 0 & 0 & 0 & 0 & 0 & 0 \\ 0 & 0 & 0 & 0 & 0 & 0 \\ 0 & 0 & 0 & 0 & 0 & 0 \\ -1 & 0 & 0 & 0 & 0 & 0 \\ 0 & -1 & 0 & 0 & 0 & 0 \\ 0 & 0 & -1 & 0 & 0 & 0 \\ 0 & 0 & 0 & -1 & 0 & 0 \\ 0 & 0 & 0 & 0 & -1 & 0 \\ 0 & 0 & 0 & 0 & 0 & -1 \end{bmatrix} \begin{bmatrix} p^1_{R_1} \\ p^1_{R_2} \\ p^2_{R_1} \\ p^2_{R_2} \\ p^3_{R_1} \\ p^3_{R_2} \end{bmatrix} + \begin{bmatrix} 0 & 0 & 0 \\ 0 & 0 & 0 \\ 0 & 0 & 0 \\ 0 & 0 & 0 \\ 0 & 0 & -1 \\ 1 & 0 & 0 \\ 0 & 0 & 0 \\ 0 & 1 & 0 \\ 0 & 0 & 0 \\ 0 & 0 & 0 \\ 0 & 0 & 0 \end{bmatrix} \begin{bmatrix} p^1_{in} \\ p^2_{in} \\ q_{out} \end{bmatrix} \tag{6.26}$$

$$\begin{bmatrix} q^1_{R_1} \\ q^1_{R_2} \\ q^2_{R_1} \\ q^2_{R_2} \\ q^3_{R_1} \\ q^3_{R_2} \end{bmatrix} = \begin{bmatrix} 0 & 0 & 0 & 0 & 0 & 0 & 1 & 0 & 0 & 0 & 0 \\ 0 & 0 & 0 & 0 & 0 & 0 & 0 & 1 & 0 & 0 & 0 \\ 0 & 0 & 0 & 0 & 0 & 0 & 0 & 0 & 1 & 0 & 0 \\ 0 & 0 & 0 & 0 & 0 & 0 & 0 & 0 & 0 & 1 & 0 \\ 0 & 0 & 0 & 0 & 0 & 0 & 0 & 0 & 0 & 0 & 1 \\ 0 & 0 & 0 & 0 & 0 & 0 & 0 & 0 & 0 & 0 & 1 \end{bmatrix} \begin{bmatrix} p^1_{C_1} \\ p^2_{C_1} \\ p^3_{C_0} \\ p^3_{C_1} \\ p^3_{C_2} \\ q^1_{L_1} \\ q^1_{L_2} \\ q^2_{L_1} \\ q^2_{L_2} \\ q^3_{L_1} \\ q^3_{L_2} \end{bmatrix} \tag{6.27}$$

The consititutive equations are

$$C^1_1 \frac{dp^1_{C_1}}{dt} = q^1_{C_1},\ C^2_1 \frac{dp^2_{C_1}}{dt} = q^2_{C_1},\ C^3_0 \frac{dp^3_{C_0}}{dt} = q^3_{C_0},\ C^3_1 \frac{dp^3_{C_1}}{dt} = q^3_{C_1},\ C^3_2 \frac{dp^3_{C_2}}{dt} = q^3_{C_2} \tag{6.28}$$

$$\begin{aligned} L^1_1 \frac{dq^1_{L_1}}{dt} &= p^1_{L_1}, \quad L^1_2 \frac{dq^1_{L_2}}{dt} = p^1_{L_2}, \quad L^2_1 \frac{dq^2_{L_1}}{dt} = p^2_{L_1}, \\ L^2_2 \frac{dq^2_{L_2}}{dt} &= p^2_{L_2}, \quad L^3_1 \frac{dq^3_{L_1}}{dt} = p^3_{L_1}, \quad L^3_2 \frac{dq^3_{L_2}}{dt} = p^3_{L_2} \end{aligned} \tag{6.29}$$

$$\begin{aligned} p^1_{R_1} &= R^1_1 q^1_{R_1}, \quad p^1_{R_2} = R^1_2 q^1_{R_2}, \quad p^2_{R_1} = R^2_1 q^2_{R_1}, \\ p^2_{R_2} &= R^2_2 q^2_{R_2}, \quad p^3_{R_1} = R^3_1 q^3_{R_1}, \quad p^3_{R_2} = R^3_2 q^3_{R_2}. \end{aligned} \tag{6.30}$$

Substituting (6.27-6.30) in (6.26), yields the system of differential equations

$$\begin{bmatrix} C^1_1 \frac{dp^1_{C_1}}{dt} \\ C^2_1 \frac{dp^2_{C_1}}{dt} \\ C^3_0 \frac{dp^3_{C_0}}{dt} \\ C^3_1 \frac{dp^3_{C_1}}{dt} \\ C^3_2 \frac{dp^3_{C_2}}{dt} \\ L^1_1 \frac{dq^1_{L_1}}{dt} \\ L^1_2 \frac{dq^1_{L_2}}{dt} \\ L^2_1 \frac{dq^2_{L_1}}{dt} \\ L^2_2 \frac{dq^2_{L_2}}{dt} \\ L^3_1 \frac{dq^3_{L_1}}{dt} \\ L^3_2 \frac{dq^3_{L_2}}{dt} \end{bmatrix} = \begin{bmatrix} 0 & 0 & 0 & 0 & 0 & 1 & -1 & 0 & 0 & 0 & 0 \\ 0 & 0 & 0 & 0 & 0 & 0 & 0 & 1 & -1 & 0 & 0 \\ 0 & 0 & 0 & 0 & 0 & 0 & 1 & 0 & 1 & -1 & 0 \\ 0 & 0 & 0 & 0 & 0 & 0 & 0 & 0 & 0 & 1 & -1 \\ 0 & 0 & 0 & 0 & 0 & 0 & 0 & 0 & 0 & 0 & 1 \\ -1 & 0 & 0 & 0 & 0 & -R^1_1 & 0 & 0 & 0 & 0 & 0 \\ 1 & 0 & -1 & 0 & 0 & 0 & -R^1_2 & 0 & 0 & 0 & 0 \\ 0 & -1 & 0 & 0 & 0 & 0 & 0 & -R^2_1 & 0 & 0 & 0 \\ 0 & 1 & -1 & 0 & 0 & 0 & 0 & 0 & -R^2_2 & 0 & 0 \\ 0 & 0 & 1 & -1 & 0 & 0 & 0 & 0 & 0 & -R^3_1 & 0 \\ 0 & 0 & 0 & 1 & -1 & 0 & 0 & 0 & 0 & 0 & -R^3_2 \end{bmatrix} \begin{bmatrix} p^1_{C_1} \\ p^2_{C_1} \\ p^3_{C_0} \\ p^3_{C_1} \\ p^3_{C_2} \\ q^1_{L_1} \\ q^1_{L_2} \\ q^2_{L_1} \\ q^2_{L_2} \\ q^3_{L_1} \\ q^3_{L_2} \end{bmatrix} + \begin{bmatrix} 0 & 0 & 0 \\ 0 & 0 & 0 \\ 0 & 0 & 0 \\ 0 & 0 & 0 \\ 0 & 0 & -1 \\ 1 & 0 & 0 \\ 0 & 0 & 0 \\ 0 & 1 & 0 \\ 0 & 0 & 0 \\ 0 & 0 & 0 \\ 0 & 0 & 0 \\ 0 & 0 & 0 \end{bmatrix} \begin{bmatrix} p^1_{in} \\ p^2_{in} \\ q_{out} \end{bmatrix} \tag{6.31}$$

Equation (6.31) has a certain structure that makes it possible to write a generic algorithm to obtain the state-space matrices of a collection system with any kind of topology. In the following section we will come back to this system of equations to explain its structure.

6.1.2 Generic algorithm to obtain state-space matrices of a collection system

A generic algorithm is developed to calculate the state-space matrices of the hydraulic collection system with any topology. Due to the analogies between hydraulic and electrical systems, the same algorithm can be effectively applied to obtain the governing equations of electrical collection systems. The algorithm starts by creating a *PipeDataReader* object that reads the properties of the pipes in the collection system from an Excel sheet. The properties of the pipes that need to be read are the coordinates of beginning and end of the pipes, and lengths and areas of each pipe section. The direction of the pipe is the same as the direction of the flow in the high-pressure pipes, i.e. along the direction of the flow the end of a pipe is always closer to the tower than the beginning of the pipe. The properties of the pipes can be directly obtained from any professional drawing tool and stored in an Excel sheet. Figure 6.5 demonstrates the structure of the Excel sheet with the pipe properties. Column A is an enumeration of the pipes. Columns B-D and E-F are the coordinates respectively of the beginning and end of the pipes. Columns H-I and J-K are respectively lengths and areas of each pipe section. The number of columns with lengths and/or areas indicates the maximum number of pipe sections that any of the pipes have. For instance, in Figure 6.5 the number of length/area columns are two. This indicates that there is a pipe or pipes, comprising of two pipe sections with different cross section areas. It is obvious to see that pipes 1-8 and 17 have two sections (the cells in the second column for these rows are filled with some values) and the rest comprise of only one pipe section (the cells in the second column is left empty for these rows).

	A	B	C	D	E	F	G	H	I	J	K
1	Nr	Coordinate IN			Coordinate OUT			Length		Area	
2		X	Y	Z	X	Y	Z				
3	1	-320	138,564065	60	-280	69,2820323	0	60	80	0,004553	0,016674
4	2	-240	138,564065	60	-200	69,2820323	0	60	80	0,004553	0,016674
5	3	-80	138,564065	60	-40	69,2820323	0	60	80	0,004553	0,016674
6	4	-160	138,564065	60	-120	69,2820323	0	60	80	0,004553	0,016674
7	5	80	138,564065	60	40	69,2820323	0	60	80	0,004553	0,016674
8	6	160	138,564065	60	120	69,2820323	0	60	80	0,004553	0,016674
9	7	240	138,564065	60	200	69,2820323	0	60	80	0,004553	0,016674
10	8	320	138,564065	60	280	69,2820323	0	60	80	0,004553	0,016674
11	9	-280	69,2820323	60	-280	69,2820323	0	60		0,004553	
12	10	-200	69,2820323	60	-200	69,2820323	0	60		0,004553	
13	11	-120	69,2820323	60	-120	69,2820323	0	60		0,004553	
14	12	-40	69,2820323	60	-40	69,2820323	0	60		0,004553	
15	13	40	69,2820323	60	40	69,2820323	0	60		0,004553	
16	14	120	69,2820323	60	120	69,2820323	0	60		0,004553	
17	15	200	69,2820323	60	200	69,2820323	0	60		0,004553	
18	16	280	69,2820323	60	280	69,2820323	0	60		0,004553	
19	17	-320	0	60	-240	0	0	60	80	0,004553	0,016674
20	18	-240	0	60	-240	0	0	60		0,004553	

Figure 6.5: Structure of the Excel sheet with pipe properties

The *PipeDataReader* object holds the properties, which were read, sorts the pipes in a special way and gives a unique ID to each pipe based on this sorting. Figure 6.6 shows a top view of a general topology of a collection system. The buoys and the tower are illustrated respectively with circles and a square. The numbers with black color are the unique IDs, assigned to each pipe after the sorting, and the red numbers in brackets indicate the number of buoys that the beginning of the pipe is

directly or indirectly connected. A pipe from each buoy and tower extends to the sea bed. The pipes, enumerated with 1, 2, 7 and 8 consists of two sections - one that goes down to the sea bed (not seen in the figure) and one that is on the sea bed.

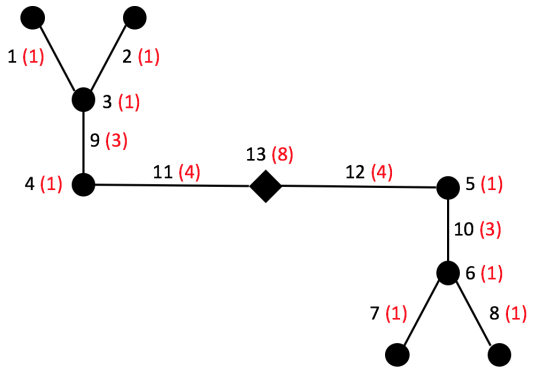

Figure 6.6: General topology to explain the sorting algorithm

The sorting of the pipes is based on the the number of buoys that they are connected to. A recursive algorithm, shown in Algorithm 1, is developed to find that. The recursive algorithm is initialized with the coordinate of the beginning and the index (in the initial list of pipes) of the tower pipe. The beginning of the tower pipe must be always placed at the center of the reference frame, i.e. it must have the coordinate $(0, 0, 0)$. The algorithm searches for the ends of pipes connected to the beginning of the tower pipe, i.e. searches for pipes that end at $(0, 0, 0)$ coordinate. If a match or several matches are found, the function calls itself subsequently with an input that is the coordinate of the beginning of the pipe with an end connected to the tower pipe. For the topology in Figure 6.6, the algorithm finds that pipes with IDs 11 and 12 (the IDs are assigned after the algorithm completes, i.e. they are not known at this stage, but we will use them to clarify which pipe we are referring to) are connected to the tower pipe with ID 13. Let us assume that pipe number 11 is found before number 12 by the algorithm. Therefore, it is the first pipe that is searched for neighbouring pipes. The algorithm finds that pipe 11 is connected to pipe 4 and 9. The function calls itself subsequently, for instane, first with the coordinate of the beginning of pipe 4 and then the beginning of pipe 9. Searching for the beginning coordinate of pipe 4 among the list of end coordinates, the algorithm does not find a match since pipe 4 is connected to a buoy. Then, the algorithm increments the buoy counter of pipe 4 and returns to the calling function and increments the counter of 11. The function calls itself for the second time with the beginning coordinate of pipe 9, which was the second neighbour of pipe 11. The algorithm finds that the pipe 9 is connected to three pipes, namely 1, 2 and 3. The function calls itself subsequently with an input that is the beginning coordinate of the neighbouring pipes and finds that all of them are connected to a buoy. Then, the algorithm increments the buoy counters of pipe 1, 2 and 3 to 1, and subsequently increments the counter of pipe 9 to 3. The function of pipe 9 returns to the calling function the function of pipe 11 and increments the counter of pipe 11 by 3 and it becomes equal to 4. Since pipe 11 does not have any other neighbours, the function

returns to the calling function - the function of the tower pipe with ID 13. The function of pipe 13 calls itself with an input that is the beginning coordinate of pipe 12 - the second neighbour of pipe 13. The algorithm proceeds in a similar manner until all the pipes know the number of buoys that they are connected to.

Algorithm 1 Recursive method to count the number of buoys connected to each pipe

Require: $startCoordList$, $endCoordList$, $startCoord \leftarrow \mathbf{0}^{1\times 3}$, $counter \leftarrow \mathbf{0}^{1\times n}$, $index \leftarrow towerIndex$
  procedure FindNrOfBuoysToEachPipe
    $indexNeighbours \leftarrow$ **find all** $startCoord$ **in** $endCoordList$
    if $indexNeighbours$ **is empty then**
      $counter(index) \leftarrow counter(index) + 1$
    else
      for $i = 1$ to **length of** $indexNeighbours$ **do**
        $startCoord \leftarrow startCoordList(indexNeighbours(i))$
        $index \leftarrow indexNeighBours(i)$
        $counter \leftarrow$ FindNrOfBuoysToEachPipe$(startCoord, index, counter)$
        $counter(index) = counter(index) + counter(indexNeighbours(i))$
      end for
    end if
  end procedure

After that the pipes are sorted and given a unique ID based on the number of buoys in the counter and the location of each pipe. The pipe that has the lowest number of buoys in its counter and it is situated top-left obtains ID 1 and comes first in the array of pipes, and the pipe that has the highest number of buoys in its counter - this will be always the tower pipe - gets the last ID and takes the last entry in the array of pipes, i.e. its ID and index are equal to the total number of pipes in the topology. Moreover, an output ID is assigned to each pipe based on the end coordinate that is used to identify which pipe the given pipe is connected to. For instance, in Figure 6.6 pipes with ID 4 and 9 are connected to 11. Therefore, their output ID will be 11.
Two classes are created: *Fluid* class stores properties of the fluid, such as type, density and bulk modulus, and *Pipes* class stores the properties of the pipes filled with the chosen fluid. The *Pipes* class contains the following properties: ID, output ID, length, cross-section area, volume, number of lumps, total and per lump inertia and compressibility. When creating a *Pipes* object, IDs, output IDs, lengths and areas of the pipes in the topology are passed as argument to the constructor of the object. Based on these arguments and the imported fluid properties, the rest of the properties are calculated. The pipes are divided into lumps comprising of inertia and compressibility components. The number of the lumps in each pipes is calculated based on the total length of the pipe and the length per lump property, which is defined as constant for the class. The inertia and compressibility of each lump is calculated based on the total inertia and compressibility and the number of lumps in each pipe.

In order to generate the state-space matrices for a chosen topology the structure of the state-space matrices of a junction is exploited. The system of differential equations of a T-junction was derived in the previous section and is given by equation (6.31), which is marked with rectangles in figure 6.7 to serve as an example for gaining intuition of the formed patterns, which can be used to derive the complete model of the hydraulic collection.

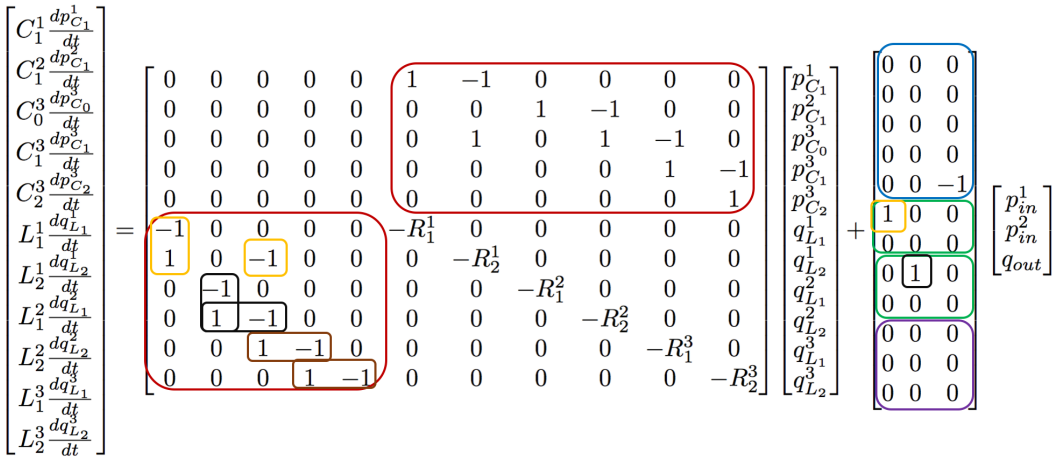

Figure 6.7: Structure of the state-space matrices at a junction

Before going to describe the structure of the state-space matrices, we need to emphasize the importance of the ordering of the state variables. As it can be seen from figure (6.7), the pressure variables are listed first and then the flow variables, while keeping the same ordering for both variables. This makes the matrices inside the red rectangles to be skew-symmetric of each other, hence, by knowing only one of them, let's name it Q, the other one can be obtained by just finding $-Q^T$. The yellow, black and brown rectangles are the diagonal and super-diagonal entries of the bottom-left red-rectangled matrices with dimension $n_{pipe} * n_{lumps} \times n_{pipe} * n_{lumps} - 1$ (in this case there are three pipes and each pipe had two lumps, thus, 6×5). The top-right red-rectangled matrix is negative transpose of bottom-left red-rectangled matrix. The top-left matrix with dimension $n_{pipe} * n_{lumps} - 1 \times n_{pipe} * n_{lumps} - 1$ is a null matrix. The bottom-right matrix is a diagonal matrix with diagonal entries equal to the linear friction coefficient of each lump. Its dimension is $n_{pipe} * n_{lumps} \times n_{pipe} * n_{lumps}$. The blue rectangle at the input matrix has dimension $n_{pipe} * n_{lumps} - 1 \times n_{pipe}$. Its entries are all 0 except the bottom-right entry, which is equal to -1. The green rectangles at the input matrix are with dimension $n_{lumps} \times n_{pipe}$. It can be seen that the only non-zero entry for each green-rectangled matrix is placed on the top row and on the column with index equal to the number of the green- rectangled matrix, i.e. the column index shifts with each green rectangle. The purple rectangle at the input matrix has dimension equal to the number of connected pipes, i.e. $n_{pipe} \times n_{pipe}$, and all of its entries are equal to 0.

Using the generated patterns state-space equations of any number of connected pipes with any number of lumps can be formed and the complete model of a hydraulic collection system with any topology can be derived.

6.2 Modelling hydraulic accumulators

One of the main components of the hydraulic collection system is the hydraulic accumulator. This section presents modelling of hydraulic accumulators.

6.2.1 Modelling of a piston accumulator

The principle operation of the piston accumulator is the following. As the fluid pressure at the accumulator inlet becomes greater than the precharge pressure, fluid enters the accumulator and compresses the gas, storing hydraulic energy. A decrease in the fluid pressure causes the gas to decompress and discharge the stored fluid into the system.
During typical operations, the pressure in the gas chamber is equal to the pressure in the fluid chamber. However, if the pressure at the accumulator inlet drops below the precharge pressure, the gas chamber becomes isolated from the system. In this situation, the fluid chamber is empty and the pressure in the gas chamber remains constant and equal to the precharge pressure. The pressure at the accumulator inlet depends on the hydraulic system to which the accumulator is connected. If the pressure at the accumulator inlet builds up to the precharge pressure or higher, fluid enters the accumulator again.
The motion of the separator between the fluid chamber and the gas chamber is restricted by two hard stops that limit the expansion and contraction of the fluid volume. The fluid volume is limited when the fluid chamber is at capacity and when the fluid chamber is empty. The hard stops are modeled with finite stiffness and damping.
A model of a piston accumulator with its variables and parameters is shown in figure 6.8.

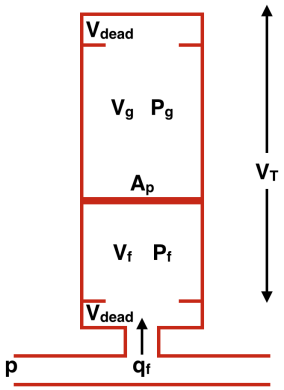

Figure 6.8: Piston accumulator

The flow through the inlet of the accumulator is modelled as a turbulent flow through an orifice. It is found by

$$q_f = C_d A_i \sqrt{\frac{2\Delta P}{\rho}}, \tag{6.32}$$

where

- C_d - discharge coefficient (*typ.* $C_d = 0.6 - 0.7$),
- A_i - area of the inlet,
- $\Delta P = P - P_f$ - pressure difference at the inlet,
- ρ - density of the hydraulic fluid.

Rearranging (6.32) to find the pressure drop ΔP, yields,

$$\Delta P = \frac{\rho}{2A^2C_d^2}q_f^2. \tag{6.33}$$

The compressibility of fluid in high-pressure application is an important phenomenon that needs to be considered. The bulk modulus of the fluid is a parameter that indicates the stiffness of the fluid and it is defined as the pressure needed to cause a given decrease in volume,

$$\beta = \frac{\Delta P_f}{\Delta V_f / V_f}, \tag{6.34}$$

where V_f is the volume of liquid and ΔV_f is the change in volume of the liquid when subjected to a pressure change of ΔP. The fluid volume is

$$V_f = A_p x + V_{dead_f} \tag{6.35}$$

where

- A_p - piston area,
- x - piston displacement,
- V_{dead_f} - fluid chamber dead volume.

The bulk modulus varies for different fluids. Rearranging (6.34) and considering an infinitesimal change, yields

$$dP_f = \frac{\beta}{V_f} dV_f \tag{6.36}$$

We divide (6.36) by dt and obtain the continuity equation

$$\dot{P}_f(t) = \frac{\beta}{V_f}\dot{V}_f(t). \tag{6.37}$$

The rate of change of fluid volume is

$$\dot{V}_f(t) = q_f(t) - A_p\dot{x}(t). \tag{6.38}$$

Combining (6.37) and (6.38), yields

$$\dot{P}_f(t) = \frac{\beta}{V_f}(q_f(t) - A_p\dot{x}(t)). \tag{6.39}$$

The dynamics of the accumulator piston can be modelled as a mass-damper system,

$$m_p\ddot{x}(t) + F_f(\dot{x}(t)) = (P_f(t) - P_g(t) - P_{HS}(t))A_p, \tag{6.40}$$

where

- m_p - mass of the piston,

- $F_f(\dot{x})$ - friction term,
- P_g - gas pressure,
- P_{HS} - pressure due to the hardstop.

The hard stop contact pressure is modeled with a stiffness term and a damping term.

$$P_{HS} = \begin{cases} K_{s,up}(V_f - V_T + V_{dead_g}) + K_{d,up}\dot{V}_f^+(V_f - V_T + V_{dead_g}), & \text{if } V_f \geq V_T - V_{dead_g} \\ K_{s,down}(V_f - V_{dead_f}) - K_{d,down}\dot{V}_f^-(V_f - V_{dead_f}), & \text{if } V_f \leq V_{dead_f} \\ 0, & \text{otherwise} \end{cases} \tag{6.41}$$

$$\dot{V}_f^+ = \begin{cases} \dot{V}_f, & \text{if } \dot{V}_f \geq 0 \\ 0, & \text{otherwise} \end{cases}$$

$$\dot{V}_f^- = \begin{cases} \dot{V}_f, & \text{if } \dot{V}_f \leq 0 \\ 0, & \text{otherwise} \end{cases}$$

where

- $K_{s,up}$ - stiffness constant of the hardstop of the upper end stop,
- $K_{d,up}$ - damping constant of the hardstop of the upper end stop,
- $K_{s,down}$ - stiffness constant of the hardstop of the lower end stop,
- $K_{d,down}$ - damping constant of the hardstop of the lower end stop,
- V_T - total volume of the accumulator
- V_{dead_g} - gas chamber dead volume

The thermal losses occupy a great portion of the total accumulator losses. Therefore, it is important to include thermodynamic effects when building the accumulator model. The thermal losses are mostly due to the convection of heat from the gas chamber to the ambient through the walls of the accumulator.
The first law of thermodynamics states that the energy neither can be created nor destroyed, but change forms. The energy balance can be written as

$$\dot{Q} - \dot{W} = \dot{U} \tag{6.42}$$

where $\dot{Q}$ is the change in heat, $\dot{W}$ is the change in work and $\dot{U}$ is the change in internal energy. The internal energy Q for real gases can be calculated as

$$\dot{U} = m_g C_v \frac{dT_g}{dt} + m_g \left(T_g \left(\frac{\partial P_g}{\partial T_g} \right)_v - P_g \right) \frac{dV_g}{dt} \tag{6.43}$$

The transferred heat through the walls of the accumulator by convection is proportional to the temperature difference between the gas and the ambient

$$\dot{Q}_{conv} = hA_w(T_a - T_g) \tag{6.44}$$

where h is the convection coefficient that depends on the properties of the material that makes the walls of the accumulator, A_w is the area of the walls, T_a is the ambient temperature and T_g is the gas temperature.
The work W can be calculated as

$$\dot{W} = P_g \frac{dV_g}{dt} \tag{6.45}$$

Substituting (6.43), (6.44) and (6.45) in (6.42) yields

$$hA_w(T_a - T_g) - P_g\frac{dV_g}{dt} = m_g C_v \frac{dT_g}{dt} + \left(T_g\left(\frac{\partial P_g}{\partial T_g}\right)_v - P_g\right)\frac{dV_g}{dt} \tag{6.46}$$

where C_v is the specific heat ratio at constant volume. $\left(\frac{\partial P_g}{\partial T_g}\right)_v$ can be calculated for different gas models. For an ideal gas, the pressure p, volume V and temperature are related as

$$pV = nRT, \tag{6.47}$$

where n is the number of moles and R is the universal gas constant. Hence,

$$\left(\frac{\partial P_g}{\partial T_g}\right)_v = \frac{nR}{V_g} \tag{6.48}$$

Substituting (6.48) in (6.46), yields

$$hA_w(T_a - T_g) - P_g\frac{dV_g}{dt} = m_g C_v \frac{dT_g}{dt} + \left(T_g\frac{nR}{V_g} - P_g\right)\frac{dV_g}{dt} \tag{6.49}$$

Simplifying (6.49), yields

$$m_g C_v \dot{T}_g = -P_g\dot{V}_g - hA_w(T_g - T_a) \tag{6.50}$$

Change of gas volume can be found by

$$\dot{V}_g = -A_p\dot{x} \tag{6.51}$$

Using the ideal gas law, we can find the gas pressure.

$$P_g = \frac{nRT_g}{V_g} \tag{6.52}$$

The area of the walls of the accumulator changes with the displacement of the piston. If a cylindrical surface is assumed, then the area will be

$$A_w = 2A_p + 2\pi r_p\frac{V_g}{A_p} \tag{6.53}$$

where r_p is the radius of the piston.
The structure of the developed model is shown in Figure 6.9. Input to the system is the input flow to the accumulator q_{in} and the ambient temperature T_{amb} and output is the pressure before the inlet P_{pipe}.

6.2.2 Linearization of the nonlinear model

The nonlinear system of equation that describes the accumulator dynamics is

$$\begin{aligned}
\dot{x} &= v \\
\dot{P}_f &= \frac{\beta}{A_p x + V_{dead_f}}(q_f - A_p v) \\
\dot{v} &= \frac{A_p}{m_p}\left(P_f - \frac{nRT_g}{V_T - A_p x - V_{dead_f}} - P_{HS}\right) - \frac{F_f(v)}{m_p} \\
\dot{T}_g &= \frac{A_p nRT_g}{m_g C_v (V_T - A_p x - V_{dead_f})}v - \frac{h}{m_g C_v}\left(2A_p + 2\pi r_p\frac{V_T - A_p x - V_{dead_f}}{A_p}\right)(T_g - T_a)
\end{aligned} \tag{6.54}$$

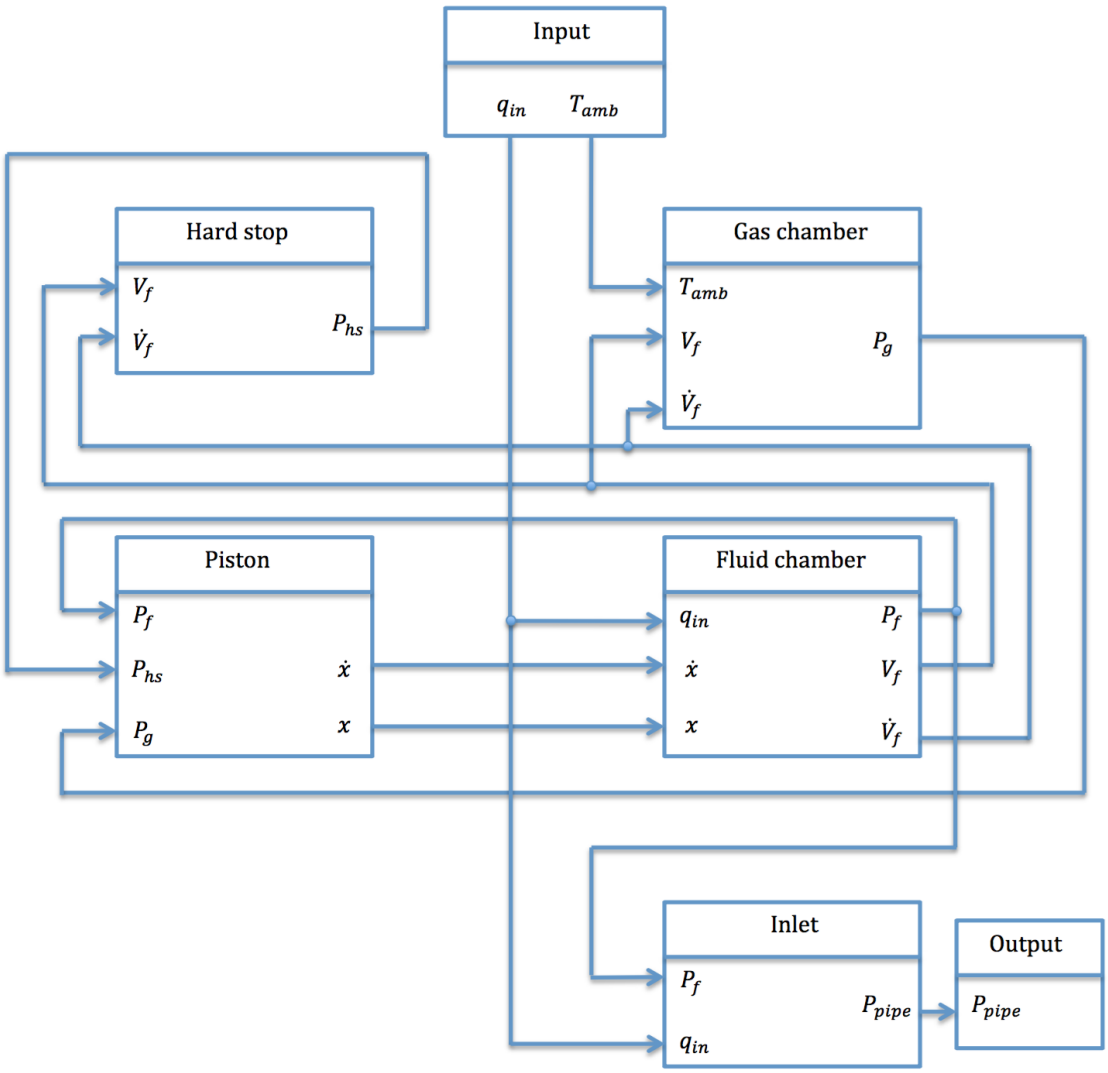

Figure 6.9: Structure of the model

The state vector of the system is

$$\begin{aligned} x_s &= \begin{bmatrix} x & P_f & v & T_g \end{bmatrix}^T \\ u_{s0} &= \begin{bmatrix} q_{f0} & T_{g0} \end{bmatrix}^T \end{aligned} \tag{6.55}$$

Stationary point of the system is

$$\begin{aligned} x_{s0} &= \begin{bmatrix} 0 & p_{pre} & 0 & T_a \end{bmatrix}^T \\ u_{s0} &= \begin{bmatrix} 0 & T_a \end{bmatrix}^T \end{aligned} \tag{6.56}$$

The pressure due to the hard-stop changes depending on the position of the piston as described by (6.41). The system needs to be linearized for all cases to see how the dynamics change when the piston hits the end stops. Firstly, the system is linearized for the case when the piston is within the operating range, i.e. $V_{dead_f} \leq$

$V_f \leq V_T - V_{dead_f}$. Then, $P_{HS} = 0$. The linearized system is

$$\Delta x_s = A\Delta x_s + B\Delta u_s \tag{6.57}$$

where A and B are the found by finding the Jacobian matrices

$$A = \begin{bmatrix} \frac{\partial f_1}{\partial x} & \frac{\partial f_1}{\partial P_f} & \frac{\partial f_1}{\partial v} & \frac{\partial f_1}{\partial T_g} \\ \frac{\partial f_2}{\partial x} & \frac{\partial f_2}{\partial P_f} & \frac{\partial f_2}{\partial v} & \frac{\partial f_2}{\partial T_g} \\ \frac{\partial f_3}{\partial x} & \frac{\partial f_3}{\partial P_f} & \frac{\partial f_3}{\partial v} & \frac{\partial f_3}{\partial T_g} \\ \frac{\partial f_4}{\partial x} & \frac{\partial f_4}{\partial P_f} & \frac{\partial f_4}{\partial v} & \frac{\partial f_4}{\partial T_g} \end{bmatrix}_{x_s=x_{s0},\, u_s=u_{s0}} \qquad B = \begin{bmatrix} \frac{\partial f_1}{\partial q_f} & \frac{\partial f_1}{\partial T_a} \\ \frac{\partial f_2}{\partial q_f} & \frac{\partial f_2}{\partial T_a} \\ \frac{\partial f_3}{\partial q_f} & \frac{\partial f_3}{\partial T_a} \\ \frac{\partial f_4}{\partial q_f} & \frac{\partial f_4}{\partial T_a} \end{bmatrix}_{x_s=x_{s0},\, u_s=u_{s0}} \tag{6.58}$$

Hence,

$$A = \begin{bmatrix} 0 & 0 & 1 & 0 \\ 0 & 0 & -\frac{A_p\beta}{V_{dead_f}} & 0 \\ -\frac{A_p^2 nRT_a}{m_p(V_T - V_{dead_f})^2} & \frac{A_p}{m_p} & 0 & -\frac{A_p nR}{m_p(V_T - V_{dead_f})} \\ 0 & 0 & \frac{A_p p_{pre}}{m_g C_v} & -\frac{h}{m_g C_v}\left(2A_p + 2\pi r_p \frac{V_T - V_{dead_f}}{A_p}\right) \end{bmatrix}$$

$$B = \begin{bmatrix} 0 & 0 \\ \frac{\beta}{V_{dead_f}} & 0 \\ 0 & 0 \\ 0 & \frac{h}{m_g C_v}\left(2A_p + 2\pi r_p \frac{V_T - V_{dead_f}}{A_p}\right) \end{bmatrix} \tag{6.59}$$

6.2.3 Modelling of Hydac's double piston accumulator

In this section, the derivation of the mathematical model of Hydac's double piston accumulator is presented. The schematic of the accumulator is shown in figure 6.10.

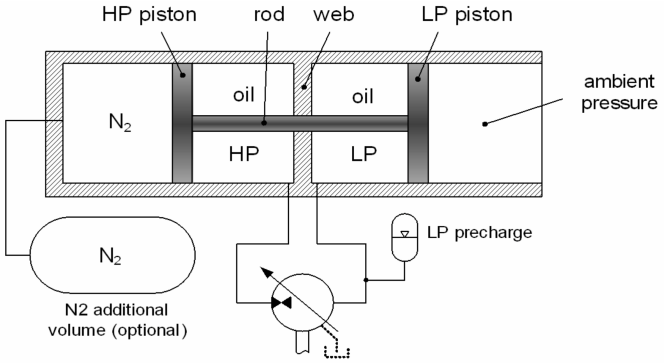

Figure 6.10: Sketch of the double piston accumulator, connected to a hydraulic pump, [34]

As it can be seen from the figure the accumulator consists of four chambers and two pistons that are rigidly connected with a rod. The first chamber from left to right is filled with nitrogen that is used to store the energy by compression of the gas. The second chamber and third chamber, whose total volume is constant, are filled with hydraulic oil. The two chambers (HP and LP) are separated by the web. The fourth chamber is open at one end and hence, has the ambient pressure. The LP oil chamber is preloaded with a small diaphragm accumulator, which keeps the pressure at the suction side of the pump constant (equal to preload LP).
Before starting to model the double piston accumulator, we consider the pump as an ideal flow source which pumps fluid with a flow rate q_{in}. The pressure at the LP chamber is equal to the pressure of the diaphragm accumulator that can be calculated using the ideal gas law.

$$PV = nRT, \tag{6.60}$$

where P is pressure, V - volume, T - temperature, R is the universal time constant, n is the number of moles. If we assume that there is no heat transfer to the environment, the process is reversible, adiabatic, the ideal gas law can be approximated by

$$P_{g,diaphragm} V^k_{g,diaphragm} = const \tag{6.61}$$

where k is the ratio between specific heat at constant pressure and specific heat at constant volume (for nitrogen $k = 1.4$) and $const$ is determined for a certain operating condition. Differentiating (6.61), we get

$$\dot{P}_{g,diaphragm} V^k_{g,diaphragm} + k P_{g,diaphragm} V^{k-1}_{g,diaphragm} \dot{V}_{g,diaphragm} = 0 \tag{6.62}$$

Rearranging (6.62),

$$\dot{P}_{g,diaphragm} = -\frac{k P_{g,diaphragm} \dot{V}_{g,diaphragm}}{V_{g,diaphragm}}. \tag{6.63}$$

total volume of the diaphragm accumulator is equal to the sum of the oil and gas volume in it.

$$V_{g,diaphragm} + V_{o,diaphragm} = V_{T,diapragm} \tag{6.64}$$

where $V_{T,diaphragm}$ denotes the total accumulator volume. Noting that $P_{g,diaphragm} = -P_{o,diaphragm}$ and using (6.64), we obtain

$$\dot{P}_{LP} = \dot{P}_{o,diaphragm} = \frac{k P_{o,diaphragm} \dot{V}_{o,diaphragm}}{V_{T,diaphragm} - V_{o,diaphragm}} \tag{6.65}$$

Assuming that there is no leakage fluid from the pump and there are no losses in the diaphragm accumulator, there will not be any flow in or our from the diaphragm accumulator ($\dot{V}_{o,diaphragm}$), since the input flow to the HP chamber must be always equal to the output flow from the LP chamber. Therefore, the pressure of the diaphragm accumulator and the LP chamber remain always constant.

6.3 Modelling hydraulic losses

One of the main tasks of the thesis was to correctly model the losses in the hydraulic system, that is the focus of this section. The expressions and friction coefficients and/or factors for calculating different losses in the pipes are obtained from [13].

The change in static pressure for incompressible flow between two points in some medium can be expresses by the Bernoulli equation

$$p_1 - p_2 = \frac{1}{2}\rho(v_2^2 - v_1^2) + \frac{1}{2}\rho v^2 K + \rho g(z_2 - z_1), \tag{6.66}$$

where p is static pressure, ρ is fluid density, v is fluid velocity, K is irreversible loss coefficient, g acceleration due to gravity and z is the elevation. The irreversible loss coefficient is a complex function of the flow rate and geometry of the medium. In this chapter experimentally determined values of K for various pipeline components will be presented with reference to [2]. These constants need to be verified by comparing with an experimental data or CFD simulations.

Before we start with the derivation of the loss model, two well-known non-dimensional parameters among the hydraulics society are introduced. One of them is the *Euler number*, which is the ratio between the difference in static pressure between two points and the characteristic dynamic pressure of the flow,

$$Euler\ number = \frac{p_1 - p_2}{\frac{1}{2}\rho v^2} = \frac{difference\ in\ static\ pressure}{characteristic\ dynamic\ pressure} \tag{6.67}$$

Comparing equation (6.66) and (6.67), it is easy to see that the Euler number actually is equivalent to the irreversible loss coefficient. The second dimensionless parameter is the *Reynolds number*, which is the ratio of the inertia force of the flow to viscous forces:

$$Re = \frac{vD}{\nu} = \frac{inertia\ force}{viscous\ force}, \tag{6.68}$$

where D is the hydraulic diameter of the medium and ν is the kinematic viscosity. For a circular pipe the hydraulic diameter and the geometrical diameter coincide.

The losses in an hydraulic system can be classified as major and minor losses. The major ones constitute the fluid pressure losses in straight uniform pipes. The minor ones comprise of the losses due to orifices, valves, bends, manifolds etc.

The major losses for incompressible and fully-developed flow can be calculated by the Darcy-Weisbach formula

$$\Delta p = \frac{\rho v^2}{2}\frac{fL}{D} \tag{6.69}$$

where f is the dimensionless friction factor and L is the length of the pipe. The friction factor for fully developed flow in uniform pipes depends on the cross section, the Reynolds number and on the surface roughness when the flow is turbulent:

$$f = \begin{cases} \dfrac{k}{Re}, & Re < 2000 \\ \left[1.14 - 2log_{10}\left(\dfrac{\epsilon}{D} + \dfrac{21.25}{Re^{0.9}}\right)\right]^{-2}, & Re > 4000 \end{cases} \tag{6.70}$$

where k is a geometry factor and it is equal to 64 for circular cross sections, ϵ is the surface roughness relative to the hydraulic diameter D. The friction factor in the transition region ($2000 < Re < 4000$) is uncertain. It can be approximated with some curve, for instance a linear curve that connects the friction factors $f(Re = 2000)$ and $f(Re = 4000)$. The expression for the friction factor in the turbulent region, $Re < 4000$ is an approximate explicit equation of the more accurate Colebrook-White equation.

$$\frac{1}{f^{1/2}} = 1.74 - 2log_{10}\left(\frac{2\epsilon}{D} + \frac{18.7}{f^{1/2}Re}\right) \tag{6.71}$$

The implicit nature of (6.71) puts a great burden on the simulation performance. That is why the approximation is the prefered choice.
The minor losses can constitute big portion of the total hydraulic losses. They can be calculated by

$$\Delta p = \frac{1}{2}\rho v^2 K \tag{6.72}$$

where K is the sum of the dimensionless loss coefficients of the components that contribute to the minor losses in a certain section of the pipe.
The pipe section inside the buoy has three main components contributing to the minor losses. These components are depicted in figure 6.11 for the low-pressure side of the pumps: 1) dividing manifold, 2) 90^o elbow, 3) dividing T connection. The picture is the same when we look at the high-pressure side with the only difference that the flows from each pipe join together.

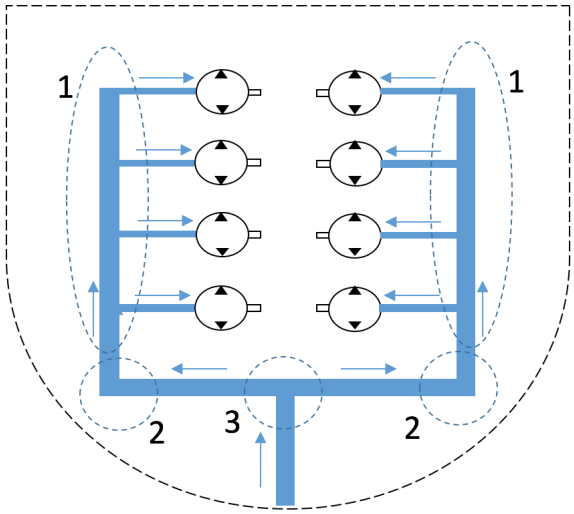

Figure 6.11: Loss components at the low-pressure side of the pumps 1) Dividing manifold 2) 90^o elbow 3) T-connection

The pressure loss for turbulent flow in a sharp bend is independent of Reynolds number. For $R/D \leq 2$ and $Re \geq 5 \times 10^5$. The loss coefficient for a 90^o elbow is shown in table 1.

R/D	K
0.5	1.1
0.75	0.4
1.0	0.25
1.5	0.18
2.0	0.16

Table 6.1: Loss coefficient of 90^o elbow for $R/D \leq 2$ and $Re \geq 5 \times 10^5$

For $4 \times 10^3 < Re < 5 \times 10^5$ the loss coefficient is

$$K|_{Re} = (K|_{Re \geq 5 \times 10^5}) \left(\frac{5 \times 10^5}{Re} \right)^{0.17} \tag{6.73}$$

Typical values for the loss coefficient for 90^o elbow when the flow is laminar are plotted in figure 6.12.

Figure 6.12: Typical values for the loss coefficient for 90^o elbow for $Re < 2000$

The loss coefficient in the transition region, $2000 < Re < 4000$, is uncertain. It can be approximated by using interpolation.
At a T-connection the Bernoulli equation is given by

$$p_i - p_j + \frac{1}{2}\rho(v_i^2 - v_j^2) = \frac{1}{2}v_n^2 K_{ij} + \frac{1}{2}v_i \rho \frac{f_i L_i}{D_i} + \frac{1}{2}\rho v_j^2 \frac{f_j L_j}{D_j} \tag{6.74}$$

where $i = 1, 2, 3$ is an index denoting the branch supplying flow to the junction, $j = 1, 2, 3$ - an index denoting a branch conveying fluid from the junction and $n = 1, 2, 3$ - an index denoting which branch velocity is used in constructing loss term. When the flow is turbulent, $Re > 10^4$, for a dividing T-connection shown in

figure 6.13a, the dimensionless loss coefficient K_{ij} is

$$K_{31} = 0.59 + \left[1.18 - 1.84\left(\frac{R}{D}\right)^{1/2} + 1.16\frac{R}{D}\right]\frac{v_3}{v_1} - \left[0.68 - 1.04\left(\frac{R}{D}\right)^{1/2} + 1.16\frac{R}{D}\right]\left(\frac{v_1}{v_3}\right)^2, \tag{6.75}$$

$$0 \leq \frac{R}{D} \leq 0.5, 0.2 \leq \frac{v_1}{v_3} \leq 0.8, v_1 = v_2$$

We see that $i = 3$, $j = 1$, $j = 3$. For a combining T-connection shown in figure 6.13b, the dimensionless loss coefficient K_{ij} is

$$K_{13} = 1.19 - 1.16\left(\frac{R}{D}\right)^{1/2} + 0.46\frac{R}{D} - 1.73\left(1 - \frac{R}{D}\right)\frac{v_2}{v_3} + \left(1.34 - 1.69\frac{R}{D}\right)\left(\frac{v_1}{v_3}\right)^2, \tag{6.76}$$

$$0 \leq \frac{R}{D} \leq 0.5, 0 \leq \frac{v_2}{v_3} \leq 1, v_1 = v_2$$

We see that $i = 3$, $j = 1$, $j = 3$.

(a) Dividing T-connection **(b)** Combining T-connection

Figure 6.13: 90^o T-connections

The losses through a T are considerably reduced by rounding the edges of the T. For a symmetric flow through a dividing and combining T with $v_1 = v_2 = v_3/2$ the loss coefficients as a function of rounding are shown respectively in table 2 and 3.

R/D	0.0	0.1	0.2	0.3	0.4	0.5
K_{31}	1.01	0.83	0.77	0.74	0.71	0.68

Table 6.2: Loss coefficient of 90^o dividing T-connection with $v_1 = v_2 = v_3/2$

R/D	0.0	0.1	0.2	0.3	0.4	0.5
K_{13}	0.66	0.38	0.32	0.3	0.29	0.29

Table 6.3: Loss coefficient of 90^o combining T-connection with $v_1 = v_2 = v_3/2$

When the flow through the T is laminar, $Re < 2000$ the total pressure losses are inversely proportional to the Reynolds number. The coefficient of proportionality can be determined experimentally.

A dividing manifold is shown in figure 6.14.

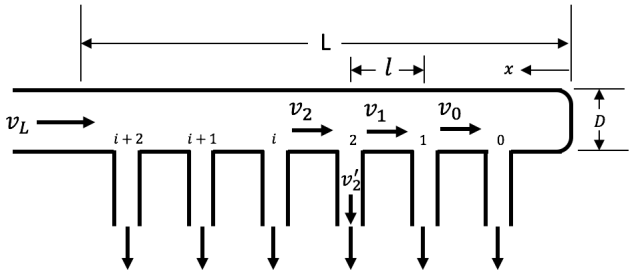

Figure 6.14: A uniform dividing manifold

The pressure change in the main pipe between the i and $i-1$ branch pipes is given by

$$p_i - p_{i-1} = \frac{1}{2}\rho v_i^2 K_i - \frac{1}{2}\rho(v_i^2 - v_{i-1}^2) + \frac{1}{2}\rho v_{i-1}^2 \frac{f_{i-1} l_{i-1}}{D_{i-1}} + \rho g(z_{i-1} - z_i) \tag{6.77}$$

where ρ is the fluid density, v is the main pipe flow velocity averaged over the cross section, D is main pipe diameter, l is the length between points i and $i-1$, z is the elevation, f is the major loss friction factor and K is dimensionless loss coefficient, which is equal to the dimensionless friction factor of the dividing T connection, shown in figure 6.15.

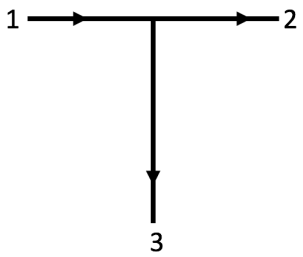

Figure 6.15: Dividing T-connection

The dimensionless friction factor for the main path of a diving T is given by

$$K_{12} = \begin{cases} 1.55\left(0.22 - \dfrac{v_3}{v_1}\right)^2 - 0.03, & 0 \leq \dfrac{v_3}{v_1} \leq 0.22 \\ 0.65\left(\dfrac{v_3}{v_1} - 0.22\right)^2 - 0.03, & 0.2 \leq \dfrac{v_3}{v_1} \leq 1 \end{cases} \tag{6.78}$$

The friction factor of the branch pipe for a diving T connection is

$$K_{13} = 0.99 - 0.23\sqrt{\frac{R}{D}} - \left[0.82 + 0.29\sqrt{\frac{R}{D}} + 0.3\frac{R}{D}\right]\frac{v_3}{v_1} - \left[1.02 - 0.64\sqrt{\frac{R}{D}} + 0.76\frac{R}{D}\right]\left(\frac{v_3}{v_1}\right)^2 \tag{6.79}$$

A combining manifold joins the flow from branch pipes into a single stream and it can be visualized as 6.14 but with the flow direction reversed. The pressure in the

main pipe reduces with distance from the dead end and the pressure drop between two branches can be calculated by (6.77), in which the dimensionless friction factor is equal to the dimensionless friction factor of a combining T connection, shown in figure 6.16.

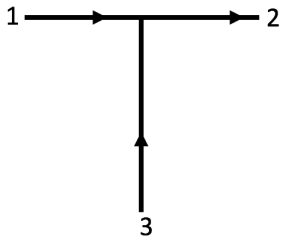

Figure 6.16: Combining T-connection

The friction factor for the main path is

$$K_{12} = 0.045 + \left[1.38 - 1.94\sqrt{\frac{R}{D}} + 1.34\frac{R}{D}\right]\frac{v_3}{v_2} - \left[0.9 - 0.95\sqrt{\frac{R}{D}} + 1.23\frac{R}{D}\right]\left(\frac{v_3}{v_2}\right)^2 \tag{6.80}$$

The friction factor of the branch pipe for a combining T connection is

$$K_{32} = 1.09 - 0.8\sqrt{\frac{R}{D}} - \left[0.53 + 1.27\sqrt{\frac{R}{D}} - 1.86\frac{R}{D}\right]\frac{v_1}{v_2} - \left[1.48 - 2.28\sqrt{\frac{R}{D}} + 1.8\frac{R}{D}\right]\left(\frac{v_1}{v_2}\right)^2 \tag{6.81}$$

The engagement and disengagement of pumps is controlled by directional valves. The losses through the directional valve can be modelled as equivalent to the sum of losses through two orifices with the same variable cross section area. The friction factor of a sharp edged orifice, shown in figure 6.17 for different ratios between orifice and pipe diameter are tabulated in table 6.4.

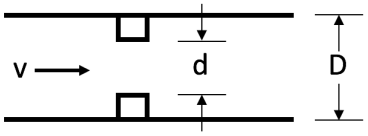

Figure 6.17: Sharp-edged orifice

d/D	0.20	0.25	0.30	0.35	0.40	0.45	0.50	0.55	0.60	0.65	0.70	0.75	0.80	0.85	0.90
K	1600	620	300	155	87.5	49	30.8	19	12	7.3	4.7	2.7	1.5	0.76	0.32

Table 6.4: Friction factor of a sharp edged orifice for different d/D

The connection from the buoy to the sea bed is still under question. One option that is considered is that a dynamic hose cable coils from the buoy down to the sea bed as shown in figure 6.18.

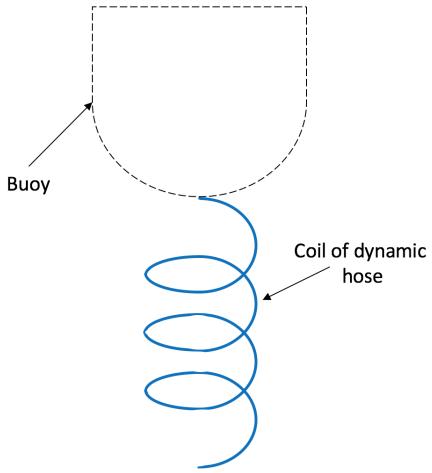

Figure 6.18: Connection from the buoy to the sea bed with dynamic power cable

The dynamic power hose can be modelled as a coil of circular pipe as shown in figure 6.19.

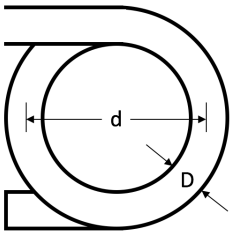

Figure 6.19: Coil of circular pipe

The pressure drop of a coil of circular pipe is given by

$$\Delta p = \frac{1}{2}\frac{f_c L}{D}\rho v^2 \tag{6.82}$$

where L is the length of the pipe in the coil, i.e $L = \pi d \times number\,of\,turns$, D is the diameter of the pipe and f_c is the dimensionless friction factor. The dimensionless friction factor for laminar flow, $Re < 2100\left(1 + 12\sqrt{\frac{D}{d}}\right)$ is

$$f_c = \begin{cases} \dfrac{64}{Re}, & 0 < N = Re\sqrt{\frac{D}{d}} < 11.6 \\ \dfrac{11}{1 - \left[1 - \left(\frac{11.6}{N}\right)^{0.45}\right]^{2.2}}, & 11.6 < N < 2000 \\ 0.11\sqrt{N}, & N > 2000 \end{cases} \tag{6.83}$$

For turbulent flow, $Re > 2100\left(1 + 12\sqrt{\frac{D}{d}}\right)$, the dimensionless friction factor is

$$f_c = \frac{0.336}{\left(Re\sqrt{\frac{d}{D}}\right)^{0.2}}. \tag{6.84}$$

Another option is to have an intermediate buoy to raise the connection point of the hose from the sea bed as shown in figure 6.20.

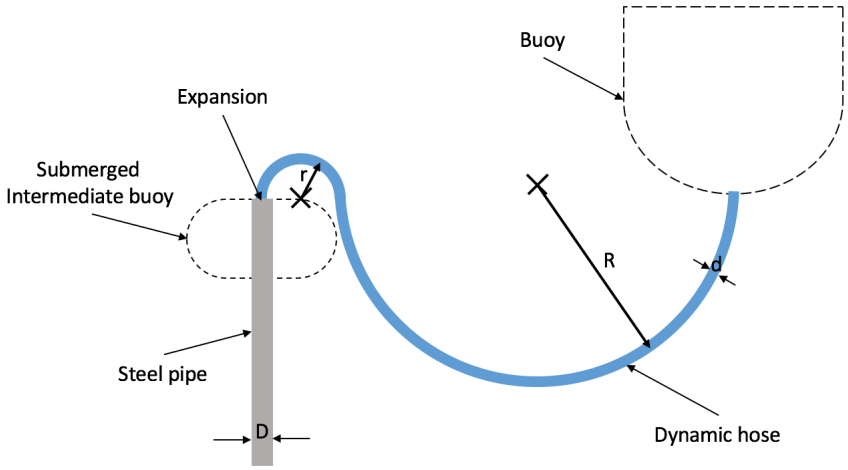

Figure 6.20: Connection of the buoy to the sea bed through an intermediate buoy

A dynamic hose is used to connect from the buoy to the intermediate buoy. It is assumed that the hose will have two circular bends with radii R and r. The losses through the dynamic hose can be calculated by (6.82), with friction factor equal to the friction factor of a coil of circular pipe and with length $L = \pi(R + r)$. The dynamic hose can be connected to a steel pipe with a bigger diameter. If this is the case. there will be an expansion and contraction at the high- and low-pressure sides respectively. The expansion and contraction can be abrupt or gradual. The friction factor for a gradual contraction and/or expansion is lower than a gradual one. Hence, the design choice is to have a gradual contraction and expansion, shown in figure 6.21.

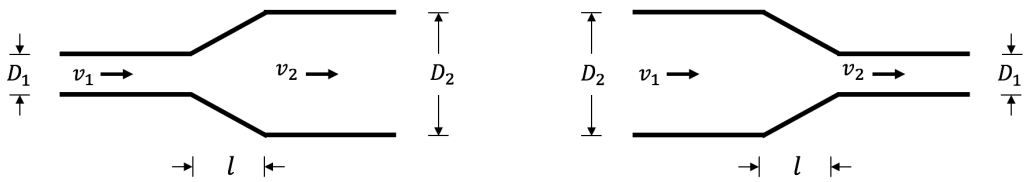

(a) Expansion **(b)** Contraction

Figure 6.21: Gradual contraction and expansion

The friction factors for the gradual expansion and contraction are summarized in table 5 and 6 respectively. At the sea bottom, the dynamic hoses are connected to the steal pipes with either a 90^o elbows, T-connections or quatrofurcations (quatrofurcation is a connection with four incoming or outgoing branches). The friction losses for elbows and T-connections are already presented above. No analytical expression has been found in the hydraulics literature to calculate the friction losses

$\frac{A_2}{A_1}$	K							
	$2l/D_1$							
	0.1	0.2	0.3	0.5	1.0	2.0	3.0	5.0
1.2	0.06	-	-	-	-	-	-	-
1.4	0.10	0.09	0.08	0.07	0.06	-	-	-
1.6	0.17	0.13	0.12	0.10	0.08	0.06	-	-
2.0	0.25	0.25	0.23	0.20	0.15	0.08	0.06	-
2.5	0.35	0.35	0.32	0.35	0.25	0.10	0.08	0.06
3.0	0.45	0.45	0.45	0.45	0.37	0.22	0.15	0.10
4.0	0.60	0.60	0.60	0.60	0.55	0.42	0.40	0.30

Table 6.5: Friction factor for a gradual expansion

$\frac{A_1}{A_2}$	K				
	l/D_2				
	0	0.05	0.1	0.15	0.6
1.2	0.08	0.06	0.04	0.03	0.03
1.5	0.17	0.12	0.09	0.07	0.06
2.0	0.25	0.23	0.17	0.14	0.06
3.0	0.33	0.31	0.27	0.23	0.08
5.5	0.40	0.35	0.32	0.35	0.25
10.0	0.45	0.45	0.41	0.39	0.27

Table 6.6: Friction factor for a gradual contraction

for a quatrofurcation. We can assume that the 90^o branch is shifted towards the incoming branch. Therefore, we can approximate losses at a quatrofurcation by considering it as a T-connection with trifurcation, for which analytical expressions to calculate the losses is available. A trifurcation and a quatrofurcation are shown in figure 6.22.

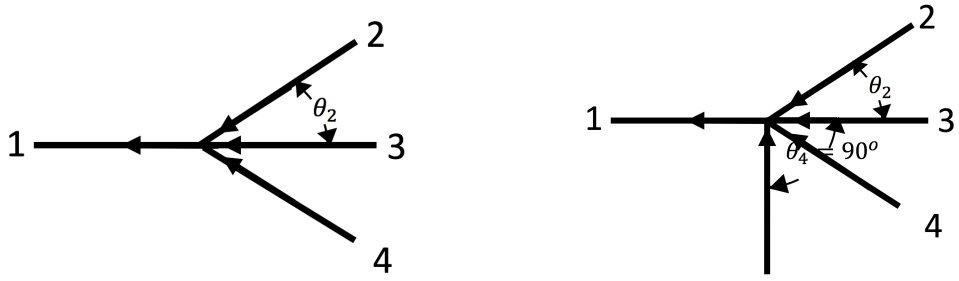

(a) Trifurcation

(b) Quatrofurcation

Figure 6.22: Trifurcation and Quatrofurcation

The dimensionless friction factor of a trifurcation is given by

$$K_{1j} = 0.86 sin^2\theta_j + \alpha_j \left(cos\theta_j - \frac{v_j}{v_1} \right)^2 + \beta_j \frac{v_j}{v_1}, \tag{6.85}$$

where

$$\alpha_j = 0.0227\theta_j cos\theta_j + 1.2 sin\theta_j sin|60^o - \theta_j|$$
$$\beta_j = \left[0.00698(45^o - \theta_j) + 0.075\frac{A_j}{A_1} + 0.0262\theta_j\right] sin(75^o - \theta_j)$$

The connection of the flows from all buoys at the tower is shown in figure 6.23. As we can see from the figure, the flows from each side of the farm join at two

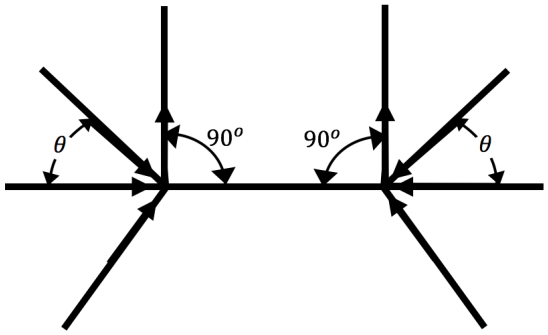

Figure 6.23: Connection of flows from all buoys at the tower

junctions respectively at each side of the tower on the sea bed. The two junctions are connected with a hydraulic pipe to ensure the pressures at both junctions are the same. High-pressure fluid flows up through two steel pipes on each side of the rack to connect to the motor ports with as few bends as possible. The picture is the same for the low-pressure side, with the only deference that the flow directions are reversed. The losses at this connection can be modelled as the sum of losses of two quatrofurcations.
At the tower the flow is distributed to each hydraulic motor through a manifold, whose loss model is already presented above.

The friction factor of a fully-open ball valve is negligible, $K \approx 0$, [2].

The losses of a hydraulic pump/motor comprises of mechanical losses, pressure losses and volumetric/flow losses, that can be obtained from manufacturer data sheets. OHT latest configuration uses CA50 pumps in the buoy and CBP140-100 motors in the tower from Hägglunds (now Bosch Rexroth). The mechanical efficient of the CA and CBP series are respectively $\eta_p = 97\%$ and $\eta_m = 98\%$. The pressure and flow losses and as well as their efficiency maps are presented in Appendix 1.

7

Modelling of the Collection Tower

This section presents the complete drive train model inside the tower. It starts with modelling a planetary gearbox, which is a core component in the drive train.

7.1 Planetary gearbox model

A planetary gearbox can be described as a second-order system, where the angular velocities of any of the two shafts can be used as state variables. In OHT's collection tower the ring and sun gears are connected respectively to the input and output shafts. Therefore, the sun and ring gear angular velocities are chosen as state variables for the planetary gearbox model. Inputs to the system are the torques on the sun gear, carrier and ring gear. The second-order planetary gearbox model was obtained by reducing the sixth-order planetary gearbox model, derived in [15]. The reduction technique is outlined in detail in [15] and is omitted here. The end result of the reduced planetary gearbox model is in the form

$$J\dot{x}(t) = \tilde{A}x(t) + \tilde{B}u(t) \tag{7.1}$$

where

$$J = \begin{bmatrix} J_{11} & J_{12} \\ J_{21} & J_{22} \end{bmatrix}$$

$$J_{11} = J_s + J_c\left(\frac{r_s}{r_r + r_s}\right)^2 + J_p\left(\frac{r_r r_s}{r_p(r_r + r_s)}\right)^2$$
$$J_{12} = J_{21} = J_c\frac{r_r r_s}{(r_r + r_s)^2} - J_p\left(\frac{r_r r_s}{r_p(r_r + r_s)}\right)^2$$
$$J_{22} = J_r + J_c\left(\frac{r_r}{r_r + r_s}\right)^2 + J_p\left(\frac{r_r r_s}{r_p(r_r + r_s)}\right)^2$$

$$\tilde{A} = \begin{bmatrix} \tilde{a}_{11} & \tilde{a}_{12} \\ \tilde{a}_{21} & \tilde{a}_{22} \end{bmatrix}$$

$$\tilde{a}_{11} = -b_s - b_c\left(\frac{r_s}{r_r + r_s}\right)^2 - b_p\left(\frac{r_r r_s}{r_p(r_r + r_s)}\right)^2$$
$$\tilde{a}_{12} = \tilde{a}_{21} = -b_c\frac{r_r r_s}{(r_r + r_s)^2} + b_p\left(\frac{r_r r_s}{r_p(r_r + r_s)}\right)^2$$

$$\tilde{a}_{22} = -b_r - b_c \left(\frac{r_r}{r_r + r_s}\right)^2 - b_p \left(\frac{r_r r_s}{r_p(r_r + r_s)}\right)^2$$

$$\tilde{B} = \begin{bmatrix} \tilde{b}_{11} & \tilde{b}_{12} & \tilde{b}_{13} \\ \tilde{b}_{21} & \tilde{b}_{22} & \tilde{b}_{33} \end{bmatrix} = \begin{bmatrix} 1 & \frac{r_s}{r_r + r_s} & 0 \\ 0 & \frac{r_r}{r_r + r_s} & 1 \end{bmatrix}$$

$$x = \begin{bmatrix} \omega_s & \omega_c \end{bmatrix}^T$$

$$u = \begin{bmatrix} \tau_s & \tau_c & \tau_r \end{bmatrix}^T$$

- J_s, J_p, J_r, J_c - inertia of sun, planet, ring and carrier, respectively;
- b_s, b_p, b_r, b_c - viscous friction coefficient of sun, planet, ring and carrier, respectively;
- r_s, r_p, r_r - radii of sun, planet, ring and carrier gears, respectively;
- ω_s, ω_c, ω_r - angular velocities of sun, carrier and ring, respectively;
- τ_s, τ_c, τ_r - torques applied to sun, carrier and ring, respectively;

The third angular velocity is algebraically related to the other two. Hence, in this case the carrier velocity can be expressed in terms of the sun and ring gear velocities,

$$\omega_c = \frac{r_s}{r_r + r_s}\omega_s + \frac{r_r}{r_r + r_s}\omega_r \tag{7.2}$$

Multiplying (7.1) with the inverse of matrix J, yields the planetary gearbox model in state-space form,

$$\dot{x} = Ax + Bu, \tag{7.3}$$

where

$$A = J^{-1}\tilde{A}$$
$$B = J^{-1}\tilde{B}$$

A planetary gearbox is more commonly characterized with its gear ratio, which is defined as

$$R = -\frac{r_r}{r_s}. \tag{7.4}$$

The system matrices can be expressed in terms of the planetary gear ratio instead of the radii of the individual gears. By noting that

$$r_p = \frac{r_r - r_s}{2},$$

and substituting the planetary gear ratio in the system matrices in (7.1), it yields

$$L = \begin{bmatrix} J_s + J_c \left(\frac{1}{1-R}\right)^2 + J_p \left(\frac{2R}{1-R^2}\right)^2 & -J_c \frac{R}{(1-R)^2} - J_p \left(\frac{2R}{1-R^2}\right)^2 \\ -J_c \frac{R}{(1-R)^2} - J_p \left(\frac{2R}{1-R^2}\right)^2 & J_r + J_c \left(\frac{R}{R-1}\right)^2 + J_p \left(\frac{2R}{1-R^2}\right)^2 \end{bmatrix} \tag{7.5}$$

$$A = \begin{bmatrix} -b_s - b_c\left(\frac{1}{1-R}\right)^2 - b_p\left(\frac{2R}{1-R^2}\right)^2 & b_c\frac{R}{(1-R)^2} + b_p\left(\frac{2R}{1-R^2}\right)^2 \\ b_c\frac{R}{(1-R)^2} + b_p\left(\frac{2R}{1-R^2}\right)^2 & -b_r - b_c\left(\frac{R}{R-1}\right)^2 - b_p\left(\frac{2R}{1-R^2}\right)^2 \end{bmatrix} \tag{7.6}$$

$$B = \begin{bmatrix} 1 & \frac{1}{1-R} & 0 \\ 0 & \frac{R}{R-1} & 1 \end{bmatrix} \tag{7.7}$$

The main friction in a gear gear system are Coulomb-like. The Coulomb losses of the planetary gearbox model are modelled as percentage loss of the rated torque on each shaft of the planetary gearbox, i.e.

$$\tau_{Coulomb} = \begin{bmatrix} -c_s\tau_s^{rated} sign(\omega_s) \\ -c_c\tau_c^{rated} sign(\omega_c) \\ -c_r\tau_c^{rated} sign(\omega_r) \end{bmatrix} \tag{7.8}$$

where $sign(\cdot)$ is the signum function, c_s, c_c and c_r are the Coulomb friction coefficients, i.e. the percentage of loss torque, and τ_s^{rated}, τ_c^{rated} and τ_r^{rated} are the rated torques respectively of the sun gear, carrier and ring gear shafts. The Coulomb friction forces can be incorporated as input to the planetary gearbox model. Hence, the input vector changes to

$$u = \begin{bmatrix} \tau_s - c_s\tau_s^{rated} sign(\omega_s) \\ \tau_c - c_c\tau_c^{rated} sign(\omega_c) \\ \tau_r - c_r\tau_c^{rated} sign(\omega_r) \end{bmatrix} \tag{7.9}$$

7.2 Drive train model

As it was outlined in Chapter 1, the drive train inside the tower consists of multiple identical modules. Each module comprises a planetary gearbox, a hydraulic pump connected to the ring gear of the planetary gearbox, an electric generator, connected to the sun gear of the planetary gearbox, and a pinion, that is on the same shaft with the carrier of the planetary gearbox. The pinions in all drive train modules are engaged with a common rack that lifts the gravity storage.

Due to the large mass of weight, all components inside the operate at their rated torques irrespective of the input power to the drive train. This implies that at low power conditions generators will operate with high torque and low speed, a condition, in which the generator efficiency is poor. During the project, it was found that set of generator shafts can be locked to route the power to the remaining set of generators, thus increasing the speed and efficiency of each generator. We will refer to the drive train module with locked and not locked generator shaft respectively as inactive and active drive train module.

The model of the drive train is derived considering the power routing feature and assuming a perfectly balanced system. Hence, the pressure difference around each hydraulic motor in the module is equal,

$$\Delta p = p_h - p_l, \tag{7.10}$$

where p_h and p_l are the absolute pressures at the high and low pressure sides. The flow through the main pipe q is the sum of the flows through motors in the inactive and active drive train modules, respectively q_1 and q_2

$$q = q_1 + q_2 \tag{7.11}$$

Assuming that the flow through each motor in the inactive modules and the flow in each active module are the same . Hence,

$$q_1 = N_{inactive} \cdot q_1' \qquad q_2 = N_{active} \cdot q_2', \tag{7.12}$$

where $N_{inactive}$ and N_{active} are respectively the number of inactive and active drive train modules, and q_1' and q_2' are the flows though one inactive and active module respectively. The hydraulic motor is modelled as a gyrator with volumetric, pressure and mechanical losses. The flow through each inactive and active motor is respectively found by

$$q_1' = T_s\omega_{r_1} + q_{l_1} \cdot sign(\omega_{r_1}) \qquad q_2' = T_s\omega_{r_2} + q_{l_2} \cdot sign(\omega_{r_2}) \tag{7.13}$$

where T_s is the displacement and/or specific torque of the motor; ω_{r_1} and ω_{r_2} are the angular speeds of the motor shafts (that are connected to the ring gear of the planetary gearbox) of the inactive and active drive modules respectively; q_{l_1} and q_{l_2} are the volumetric losses through the motors of the inactive and active drive modules respectively. The sign of the volumetric loss depends on the direction of power flow through the motor - positive if the power is transformed from hydraulic to mechanical and negative if vice versa. Since the pressure difference and/or the torque on the motor is always positive, the direction of the power flow coincides with the sign of the angular velocity of the motor. The volumetric losses are a function of the motor speeds that are obtained from the loss maps in the motors data sheets.

$$q_{l_1} = Q_l(\omega_{r_1}) \qquad q_{l_2} = Q_l(\omega_{r_2}) \tag{7.14}$$

where $Q_l(.)$ is a function operator for the volumetric losses. The torques on the motors of the inactive and active modules are given by

$$\tau_{r_1} = T_s(\Delta p - p_{l_1})\eta_m \qquad \tau_{r_2} = T_s(\Delta p - p_{l_2})\eta_m \tag{7.15}$$

if the sign of the velocity of the motor is positive, and

$$\tau_{r_1} = T_s(\Delta p + p_{l_1})/\eta_m \qquad \tau_{r_2} = T_s(\Delta p + p_{l_2})/\eta_m \tag{7.16}$$

if the sign of the velocity of the motor is negative. In the above equations p_{l_1} and p_{l_2} are the pressure drops on the motors respectively of the inactive and active modules and η_m is the mechanical efficiency of the motor.
In the inactive modules, the sun shaft is locked. Therefore, sun speed is 0.

$$\omega_{s_1} = 0 \tag{7.17}$$

Substituting (15) in (8), we obtain the dynamic equation for the inactive module.

$$J_{22}\dot{\omega}_{r_1} = b_{22}\omega_{r_1} + \frac{R}{R-1}\tau_{c_1} + \tau_{r_1} \tag{7.18}$$

where τ_{c_1} is the torque on the carrier shaft of any of the inactive modules. The dynamic equation for the any of the active modules is

$$\begin{bmatrix} J_{11} & J_{12} \\ J_{21} & J_{22} \end{bmatrix} \begin{bmatrix} \dot{w}_{s_2} \\ \dot{w}_{r_2} \end{bmatrix} = \begin{bmatrix} b_{11} & b_{12} \\ b_{21} & b_{22} \end{bmatrix} \begin{bmatrix} \omega_{s_2} \\ \omega_{r_2} \end{bmatrix} + \begin{bmatrix} 1 & -\frac{1}{R-1} & 0 \\ 0 & \frac{R}{R-1} & 1 \end{bmatrix} \begin{bmatrix} \tau_{s_2} \\ \tau_{c_2} \\ \tau_{r_2} \end{bmatrix} \tag{7.19}$$

where ω_{s_2} is the angular velocity of the sun shaft, and τ_{s_2} and τ_{c_2} are respectively the sun and carrier torques of the active modules. Since the carriers of the inactive and active drive train modules are connected to the same rack, they share the same angular velocity. For both modules the following kinematic constraint is valid

$$\omega_s - R\omega_r = (1 - R)\omega_c \tag{7.20}$$

We can express the carrier velocity of the active module from the equation above.

$$\omega_c = \frac{R}{R-1}\omega_{r_2} - \frac{1}{R-1}\omega_{s_2} \tag{7.21}$$

Since the sun shaft of the inactive module is locked, we have

$$\omega_c = \frac{R}{R-1}\omega_{r_1} \tag{7.22}$$

Equating (7.21) and (7.22), yields

$$\omega_{r_1} = \omega_{r_2} - \frac{1}{R}\omega_{s_2} \tag{7.23}$$

The total carrier torque on all modules is

$$\tau_c = mgr_p \tag{7.24}$$

where m is the mass of the counterweight and r_p is the pinion radius. The total carrier torque is also equal to

$$\tau_c = N_{inactive}\tau_{c_1} + N_{active}\tau_{c_2} \tag{7.25}$$

Dividing equation (7.25) by the total number of modules $N = N_{inactive} + N_{active}$, we obtain

$$\tau_c' = \alpha\tau_{c_1} + (1 - \alpha)\tau_{c_2} \tag{7.26}$$

where

$$\tau_c' = \frac{\tau_c}{N} \qquad \alpha = \frac{N_{inactive}}{N} \tag{7.27}$$

Expressing τ_{c_2} from (7.25) and substituting it in (7.19), yields

$$\begin{bmatrix} J_{11} & J_{12} \\ J_{21} & J_{22} \end{bmatrix} \begin{bmatrix} \dot{w}_{s_2} \\ \dot{w}_{r_2} \end{bmatrix} = \begin{bmatrix} b_{11} & b_{12} \\ b_{21} & b_{22} \end{bmatrix} \begin{bmatrix} \omega_{s_2} \\ \omega_{r_2} \end{bmatrix} + \begin{bmatrix} 1 & -\frac{1}{R-1} & 0 \\ 0 & \frac{R}{R-1} & 1 \end{bmatrix} \begin{bmatrix} \tau_{s_2} \\ \frac{1}{1-\alpha}\tau_c' - \frac{\alpha}{1-\alpha}\tau_{c_1} \\ \tau_{r_2} \end{bmatrix} \tag{7.28}$$

We express τ_{c_1} from (7.18). It yields

$$\tau_{c_1} = \frac{R-1}{R}\left(J_{22}\dot{\omega}_{r_1} - b_{22}\omega_{r_1} - \tau_{r_1}\right) \tag{7.29}$$

Substituting (7.29) in (7.28) we obtain

$$\mathbf{J}\dot{\mathbf{x}}(t) = \mathbf{A}\mathbf{x}(t) + \mathbf{B}\mathbf{u}(t) \tag{7.30}$$

where

$$\mathbf{x} = \begin{bmatrix}\omega_{s_2}\\ \omega_{r_2}\end{bmatrix} \qquad \mathbf{u} = \begin{bmatrix}\tau_{s_2}\\ \dfrac{1}{1-\alpha}\tau_c' + \dfrac{\alpha(R-1)}{(1-\alpha)R}\tau_{r_1}\\ \tau_{r_2}\end{bmatrix} \tag{7.31}$$

$$\mathbf{J} = \begin{bmatrix} J_{11} + \dfrac{\alpha}{(1-\alpha)R^2}J_{22} & J_{12} - \dfrac{\alpha}{(1-\alpha)R}J_{22}\\ J_{21} - \dfrac{\alpha}{(1-\alpha)R}J_{22} & \dfrac{1}{1-\alpha}J_{22}\end{bmatrix} \tag{7.32}$$

$$\mathbf{A} = \begin{bmatrix} b_{11} + \dfrac{\alpha}{(1-\alpha)R^2}b_{22} & b_{12} - \dfrac{\alpha}{(1-\alpha)R}b_{22}\\ b_{21} - \dfrac{\alpha}{(1-\alpha)R}b_{22} & \dfrac{1}{1-\alpha}b_{22}\end{bmatrix} \tag{7.33}$$

$$\mathbf{B} = \begin{bmatrix} 1 & -\dfrac{1}{R-1} & 0\\ 0 & \dfrac{R}{R-1} & 1\end{bmatrix} \tag{7.34}$$

The generator torque is modelled as

$$\tau_s = -K_s(\omega_s - \omega_0), \tag{7.35}$$

where K_s and ω_0 respectively the generator droop rate and offset, that is controlled to keep the gravity weight within the allowed span and to smooth the power output. The control of the generator is done in the following way. First, a simulation is run in each sea state bu assuming infinite weight stroke to determine the average generator output. Based on the average output and the rated power of each generator, the number of engaged and/or active drive modules is determined, so that the engaged generators can operate at their rated speed. Due to the constant torque on the sun gear, there is a linear relation between the generator speed and offset, which can be find from (7.35),

$$\omega_s = \omega_0 - const \tag{7.36}$$

where $const = \dfrac{\tau_s}{K_s}$. Therefore, controlling the generator offset, corresponds to controlling the speed of the generator. The generator offset is regulated with a PID to control the weight position towards a set-point, that is chosen to be a value close to the bottom end-stop of the stroke. Moreover, the offset is saturated with a minimum and maximum value that correspond to zero and rated speed of the generator. Due to the low value of the set-point, the weight is operated most of the time above the setpoint, i.e. integrating a negative error, corresponding to the increase of the offset

until it gets saturated. Therefore, the generators operate at their rated speed rated speed, until the weight goes below the set-point. When that happens, the generator speeds are decreased to prevent the weight from moving further down. Therefore, when the weight goes below the set-point, dips in power will occur, which can be reduced by choosing a slightly lower output power than the predetermined average output power. In order to stop the integrator of the controller to build up error when the offset is saturated, which will cause delayed response of the controller when the weight goes above the setpoint, conditional integration/clamping anti-windup scheme is used (see [29]).

When there is excessive energy into the tower from the array, the position and energy of the gravity weight will increase and eventually it will hit an end-stop. The end-stop acts like a stiff nonlinear spring and damper upon contact with the weight. Therefore, it can be modelled as

$$F_{end-stop} = \begin{cases} f(z_w, \dot{z}_w), & \text{if } z_w \geq z_w^{max} \\ 0, & \text{otherwise} \end{cases} \tag{7.37}$$

where z_w and z_w^{max} are respectively the position and maximum allowed height of the weight and $f(z_w, \dot{z}_w)$ denotes that the end-stop force is a function of weight position and velocity. When the weight hits the end-stop, it results an increase of force on the rack, and thus on all shafts of the planetary gearbox. Therefore, the pressure in the hydraulic circuit increases until it reaches the set pressure of the pressure-relief valves that get open and establish a direct connection from the high-pressure to low-pressure side of the hydraulic circuit to spill the excessive energy. The set pressure of the valves need to be chosen considering the variations of the pressure in the hydraulic circuit. They should not be chosen too close to the static pressure of the hydraulic circuit, defined by the static gravity force of the weight, since the dynamic pressure variations can cause them to get activated even the weight is within the operating span. Certainly this is not desirable. Choosing a higher set pressure means higher torques on all components of the drive train and the generator, which is not desirable either, since it will strain the components and may even damage them if they are not sized to handle the increased load. Hitting the end-stop of the weight, has an indirect effect on the output power from the generator due to the increased torque. This is certainly a positive thing since it means faster removal (output) of the excessive energy from the system.

The weight can be prevented from hitting the end-stop by kicking in some inactive generators if this happens in a low-energy sea condition and not all generators are active. In a high-energy sea condition, the buoys can be detuned to capture less power. However, due to the shortage of time during the project none of these methods to keep the weight within its allowed span were tried out.

8

Simulation Framework Update and Vectorised Simulink Model

This chapter describes the update of the OHT's simulation framework and the vectorized Simulink model, developed during the project.

8.1 Simulation Framework Update

In a previous study, a simulation framework was developed by OHT to run batch simulations with different sea states and parameters, and to execute multiple simulations in parallel on multiple CPU cores to shorten the simulation time. The main Matlab script, *main_stript.m* reads a list of simulation parameter sets and simulation settings, as well as, the names of the time series to be saved after each simulation from an Excel simulation template file, *simulation_templace.xlsx*, coordinates the parallel simulations and saves the statistical values and selected time series respectively to a simulation summary file, *aSimulation_summary.xlsx* and to mat files, which are organized in a output folder structure. Selected time series are also plotted to a common png file to make it easy to compare the results between different simulations. During the thesis project, the simulation framework was updated with the new simulation parameters and settings, and workspace variables, while preserving the original structure of the framework. A lot of work has been done on organizing the simulation project folder. This changes include, but are not limited to separating OHT specific files (*parameter_script_oht.xlsx*) from buoy specific files (*parameter_script_corpower.xlsx* or *parameter_script_waves4power.xlsx*), organize files depending on their type and purpose in folders, creating classes for different hydraulic components, such as pump, motors, pipes, etc. The developed Simulink model made used of the *Variant subsystem* blocks to enable simulation of simulation of different configurations without modifying the model. The framework was updated to programatically switch between the different configurations configuration. Examples of use case of *Variant subsystems* in the developed Simulink model are buoy selection, controller selection, collection system type selection, typology selection, enabling and disabling losses at different locations of the system, hydraulic accumulator type selection, etc.

OHT's simulation framework comprises of two modes: parameter sweep mode, in which one parameter set is run for one selected sea state, which is read from *simulation_template.xlsx*, and matrix mode, in which a parameter set is run for one or many sea states, that are flagged in a separate excel file, called *seastates.xlsx*. Param-

eter sweep mode is used when it is necessary to see the influence of a set of different parameter values on the system. In this mode, the obtained statistical values of all signals are saved beside each parameter set, thus making it more convenient to compare results. Matrix mode is usually used to simulate all sea states represented in a number of scatter diagrams to produce for example power matrices at different nodes of the system, which can be matched simultaneously to a number of scatter diagrams to compare the annual power output for different sites. In matrix mode, it is also possible to run different parameter sets to compare the impact of different configuration on an annual basis. For example, during the project different storage configurations were swept throughout the whole scatter to quantify the added value from time shifting with different storage capacities.

OHT's simulation can run multiple simulations in parallel by starting multiple instances of Matlab. When the first instance is run, a simulation output folder with a unique name, which contains the time and date of the start of the simulation, and a file marker, *aOutputDirPath.mat*, that stores the name of the output folder, are created. The subsequent instances look for *aOutputDirPath.mat* in the current folder and if it exists, no new output folder and marker are created, i.e. they adopt the already existing output folder and save the results in the already created one. A work folder is created in the simulation output folder. This folder contains file markers with a unique name, containing the number of the set and row and column number of the sea state being simulated, for every simulation that has been started. Each instance of Matlab generates an identical simulation queue based on the simulation template and sea states files. The marker stores the output statistical data, generated after each simulation. The marker indicates if a simulation is already started by another instance by checking whether any data has been stored in it. If this is the case, all other instance of Matlab skips forward in the list to go past this queue slot. In matrix mode, when a simulation set is completed, the data in all marker files are collected into a data structure that is then printed to the simulation summary file.

Initially, the simulation framework could only run parallel simulations in *Normal* mode in Simulink. During the project, the simulation framework was improved by adding a functionality to run parallel simulations in *Accelerator* and *Rapid Accelerator* modes to shorten model run time. In *Accelerator* and *Rapid Accelerator* modes, the Matlab/Simulink creates executables of the model, which are saved by default on the current directory. When multiple instances are run, the consequent instances overwrite the generated executable by the previous instance, thus, creating conflicts and errors. In order to prevent overwriting the automatically generated executables from previous instances, the executables for each instance need to be saved in a different folder. This can be done with the help of the command

```
Simulink.fileGenControl('set', ...
    'CacheFolder', myCacheFolder, ...
    'CodeGenFolder', myCodeGenFolder, ...
    'createDir', true);
```

where *myCacheFolder* and *myCodeGenFolder* are the folder names for the automatically generated files and they are different for each Matlab instance.

A simple program flow diagram of the updated simulation framework is shown in 8.1.

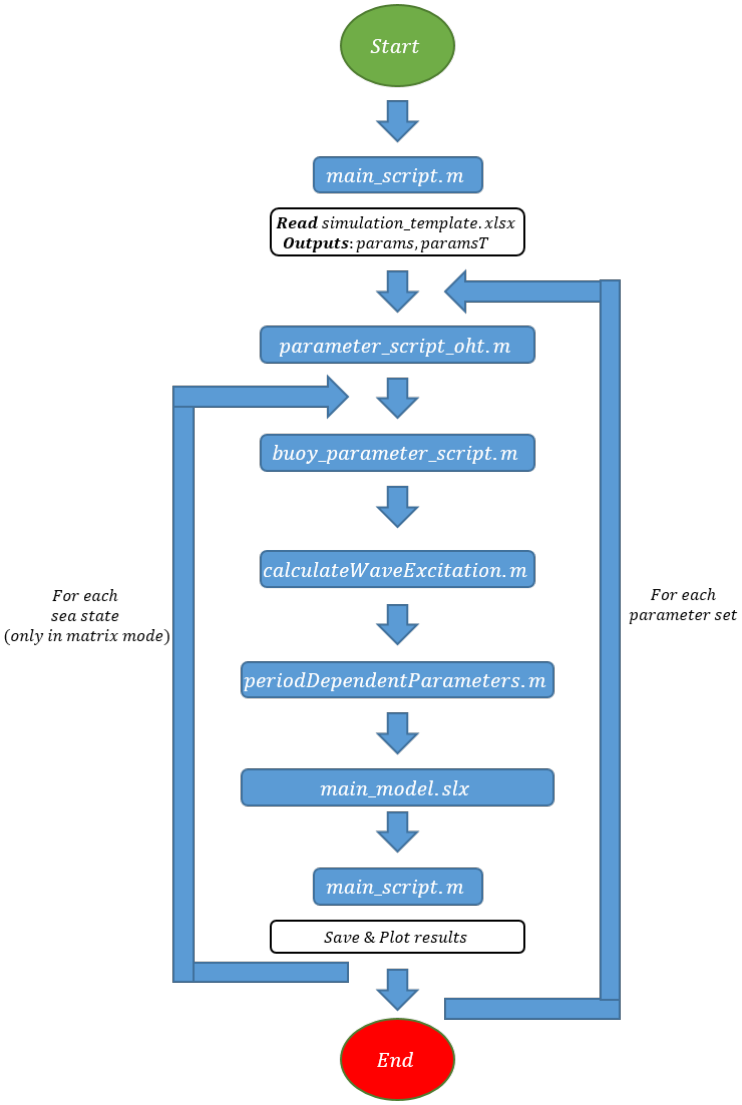

Figure 8.1: Program flow of the simulation framework.

The program starts by running the *main_script.m* file, which reads the list of simulation parameter sets and simulation settings from *simulation_template.xlsx* in the beginning. The program loops through each parameter set and assigns/updates the parameter values of the OHT's system in *parameter_script_oht.m* that are not sea state dependent. If matrix mode is on, the program loops in a nested for-loop through each sea state, characterized by significant wave height, H_s, and energy period, T_e. The simulation model *main_model.slx* is run for each parameter set and sea-state after assigning/updating buoy parameter values, generating wave elevation and wave excitation force timeseries, and assigning/updating the remaining OHT and buoy parameters and configurations, that depend on the wave energy period. At the end of each simulation, timeseries data and plots of the selected signals are saved. The statistical data of all signals from each sea state is stored in a data structure that is printed to the simulation summary file only when the whole set

is complete. This way the Excel write operation only has to be done once for a complete simulation set, which is very important for the performance due to the large number of data values.

8.2 Vectorised Simulink Modelling

Due to the large size and complexity of the wave energy array model, implementation of the Simulink model in vectorized fashion was identifies as the only viable option that will enable running simulations in reasonable time. Vectorization refers to performing operations to whole arrays at once instead of individual elements. Vectorization of a Simulink model has several advantages:

- Vectorized model runs often faster than a non-vectorized model;
- Vectorized model results in utilization of fewer blocks, which results in faster loading of the model and faster generation of executables in Accelerator and Rapid Accelerator modes;
- Vectorized model is also more visually appealing due to the fewer number of blocks and signal lines;
- Vecrorized model is less error prone and easier to troubleshoot due to the fewer number of blocks and signal lines;
- Vectorized model is often faster to implement.

The drawbacks of the vectorization of the Simulink model are:

- Not all Simulink blocks accept vector inputs. Examples of blocks that do not accept vector inputs are *if*- and *switch*-statements, *triggered* and *enabled* subsystems, *SR flip-flop*, etc. Therefore, the developer of a vectorized model need to find equivalent realizations of these non-vectorizable blocks vectorizable blocks.
- Vectorized model results in creation of multiple threads, and hence, in high utilization of all the available CPU cores. This might seem like an advantage, but it is not due to the fact that all the available computational power is utilized by only one instance of Matlab, thus, not allowing running multiple simulations in parallel. During the thesis, a solution to this problem was identified with the help of Mathwork's Support team. The Matlab instances were started with the *-singleCompThread* argument, that basically restricts the each Matlab instance to use a single computational thread.

Vectorization technique was applied througout the whole simulation model. Due to the insufficient time in the project, only CorPower's model has been able to be vectorized. Figure 8.2 shows a comparison between vectorized and a single CorPower buoy model. It can be visually validated that the vectorized model gives identical outputs.

The only part in the model, that is not vectorized is the pump controller model, which resides in a triggered *Matlab function* block. *For Each Subsystem* block was used to run the controller model. *For Each Subsystem* is a Simulink block that repeats execution on each element of a vector input signal and concatenates results.

Prints of the main parts of the Simulink model are shown in Appendix 2.

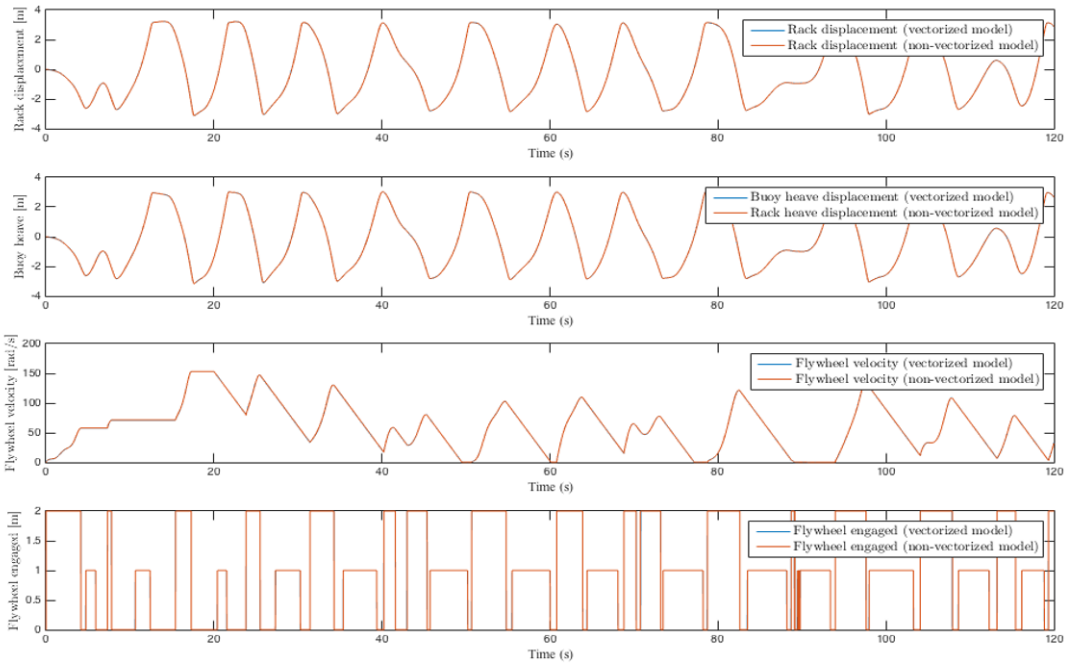

Figure 8.2: Comparison between vectorized and single CorPower model.

9

Constant Damping Force Control

In section 2.4 an MPC control was derived for a generic buoy using direct power maximization objective. This formulation assumed that the control input can change at each time instant. However, the hydraulic pumps can be engaged and disengaged only when their velocity is zero. This implies that the control input and/or damping force will remain constant until the next zero-crossing of the velocity. Moreover, due to the limited number of pumps and the constant pressure of the hydraulic system, the applied damping force can only take a set of discrete force levels, equal to the number of the pumps. In addition to that, the hydraulic rectifier bridge allows power to flow only from buoy to the hydraulic system and not vice versa. This implies that the torque/pressure of the pump can only dampen or oppose the motion of the buoy, and not drive or actuate it. Therefore, when the velocity of the buoy is zero, the buoy remains still until the total hydrodynamic force exceeds the damping force from the pumps. It was shown in Chapter 5 that a wave energy converter with rectifier bridge and pressure/force stiff load has two modes of operation, namely conducting and non-conducting. Therefore, due to all these listed nonlinearities and discrete events, the derived MPC controller in section 2.4, based on a linear wave energy converter model, cannot be applied. The controller model needs to correctly represent the actual dynamics of the system.

The logic of the predictive algorithm used to control the buoy motion to optimize power capture is outlined in Algorithm 2. The function $nmpcDiscreteForce()$ gets triggered by a zero-crossing of the buoy velocity, i.e. when condition

$$\dot{z}_b * \dot{z}_b^{prev} \leq 0 \tag{9.1}$$

is satisfied. Due to the limited number of force levels, the future state evolution is performed individually for each force level until the next zero-crossing or the end of the prediction horizon. Based on a chosen optimization criteria, the value of the cost function is evaluated for each force level and the PTO force, that gives the maximum objective value, is returned. The state evolution and cost valuation for each force level can be performed in parallel, making the execution of the the control algorithm very fast. The algorithm accounts for the non-conduction mode by penalizing the cost function for the time spent in this mode for each force level. It was found experimentally that by having a penalty term in the objective for the duration spent in non-conduction mode improves the performance. The objective function of the controller was initially chosen to be the maximization of the output power. The discrete version of the objective function is

$$V = \sum_{i=1}^{N} v(k+i)u(k+i), \tag{9.2}$$

Algorithm 2 Nonlinear Model Predictive Control of Wave Energy Converter with Constant PTO Damping

Require: $\dot{z}_b * \dot{z}_b^{prev} \leq 0$, n, T_s, T_z
  function NMPCDISCRETEFORCE(z_{b_0}, $F_{exc}(k:k+N)$)
    $p \leftarrow \mathbf{0}^{1\times n}$
    $n_{nc} \leftarrow \mathbf{0}^{1\times n}$
    for $i = 0 \rightarrow n$ **do**
      $z_b \leftarrow z_{b_0}$
      $\dot{z}_b^{prev} \leftarrow 0$
      $\dot{z}_b \leftarrow 0$
      $j \leftarrow 1$
      $overdamped \leftarrow 0$
      while $|F_{exc}(k+j) - k_h z_b| \leq F_{PTO}(i)$ **do**
        $j \leftarrow j + 1$
        if $j > \dfrac{T_z}{2T_s}$ **then**
          $overdamped \leftarrow 1$
          $n_{nc} \leftarrow j$
          break
        end if
      end while
      if $overdamped == 0$ **then**
        while $\dot{z}_b * \dot{z}_b^{prev} \geq 0$ **or** $j <= N$ **do**
          $\dot{z}_b^{prev} \geq \dot{z}_b$
          $(z_b, \dot{z}_b) \leftarrow stateUpdate(z_b, \dot{z}_b, F_{PTO}(i), F_{exc}(k+j)$
          $j \leftarrow j + 1$
          $p(j) \leftarrow p(j) + objectiveFunction(F_{PTO}(i), \dot{z}_b)$
        end while
      end if
    end for
    $n_{nc}^{max} \leftarrow max(n_{nc})$
    if $n_{nc} == 0$ **then**
      $penalty \leftarrow \mathbf{1}^{1\times n}$
    else
      $penalty \leftarrow \dfrac{n_{nc}^{max} - n_{nc}}{n_{nc}^{max}}$
    end if
    $(p^{opt}, n^{opt}) \leftarrow max(p. * penalty)$
    $F_{PTO}^{opt} \leftarrow F_{PTO}(n^{opt})$
    return F_{PTO}^{opt}
  end function

where N is the prediction horizon, v is the velocity of the buoy and u is the PTO force. However, it was found that maximization of the output power did not result in highest power yield throughput the whole simulation. It was even found that in some sea states this objective function gave worse performance than keeping one force level constant for the whole simulation duration, i.e. worse than not having a controller. Figure 9.1 shows a comparison of average power with constant force levels and discrete force control using the power maximization objective in sea state $H_s = 1.75m$, $T_e = 6.5s$. It can be seen that the controller is outperformed by just keeping the force constant both at 50kN and 100kN.

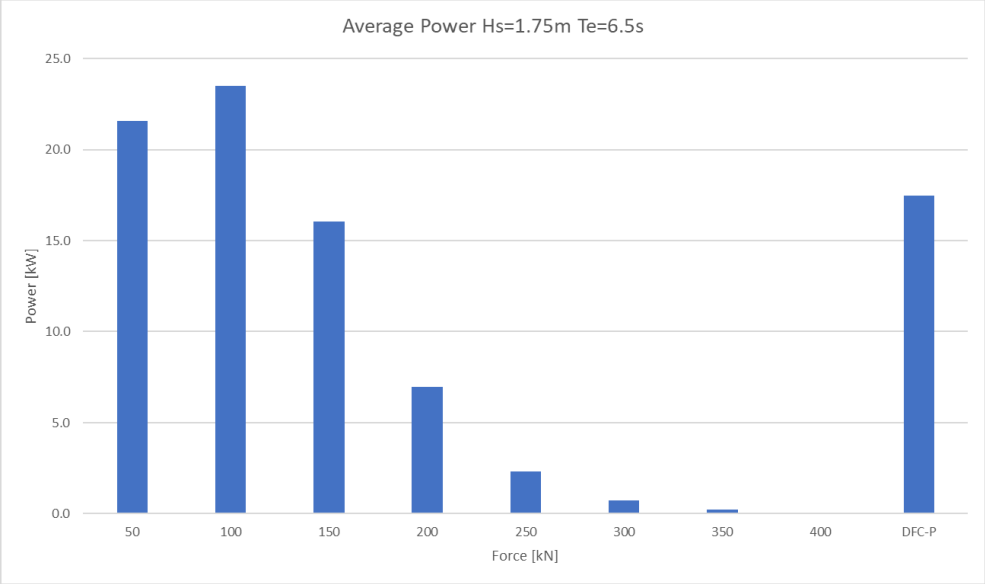

Figure 9.1: Average power comparison with constant force levels and discrete force control with power maximization objective in sea state $H_s = 1.75m$, $T_e = 6.5s$

The reason for the poor performance was that the controller picked up a higher force level than the optimal one in its attempt to maximize the output power during the next stroke. This caused over-dampening of the system, and thus not allow the buoy to develop momentum, which is necessary for better power capture. The controller applied the optimal damping force for the next stroke, but at the same time killed the potential to capture more power in the stroke after. Therefore, we can simply say that the controller with direct maximization of the output power resulted in a local optimum, but not a global one.

The performance of the buoy was improved by adding a term in the objective to maximize the kinetic energy of the system. The discrete version of the objective function is

$$V = \sum_{i=1}^{N} v(k+i)u(k+i) + \frac{1}{2}qv^2(k+i) \tag{9.3}$$

where q is a tuning factor for the kinetic energy term. The controller with this objective resulted in a better power yield than the one with the power maximization objective. Figure 9.2 shows a comparison of the average powers in different sea states with optimized sea-state tuned constant damping (CD), wave-by-wave tuned

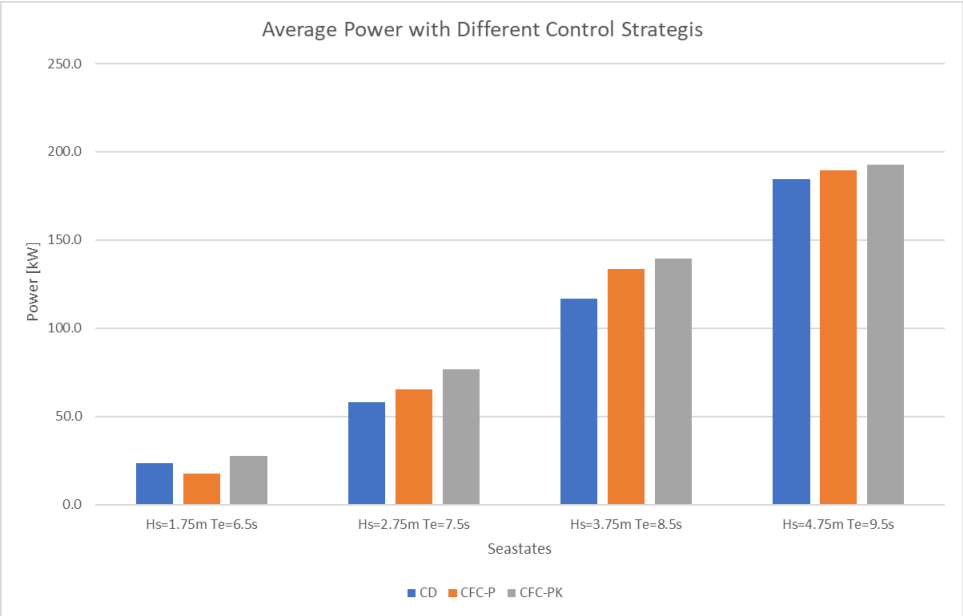

Figure 9.2: Average power comparison with sea-state tuned constant damping (CD), discrete force control with power maximization objective (DFC-P) and discrete force control with power capture and kinetic energy maximization (CFC-PK)

discrete force control with power capture maximization objective (DCF-P) and wave-by-wave tuned discrete force control with combined power capture and kinetic energy maximization objective (DCF-PK). It can be seen that DCF-PK outperforms both CD and DCF-P in all sea states. DCF-P results in higher power capture in all the sea-states, except in sea state $H_s = 1.75m$, $T_e = 6.5s$. The improvement in power capture between sea-state-tuned (CD) and wave-by-wave-tuned PTO force (DCF-PK) decreases in smaller and larger sea states. This is due to the fact that in smaller and larger sea-states the controller keeps for most of the time respectively the lowest (50kN) and highest (400kN) PTO force.

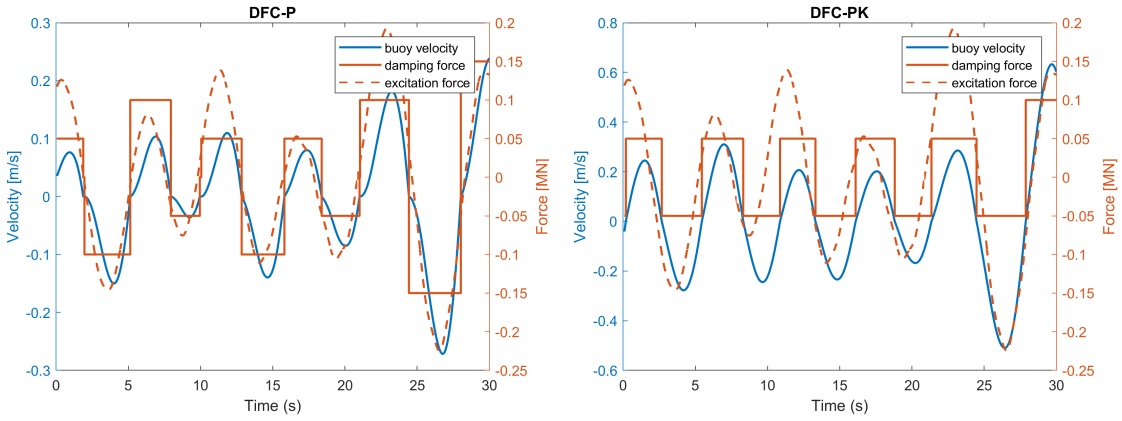

Figure 9.3: Comparison of buoy velocity and PTO force between DFC-P (left) and DFC-PK (right) in sea state $H_s = 1.75m$, $T_e = 6.5s$

Figure 9.3 shows the comparison of buoy velocity and PTO force between DFC-P and DCF-PK in sea state $H_s = 1.75m$, $T_e = 6.5s$. It can be seen that DCP-P results in motion with lower peak velocity compared to DCP-PK due to the higher PTO force picked-up with DCP-P. In addition, the velocity with DCP-P is discontinuous at the zero-crossing, indicating that the system enters non-conductive state. On the contrary, the velocity is continuous with DCP-PK, indicating that the system is in conductive state all the time. It can be also observed that the PTO force varies quite a lot with DCP-P, while it stays at one value (50 kN in this case) for most of the time.

10

Grid Frequency Control

For satisfactory operation of a power system, the frequency should remain nearly constant, 50Hz or 60Hz depending on the country. Frequency of the grid depends on the active power balance between generation and consumption. When the generation is higher than consumption, the frequency increases, and vice versa.

Different grid have different requirement for the allowable range for the grid frequency. For example, in the Australian system the allowable range for the grid frequency is 48.5-50.15, see [32]. For a different system, this range is different. Moreover, each grid offers different markets for frequency control ancillary services (FCAS) at any given time. According to [32], there are two types of frequency control services offered by the Australian Energy Market Operator: regulation and contingency. The former refers to the continuous correction of the generation-demand balance in response to a small deviations in consumption or generation and the later is the occasional correction of the generation-demand balance after a major contingency event such as the loss of a generating unit, a major industrial load, or a main component in the transmission. The regulation frequency control services are provided by generators on Automatic Generation Control (AGC). The AGC system allows AEMO to continually monitor the system frequency and to send control signals out to generators providing regulation in such a manner that the frequency is maintained within the normal operating band of 49.85Hz to 50.15Hz. More information about the different markets for frequency regulation, the payment policy for servicing these markets, etc. can be found in [32].

During this project a simple algorithm was implemented for grid frequency regulation in order to quantify the added value from time-shifting capabilities of the gravity storage. A strong grid is assumed, meaning that the 10MW wave energy plant cannot affect the grid frequency. The stateflow of the underlying logic is shown in figure 10.1. Input to the stateflow is the grid frequency and the state of charge (height) of the gravity weight. In the simulations, a real historic grid frequency data was used, that was taken from the databases of UK's National Grid. A sample frequency of the UK grid on 1st January 2015 is shown in figure 10.2. The output of the stateflow is the demanded power output, corresponding to certain generator speed, which is fed as a set point to the PID controller that regulates the generator offset to provide the requested output power. Note, that in the case without frequency regulation, set point to the controller was a set height for the gravity weight. The generator offset was saturated to provide constant power equal to the average of the collected power when the weight was above the set height, and the power was slowly decreased when the weight was below the set height.

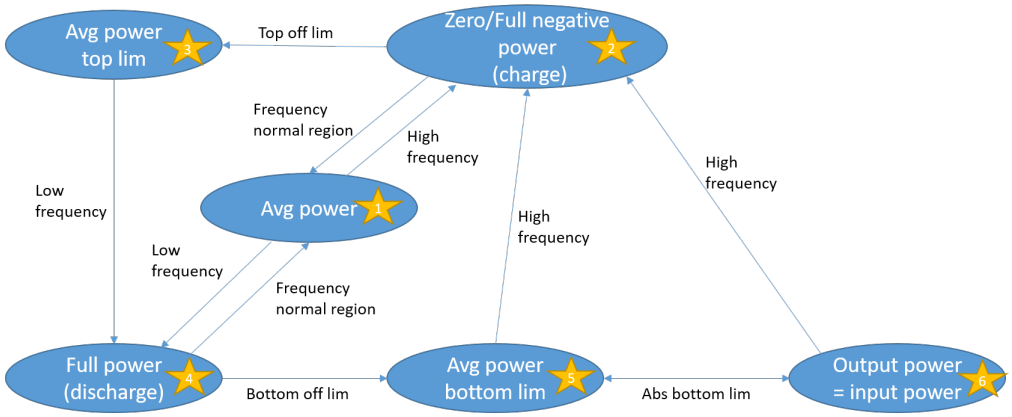

Figure 10.1: Stateflow of the underlying logic for grid frequency regulation.

With frequency regulation, the generators output the average power, captured in the simulated sea state, when the weight is within the bottom and top limits, and the frequency of the grid is within a normal operating region around 50Hz. This is marked as state number 1 in figure 10.1. At state 1, if the frequency of the grid

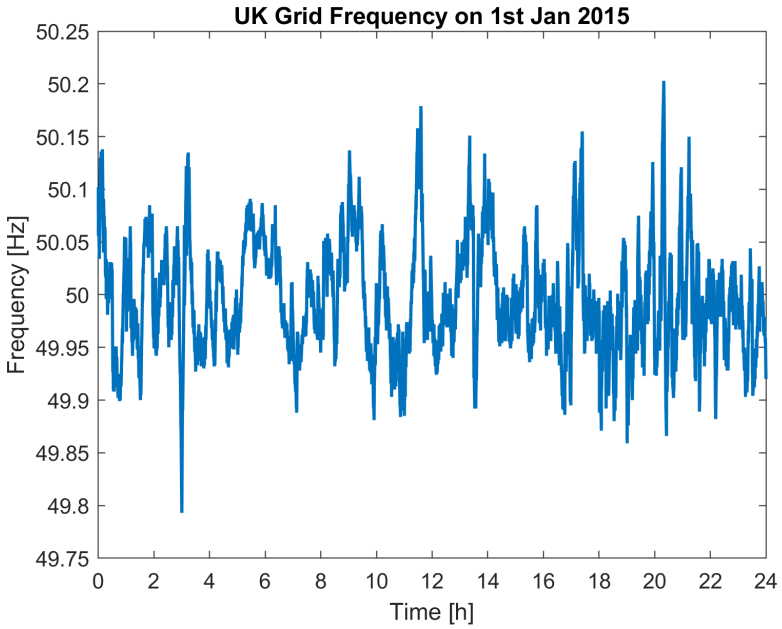

Figure 10.2: Measured grid frequency in UK on 1st January 2015.

increases above the upper limit of the normal operating region, the state changes to 2 and the generators are either stopped outputting any power if grid charging is not enabled, or input full power from the grid if grid charging is enabled. Since there is only input power to the storage, the height of the gravity weight increases. At state 1, if the grid frequency decreases below the lower limit of the normal operating region, the state changes to 4 and the generators are requested to output full rated power. At state 2 and 4, return of the grid frequency to the normal operating region, shifts the state back to 1. At state 2, if the grid frequency keeps above the normal

region and the weight reaches a predefined top limit (lower than the physical limit of the tower), the state changes to 3 and the generators are requested to output average power. At stage 3, if the input power is higher than the the average power and the grid frequency remains high, there is a chance that the weight will hit the top limit of the tower and excessive energy will be spilled through the pressure relief valve. The spill of power can be prevented by outputting higher power than the average power, but this will result in paying a penalty fee to the grid. At state 3, if the grid frequency goes below the normal region, the state will change to 4 and the generators will start outputting full power, that will cause discharge of the stored energy, if the input power is lower than the output power. At state 4, if the weight reaches a predefined bottom limit (higher than the physical limit of the tower), the state will change to 5 and the generators will start outputting average power. At state 5, if the input power to the array is lower than the output power, there is a chance that the weight will reach another predefined bottom limit, at which the weight is controlled to stay still, and hence, the output power will be equal to the input power (state 6). When this scenario happens, the plant needs to pay penalty fee to the grid for not delivering the promised average power. At state 5 and 6, the increase of the grid frequency above the normal region, causes the state to move to 2 and the output of the generators stop outputting any power or inputting full power from the grid.

The change of generator power/velocity from average to full/zero and vice versa causes acceleration and deceleration of the gravity weight, and thus increase and decrease of the load on the drive train. In order to limit the acceleration and deceleration of the weight, the sharp step changes of the velocity set point are replaced with a smooth transitional trajectory with a desired maximum acceleration.

The trajectories are generated using the spline method. A desired velocity trajectory at each time instant t is defined as a quadratic polynomial,

$$\dot{q}(t) = a_0 + a_1 t + a_2 t^2. \tag{10.1}$$

where a_0, a_1 and a_2 are polynomial coefficients.
The desired acceleration is found by differentiating (10.1) with respect to time t,

$$\ddot{q}(t) = a_1 + 2a_2 t. \tag{10.2}$$

Let us assign a trapezoidal profile to the desired acceleration with maximum acceleration a_{max}, as shown in figure 10.3. It can be seen from the figure that the total acceleration profile comprises of three regions: ramp-up, constant and ramp-down. In the figure, t_0, t_1 and t_2 denotes respectively the beginning of the ramp-up, constant and ramp-down acceleration regions, and t_f denotes the final time of the trajectory. Let us also assume that the trapezoid is symmetric, hence, $t_1 - t_0 = t_f - t_2 = \Delta t_{ramp}$ and $t_f - t_0 - 2\Delta t_{ramp} = \Delta t_{const}$. Our objective is to change the velocity of the generator from one level to another. Let us denote the starting velocity as $\dot{q}_0$ and the final velocity as $\dot{q}_f$. By evaluating 10.1 and 10.2 at t_0, t_1, t_2 and t_f, we can find the coefficients of the polynomial, and obtain a conditional expression for the desired

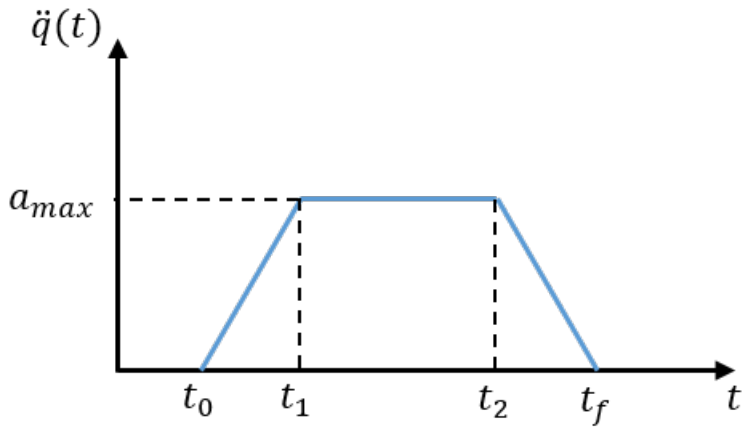

Figure 10.3: Trapezoidal acceleration profile.

velocity trajectory,

$$\dot{q} = \begin{cases} \dot{q}_0 + \dfrac{a_{max}}{2\Delta t_{ramp}}(t - t_0)^2, & \text{if } t_0 < t \leq t_1 \\ \dot{q}_1 + a_{max}(t - t_1), & \text{if } t_1 < t \leq t_2 \\ \dot{q}_2 + a_{max}(t - t_2) - \dfrac{a_{max}}{2\Delta t_{ramp}}(t - t_2)^2, & \text{if } t_2 < t \leq t_f, \end{cases} \tag{10.3}$$

where

$$\begin{aligned} \dot{q}_1 &= \dot{q}_0 + \frac{a_{max}}{2}\Delta t_{ramp} \\ \dot{q}_2 &= \dot{q}_1 + a_{max}\Delta t_{const} \end{aligned} \tag{10.4}$$

The requirement that the velocity at the final time instant, t_f, must be equal to the desired velocity, $\dot{q}_f$, i.e. $\dot{q}(t_f) = \dot{q}_f$, imposes the following constraint

$$\dot{q}_f = \dot{q}_2 + \frac{a_{max}}{2}\Delta t_{ramp} \tag{10.5}$$

Combining (10.4) and (10.5), we can find the ramp duration, Δt_{ramp}, as a function of the maximum acceleration, the difference between initial and final desired velocities, and the duration of the transition, $\Delta t_0^f = t_f - t_0$,

$$\Delta t_{ramp} = \Delta t_0^f - \frac{\dot{q}_f - \dot{q}_0}{a_{max}} \tag{10.6}$$

In the simulations, the duration of the transition from an initial velocity, $\dot{q}_0$, to a final velocity, $\dot{q}_f$, is calculated as a fraction of the duration of the transition from minimum velocity (0 speed, when no grid charging, and negative rated speed, when grid charging) to maximum velocity (rated speed), Δt_{min}^{max},

$$\Delta t_0^f = \frac{|\dot{q}_f - \dot{q}_0|}{\dot{q}_{min}^{max}}\Delta t_{min}^{max}. \tag{10.7}$$

For instance, if the transition from minimum to maximum velocity is chosen to be 5s, and the transition occurs from half the rated speed to full rated speed, the duration

of the transition will be 2.5s, when there is no gird charging. In the simulations, the maximum acceleration and deceleration is chosen to be constant irrespective of the difference in velocity at the end and beginning of the transition. This implies that, there will be constant torque increase/decrease during the transition region irrespective of the velocity difference at the end and beginning of the transition.

11
Simulation Results and Discussion

Wave scatters and environmental data for two selected sites have been used for this study, BillaCro at EMEC and WaveHub test sites. Due to the large number of simulations needed to calculate annual data for different control strategies and selected configurations, results are reported exclusively for the BillaCro site. Due to insufficient time in project and limited modelling information about Waves4Power buoys, the integration of OHT's Hub system is performed only with CorPower's buoys.

The initially 40-buoy array design was insufficient in delivering the 10-MW power output target in the design sea state. Therefore, the size of the array has been increased to 42 buoys. Moreover, during the project it was found that the initial fish-bone topology, comprising of steel pipes, was costly and impractical to implement in reality. Therefore, the hydraulic topology was replaced with one that comprises of 6 clusters with 7 WECs in each cluster, all connected with composite flexible pipes. Even though, this conclusion was drawn close to the end of the project, it was relatively quick to adapt the model to the new topology due to the automatic collection system model generator algorithm, developed during the thesis. However, this does not change the fact that most simulations were performed and results were produced using the fish-bone topology, that in practice turned out to be not so useful. Since the fish-bone topology does not represent a practical system, the presented results below are solely obtained using the cluster topology.

Due to confidentiality, parts with WEC-related results are removed for publication.

11.1 Parameter selection for the collection hub system

This section presents the chosen collection hub system parameters used in the simulation and the describes the motivation for this choice. Detailed presentation of the results from the simulations sweeps to size the components is omitted here.

Composite flexible pipes from Airborne have been selected to be used in the collection system. The pipes are grouped in two categories depending on their widths and/or whether they stem out from the buoy or tower. The parameters of the pipes for both groups are shown in table 11.1. The lump length of 40 meters is found to give sufficient model accuracy and good simulation speed. During the project, it was learned that the pressure of the hydraulic system affects greatly the life time of the hydraulic components. The initial design pressure was reduced greatly to increase

	Buoy	Tower
Number of pipes	7	6
Length [m]	120	360
Diameter [in]	3.5	7
Lump length [m]	40	40
Number of lumps	3	9
Roughness [mm]	5e-3	5e-3

Table 11.1: Parameter values of the flexible composite pipes

the life time of the hydraulic components. However, decreasing the pressure in the system, leads to an increase in the flow rate to transfer the same amount of power through the pipes, thus increasing the losses in the system. The static pressure difference around the hydraulic motors is dictated by the mass of the gravity weight, the total gear ratio from weight to hydraulic motors and the displacement of the hydraulic motors,

$$\Delta p_m = -\frac{R}{T_s \eta_m (1-R) N} m g r_p^{tower} \tag{11.1}$$

where T_s and η_m are respectively the displacement/specific torque and mechanical efficiency of hydraulic motor, R is the planetary gear ratio, r_p^{tower} is the radius of the pinions that lift the gravity weight, N is the number of drive train modules and m is the weight mass. The pressure of the high-pressure side of the collection system increases from tower to buoys (or decreases from buoys to tower), due to the fact that fluid flows from buoys to tower in the high-pressure side. On the contrary, the pressure of the low-pressure side of the collection system decreases from tower to buoys (or increase from buoys to tower), due to fact that fluid flows from tower to buoys in the low-pressure side. As a result the pressure difference in the collection system increases gradually towards the buoys (or decreases towards the tower). Therefore, one needs to account also for this variation of pressure difference when designing the pressure in the system. Hydraulic accumulators help in reducing the pressure fluctuations by smoothing the flow, which leads to a more even pressure drop across the collection system. The low-pressure accumulator needs to be designed to hold enough charge pressure, which is required by the hydraulic pumps and motors for normal operation. The high-pressure accumulator needs to be designed to keep the pressure above the pre-charge pressure in order to make the required damping force range available to the buoys at all time. Simulations sweeps were run to identify the required accumulator fluid and total volumes to accomplish the listed objectives. The chosen accumulator parameters are summarized in table 11.2. It can be seen that the low-pressure accumulator requires a larger fluid volume than the high-pressure one in order to maintain the pressure above its pre-charge pressure. Table 11.3 shows the minimum, maximum and average pressures, obtained by simulating all sea states in the Billia Cro site: minimum and maximum values are respectively the minimum and maximum value in all sea states, and the average value is the average pressure at the design sea state, $H_s = 4.75m$ and $T_e = 9.5s$. It can be noted that the pressure fluctuations at the high-pressure tower side are lower than

	High	Low	Unit
p_{pre}	150	15	[bar]
V_{total}	250	300	[lit]
ΔV_{fluid}	75	160	[lit]

Table 11.2: Parameter values of the hydraulic accumulators.

	Buoy		Tower		
	High	Low	High	Low	Unit
p_{min}	172	15	188	14	[bar]
p_{max}	301	52	255	85	[bar]
p_{avg}^{design}	218	33	214	41	[bar]

Table 11.3: Pressures in the collection system.

the high-pressure buoy side. This is due to the fact that the flow rate gets smoother at the tower side from the addition of flows from all buoys and the filtering effect of the collection system itself. It can be observed that the maximum pressure at the low-pressure tower side is high (85 bar). The reason for this is the pressure relief valve, which creates a short circuit from high- to low- pressure side in its attempt to spill excessive energy when the gravity weight hits its top bumper. Therefore, a flow with high rate flows from the high- to the low-pressure side, that results in a pressure increase at the low-pressure side. By comparing the minimum pressure at the buoy low-pressure side and the pre-charge pressure of the low-pressure accumulators, it can be seen that there is no margin between them. This is an indication that the low-pressure accumulators need to be sized up in order to prevent losing charge pressure for pumps and motors. Sizing up the accumulators will also decrease the average pressure of the low-pressure side, which is much higher than the required charge pressure of the pumps and motors, approx. 12 bar. Lower pressure of the low-pressure side will result in a lower pressure of the high-pressure side, that would extend the life time of the hydraulic pumps and motors significantly. Due to changing the topology at the end of the project, higher accumulator volumes could not be tested. Simulation sweeps were run to determine the number and interval of the discrete force levels and it was found that eight force levels with an interval of 50 kN gives good compromise between performance and cost. The design of pinions (buoy rack) and the choice of the pumps are made to achieve the force range with 50 kN force interval for a given static pressure difference in the collection system without exceeding the ratings of the chosen pumps. Pinion radius of $r_p^{buoy} = 0.172m$ and CA50 model pumps from Hägglunds are chosen for the PTO drive train. The main characteristics of the chosen hydraulic pumps is shown in table 11.4.

The tower drive train is designed to handle the power input from the array and the load from the gravity weight. The gear ratio of the planetary gearboxes in the drive train is selected to give the best load-to-weight ratio, which generally is achieved when the gear ratio is anywhere between 4 and 6. Therefore, a gear ratio of 6,

	CA50	CBP140-100	Unit
Displacement	3140	6280	[cm^3/rev]
Specific torque	50	100	[Nm/bar]
Rated speed	200	270	[rpm]
Max speed	280	390	[rpm]
Max pressure	350	350	[bar]
Mechanical efficiency	97	98	[%]

Table 11.4: Characteristics of the chosen hydraulic pumps and motors.

i.e. $R = -6$, is chosen for OHT's tower drive train. The type of hydraulic motor is chosen to match the 1500 rpm rating of the generators. Therefore, CBP140-100 model motor from Hägglund (now Bosch Rexroth), that has a rated speed of 270 rpm, is selected. The main characteristics of the chosen hydraulic pumps is shown in table 11.4. In order to handle the input power from the array, it was found that 30 CBP-140-100 motors, hence drive units, were required. The pinion (tower rack) radii are chosen to give a desired static pressure difference in the hydraulic system. The static pressure is designed to be 175 bar in order to have around 200 bar average pressure in the high-pressure side. Therefore, the required pinion radius can be found using equation (11.1) for given mass of the gravity weight. For a weight with mass 500 ton, that, in combination with 70m-stroke, was found to be sufficient for power smoothing, the pinion radius is $r_p^{tower} = 0.122m$. During the thesis, simulation sweeps were run with different storage capacity of the gravity storage, i.e. with different mass and stoke. The pinion radius was adjusted according to expression (11.1), in order to maintain the desired static pressure difference in the hydraulic system.

11.2 Power capture and wave-to-wire efficiency benchmarking

This section presents a comparison of the performance with electric and hydraulic collection system.

For the case with electric collection of power, CorPower uses their own control that selects an optimal control force at each zero-crossing of the rack velocity to maximize power capture. The cascade gearbox alternates between two sets of one-way flywheels and generators, depending on the direction of the buoy. In this configuration one set is engaged with the rack at a time, and the other one is gradually slowed down by the damping of the generator. Therefore, an overlap between the powers thorough both generators occurs, that leads to a smoothing of the output power from the wave energy converter. CorPower has also provided an efficiency map of the generator-converter pair. For the collection system, constant efficiency of 93% was suggested from CorPower.

For the case with hydraulic collection power, the model predictive control, developed during this project, was used. The objective of the controller was to optimize the

damping force in discrete steps, represented by the number of engaged pumps, for each up and down stroke of the wave. A complete dynamic model of the hydraulic collection and the drive train inside the tower was developed. The initial fish-bone topology included both major an minor head losses in the piping system. Due to the change to the cluster topology at the very end of the project, only the major head losses were accounted for in the model. The minor losses are considered to be much smaller relative to the major ones due to the longer length and reduced width of the pipes with the cluster topology. The hydraulic pumps and motors were modelled with loss curves of the real components, extracted from the datasheets, provided by the manufacturer. The loss per each gear stage in the buoy and tower drive train was assumed to be 2% of the transferred torque. The viscous friction coefficient on all shafts is

$$b_{viscous} = \frac{0.2}{100} \frac{\tau^{rated}}{\omega^{rated}} \tag{11.2}$$

The expression in (11.2) can be interpreted as 0.2% loss of the rated torque/power when the shaft is rotating with rated speed. The efficiency mapping data for the OHT's generators and inverters selected in the project was never received from the supplier. Therefore, the efficiency map of CorPower's generator-converter pair was scaled up to the rated power of OHT's generator-converter pair and used to calculate the losses, associated with converting mechanical to electrical energy.

The same buoy design has been used when comparing the CorPower WEC with electric system to a WEC adapted for hydraulic collection of power.

The presentation of the actual numbers of the benchmarking is omitted due to confidentiality. However, we can conclude that electrical collection resulted in higher output power at the collection point despite the lower power capture from the buoys because of the higher overall efficiency of the electrical system.

11.3 Results in the design sea state

This section presents some of the plots produced during the simulation study. Again due to confidentiality the results with CPO buoys and electrical collection are removed for publishing.

Figure 11.1 shows 30-minute plots of different signals, produced with the simulation model with 42 CPO WECs and hydraulic collection and central tower with 70-meter height and 500-ton gravity storage weight. Figure 11.2 shows the plots of the same signals for the same configuration as figure 11.2 but with a unlimited height limit. All simulations are performed with the same wave profile, which has been generated in the design sea state, $H_s = 4.75m$, $T_e = 9.5s$. The plots for damping force and powers before and after hydraulic accumulators is omitted in figure 11.2 since the impact of the dynamics at the tower-side are assumed to be minimal on the buoy-side. By looking at the first plot of figure 11.1, we can see that the damping force to the rack is varying due to the controller action. By looking at the first plot of figure 11.1, it can be observed that the peak output power from all pumps in one

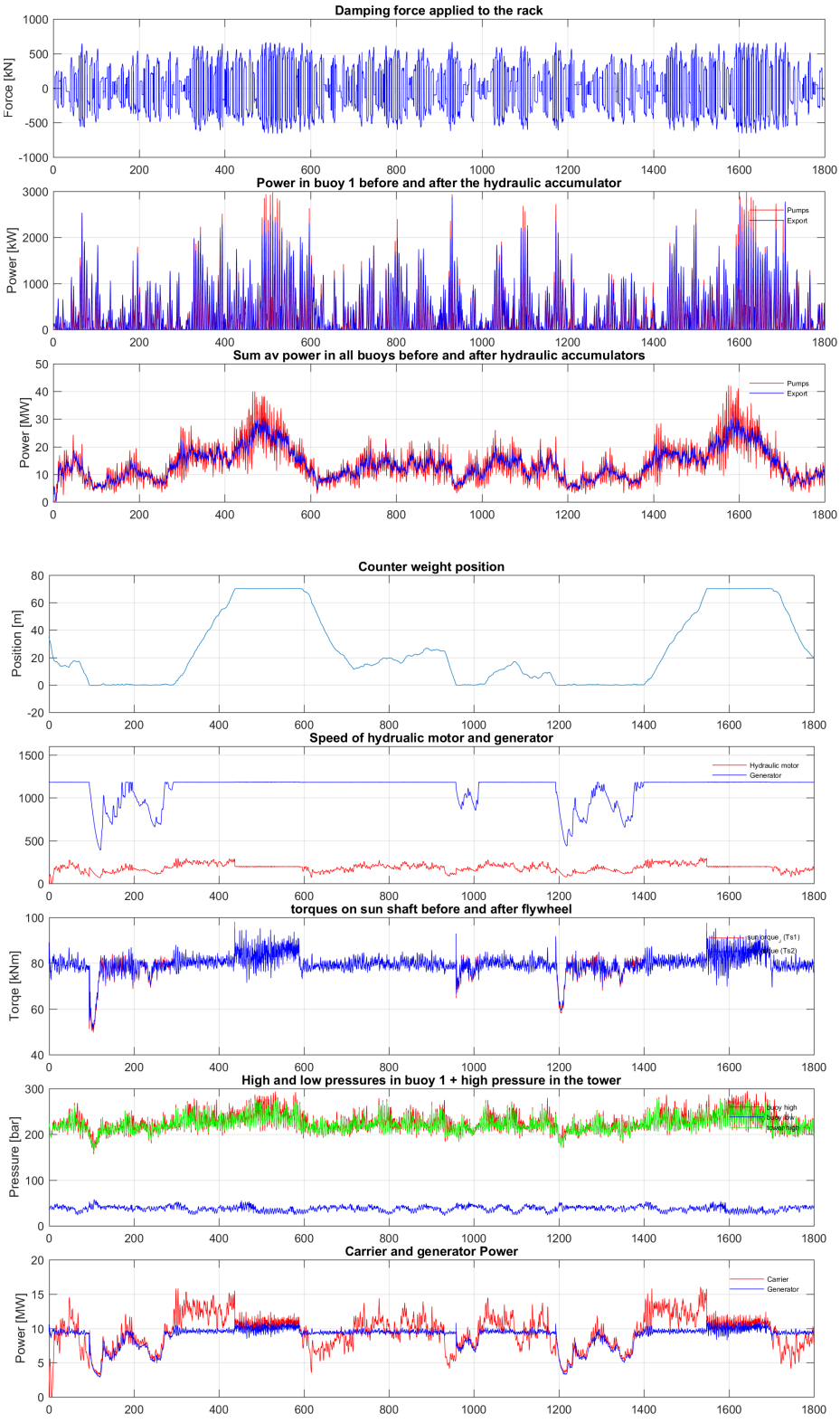

Figure 11.1: Simulation plots with 42 WECs and hydraulic collection with central tower with 70-meter height and 500-ton counterweight.

buoy is 3MW, and there is only insignificant reduction of the peak power due to the

small size of the accumulators. The third plot of the same figure shows the combined power from all buoys before and after the hydraulic accumulators. Note that these power curves are obtained by directly summing the powers from all buoys at the selected nodes, hence, they do not represent realistic signals. However, the curves illustrate the magnitude and variance of the input power to the array. It can be observed that the sum of powers from all buoys before the hydraulic accumulators varies between approx. 5MW and 40MW. The hydraulic accumulators decrease the peak power to 35MW and reduce the high-frequency variations of the power.

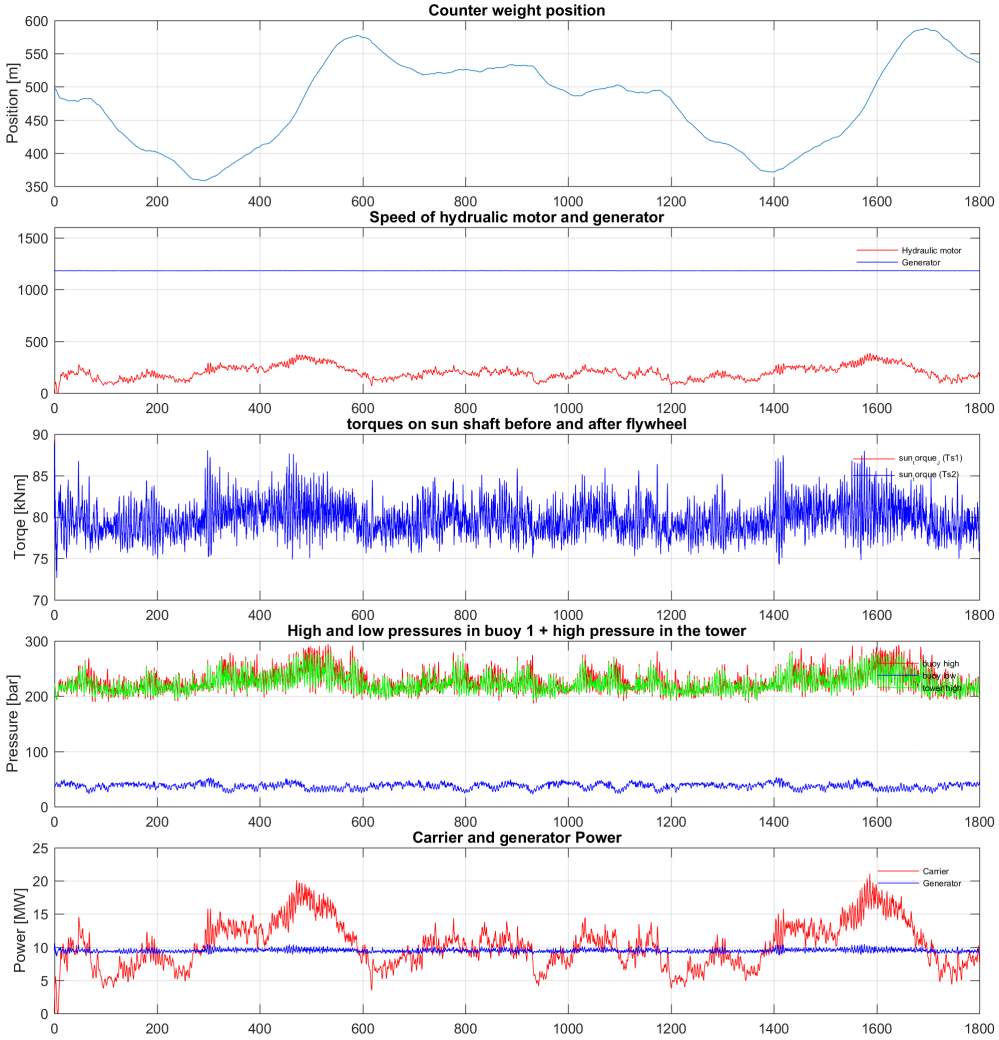

Figure 11.2: Simulation plots with 42 WECs and hydraulic collection with central tower with unlimited height and 500-ton counterweight.

In order to quantify the variation of the combined power from all buoys at the collection point, we need to look at the motor/carrier power of the unconstrained system, i.e. the one in which the spill valve never gets activated. This is the red curve in the fifth plot of figure 11.2. It can be observed that the combined power from all 42 WEC's varies between approx. 5MW and 20 MW (excluding the initialization phase) at the collection point. In the case of hydraulic collection, the output power is limited to 10 MW while the gravity storage in the tower intermediately stores

excess power above this limit, which is then used to maintain power when the input power is below 10 MW. By looking at the same plot of the constrained system, i.e. the 6th plot of figure 11.1, It can be seen that the spill function limits the peak input power to the tower to approx. 15MW.

By comparing the generator power curves of the constrained and unconstrained system, we can see that the maximum power is effectively limited to 10MW and there are no dips in output power with the unconstrained system, whereas, with the constrained system, the output power increases to approx 12MW due to the increased torque from hitting the end stop buffer and the output power experiences occasional power dips due to the lower input power and insufficient storage capacity of the gravity weight.

11.4 Added value from gravity storage, time shifting and grid charging

The reference configuration for the project is a 500-ton counterweight with 70-meter available lift height is corresponding to 35 seconds full discharge time. This storage capacity is sufficient to smooth the captured power from a 10 MW array to a constant electric power output at a level that corresponds to the average captured power in the given sea state. The main benefit from this is that the complete electric system can be down rated to 10 MW, resulting in an increased utilization factor for the electrical portion of the system. The power production can also be predicted for the next day instead of varying with the incoming waves. This way penalties from over or under producing relative to contracted energy volumes / power levels can be avoided.

The mechanisms in the current electricity market are designed for a system where the power production can be planned ahead and only the demand changes. The future energy market, with an increasing share of renewable energy, faces major challenges to provide security of supply. This will require new market mechanisms, including incentives for power producers to control the output power in a way that helps stabilizing the grid. It is not clear how the future energy market will function, but one example on needed mechanisms can be found in an analysis of the market in the Netherlands, see [30]. In short, power producers will trade with different markets defined as day-ahead, six-hour ahead and real time. Different price mechanisms are used for the ahead markets with penalties/bonuses for not delivering energy according to contract depending on the grid frequency. And a real market directed to energy storage services where power can be bought at low price when grid frequency is high and sold at a high price when grid frequency is low.

To illustrate how OHT's gravity storage device can play an important role in a future energy markets, a time shifting control strategy that reacts on the grid frequency have been tested in a simulation model, with different capacities of the accumulator according to the table in figure 11.3. In this simulation, the grid frequency from the national grid in UK was used. When the frequency is > 50.01 Hz, power output is halted until the accumulator is fully charged, after which average power is resumed.

When frequency is < 49.99 Hz, power output is increased to 10 MW until accumulator is fully discharged after which average power is resumed. Sufficient margins are set to ensure there always is enough storage capacity to provide the average power output for the day ahead market.

Gravity storage summary						
Max charge power	20 000	20 000	20 000	20 000	20 000	kW
Max electric charge/discharge power	10 000	10 000	10 000	10 000	10 000	kW
Mass in gravity storage	500	1 000	2 500	5 000	7 500	ton
Lift height for the weight	122	122	122	122	122	meter
Energy storage capacity	0,17	0,33	0,83	1,67	2,50	MWh
Full output disscharge time @ 0% load	1,00	2,00	5,0	10,0	15,0	minutes
Full output disscharge time @ 25% load	1,33	2,67	6,7	13,3	20,0	minutes
Full output disscharge time @ 50% load	2,00	4,00	10,0	20,0	30,0	minutes
Full output disscharge time @ 75% load	4,00	8,00	20,0	40,0	60,0	minutes
charge power @ 0% load	10 000	10 000	10 000	10 000	10 000	kW
charge power @ 25% load	15 000	15 000	15 000	15 000	15 000	kW
charge power @ 50% load	20 000	20 000	20 000	20 000	20 000	kW
charge power @ 75% load	20 000	20 000	20 000	20 000	20 000	kW
Min charge time @ 0% load	1,00	2,00	5,0	10,0	15,0	minutes
Min charge time @ 25% load	0,67	1,33	3,3	6,7	10,0	minutes
Min charge time @ 50% load	0,50	1,00	2,5	5,0	7,5	minutes
Min charge time @ 75% load	0,50	1,00	2,5	5,0	7,5	minutes
max rack velocity	4,08	2,04	0,82	0,41	0,27	m/s
min rack velocity	-2,04	-1,02	-0,41	-0,20	-0,14	m/s

Figure 11.3: Gravity storage configurations.

Energy volumes are calculated and valued for different categories shown in the table in figure 11.4, representing energy sold to the day-ahead market (spot market) and to the real-time market. Virtual volumes are calculated and valued also for day ahead market hold, which gives an incentive to power producers with revenues to hold/reduce the power production when there is low demand for power (grid frequency is > 50.01 Hz). Day-ahead market penalty is a fine for power producers that did not maintain the contracted energy volume during a period of high demand (grid frequency < 49.99 Hz). For the OHT case, this represents a fully discharged accumulator where power output to the grid has to follow the power input from the array. Finally, there is a volume of energy that is purchased from the grid to reduce the charge time of the accumulator, which shows a great increase in the energy that can be sold to the real-time market as shown in the table in figure 11.6. For all

Energy Volume Category	EUR/MWh
day ahead market sell	150
day ahead market hold	50
day ahead market penalty	-300
Real time market sell	250
Real time market buy	-50

Figure 11.4: Pricing categories and reference volume and revenues to the spot market.

Produced volume [MWh]	500 ton	1000 ton	2500 ton	5000 ton	7500 ton
real time market sell	1 207	2 725	5 193	6 611	7 071
day ahead market sell	27 889	26 516	23 606	21 851	21 377
	29 095	29 242	28 800	28 462	28 448
Virtual volumes [MWh]					
day ahead market hold	1 074	2 495	5 406	7 214	7 699
day ahead market penalty	209	160	160	107	96
	1 283	2 655	5 566	7 320	7 794
Revenues [KEUR]					
day ahead market sell	4 183	3 977	3 541	3 278	3 207
real time market sell	302	681	1 298	1 653	1 768
day ahead market hold	54	125	270	361	385
day ahead market penalty	-63	-48	-48	-32	-29
total revenue	4 476	4 735	5 062	5 259	5 331
Increase	2,9%	8,9%	16,4%	20,9%	22,5%

Figure 11.5: Revenues from time shifting without grid charging.

categories a price has been assumed with reference to Lazard, [31], and reliability options analysis, [30]. The energy volumes are calculated based on the predicted average power output from the array for each sea state.

Produced volume [MWh]	500 ton	1000 ton	2500 ton	5000 ton	7500 ton
real time market sell	1 553	3 997	8 620	13 336	16 433
day ahead market sell	28 518	28 084	27 088	26 257	25 678
	30 070	32 082	35 708	39 593	42 111
Virtual volumes [MWh]					
day ahead market hold	388	916	1 997	2 882	3 479
day ahead market penalty	266	171	87	33	15
real time market buy	1 009	2 921	7 003	11 176	14 359
	1 663	4 008	9 087	14 091	17 853
Revenues [KEUR]					
day ahead market sell	4 278	4 213	4 063	3 938	3 852
real time market sell	388	999	2 155	3 334	4 108
day ahead market hold	19	46	100	144	174
day ahead market penalty	-80	-51	-26	-10	-4
Real time market buy	-50	-146	-350	-559	-718
total revenue	4 555	5 060	5 942	6 848	7 412
increase	4,7%	16,3%	36,6%	57,4%	70,4%

Figure 11.6: Revenues from time shifting with grid charging.

Increasing the storage capacity to 7 500 ton increases the revenues by 22% when only time shifting is used as shown by the table in figure 11.5, and with 70% when time shifting is combined with grid charging as shown by the table in figure 11.6. The large increase in revenues from grid charging is due to the increased utilization of the plant when the power capture from the array is low. The total volume of sold energy increases from 29GWh to 42GWh, which corresponds to 50% capacity factor for the 10 MW installation.

It should be noted that the day-ahead market sell price of 150 EUR/MWh suggested in this simulation, is selected as the short term pricing for the 10 MW installation. The long term cost reduction target for marine energy is to reduce the LCoE to

60 EUR/MWh. The real-time market sell price is on the contrary predicted to rise in the future according to Lazard. The value from the real-time services that can be provided with the OHT gravity storage technology is expected to increase significantly in the future energy market. At 60 EUR/MWh the revenues from the power plant would be tripled with the 7500 ton storage from time shift and grid charging, with the pricing model used in the simulation.

11.5 Life time calculations for pumps and motors

The life time of pumps and motors has been calculated according to annual load data as presented respectively in tables 11.7 and 11.8. The load data is basically a histogram with 10 bins, where the entries in each bin (row of tables) are the average values of the listed variables. This data has been used as input in a life time calculation tool used by Bosch Rexroth. Histogram of the occurrence of a set of load conditions is most commonly used measure by manufacturers to calculate the life time of a certain component, which is not limited to only hydraulic pumps and motors.

Pump CA50, 4 ports

Bin nr	Torque [kNm]	High pressure [bar]	Low pressure [bar]	Speed [rpm]	Time [h]	%
1	0,7	0	0	0	0	0,0%
2	2,2	0	0	0	0	0,0%
3	3,6	0	0	0	0	0,0%
4	5,0	0	0	0	0	0,0%
5	6,5	200	40	20	49	1,6%
6	7,9	215	34	26	2393	75,8%
7	9,4	218	31	55	533	16,9%
8	10,8	236	27	94	142	4,5%
9	12,2	250	23	139	36	1,1%
10	13,7	272	21	187	4	0,1%
					3156,7	100,0%

Figure 11.7: Load data for the pumps in the buoy.

Motor CBP140-100, 8 ports

Bin nr	Torque [kNm]	High pressure [bar]	Low pressure [bar]	Speed [rpm]	Time [h]	%
1	1,3	0	0	0	0	0,0%
2	3,9	0	0	0	0	0,0%
3	6,6	0	0	0	0	0,0%
4	9,2	0	0	0	0	0,0%
5	11,8	181	52	91	5	0,1%
6	14,4	208	43	58	3275	38,5%
7	17,1	210	42	76	5223	61,4%
8	19,7	236	36	97	7	0,1%
9	22,3	257	15	1	1	0,0%
10	24,9	265	9	1	1	0,0%
					8511,9	100,0%

Figure 11.8: Load data for the motors in the collection tower.

In the WEC the load data has been calculated for pump number 1 in the WEC, which is always engaged in the simulation. The hours of occurrence for each bin is multiplied by the average number of pumps engaged, divided by the total number of pumps engaged. This gives the average operating time of each pump, under the assumption that the control system will distribute the hours evenly between all units. In the tower all motors are engaged all the time. Comparing the total number of hours in operation of a pump and a motor, it can be seen that each pump runs for approx. 1/3 of the time that a motor operates.

Figures 11.9 and 11.10 show the output from the L10 life[1] time calculation tool of Bosch Rexroth respectively for CA50 and CBP140-100. As can be seen, the L10

PERFORMANCE DATA HYDRAULIC PUMP

Overall efficiency 0,96
Modified rating life L10mh > 100000 h valid for motors with coated pistons
Required flushing 12 lpm

Load case		1	2	3	4	5	6	7	8	9	10
Input torque	[Nm]	700	2200	3600	5000	6500	7900	9400	10800	12200	13700
Input power	[kW]	0,1	0,2	0,4	0,5	12,9	21,5	54,1	106,3	177,6	268,3
Speed	[rpm]	1	1	1	1	19	26	55	94	139	187
Relative time	[-]	1	1	1	1	2	76	17	5	1	1
High pressure	[bar]	23	50,6	76,4	102,2	139,7	167,2	196,1	222,3	247,3	273
Charge pressure	[bar]	12	12	12	12	12	12	12	12	12	12
Flow rate	[lpm]	3	3	3	3	58	80	168	287	423	567
External leakage	[lpm]	0	0	0	0	1	1	1	1	2	3
Required flushing	[lpm]	0	0	0	0	0	0	0	4	8	12
Volumetric eff.	[-]	0,91	0,93	0,91	0,90	0,98	0,98	0,98	0,98	0,97	0,97
Hydromech. eff.	[-]	0,79	0,88	0,89	0,90	0,98	0,98	0,98	0,97	0,96	0,95
Overall eff.	[-]	0,71	0,81	0,82	0,81	0,96	0,96	0,96	0,95	0,94	0,93
Mod rating life L10mh	[h]	> 100000	> 100000	> 100000	> 100000	> 100000	> 100000	> 100000	47000	20000	9600

Figure 11.9: Life time calculation for the CA50 pumps in the buoys by Bosch Rexroth

PERFORMANCE DATA HYDRAULIC MOTOR

Overall efficiency 0,95
Modified rating life L10mh > 100000 h valid for motors with coated pistons
Required flushing 11 lpm

Load case		1	2	3	4	5	6	7	8	9	10
Output torque	[Nm]	1300	3900	6600	9200	11800	14400	17100	19700	22300	24900
Output power	[kW]	0,1	0,4	0,7	1	112,4	87,5	136,6	199,5	2,3	2,6
Speed	[rpm]	1	1	1	1	91	58	76,3	96,7	1	1
Relative time	[-]	1	1	1	1	1	34	58	1	1	1
High pressure	[bar]	46	75,3	105,7	135	147,6	173	200,9	228,1	282,7	312
Charge pressure	[bar]	25	25	25	25	25,9	25,4	25,6	26	25	25
Flow rate	[lpm]	7	7	7	7	581	372	490	622	8	9
External leakage	[lpm]	1	1	1	1	3	3	4	5	2	3
Required flushing	[lpm]	0	0	0	0	0	0	7	11	0	0
Volumetric eff.	[-]	0,82	0,84	0,83	0,81	0,98	0,98	0,97	0,97	0,72	0,70
Hydromech. eff.	[-]	0,62	0,78	0,82	0,84	0,97	0,98	0,98	0,97	0,87	0,87
Overall eff.	[-]	0,51	0,65	0,68	0,68	0,95	0,95	0,95	0,95	0,62	0,61
Mod rating life L10mh	[h]	> 100000	> 100000	> 100000	> 100000	> 100000	> 100000	89000	41000	14000	9200

Figure 11.10: Life time calculation for the CBP140-100 motors in the tower by Bosch Rexroth.

life time is > 100 000 hours for both pumps and motors. The total operating hours in the 25 year life time of the installation is 78 900 hours for the pumps and 213 000 hours for the motors.

[1]L10 life is a statistical measure that shows the number of hours that 10% of set of identical components will have failed.

The result means that $< 10\%$ of the pump units will have to be taken out of operation or removed for a major overhaul in the 25 year life time of the array. As the buoy can still operate with a reduced number of operational pumps, no replacement of pump units are expected during the life time of the array. There will still be need for normal maintenance and inspection to check/replace oil filters etc.

The result for the motors means that $< 20\%$ of the motors in the tower will need a major overhaul in the life time of the array. Drive units can be taken out of operation for a limited time. The system is still operational with increased load on the remaining drive units and increased pressure in the collection system, but will reduce the life time of the system components.

The high pressure on pumps and motors are higher in the simulations that they will be in reality. The 20-bar minimum charge pressure was assumed based on catalogue data but this was conservative and 12 bar is sufficient according to Bosch Rexroth. Also, feed pumps in the buoys are recommended by Bosch Rexroth to boost the pressure at high pump speeds so that even lower pressures can be accepted in the low pressure accumulator. Approx. 15-20 bar reduction on the low pressure should be possible, which would extend the life time of the motors significantly.

12

Development of HIL Simulation Environment

During the project, OHT has built a new test rig, reusing some components from a previous design. The electrical cabinet and control system hardware have been reused as well as the main components in the drive train, i.e. electric generator, planetary gearbox, winch drum and sensors. A new hydraulic system has been installed in the rig to input the hydraulic flow to a hydraulic motor in the drive train. The hydraulic circuit incorporates over-pressure relief valves to spill power when the accumulator weight is fully charged, i.e. when the weight press against the top end stop buffers. The complete hydraulic system has been built on a separate frame by PMC hydraulics, placed under the main drive unit as shown on picture 12.4.

The new drive unit is built into an aluminum profile frame and held in a steady position. New machine interfaces have been designed and procured to mount the components in the new frame. The drive unit in the test rig represents the main functionality and assembly of one drive unit in the collection tower. A drum and wire is still used for the counterweight instead of a gear rack. To get more height for the weight in the new location (with lower height available), the wire to the weight goes up and around two sheaves. A new counterweight has been designed with integrated guide wheels and end stop buffers are used to limit the stroke length. When the weight pushes against the top buffers, the pressure increases in the hydraulic circuit and the over-pressure relief valve is triggered to spill fluid to the low pressure side. To deal with the highly variable input flow to the motor in the drive unit, a hydraulic accumulator is charged by a hydraulic power pack (hydraulic pump driven by an electric motor) and a proportional valve (flow regulator) is used to output the requested flow, which is determined by a simulation model of one or more WEC´s connected with pressure feedback from the rig, i.e. in a hardware-in-the-loop simulation.

A hardware-in-the-loop simulation environment has been set up to validate the developed models during the Project - the gravity storage and central conversion to electricity of power from simulated buoys from CorPower, and to demonstrate the working principle of the OHT's collection system. The control and data acquisition system from the previous test rig was updated to provide the control signals to the new actuators (for example, to the proportional valves) and to acquire the data signals from the new sensors (for example, from the flow and pressure sensors). The previous test rig could run only as a forced response, meaning that there was no

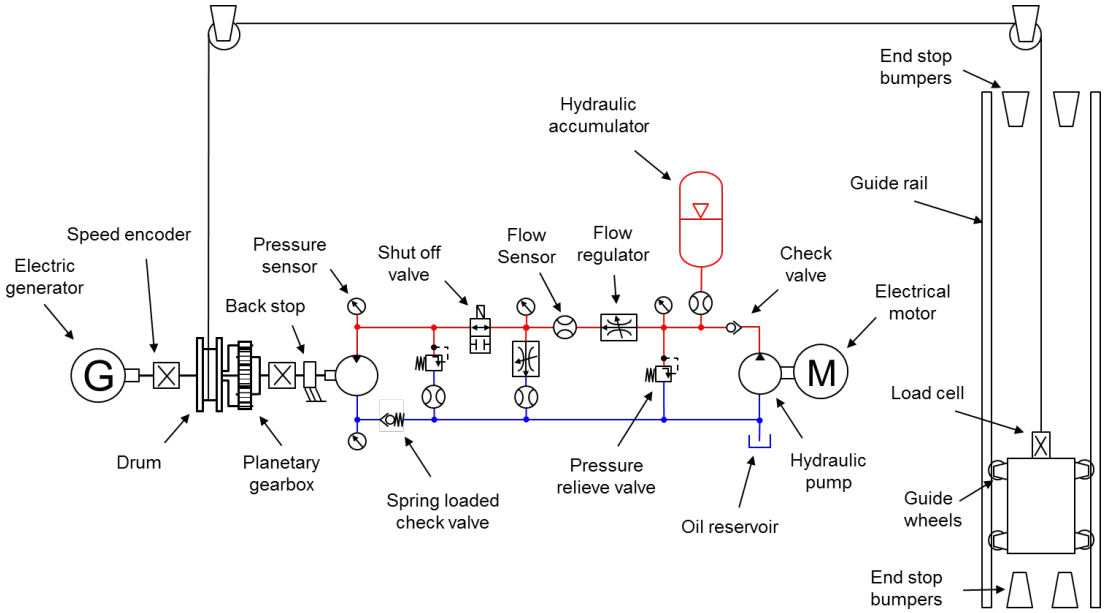

Figure 12.1: Schematic overview of components in the test rig.

feedback from the machinery to the buoy model running in the control system and therefore it was not possible to test the influence of OHT's system on the buoy dynamics. Now, with the new test rig, the machinery and the control system are in a loop. The simulation model of the CPO WEC calculates the required flow based on simulated wave excitation and measured pressure feedback from the test rig. The control system requests the proportional flow control valve to provide that flow. Thereafter, a new pressure value is measured and sent to the simulation model, which simulates the buoy dynamics for the next time period. The simulation model calculates the required flow and sends it back to the actuator and this goes on in a continuous loop. A high-level overview of the HIL simulation environment is shown on figure 12.2. In order to reduce the costs of the test rig, the functions that require more computational power, such as WEC simulation models and the damping force control, were run on a PC instead of a real-time hardware. The data acquisition and control were handled on a real-time hardware, CompactRio from National Instruments, that was reused from the previous test rig.

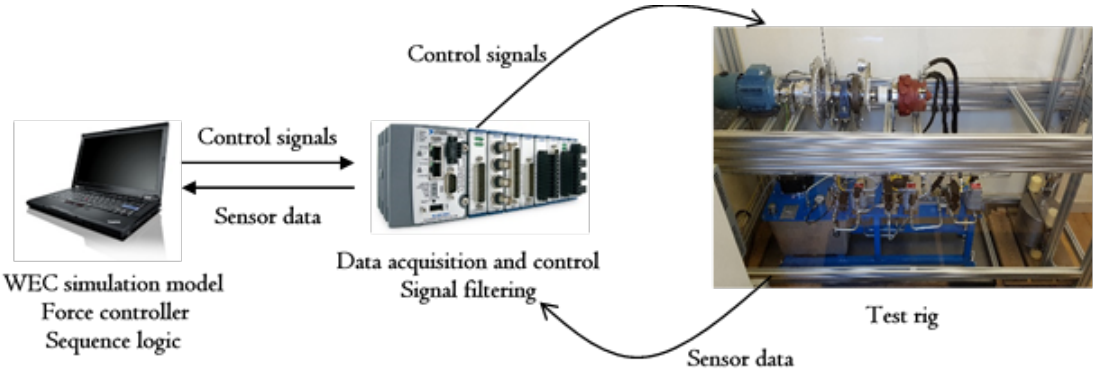

Figure 12.2: High-level overview of the HIL simulation environment.

The HIL simulation environment is based on National Instruments products Labview and Veristand, which integrate well with Mathworks Simulink that had to be expanded with Matlab coder and Simulink coder tool boxes. Labview is used to program the CompactRio hardware to do different tasks, such as receive and filter sensor data, send control signals to actuators, receive and send data to the simulation PC, handle emergency scenarios etc. Veristand is used to connect the inputs and outputs of the different simulation models and functions that were compiled using the Matlab and Simulink coder toolboxes to a file format that can be executed on Veristand. Veristand is also used to define an execution order for the simulation models. Moreover, an extension of Veristand called Stimulus Profiler Editor is used to define a sequence for running the test rig. A custom device was created in Veristand to share variables between the simulation PC and the CompactRio. Finally, a simple GUI was created in Veristand to easily control and monitor the test rig. A screenshot of the GUI for a test program is shown in figure 12.3.

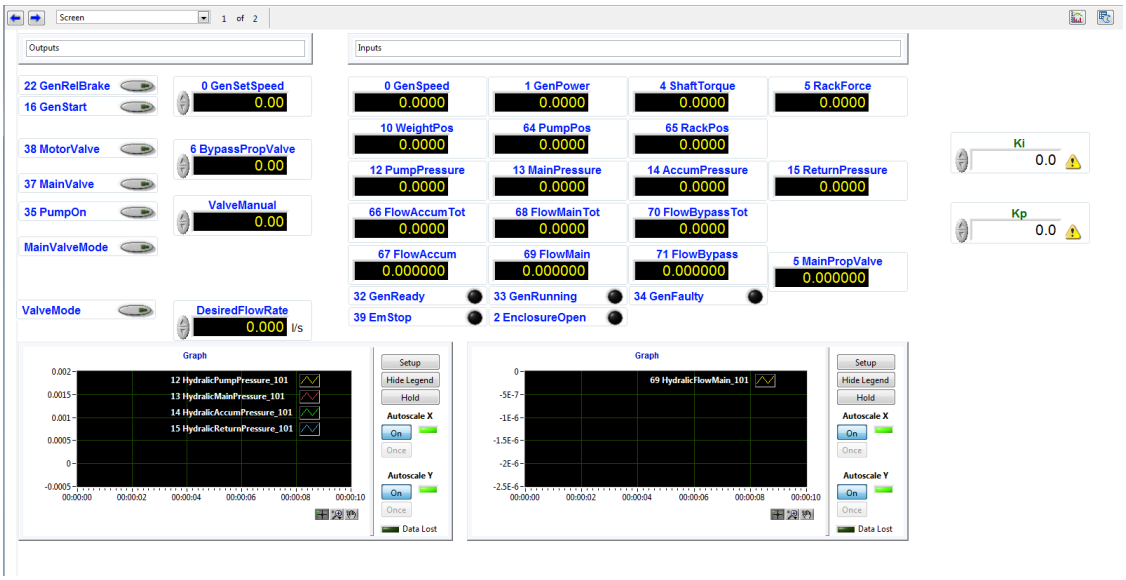

Figure 12.3: GUI of the test program for the test rig.

Due to insufficient time in the project and the delay in the delivery of the hydraulic system by PMC, no HIL simulation was able to be conducted. However, a simple test program was developed to demonstrate the working principle of the OHT's system. A video of a demonstration can be found on the following link. In the video the hydraulic pump is rotating with a varying speed, i.e. varying power, representing the irregular motion of the waves. One can clearly see that the irregular motion of the waves is transferred to the weight, making the weight follow the wave/buoy motion and at the same time the electric generator is rotating with a constant speed, i.e. outputting constant power.

Figure 12.4: A picture of the test rig built during the project.

13

Conclusions

In this thesis, a complete model of a hydraulic collection system with central storage and conversion to electricity, was developed and implemented in Matlab/Simulink. Much effort was put on modelling of the losses in the hydraulic system and vectorization of the complete model, including the wave energy converter, to enable efficient simulations. A model predictive control strategy was implemented that controls the PTO force in a discrete manner by determining the optimal number of engaged pumps at the beginning of each stroke. It was found that direct maximization of the captured power with one control input horizon does not lead to an optimal solution. The objective function was modified by adding a kinetic energy term to maximize the captured power and preserve energy in the buoy for the stroke after. Simulation study was performed with the developed simulation model and control strategy to understand system dynamics, produce necessary load data for system design and component sizing, and measure performance of the system. Moreover, a simple grid frequency control algorithm was implemented and simulation sweeps were performed with different storage configuration to estimate added value from increasing the storage capacity of the system. In addition, a new test rig was built and a hardware-in-the-loop simulation was set up. A simple program was developed in Veristand to test the operation of the test rig and demonstrate the basic functionality of the OHT's storage system. Finally, an extensive report was written that describes the work done during the project.

The project has demonstrated that the power capture in larger waves, $H_s > 2.25m$, can be increased with the hydraulic PTO with multiple pump damping force technology compared to the electric PTO with two sets of one-way flywheel and generator. This resulted in higher overall power capture in the Billia Cro site with the hydraulic PTO. Nevertheless, the final electric output was lower with the hydraulic system due to higher losses.

A 500-ton counterweight with 70-meter available height and the hydraulic collection system makes it possible to down-rate the complete electrical power generation system to 10 MW, which is located in the central tower. Constant power output corresponding to the average captured power in each sea state could however not always be maintained. Maintaining constant output power is anticipated to be an important feature in a future energy market with a higher share of renewable energy, for which pricing mechanisms are suggested to give revenue incentives to power producers, that can provide a stable and planned power production.

Furthermore, considerable added value from scaling up the gravity storage to larger capacity and applying time shifting and grid charging features to the system has been

quantified with simulations where suggested future energy market mechanisms have been used. A 7500-ton weight with 122-meter height increases the annual output from 29 GWh to 42 GWh. Revenues from the array installation increased by 70% with an assumed pricing model for the day-ahead and real-time markets. This is believed to be a conservative result based on early LCoE targets for the wave energy sector of 150 EUR/MWh. With future cost reduction targets to 60 EUR/MWh for the wave and tidal sector, while the trend for the LCoE for real-time services is increasing, these features would triple the revenues from the installation.

Finally, the life time of the pumps and motors were calculated based on a load data produced with the help of the developed model. The results show that less than 10% of the pump units and less than 20% of the motors are expected to be replaced during the 25-year life time of the system.

To conclude, during the project, a lot of new insights were gained and lessons learned, which lead to modifications of the initial design of the system and change of some of the objectives that were assigned in the beginning of the project. Therefore, some of the initial goals were not accomplished at all or partially accomplished. However, they were compensated by achieving other objectives that appeared during the course of work. Due to insufficient time, it was not possible to perform simulation study with W4P's buoy. Moreover, there was a long delay with the delivery of the hydraulic system for the test rig that did lot leave any time for performing an actual HIL simulation. However, the efficient and flexible simulation model, developed during the project, allowed us to achieve the main objectives and adapt to the system changes. As a result, despite some delay, the project got successfully delivered to the Swedish Energy Agency.

14

Future work

Further work is required in several areas of the system, which are outlined in this section.

Power capture can be further increased. More detail to the multi-pump damping force technology may be beneficial, which can be provided by selecting different sizes of the pump units. Also the algorithms to select the optimal damping force for each wave stroke can be improved, for instance, by taking into account the losses in the drive train. Constraints to limit stroke length and maximum velocity need to be added to the algorithm and their impact on the performance needs to be investigated. The developed controller needs to be tested in terms of robustness to model and prediction errors. Furthermore, a decentralized control strategy can be used to decrease the peak power before the storage and to enable a more optimal usage of the storage by reducing or eliminating the spilled energy from the system. This is actually one of the unaccomplished objectives during the project due to the insufficient time of the project.

The drive train of the buoys and tower were modelled by assuming ideal load sharing. Due to finite machine precision, finite stiffness of shafts and gears and nonlinear frictions effects, load balancing issues can occur. Therefore, each drive train unit needs to be modelled individually by accounting for these effects and vibration analysis needs to be performed.

During the project, the test rig was run only in open loop for demonstration purposes. Therefore, an actual HIL simulation can be performed to test the developed models and control strategy.

The wave-to-wire efficiency of the hydraulic collection system can be improved in several ways. The generator loss map needs to be updated to the most suitable generator model for the tower. Pipe losses can be reduced by increasing the pipe diameter or reducing the peak flow rates in the system by selecting larger accumulators or by using flywheels together with the pumps.

The mechanisms of the future energy market needs to be further investigated and modeled to get a more detailed and accurate view on the added value from integrating storage in a wave energy array.

The gravity storage technology needs to be benchmarked against other storage technologies, like flywheels and especially Li-on batteries, which has experienced rapid advancement in the recent years due to trend for electrification of vehicles and need for decentralization of the grid.

The practical viability of the proposed hydraulic PTO and collection system would

need to be validated by detailed testing of the physical components and system.

Bibliography

[1] A. Rashid, A. Ghodrati, "Modelling and Simulation of a Power Take-off in Connection with Multiple Wave Energy Converters", *Bachelor's Thesis in Electrical Engineering*, Blekinge Institute of Technology, Karlskrona, Sweden, 2015.

[2] M. Sidenmark, A. Rashid, A. Ghodrati, A. Hultgren, "Modelling and Simulation of a Collector Hub System Combining Core Technologies", *Proc. 11th European Wave Tidal Energy Conf.*, Nantes, France, 2015

[3] J. Falnes, "Ocean Waves and Oscillating Systems", *Cambridge University Press*, 2002.

[4] J. V. Ringwood, G. Bacelli, F. Fusco, "Energy-Maximizing Control of Wave-Energy Converters", *IEEE Control Systems Magazine*, vol. 34, no. 5, pp. 30-55, 2014.

[5] F. Fusco and J. Ringwood, "A simple and effective real-time controller for wave energy converters", *IEEE Trans. Sust. Energy*, vol. 4, no. 1, pp. 21–30, 2013.

[6] J. Hals, J. Falnes, and T. Moan, "Constrained optimal control of a heaving buoy wave-energy converter", *J. Offshore Mech. Arct. Eng.*, vol. 133, pp. 011401.1–.15, Nov. 2010.

[7] G. Li and M. Belmont, "Model predictive control of an array of wave energy converters," in *Proc. 10th European Wave Tidal Energy Conf.*, Aalborg, Denmark, 2013.

[8] J. Cretel, A. Lewis, G. Lightbody, and G. Thomas, "An application of model predictive control to a wave energy point absorber", in *Proc. IFAC Conf. Control Methodologies Technology Energy Efficiency*, 2010, pp. 267–272.

[9] J. Hals, J. Falnes, and T. Moan, "A comparison of selected strategies for adaptive control of wave energy converters", *J. Offshore Mech. Arct. Eng.*, vol. 133, no. 3, pp. 031101–031113, 2011.

[10] http://www.corpowerocean.com

[11] http://www.waves4power.com

[12] "Flow of Fluids Through Valves, Fittings, and Pipe, Crane Valves", North America, Technical Paper No. 410M

[13] R. D. Blevins, "Applied Hydraulics Handbook", *Kriegel Publishing Company*, Malabar, Florida, 1984

[14] L. Ljung, T. G, "Modelling of Dynamical Systems", *PTR Prentice Hall*, New Jersey, 1994

[15] R. Zanasi, "Power Oriented Modelling of Dynamical System for Simulation", *IMACS Symp. on Modelling and Control of Technological System*, Lille, France, May 1991.

[16] West D. B., "Introduction to Graph Theory", *Prentice Hall*, 2001.

[17] A. Hultgren, M. Lenells, "Stability of a Nonlinear Hamiltonian Observer Applied to a General Electrical Network", *43rd IEEE Conference on Decision and Control*, December 14-17, 2004, The Atlantis Paradise Island, The Bahamas, pp 4806-4811

[18] H.E. Koenig, W.S. Blackwell, "Linear graph theory – a fundamental engineering discipline", *IRE Transactions on Education 3* (1960) 42-49.

[19] A. Bozzetto, N. Bianchi, E. Tedeschi, "Modeling, Control and Performance Assesment of a Wave Energy Converter, equipped with an All-Electric Power Take-Off", *M.Sc. Thesis, Norwegian University of Science and Technology,* Norway, 2013

[20] E. Jansson, "Multi-buoy Wave Enegy Converter", *M.Sc. Thesis, Uppsala University,* Sweden, 2016

[21] K. Hasselman, T.P. Barnett, E. Bouws, H. Carlson, D.E. Cartwright, K. Enke, J.A. Ewing, H. Gienapp, D.E. Hasselmann, P. Kruseman, A. Meerburg, P. Mller, D.J. Olbers, K. Richter, W. Sell, and H. Walden. "Measurements of wind-wave growth and swell decay during the Joint North Sea Wave Project (JONSWAP)". Technical Report 12, German Hydrographic Institute, 1973.

[22] Det Norske Veritas AS, "Environmental Conditions and Environmental Loads", 2014

[23] J. Falnes, "On non-causal impulse response functions related to propagating water waves", *Applied Ocean Research*, 17(6):379-389, 1995.

[24] W.E. Cummins, "The Impulse Response Function and Ship Motions" Technical Report, David Taylor Model Dasin-DTNSRDC, 1962.

[25] S. Kung. "A new identification and model reduction algorithm via singular value decomposition". *In Proc. Twelth Asilomar Conf. on Circuits, Systems and Computers*, pages 705–714, November 6-8 1978.

[26] M. Hall and A. Goupee, "Validation of a lumped-mass mooring line model with DeepCwind semisubmersible model test data", *Ocean Engineering*, vol. 104, pp. 590–603, Aug. 2015.

[27] J. H. Todalshaug, G. S. Asgeirsson, E. Hijalmarsson, J. Maillet, P. Möller, P. Pires, M. Guerinel, M. Lopes, "Tank testing of an inherently phase controlled Wave Energy Converter", *Proceedings of the 11th European Wave and Tidal Energy Conference*, September 2015, Nantes, France

[28] Leon E. Borgman. "Random hydrodynamic forces on objects." *Ann. Math. Statist.*, pages 37–51, 1967

[29] Åström, Karl J. Hägglund, Tore. (2006). "Advanced PID Control." ISA.

[30] Carlos Vazquez, "Security of supply in the Dutch electricity market: the role of reliability options", Report IIT-03-084IC, 2003.

[31] Lazard, "Lazard's levelized cost of storage, v2.0", 2016.

[32] Australian Energy Market Operator, "Guide to ancillary services in the national electricity market", 2015

[33] Tianzhi Zhou, "Damping Profile Research for Corpower Ocean's Wave Energy Converter", *Master's Thesis in Optimization and Systems Theory*, Royal Institute of Technology, Stockholm, Sweden, 2016.

[34] https://www.hydac.com/uploads/media/E3554-0-06-11_DKS_lq.pdf

[35] http://www.hydba.com/es/wp-content/uploads/2017/01/Ficha-t%C3%A9cnica-CA-Ingl%C3%A9s.pdf
[36] http://www.hydba.com/es/wp-content/uploads/2017/01/Ficha-t%C3%A9cnica-CBP-Ingl%C3%A9s.pdf

A

Appendix 1

The pressure losses of 4-port CA50 and 8-port CBP140 series are shown respectively in figure A.1 and A.2.

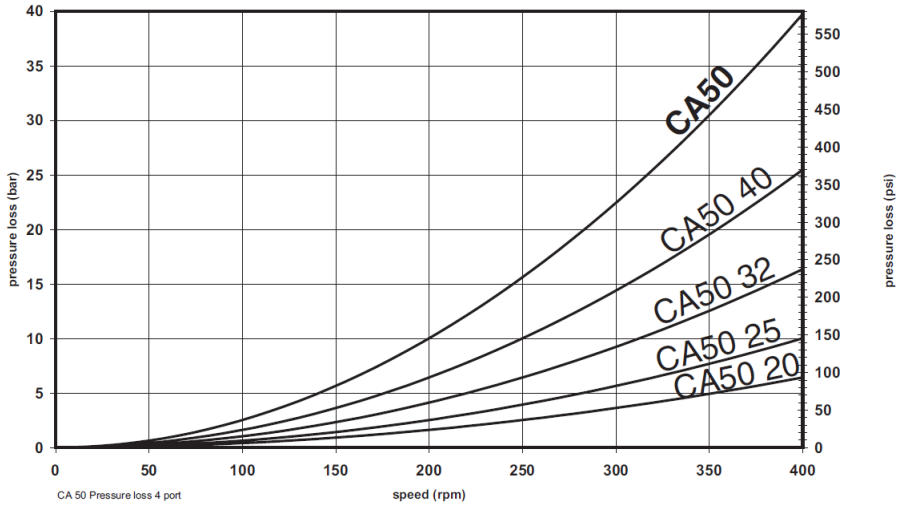

Figure A.1: 4-port CA50 motors hydraulic pressure loss.

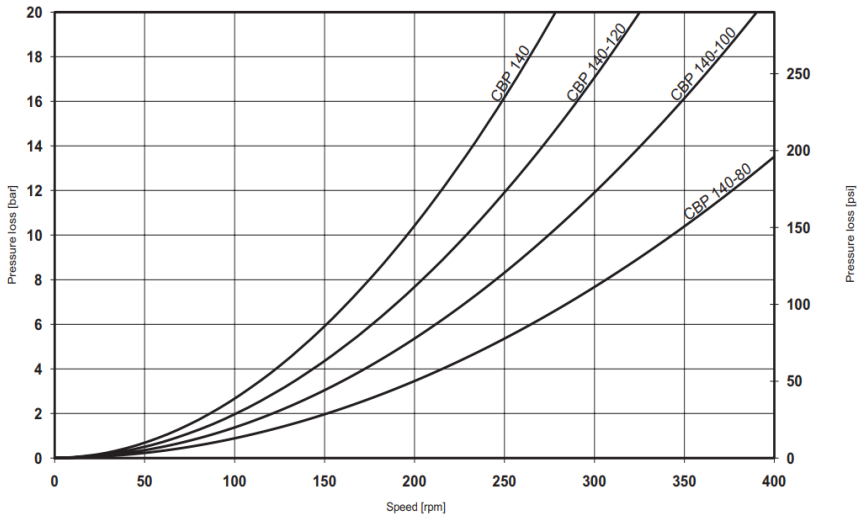

Figure A.2: 8-port CBP140 motors hydraulic pressure loss.

The volumetric losses of the 4-port CA50 and 8-port CBP140 motors for oil viscosity of 40 cSt are shown respectively in figure A.3 and A.4. For a different oil visocisty the graph for the volumetric losses must be rescaled according to the graph A.5.

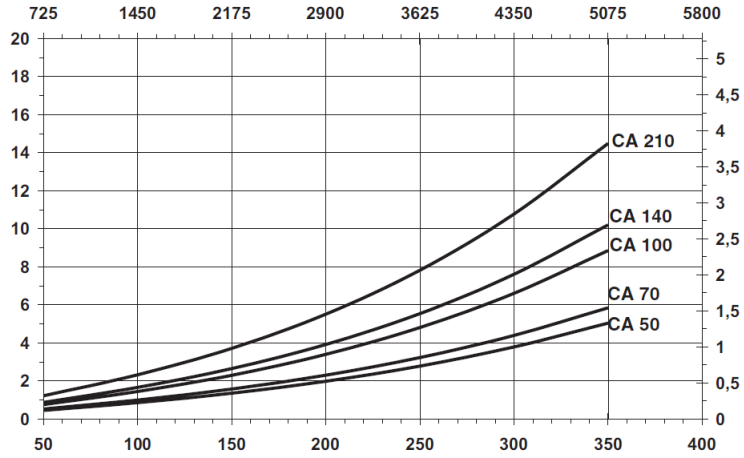

Figure A.3: 4-port CA50 volumetric losses with oil viscosity of 40 cSt.

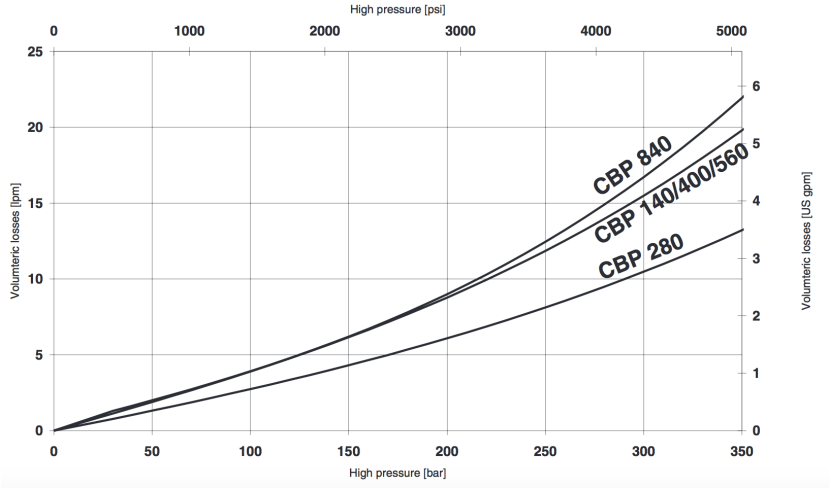

Figure A.4: 8-port CBP140 volumetric losses for oil viscosity of 40 cSt.

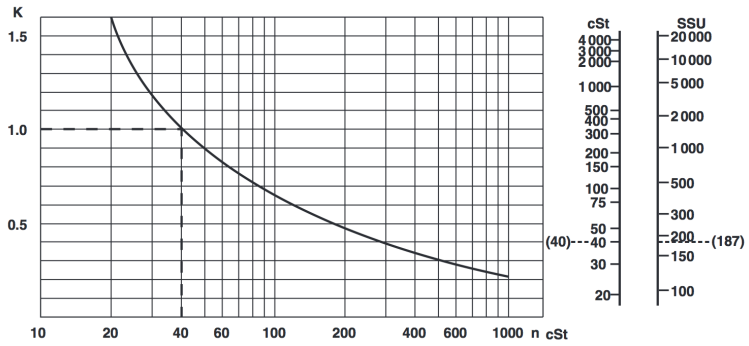

Figure A.5: Scaling of the volumetric losses for different oil viscosity.

The efficiency mapping of the 4-port CA50 and 8-port CBP140 motors as a function of speed and torque are shown respectively in figure A.6 and A.7. It can be seen that the most optimal operating region for hydraulic pumps and motors is the low-speed and low-torque region.

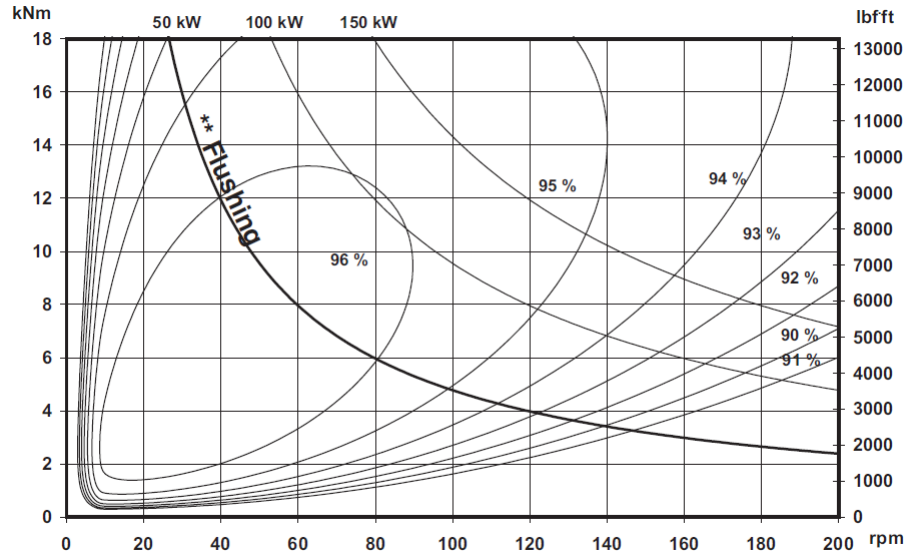

Figure A.6: 4-port CA50 efficiency map.

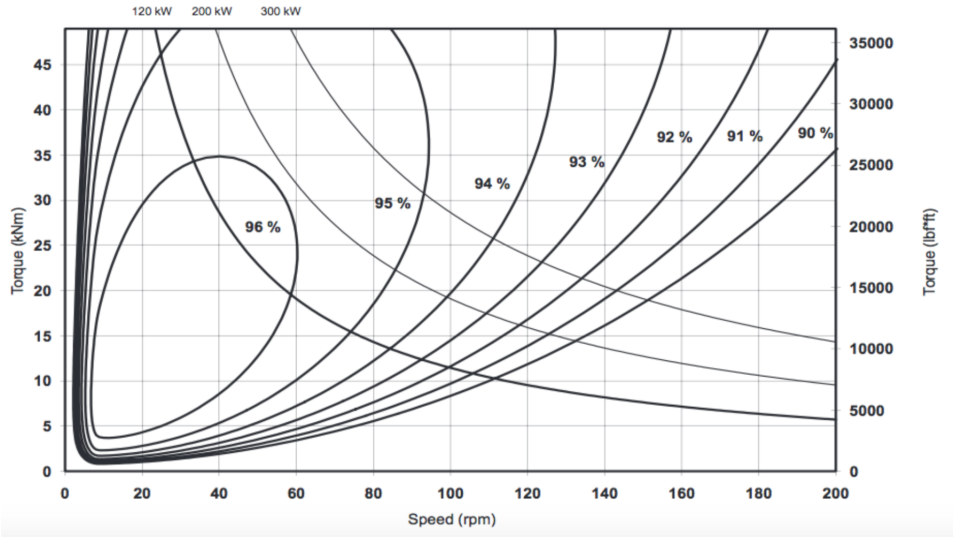

Figure A.7: 8-port CBP140 motor efficiency map.

All loss curves and efficiency mappings are extracted from the data sheets of CA, [35], and CBP, [36], motor series.

B

Appendix 2

The Appendix shows the Simulink models of the main components of the wave energy array.

The main Simulink model is shown in figure B.1. It comprises of the *Buoy* and *Collection system* variant subsystem blocks. The *Buoy* variant subsystem holds the Waves4Power and CorPower simulation models, which are active one at a time depending on the variant condition. The *Collection system* variant subsystem enables and disables the OHT's hydraulic collection system, depending on whether hydraulic or electric collection is used.

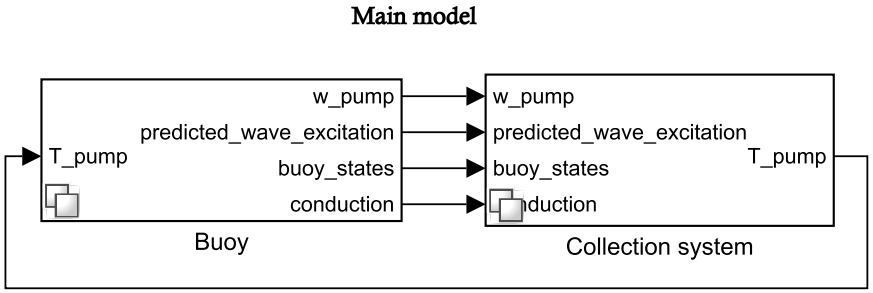

Figure B.1: Main model.

The OHT's collection system comprises of the *Hydraulic system* and *Tower* subsystems, as shown in figure B.2.

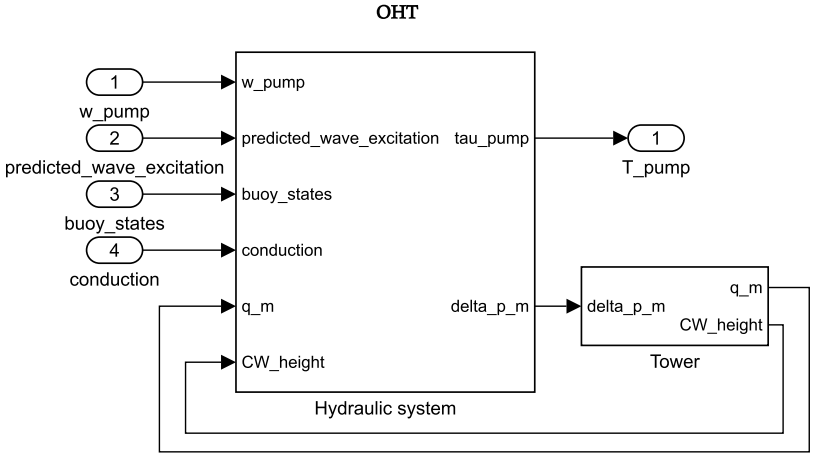

Figure B.2: OHT's hydraulic collection system and tower model.

The model under the *Hydraulic system* subsystem block hold the complete model of the hydraulic collection, comprising pumps and their control, pipes, hydraulic accumulators, pressure relief valves as shown in figure B.3. The model of the hydraulic motor is situated in the *Tower* subsystem, since motors are seen as part of the tower drive train.

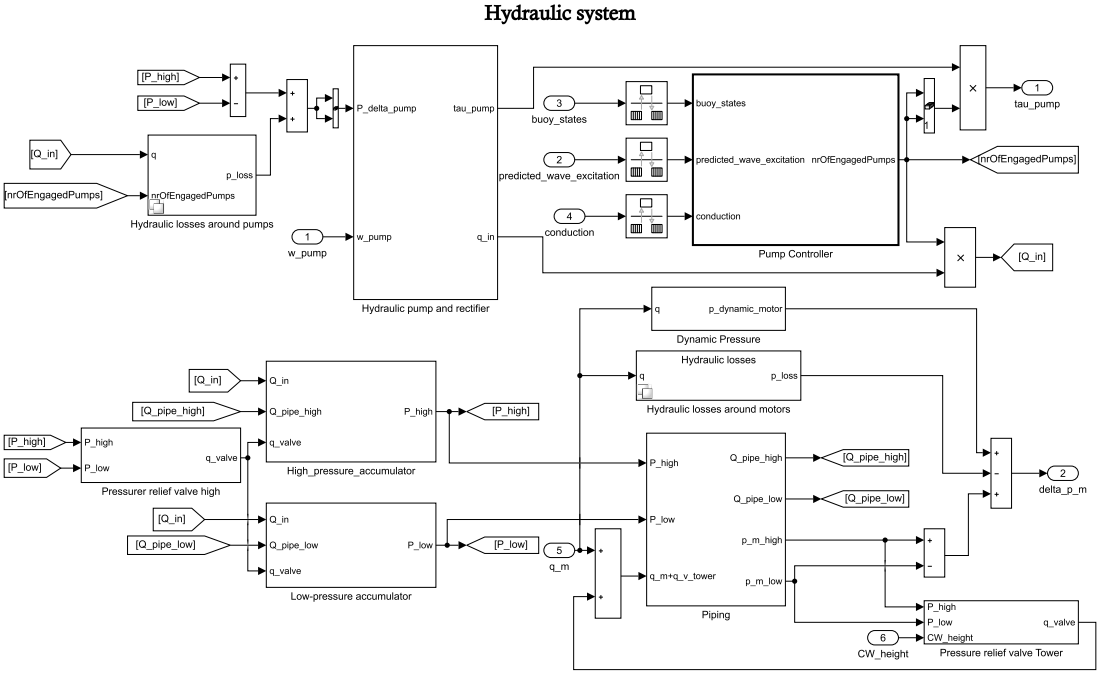

Figure B.3: OHT's hydraulic collection system.

The loss models of each components is implemented in a variant subsystem to be able to enable and disable them.

The piping model is shown in figure in B.4.

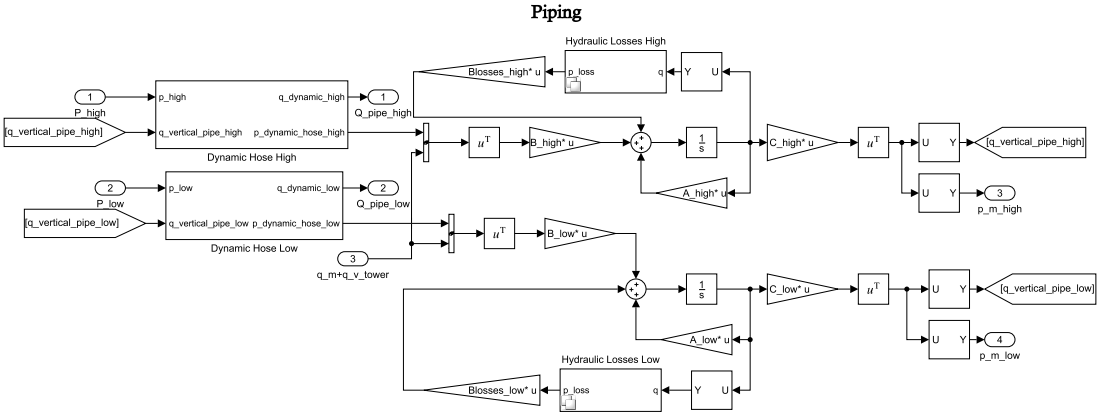

Figure B.4: Hydraulic piping model.

The pump and rectifier models are combined in one subsystem, as shown in B.5.

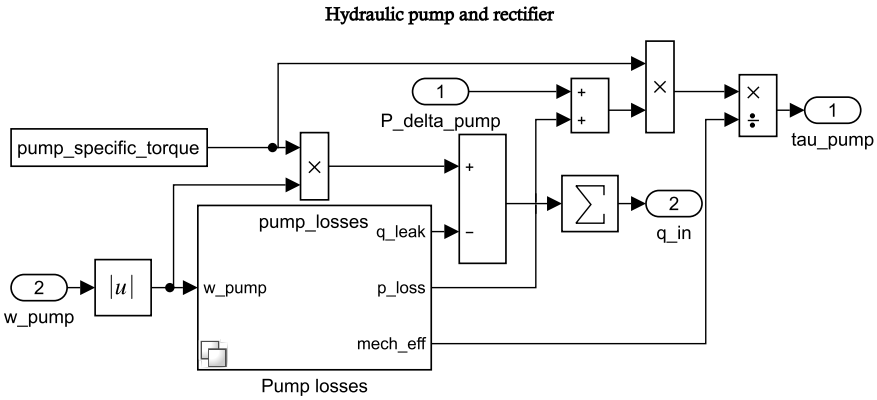

Figure B.5: Hydraulic pump and rectifier subsystem.

The pump losses comprise of volumetric/flow losses, pressure losses and mechanical losses. The flow losses and the pressure losses are modelled using *Interpolation with Prelook-up* blocks with real component loss data, ash shown in figure B.6.

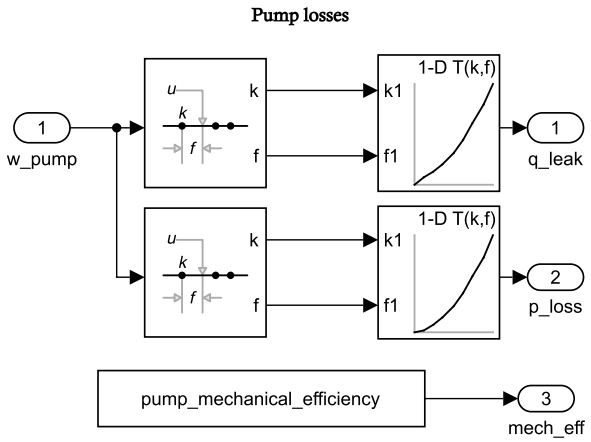

Figure B.6: Hydraulic pump losses.

The hydraulic accumulators are implemented in two different ways: one with thermodynamic equation and another with using specific heat ratio. In the former the thermodynamic losses can be incorporated. They are shown respectively in figure B.8 and B.7.

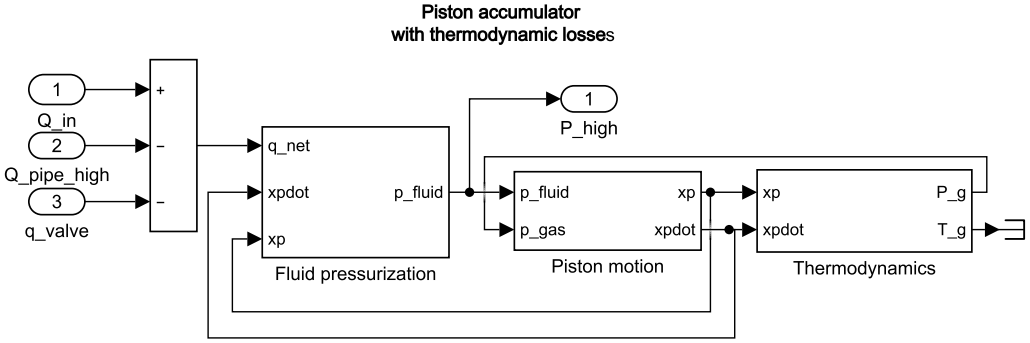

Figure B.7: Piston accumulator with thermodynamic losses.

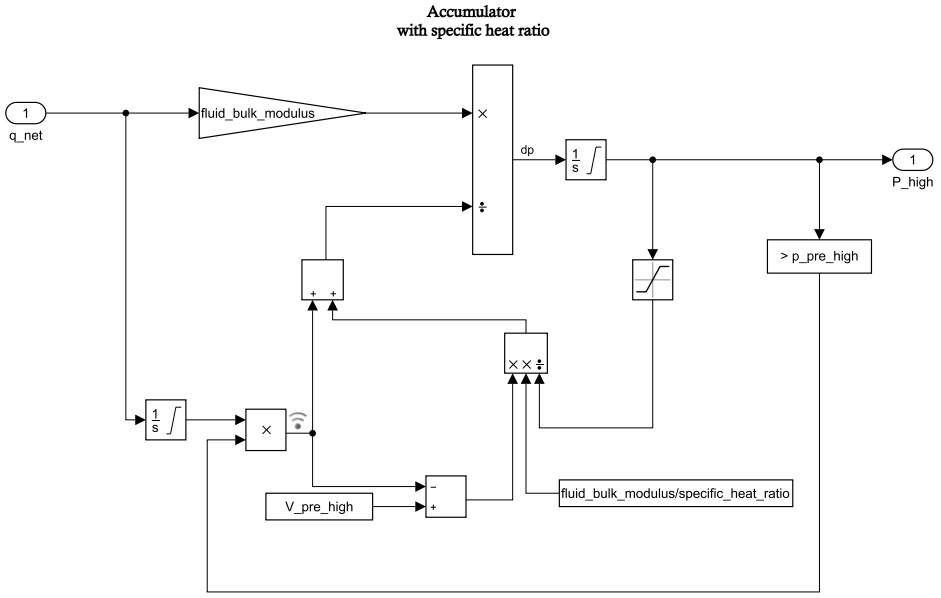

Figure B.8: Hydraulic pump losses.

The *Tower* subsystem comprises of the models of the hydraulic motors, generators and their control, planetary gearboxes and the gravity weight. It is presented in figure B.9.

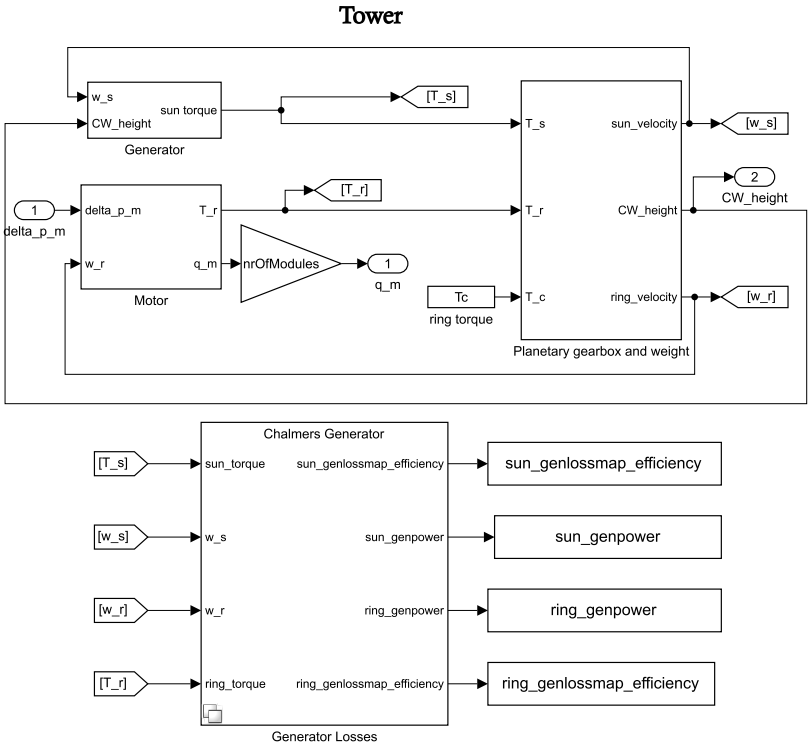

Figure B.9: Tower model.

The planetary gearbox and weight model is shown in figure B.10.

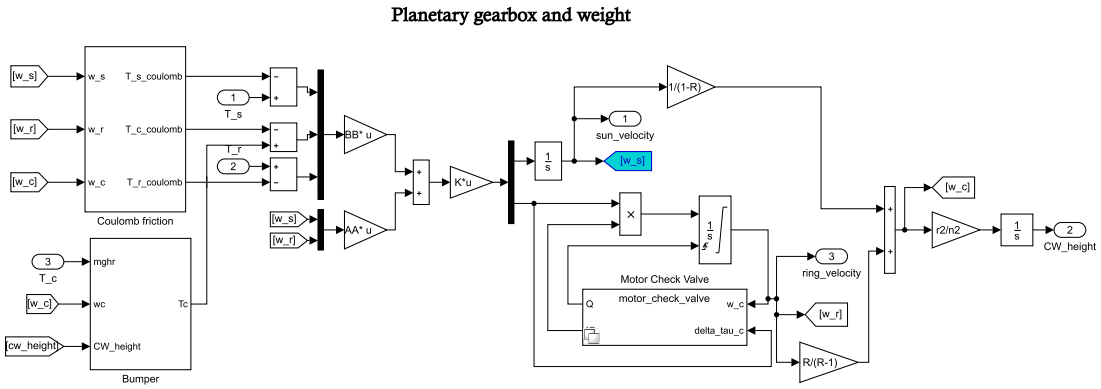

Figure B.10: Planetary gearbox and weight model.

The generator and its controller are shown in figure B.11.

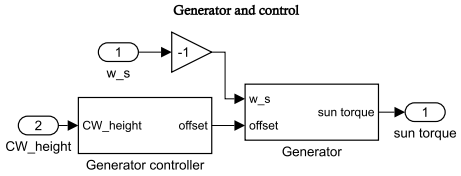

Figure B.11: Generator and its control

The hydraulic motor and its loss model is identical to one of the hydraulic pump. Therefore, we will omit presenting it here.

It should be pointed that the presentation of the Simulink model was done on a high level to solely give an idea on how everything is connected.